Deployment Dynamics Analysis of Origami-Folded Spacecraft Structures with Elastic Hinges

by

JoAnna L. Fulton

B.S., Mechanical Enginering, University of Florida

M.S., Aerospace Engineering Sciences, University of Colorado at Boulder

A thesis submitted to the

Faculty of the Graduate School of the

University of Colorado in partial fulfillment

of the requirements for the degree of

Doctor of Philosophy

Department of Aerospace Engineering Sciences

2020

Committee Members:

Prof. Hanspeter Schaub

Prof. Francisco Lopez Jimenez

Dr. Olive Stohlman

Prof. Penina Axelrad

Prof. Robert Marshall

Fulton, JoAnna L. (Ph.D., Aerospace Engineering Sciences)

Deployment Dynamics Analysis of Origami-Folded Spacecraft Structures with Elastic Hinges

Thesis directed by Prof. Hanspeter Schaub

Spacecraft design is inherently limited and dictated by available launch vehicle capabilities, motivating the development of a wide variety of deployable spacecraft structures. These structures are developed to meet the communication, operation, and scientific objectives of the spacecraft mission, and therefore the successful deployment of the structure is required for overall mission success. Typical analysis of deployable spacecraft structures spans questions of structural stiffness and stability, vibration modes, thermal stability, and deployment dynamics. In this thesis, only the deployment dynamics are of interest. Validation and verification of deployment for deployable structures is primarily achieved through rigorous testing, and this is sometimes presented in tandem with complex finite element simulation or a simplified model approximation. The key questions of this validation typically regard what the deployment motion looks like and are answered through analysis of the deployment dynamics states. Therefore, deployment dynamics analysis plays a key role while also providing a central challenge for deployable structures development.

An emerging area in the deployable structures field is referred to as origami structures and takes primary inspiration from origami folding techniques. These are developed to stow flat structures with large area to size ratio relative to the spacecraft bus, such as solar and phase arrays, star occulters, and reflector antennas. A central challenge for origami structures is the deployment dynamics and deployment actuation of the folded structure and spacecraft system. A novel lightweight solution for deployment actuation is to integrate strain energy hinges that can also facilitate folding. Deployment dynamics of such a system would typically be studied through finite element analysis (FEA). However, for a structure with multiple high strain hinges, FEA modeling would require significant computational time and skill, as these hinges exhibit large deformations of shell structures with non-linear behavior. This limits the ability to explore parameter design spaces and iterate towards more optimal solutions. An alternative method for studying the system dynamics that uses multi-body dynamics and a simplified hinge representation is the focus of this thesis. In this approach, fold panels are treated as rigid bodies and the flexible joints are represented by internal forcing functions. In this thesis, a model to represent the hinge mechanics is designed as a function of the hinge's multiple degrees of freedom, as defined by the relative position and orientation states. This model is designed to be implemented in a multibody dynamics algorithm customized for origami-folded deployable spacecraft structures. The methodology aims to provide an approximation that enables sufficient deployment dynamics simulation accuracy without a full FEA simulation of the system.

The multibody dynamics modeling approach for this thesis implements the Articulated Body Forward Dynamics algorithm and Spatial Operator Algebra for free-flying spacecraft systems with closed-chain constraint enforcements and the applications of this approach for deployable structures is demonstrated. Constraint stabilization is discovered to be the primary challenge for scaling this approach to systems of many folding panels. An approach for modeling high strain tape spring hinges for simulation of free deployment dynamics is presented and applied to a high strain composite hinge sample. This study includes both an FEA database and experimental measurements, and concludes that the high strain composite materials contain a level of variability that makes repeatability and behavior prediction challenging. An additional study of a folding hinge with two spring steel tape springs is developed and implemented in prototype structure validation efforts. A novel folded deployable structure is designed and constructed with a segmented, multi-DOF hinge, and a rigorous suite of deployment tests are conducted using videogrammetry for deployment data measurement. A full simulation of the prototype is constructed from the multibody dynamics model and the multi-DOF hinge model, and the predicted deployment behavior is evaluated against the testing. Additionally, the prototype deployment is replicated using an explicit dynamic FEA analysis for a performance comparison. The models demonstrate strong correlation for deployment time predictions across the states.

Dedication

to those who find the strength to persist.

may your dreams never end!

Acknowledgements

First I'd like to thank and acknowledge my research advisor, Dr. Hanspeter Schaub, for his support over the course of my graduate studies at CU, and for his collaboration and support of this thesis project. Thank you for giving me the opportunity to pursue my research interests and taking the risk with me on novel challenges. Thanks to Dr. Abhi Jain for chatting with me about Spatial Operator Algebras and entertaining all my questions. Thanks to my committee members, Dr. Penina Axelrad, Dr. Francisco Lopez-Jimenez, Dr. Olive Stohlman, and Dr. Robert Marshall, for your time and contributions to the development of this thesis. Additional thanks to Dr. Olive Stohlman for your time and mentorship through the NSTRF program, and for generously hosting me at NASA Langley. Thanks also to Dr. Jonathan Sauder for hosting me at JPL and for your thoughtful mentorship and advocacy. Thanks to Gregg Freebury, Tendeg, LLC, and JPL for lending me the space and equipment to complete my deployment tests. I'd also like to thank my fellow AVS lab members, past and present, for your camaraderie, collaboration, and discourse. You are too many to name, but I've appreciated sharing my time at CU with each of you.

I'd like to acknowledge the NASA Space Technology Research Fellowship program for funding this thesis project. Additional acknowledgements for the NSF Graduate Research Fellowship program and the Zonta Amelia Earhart Fellowship program for supporting me during my graduate studies. Finally, deep thanks to the Ann and H.J. Smead Department of Aerospace Engineering Sciences Smead Fellowship program for sponsoring me and for including me in this unique program. I'm grateful for all the ways the program has enriched my time at CU, professional and personal, and for the life long bond I've formed with the Smead family.

Special thanks to my father, Ted Fulton, for teaching me to prioritize my education and for giving me every opportunity to pursue it that you could. Thank you for raising me to believe there was nothing I couldn't learn how to do, and for leading me by example. Everything I have and have accomplished is because of you, so thanks Dad. Thanks also to my mother, Grace Kriese, for all your love, care, and prayers over the last few years. I'm so grateful for everything you do for us. And thanks to my sister, Liz, for being there for me like no one else could, and for always picking up the phone. I love you.

Thanks to all my fellow sisters in STEM, my fellow Pleiades - Jenny Kampmeier, Amy DeCastro, Allison Duh, Emily McAnally, Ann Dietrich, Marielle Pellegrino, Julia Taussig, Greta Parks, and so many others - for being on this journey with me. Without your friendship, acknowledgements, and validation, I really would not have found the strength to persist and finish this thesis. Our hikes, trips, belays, meals, and long chats were the sunshine and nourishment that allowed me to grow roots and flourish here. I look forward to the day where we all find ourselves exactly where we dream of being.

And finally, thanks to my sun, my moon, and all my stars, Matthew Pierson. For all the moments we've shared over the last three years, all the ways you make my every day easier, and for loving and supporting me for who I am, just as I am. I can hardly imagine completing this thesis (and surviving a pandemic!) without you in my life. Thank you.

Contents

Tables

Table

Figures

Figure

Chapter 1

Introduction

1.1 Motivation

Deployable structures have played critical roles for spacecraft missions since the beginning of the space age, and can be traced back to the spin-tensioned whip antenna of Explorer 1. Spacecraft design is inherently limited and dictated by available launch vehicle capabilities, motivating the development of a wide variety of deployable spacecraft structures. These structures are developed to meet the communication, operation, and scientific objectives of the spacecraft mission, and therefore the successful deployment of the structure is required for overall mission success.[1] Design development of deployable structures is primarily achieved through iterative prototyping and testing, a process that often yields novel research products that are shared through the community. Many examples of successful design efforts and flight projects are found in the literature,[2,3,4,5,6] and a comprehensive review of deployable structures will not be provided here as it encompasses a broad library of work. Typical analysis of deployable spacecraft structures spans questions of structural stiffness and stability, vibration modes, thermal stability, and deployment dynamics.[7] In this thesis, only the deployment dynamics are of interest. Validation and verification of deployment for deployable structures is primarily achieved through rigorous testing, and this is sometimes presented in tandem with finite element simulation or a simplified model approximation.[8] The key questions of this validation typically regard what the deployment motion looks like and are answered through analysis of the deployment dynamics states. Therefore, deployment dynamics analysis plays a key role while also providing a central challenge for deployable structures development.

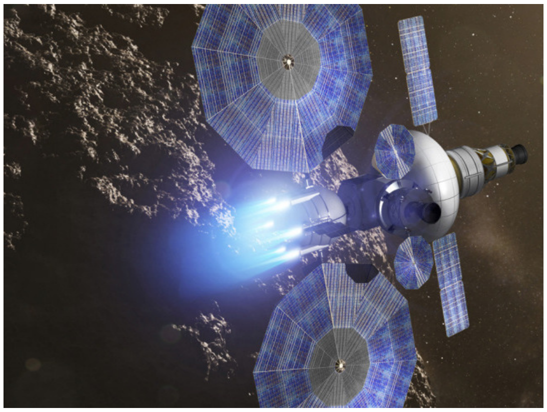

(a) ATK MegaFlex[9]

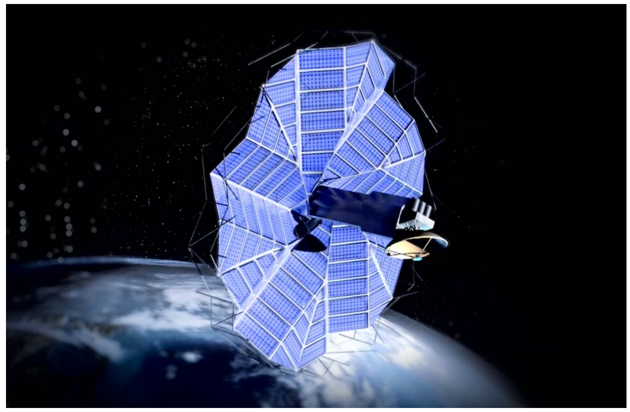

(b) BYU design[10]

Figure 1.1: Folded deployable spacecraft structure solar array concept art.

There are several classifications of deployable space structure architectures that have been studied and developed in the literature, such as membranes, shells, booms, and trusses, and several broad reviews of these have been published over time, as the field has developed.[11,12,13,14,15] An emerging area in the deployable structures field, that is discussed in these reviews, is referred to as origami structures and takes primary inspiration from origami folding techniques. These are developed to stow flat structures with large area to size ratio relative to the spacecraft bus, such as solar[16,17,18] and phase[19,20] arrays, star occulters,[21] and reflector antennas.[22,23] Concept imagery is shown for two solar array designs in Figure 1.1, where the ATK design uses a cable and motor system to actuate deployment and the BYU design uses an external perimeter truss and cable system.[24]

A central challenge for origami structures is the deployment dynamics and deployment actuation of the folded structure and spacecraft system. A novel lightweight solution for deployment actuation is to integrate strain energy hinges that can also facilitate folding.[25] Tape spring hinges are an intriguing innovation in hinge technology for deployable space structures. Compared to standard piano hinges, tape spring hinges are lightweight, eliminate rotational mechanical contact surfaces, and are self-actuating. An example of how this concept could be implemented physically with the Miura origami pattern is illustrated in Figure 1.2, and it is noted that even with minimal hinge actuation, 10 hinges are used to actuate the 12 panel assembly. Deployment dynamics of such a system would typically be studied through finite element analysis (FEA).[12] However, for a structure with multiple high strain hinges, FEA modeling would require significant computational time and skill, as these hinges exhibit large deformations of shell structures with non-linear behavior. This limits the ability to explore parameter design spaces and iterate towards more optimal solutions. An alternative method for studying the system dynamics that uses multi-body dynamics and a simplified hinge representation would provide significant gains in computation time, and is the focus of this thesis. In this approach, fold panels are treated as rigid bodies and the flexible joints are represented by internal forcing functions. In this thesis, a model to represent the hinge mechanics is designed as a function of the hinge's multiple degrees of freedom, as defined by the relative position and orientation states. This model is designed to be implemented in a multibody dynamics algorithm developed specifically for origami-folded deployable spacecraft structures. The methodology aims to provide an approximation that enables sufficient deployment dynamics simulation accuracy without a full FEA simulation of the system. The theory of this approach will be covered in Chapters 2 and 3, a deployment test campaign of the system will be presented in Chapter 4, and a final model demonstration and evaluation is presented in Chapter 5.

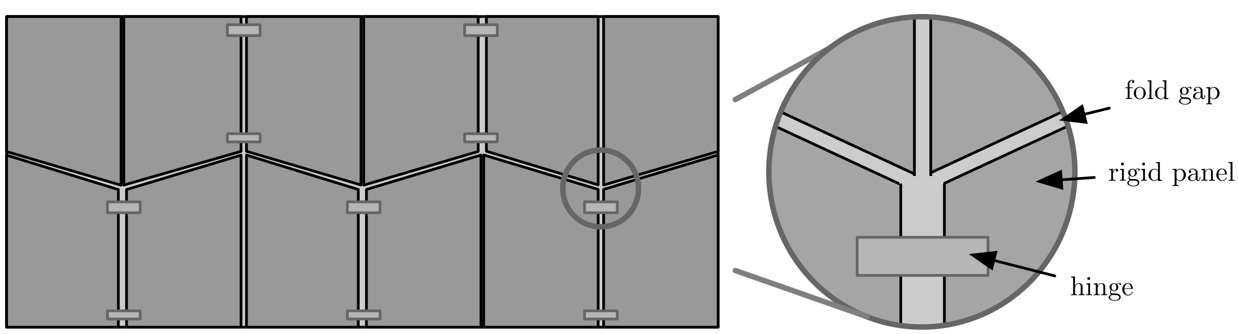

Figure 1.2: Example of a closed-chain origami-folded structure with tape spring hinge integration.

1.2 Background

1.2.1 Rigid Body Dynamics Analysis

Rigid body dynamics analysis theory traditionally begins with the classic and fundamental Newton's equation,

$$\boldsymbol{F} = m\boldsymbol{a} \tag{1.1}$$

Where $\boldsymbol{F}$ is the force applied to a body, m is the body's mass, and $\boldsymbol{a}$ is the linear acceleration of the body, as expressed in three dimensional Euclidean space, $\mathbb{R}^3$. Newtonian mechanics represents a first approach to understanding the motion of a single body or particle due to the forces acting on that body, and mathematically represents Newton's Second Law.[26] However for a general rigid body in three dimensional space, rotational motion and torques may also be applied to a body. This motion is described by the equally classic Euler's equation,

$$\dot{\boldsymbol{H}} = \boldsymbol{L} \tag{1.2}$$

Where $\dot{\boldsymbol{H}}$ is the change in angular momentum, and $\boldsymbol{L}$ is the torque or moment acting on the body.[27] For a single rigid body, the Eulerian and Newtonian equations are sufficient for describing the dynamics of a single rigid body. As additional rigid bodies are included in a model, the efficiency of the Newtonian and Eulerian approaches must be evaluated on a case-by-case basis. For example, the Eulerian approach is used extensively in the field of attitude dynamics and is appropriate for the development of models for momentum control devices, where compact and elegant solutions are often available.[28] However for multiple rigid bodies connected at several nodes, these approaches would require significant book keeping and are not ideal or feasible for implementation.

Generalized methods of analytical mechanics provide a suitable tool for larger systems of rigid bodies and provide the bases for many branches of dynamics analysis, where the coupling of rotational and translational motions across multiple rigid bodies are intrinsically captured in the expressions. For this reason, early analysis of the origami-folded system concepts were completed using Lagrangian mechanics,[29] and this work can be reviewed in Appendix A. Additionally, the author has applied this method to tethered deployable spacecraft systems analysis with good results.[30,31,32] Lagrange's equation provides an energy based approach to deriving the equations of motions by stating

$$\frac{\partial}{\partial t}\frac{\partial T}{\partial \dot{q}_i} - \frac{\partial T}{\partial q_i} = Q_i \tag{1.3}$$

where t is time, T is the kinetic energy, q_i are the generalized coordinates, and Q_i are the generalized forces and can represent conservative or non-conservative forces in the system.[28] While Lagrange's Equation is an elegant generalization of mechanics principles and is capable of generating equations of motion for any system by following this formula, in practice it is difficult to apply to large degree of freedom systems, or systems with a large number of generalized coordinates. This is due to the analytical challenges of deriving the partial derivatives of the kinetic energy and reorganizing the results into a numerically integrable format. Therefore, a significant area of dynamics research focuses on how to generate equations of motion in a manageable format and how to implement these equations in numerical integrators. A notable development from this research is Kane's Equations.[33] Kane's method develops equations of motion by first constructing a partial velocity table from the generalized coordinates and speeds, and then enforcing the equation

$$F_r + F_r^* = 0 \tag{1.4}$$

Where F_r are the external forces and F_r^* are the inertia forces with respect to the generalized coordinates q_r. This method is effective at generating analytical expressions of the equations of motion for mid-size systems where explicitly writing the equations of motion for each body is still manageable, for example in the case of robotic arms[34] or common spacecraft configurations.[35]

An alternative approach to generating equations of motion is to calculate the state derivatives numerically using a universal algorithm. In this approach, explicit analytical expressions of each body's equations of motion is not generated. This is acceptable because these expressions are not required where the solution for the state time histories are to be numerically integrated. Only descriptions of the rigid body mass properties, geometric configurations, relative hinge properties, and force conditions in terms of the generalized coordinates are required. The fundamental building block algorithm of this approach is known in the literature as the Articulated Body Forward Dynamics (ABFD) Algorithm, an $\mathcal{O}(\mathcal{N})$ algorithm for serial chain systems where $\mathcal{N}$ is the total number of velocity degrees of freedom in the system. This algorithm was developed independently by Featherstone[36] and Rodriguez,[37] and detailed in a unified manner by Jain.[38] The approach begins by considering the system equation of motion in the form

$$M(q)\ddot{q} + C(q, \dot{q}) = T \tag{1.5}$$

where $M(q)$ is the system mass matrix, $C(q, \dot{q})$ is the Coriolis acceleration term, and T is the generalized forces. Then the generalized accelerations are solved for with advanced linear algebra, where all quantities are expressed in a mathematical format described by Spatial Operator Algebra (SOA). Where the direct inverse of $M(q) \in \mathcal{R}^{\mathcal{N}\times\mathcal{N}}$ would be an $\mathcal{O}(\mathcal{N}^3)$ computation, this algorithm implements the Innovations Factorization Method to compute the mass matrix inverse recursively at computational cost $\mathcal{O}(\mathcal{N})$. This is a critical improvement for greater order systems, and as a result has produced the computationally fastest serial-chain algorithm for any system with greater than 6-8 rigid bodies.[39,40] Where an origami-folded spacecraft structure could conceivably have tens to hundreds of panels, this computational advantage is critical. Additional algorithms have been developed from the ABFD framework using SOA to expand the approach beyond single serial chain topographies, providing the tools necessary to implement this approach to origami-folded structures. An in-depth discussion of these and how the can be adapted to origami folded deployable space structures is provided in Chapter 2.

1.2.2 Tape Spring Hinges

Adapting origami folding techniques to space structures requires either creasing or segmentation of the structure surface. Creasing primarily applies to pliable membrane structures, and the challenges of membrane creasing have been[41] and continue to be[42] researched in the literature. The scope of this thesis will focus on rigid or semi-rigid segmented structures, meaning the individual segmented panels of the structure can be treated as rigid or semi-rigid with respect to the

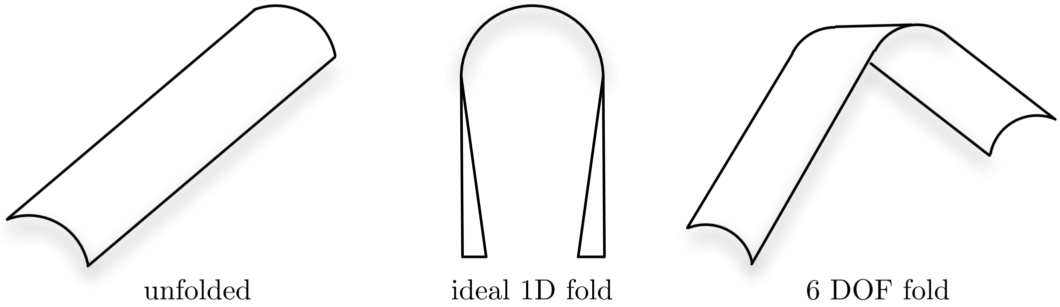

Figure 1.3: Tape spring hinge geometry and potential folding configurations.

mobility of the folds. For a structure that is segmented, these segmentations must be joined with physical hinges. Elastic, flexible hinges are ideal for this application because they provide an intuitive lightweight solution to traditional mechanical hinges. Traditional hinges such as the pin-clevis rotation joints are mechanically complex and massive. An elastic hinge, such as a composite or metallic shell, has the potential to reduce mass, eliminate friction loss, and increase compaction. Additionally, elastically folding materials will store strain energy in the system, providing a built-in deployment actuator, and can be designed to behave in desirable patterns.

1.2.3 High Strain Composite Tape Spring Hinges

Several research studies characterize the moment-curvature behavior of tape spring hinges for various materials assuming the hinge folds symmetrically, meaning through only one rotational degree of freedom (DOF). Typically, the equal-sense and opposite-sense bending moment is characterized through theoretical analysis and experimental testing.[43,44] Here, equal-sense refers to a fold where the open cross sections face each other and opposite-sense is a fold where the open cross sections face away, as is consistent with the tape spring literature. There has been further interest in characterizing the behavior of a diagonally folded hinge.[45] These studies provide fundamental understanding of a hinge's structural mechanics behavior, focusing on failure and stiffness, and demonstrate their correlation with mechanics theory.[46] However, here, the objective is to re-frame the hinge as a dynamic actuator and capture the deployment behavior of a system as actuated by the hinge. The tape spring introduces unique challenges from this perspective. A typical fold joint is treated as a single DOF revolute joint where the attachment points on each connected body are coincident and have one relative rotation. Under certain assumptions, the symmetric behavior of the tape spring hinge can be modeled as a single rotation where the moment-curvature behavior describes the internal torque due to the hinge. However, the connection points are separated by the length of the hinge and will be displaced from each other over the deployment. The actual force and torque response of the hinge will depend on the loading of either side of the hinge, and small displacements from the nominal configuration may introduce significant force and torque responses. Therefore, the established moment-curvature approach is not sufficient for the modeling fidelity desired, and a study of force and torque responses due to non-symmetric behavior is conducted. The phenomenon of undesirable non-symmetric configurations in the tape spring hinge fold is not well studied. Here, non-symmetric behavior refers to any change in position and orientation that does not follow the nominal single DOF fold rotation, as is illustrated in Figure 1.3. To guarantee symmetric behavior, additional components must be included in a hinge assembly to constrain the hinge, which can add mass and complexity where lightweight simplicity is desired. Such solutions are not addressed here. Inclusion of multiple independent state variables in this study makes it difficult to approach the problem with classical theory, therefore, to study this phenomenon, numerical and experimental techniques are employed. Additionally, high strain composites are a novel class of flexible material that are not fully understood, presenting challenges to implementing these materials. Modeling and predicting the behavior is difficult due to nonlinearity, manufacturing variability, and complex geometry. For these reasons, an experimental testing is needed for qualification of the numerical simulation data and is included in this study. These methods are discussed in detail in Chapter 3. Several challenges were uncovered in the testing of the high strain composite hinges, and proved to be an unwise choice for validation of other modeling objectives. Therefore, a more reliable model is constructed from spring steel and spring steel tape spring hinges are used for system validation efforts.

1.3 Deployment Dynamics Modeling, Testing, and Model Correlation

Design development of deployable structures is primarily achieved through iterative prototyping and testing, a process that often yields novel research products that are shared through the community. Specifically for deployment dynamics, validation and verification is primarily achieved through rigorous testing, and this is sometimes presented in tandem with complex finite element simulation or a simplified model approximation. A review of relevant deployment dynamics studies in the literature is presented as follows.

Deployment testing examples in the literature demonstrate several metrology methods for capturing adequate data of the deployment. The simplest validation that is often provided is a visual demonstration, either through video or sequential photography, of the deployment. This method is has been published for the KaPDA antenna,[47] the MARCO parabolic antenna,[48] as well as many other structure concepts. This method is considered sufficient for controlled deployments, as were the KaPDA and MARCO antennas, but can be questionable for a free-deploying system where the dynamics are not controlled and are less predictable, and potentially less repeatable. A promising videogrammetry system for deployment dynamics testing is provided by the Vicon motion capture system. This system directly measures the position of multiple reflective targets on a moving body of interest through time. A notable test campaign that implements this in the literature features the SIMPLE meter-class boom,[49] which demonstrated a free deployment of a self-actuated boom. Other high fidelity motion studies have been conducted with videogrammetry in the fields of robotics and biomechanics, and will be used in this thesis to provide deployment dynamics data for model evaluations.

Considering now the modeling portion of the literature, there are few studies in the literature that develop modeling techniques for free deploying, strain actuated spacecraft structures. One significant study of the free deployment dynamics of a tape spring actuated system is provided by the MARSIS antenna project that flew on ESA's Mars Express and was deployed in 2005.[50] This antenna was comprised of three z-folded tubes, the longest of which was 40 meters and had 12 folding hinges. A significant anomaly occurred during the deployment of the first boom, where a tape spring hinge did not deploy and therefore created an intermediate deployment shape. Additional modeling efforts were needed to determine the partially deployed state, to determine the cause of the anomaly, and to design a spacecraft maneuver to correct it.[51] In these studies, a multibody dynamics modeling software, ADAMS, was implemented to model the deployment, treating the tape springs as spline hinge joints. Additionally, Abaqus finite element simulations were created to validate the ADAMS model at the component level, modeling only a single hinge connecting two tubes, due to the infeasible computational cost of modeling a full system. Major take aways from this study are the risks taken in not being able to do a ground deployment test, and the importance of predicting hinge behavior. The original analysis of the system contained an error in the damping implementation, which was corrected after launch but before deployment, resulting in a much more dynamic and chaotic system then desired. This may have been witnessed if a ground deployment test was conducted and correlated with the model, however the system was so large that a test was infeasible.

An additional study of note is of a self actuated z-folded solar array for CubeSats that included a finite element model and a deployment test using Vicon videogrammetry.[52] This system consisted of several 10 cm by 10 cm panels connected by flexure hinges at the folds. This study found issues with the panels self-contacting through deployment, where the likelihood of such behavior for systems of more than 7 panels was high. Additionally, there was large variance in the deployment path of the array, although there was good correlation for the deployment time and final deployed distance between the simulations and experiments. While these two studies provide clear approaches to studying free-deploying systems, they are both z-folded open chain systems not subject to closure constraints, which is the dominant challenge of an origami structure. A study of the deployment of a self-deployable origami folded structure has been seen in the literature[53] and provides good overlap with research interests in this thesis. The authors created a deployment dynamics model using commercial modeling software that includes linear stiffness models of strain joints with multiple degrees of freedom. However this system was controlled with a cable system therefore does not have the challenges of a free deployment, and deployment dynamics of the design were not tested or correlated in the study. Additionally, strain joints and tape spring hinges have notable differences in behavior properties.

An additional modeling point of note is efforts to represent hinge behavior with a reduced model. A similar concept of representing a complex mechanical hinge with a force/torque model for dynamics modeling has been demonstrated using an integrated finite element and multibody software[54] for a folded open chain solar panel deployment. These hinges were traditional mechanical pin and clevis (or piano) hinges, and so the modeling challenges do not overlap well with this thesis. However this study does demonstrate interest in the community in developing reduced hinge modeling techniques to better understand deployment dynamics simulations.

1.4 Research Proposal Summary

The deployment dynamics of complex folded deployable systems must be understood to verify deployment and to ensure mission success, and should be available early in the design process to enable more efficient and reliable designs. **This thesis investigates modeling dynamics of folded deployable space structures and host spacecraft systems to address this technology need**. The free deployment of a closed-chain origami-folded structure with tape spring hinges is yet to be investigated. This thesis aims to study this problem by completing four research goals as follows:

(1) to develop a new multi-body dynamics algorithm that is specifically structured for folded deployable spacecraft systems

- implement the Articulated Body Forward Dynamics algorithm and Spatial Operator Algebra for free-flying spacecraft systems with closed-chain constraint enforcements
- validate this approach using energy and momentum conservation laws
- generalize this approach to scale up for any size fold pattern

(2) to investigate the force and torque behavior of tape spring hinges implemented into folded spacecraft structures, and to develop a reduced order model of this hinge behavior

- create a library of static force/torque data for the high strain composite hinge under multiple DOF folds using finite element tools
- design, build, and implement a testing tool for measuring the identical force/torque behaviors on physical samples
- correlate the data and assess feasibility of modeling technique
- create a static force/torque library for a spring steel tape spring hinge for full system model integration and validation

(3) to integrate the multi-body dynamics algorithm and the hinge behavior models together

- create a multi-body model that replicates the physical prototype tested
- implement multiple DOF hinge behavior at the actuated hinge
- generate time histories of the deployment for evaluation

(4) correlate the full system deployment model against the measured behavior of a physical prototype structure

- design and build a novel tape spring actuated folded deployable structure
- conduct deployment tests implementing an advanced metrology system to collect data
- evaluate performance of the multi-body model against the measured experiments
- create a finite element model of the prototype structure and conduct a deployment dynamic simulation of the full system
- evaluate performance of the FEA model and the multi-body model against the measured experiments

Analyzing deployment behavior through this dynamics model will make demonstrating concept feasibility possible, and will push the capabilities of deployable structures technology forward.

Chapter 2

Research Goal 1: Multi-Body Dynamics Modeling for Origami-Folded Structures

2.1 Introduction

This chapter develops the equations of motion of proto-typical origami folded spacecraft structures. The dynamics model is derived using the articulated body forward dynamics (ABFD) algorithm and the augmented approach for closed-chain forward dynamics using Spatial Operator Algebra (SOA) formats. These are multi-body approaches developed in the literature for complex robotic manipulator systems.[39] Here, the applicability of this approach to folded deployable spacecraft structures is investigated. This approach is desirable due to the computational efficiency of the algorithm and the ability to implement multiple types of complex internal hinge behavior without reformulation of the dynamics algorithm. Investigations following the Lagrangian approach provide initial understand of the problem,[29] and is provided in Appendix A, but are found to be insufficient for scaling to multiple closed chain systems. Additionally, Kane's method[33] is found to be insufficient in comparison to the framework provided by the spatial operator algebra based approach here, where this approach is much more conducive to scaling. The advantageous partial velocities defined by Kane's method are also represented in this model, however maintaining the full SOA model enables further algorithm implementation. Therefore, the model structure of the SOA format is viewed as a refinement of Kane's equations.[39]

Origami fold patterns with repeating structure, such as the Miura[55] and Scheel patterns,[56] are considered. These patterns share the common property of having no more than four panels meeting at each vertex. Therefore, the subsystem case of a four-panel set is analyzed in detail in Section 2.5.3 as a starting point. The scalability of the algorithm to multiple-loop systems, as would be seen in a repeating origami pattern, is a key development in this thesis. A closed-loop configuration is not uncommon for robotic manipulator systems, but these typically appear as single instances in a greater open-loop chain. The unique challenges of the repeating closed-loop topology of an origami pattern has not been investigated in the literature, and therefore this development represents a novel contribution to the field of rigid body dynamics as well as the field of origami-inspired engineering.

Previous research in the literature indicates active interest in this area. Recent studies developing folding structure concepts have adapted pre-existing software tools for dynamics analysis such as MathWorks SimScape Multibody,[53] or JPL's DARTs[57] simulation toolkit. However these tools are not necessarily intended for processing the high volume of closed-chain constraints presented by a folding system. This point is highlighted in a previous folded structure study where the fold pattern was designed specifically to avoid the presence of closed chains entirely for computational simplicity.[57] This motivates the need for a fast dynamics simulation approach to be developed. In this chapter, a custom method for modeling the dynamics using advanced multi-body techniques is developed. This method provides a fast simulation where complex hinges can be implemented at the folds to actuate the deployment.

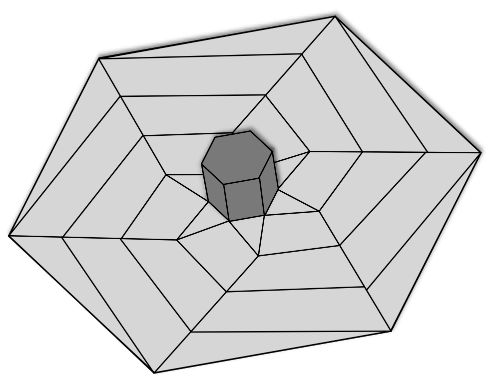

Figure 2.1: Example structure concept: A spacecraft hub with a radially folding deployable structure.

A few key assumptions are ingrained in the construction of this approach. It is assumed that any pattern modeled using this framework will only contain four panel vertices. Additionally, the fold lines of the pattern are treated as delineations between panels that are assumed to be rigid. Therefore, this approach is only appropriate for structures where the material of the fold hinge is sufficiently more flexible than the panels, and the panels are stiff enough that this assumption is valid. It is also assumed that only loop constraints are enforced on the closed chain systems. Finally, it is assumed that the base-body of the structure is a free-flying spacecraft system, meaning the body is not rigidly attached to the ground and has six degrees of freedom. This assumption enables a computation shortcut in the constraint calculations and is consistent with the scope of the research.

2.2 Dynamics and Multi-body Systems Fundamentals

2.2.1 Spatial Vector Kinematics

$$\boldsymbol{q}(\mathcal{F},\mathcal{G}) = \begin{bmatrix} \boldsymbol{\sigma}(\mathcal{F},\mathcal{G}) \\ \boldsymbol{l}(\mathcal{F},\mathcal{G}) \end{bmatrix} \tag{2.1}$$

where $\boldsymbol{\sigma}$ is a three coordinate representation of orientation and $\boldsymbol{l}$ is the position vector in 3D Euclidean space. In this application, the spacecraft orientation is represented by the standard Modified Rodriguez Parameters (MRPs)[58,59,60] with shadow set switching to avoid geometric singularities. The spatial velocity is chosen as the angular rotation rates and the linear velocities of the body

$$\boldsymbol{\beta}(\mathcal{F},\mathcal{G}) = \begin{bmatrix} \boldsymbol{\omega}(\mathcal{F},\mathcal{G}) \\ \boldsymbol{v}(\mathcal{F},\mathcal{G}) \end{bmatrix} \tag{2.2}$$

where the relative angular velocity is a non-integrable quasi-velocity, meaning it is not the time derivative of the spatial coordinates, and the notation $\boldsymbol{\omega}(\mathcal{F},\mathcal{G})$ denotes the angular velocity of frame $\mathcal{G}$ with respect to frame $\mathcal{F}$. The spatial orientations and spatial angular velocities are then related to each other using a linear transformation. For MRPs, this transformation is[28]

$$\dot{\boldsymbol{\sigma}} = \frac{1}{4}\left[(1-\boldsymbol{\sigma}^2)[I_{3\times 3}] + 2[\tilde{\boldsymbol{\sigma}}] + 2\boldsymbol{\sigma}\boldsymbol{\sigma}^{\intercal}\right]\boldsymbol{\omega} = [B]^{\omega}\boldsymbol{\omega} \tag{2.3}$$

Then the full spatial transformation from spatial velocity to generalized coordinate derivatives is

$$\dot{\boldsymbol{q}} = [B]\boldsymbol{\beta} = \begin{bmatrix} [B]^{\omega} & 0_3 \\ 0_3 & I_3 \end{bmatrix}\boldsymbol{\beta} \tag{2.4}$$

2.2.1.1 Spatial Rigid Body Transformation

A key spatial vector operation to consider is the rigid body transformation between frames. For a frame that is both translating and rotating with respect to a reference frame, the 6×6 transformation that transforms a vector expressed with respect to the $\mathcal{G}$ frame to one expressed with respect to the $\mathcal{F}$ frame is

$${}^{\mathcal{F}}\boldsymbol{q} = \phi(\mathcal{F},\mathcal{G})\,{}^{\mathcal{G}}\boldsymbol{q} \tag{2.5}$$

where a left super script denotes frame expression of the vector and

$$\phi(\mathcal{F},\mathcal{G}) = \begin{bmatrix} I_3 & [{}^{\mathcal{F}}\tilde{\boldsymbol{l}}(\mathcal{F},\mathcal{G})] \\ 0_3 & I_3 \end{bmatrix}\begin{bmatrix} [\mathcal{F}\mathcal{G}] & 0_3 \\ 0_3 & [\mathcal{F}\mathcal{G}] \end{bmatrix} \tag{2.6}$$

where the 3×3 direction cosine matrix between frames $\mathcal{F}$ and $\mathcal{G}$, that transforms a quantity expressed in $\mathcal{G}$ to one expressed in $\mathcal{F}$, is represented by $[\mathcal{F}\mathcal{G}]$, I_3 is the 3×3 identity matrix, 0_3 is a 3×3 zero matrix, and the tilde operator is the cross product matrix operation for a 3 dimensional vector, defined as

$$[\tilde{\boldsymbol{l}}] = \begin{bmatrix} 0 & -l_3 & l_2 \\ l_3 & 0 & -l_1 \\ -l_2 & l_1 & 0 \end{bmatrix} \tag{2.7}$$

In this framework, the hinge implementation does not assume that the frame of the hinge point on one rigid body coincides with the location or orientation of the frame of the hinge point on it's adjoining rigid body. Therefore, this definition of the rigid body transformation matrix is used extensively to transform information across hinges.

2.2.1.2 Spatial Rigid Body Transformation Derivative

The time derivative of the transposed spatial transformation that includes both the translation and rotation is needed throughout the dynamics development to follow. Following Equation 2.6 and the matrix property $[\tilde{\boldsymbol{l}}]^{\intercal} = -[\tilde{\boldsymbol{l}}]$,

$$\phi^{\intercal}(\mathcal{F},\mathcal{G}) = \begin{bmatrix} [\mathcal{GF}] & 0_3 \\ 0_3 & [\mathcal{GF}] \end{bmatrix} \begin{bmatrix} I_3 & 0_3 \\ -[{}^{\mathcal{F}}\tilde{\boldsymbol{l}}(\mathcal{F},\mathcal{G})] & I_3 \end{bmatrix} \tag{2.8}$$

Using the chain rules

$$\begin{aligned} \frac{\mathrm{d}}{\mathrm{d}t}\phi^{\intercal}(\mathcal{F},\mathcal{G}) = & \\ & \frac{\mathrm{d}}{\mathrm{d}t}\begin{bmatrix} [\mathcal{GF}] & 0_3 \\ 0_3 & [\mathcal{GF}] \end{bmatrix} \begin{bmatrix} I_3 & 0_3 \\ -[{}^{\mathcal{F}}\tilde{\boldsymbol{l}}(\mathcal{F},\mathcal{G})] & I_3 \end{bmatrix} \\ & + \begin{bmatrix} [\mathcal{GF}] & 0_3 \\ 0_3 & [\mathcal{GF}] \end{bmatrix} \frac{\mathrm{d}}{\mathrm{d}t}\begin{bmatrix} I_3 & 0_3 \\ -[{}^{\mathcal{F}}\tilde{\boldsymbol{l}}(\mathcal{F},\mathcal{G})] & I_3 \end{bmatrix} \end{aligned} \tag{2.9}$$

The time derivative of the direction cosine matrix is known[28] to be

$$\frac{\mathrm{d}}{\mathrm{d}t}[\mathcal{GF}] = -[\tilde{\boldsymbol{\omega}}(\mathcal{F},\mathcal{G})][\mathcal{GF}] \tag{2.10}$$

and the derivative of the position vector expressed in frame $\mathcal{F}$ is denoted as $\boldsymbol{v}_{\mathcal{F}}(\mathcal{F},\mathcal{G})$, then

$$\begin{aligned} \frac{\mathrm{d}}{\mathrm{d}t}\phi^{\intercal}(\mathcal{F},\mathcal{G}) = & \begin{bmatrix} -[\tilde{\boldsymbol{\omega}}(\mathcal{F},\mathcal{G})] & 0_3 \\ 0_3 & -[\tilde{\boldsymbol{\omega}}(\mathcal{F},\mathcal{G})] \end{bmatrix} \phi^{\intercal}(\mathcal{F},\mathcal{G}) \\ & + \begin{bmatrix} 0_3 & 0_3 \\ -[\tilde{\boldsymbol{v}}_{\mathcal{F}}(\mathcal{F},\mathcal{G})] & 0_3 \end{bmatrix} \phi^{\intercal}(\mathcal{F},\mathcal{G}) \end{aligned} \tag{2.11}$$

Simplifying,

$$\frac{\mathrm{d}}{\mathrm{d}t}\phi^{\intercal}(\mathcal{F},\mathcal{G}) = -\begin{bmatrix} [\tilde{\boldsymbol{\omega}}(\mathcal{F},\mathcal{G})] & 0_3 \\ [\tilde{\boldsymbol{v}}_{\mathcal{F}}(\mathcal{F},\mathcal{G})] & [\tilde{\boldsymbol{\omega}}(\mathcal{F},\mathcal{G})] \end{bmatrix} \phi^{\intercal}(\mathcal{F},\mathcal{G}) \tag{2.12}$$

Defining a spatial tilde operator as

$$\tilde{\boldsymbol{V}}_{\mathcal{F}}(\mathcal{F},\mathcal{G}) = \begin{bmatrix} [\tilde{\boldsymbol{\omega}}(\mathcal{F},\mathcal{G})] & 0_3 \\ [\tilde{\boldsymbol{v}}_{\mathcal{F}}(\mathcal{F},\mathcal{G})] & [\tilde{\boldsymbol{\omega}}(\mathcal{F},\mathcal{G})] \end{bmatrix} \tag{2.13}$$

Then the spatial transformation derivative is expressed as[39]

$$\frac{\mathrm{d}}{\mathrm{d}t}\phi^{\mathsf{T}}(\mathcal{F},\mathcal{G}) = -\tilde{\boldsymbol{V}}_{\mathcal{F}}(\mathcal{F},\mathcal{G})\phi^{\mathsf{T}}(\mathcal{F},\mathcal{G}) \tag{2.14}$$

Note the similarities of structure with Equation 2.10, however the inclusion of the position offset of the frames to the transformation definition leads to an additional term.

2.2.2 Serial-chain ABFD Framework

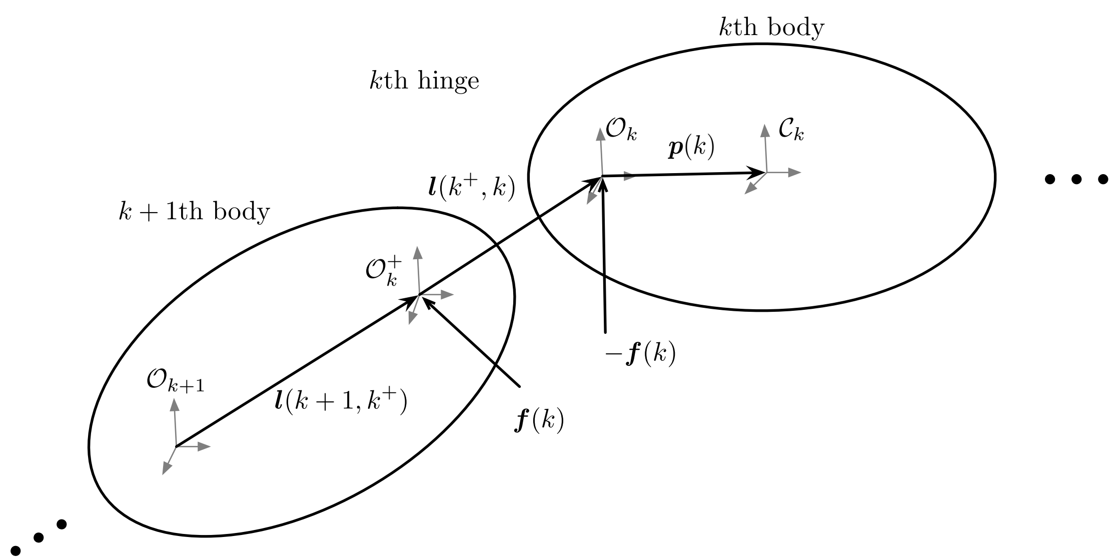

Figure 2.2: Vector and frame notation between the $k+1^{\text{th}}$ and the k^{th} body.

A prominent dynamics algorithm developed for serial chains is presented in literature as the $\mathcal{O}(\mathcal{N})$ Articulated-Body Forward Dynamics (ABFD) algorithm developed independently by Featherstone[36] and Rodriguez,[37] and detailed in a unified manner by Jain.[38] Here $\mathcal{N}$ refers to the total number of velocity degrees of freedom in the system. The algorithm is developed to be appropriate for any multi-body robotic system that is treated as a network of serial-chain rigid bodies. The full derivation of the algorithm can be reviewed in the literature, but key formulations are repeated here to provide context to the adaptations developed for spacecraft and deployable structure systems. In the articulated-body model, each of the rigid bodies down-chain of the current body being considered are treated as completely free with zero hinge force. Under this assumption, the articulated body inertia is calculated to represent those free bodies and a correction term is then developed to compensate for this assumption. This approach is in contrast to the composite body model, which treats the connected rigid bodies as fixed relative to each other, and uses a similar composite body inertia and correction term to derive the hinge force. However, the articulated body model is more appropriate for the forward dynamics problem. Additionally, the ABFD algorithm can be expanded to handle the multiple serial-chain branches of a tree-topology case.

The ABFD framework outlined by Jain[39] provides the basis of the version implemented here, with a few key adaptations that are described as needed. The generalized spatial coordinates are chosen as hinge coordinates at the k^{th} hinge, or the k^{th} rigid body's outboard hinge frame, $\mathcal{O}_k$, orientation and position with respect to the $k+1$ rigid body's inboard hinge frame, $\mathcal{O}_k^+$, as illustrated in Figure 2.2,

$$\boldsymbol{q}(k) = \begin{bmatrix} \boldsymbol{\sigma}(\mathcal{O}_k^+, \mathcal{O}_k) \\ \boldsymbol{l}(\mathcal{O}_k^+, \mathcal{O}_k) \end{bmatrix} \tag{2.15}$$

and the generalized velocities are chosen as the hinge spatial velocities, taken as the time derivative with respect to the k frame

$$\boldsymbol{\beta}(k) = \begin{bmatrix} \boldsymbol{\omega}(\mathcal{O}_k^+, \mathcal{O}_k) \\ \boldsymbol{v}(\mathcal{O}_k^+, \mathcal{O}_k) \end{bmatrix} \tag{2.16}$$

For a given set of rigid bodies, these are collected in the full coordinate and velocity sets

$$q = \begin{bmatrix} \boldsymbol{q}(1) \\ \dots \\ \boldsymbol{q}(k) \\ \dots \\ \boldsymbol{q}(n) \end{bmatrix} \qquad \beta = \begin{bmatrix} \boldsymbol{\beta}(1) \\ \dots \\ \boldsymbol{\beta}(k) \\ \dots \\ \boldsymbol{\beta}(n) \end{bmatrix} \tag{2.17}$$

Where the tip of the chain is denoted as body 1 and the base body is denoted as body n. This leads to system equations of motion in the form

$$\mathcal{M}(q)\dot{\beta} + \mathcal{C}(q,\beta) = T \tag{2.18}$$

where $\mathcal{M}(q)$ is the full system mass matrix, $\mathcal{C}(q,\beta)$ contains the Coriolis contributions, and T is the vector of system generalized forces. The use of the quasi-velocities diverges from the assumptions implemented in Jain's text.[39] In the forward dynamics problem, q, β and T are known quantities and the time derivative $\dot{\beta}$ is the desired quantity. Direct inversion of the mass matrix $\mathcal{M}$ is typically done for small order systems, but is a computationally expensive $\mathcal{O}(\mathcal{N}^3)$ matrix operation for an $\mathcal{N}$ degree of freedom problem. This becomes prohibitively slow for large DOF multi-body systems. The computational efficiency of the ABFD algorithm is achieved by applying the Innovations Operator Factorization of the mass matrix $\mathcal{M}$ and deriving an explicit and analytical expression of the inverse, $\mathcal{M}^{-1}$. The details of this factorization are left to the literature.[39] The dynamics as implemented here are derived using body frame derivatives. The algorithm is set up in the following way. First, a recursive sweep that solves the velocities and Coriolis accelerations of the chain is run from the base body to the tip. Then, the articulated body inertias and corrections are solved for in a tip to base recursion. The final step is to do a base to tip recursion to solve for the body accelerations, yielding the system equations of motion.

2.2.2.1 Recursive Articulated Body Spatial Inertia

For a general rigid body where the hinge frame is not located at the center of mass, the spatial mass matrix about the hinge frame, $M(k)$, is

$$M(k) = \begin{bmatrix} J(k) & m(k)[\tilde{\boldsymbol{p}}(k)] \\ -m(k)[\tilde{\boldsymbol{p}}(k)] & mI_3 \end{bmatrix} \tag{2.19}$$

where

$$J(k) = J(c) + m(k)[\tilde{\boldsymbol{p}}(k)][\tilde{\boldsymbol{p}}(k)]^\intercal \tag{2.20}$$

is the body inertia about point k, $J(c)$ is the body inertia about the center of mass, $m(k)$ is the mass of the body, and $\boldsymbol{p}(k)$ is the position vector from the hinge frame to the center of mass frame of the k^{th} body, illustrated in Figure 2.2 and expressed in the k^{th} frame. This is the application of the parallel axis theorem for the spatial mass matrix. The articulated body spatial inertia, $P(k)$ is then calculated as

$$P(k) = \phi(k, k-1)P^{+}(k-1)\phi^{\intercal}(k, k-1) + M(k) \tag{2.21}$$

where $P^{+}(k-1)$ is the projection of the $k-1$ articulated body inertia across the hinge frames. The correction force of the k^{th} body is then

$$\boldsymbol{\zeta}(k) = \phi(k, k^{+})\boldsymbol{\zeta}^{+}(k-1) + P(k)\boldsymbol{a}(k) + \boldsymbol{b}(k) \tag{2.22}$$

where $\boldsymbol{\zeta}^{+}(k-1)$ is the projection of the $k-1$ correction force and $\boldsymbol{b}(k)$ is the gyroscopic term, defined as

$$\boldsymbol{b}(k) = \bar{\boldsymbol{V}}(k)M(k)\boldsymbol{V}(k) \tag{2.23}$$

the spatial bar operator is related to the spatial tilde operator as $\bar{\boldsymbol{x}} = -\tilde{\boldsymbol{x}}^{\intercal}$ and $\boldsymbol{V}(k)$ is the spatial velocity of body k, and is short hand for the spatial velocity of k with respect to the inertial frame $\mathcal{I}$, or

$$\boldsymbol{V}(k) = \begin{bmatrix} \boldsymbol{\omega}(k) \\ \boldsymbol{v}(k) \end{bmatrix} = \boldsymbol{V}(\mathcal{I}, k) = \begin{bmatrix} \boldsymbol{\omega}(\mathcal{I}, k) \\ \boldsymbol{v}(\mathcal{I}, k) \end{bmatrix} \tag{2.24}$$

2.2.2.2 Recursive Velocity Kinematics

The spatial velocity kinematics for the n serial-chain bodies can be calculated recursively given the hinge coordinates and hinge velocities, where the $n+1$ body represents the non-accelerating fixed inertial frame and the recursion runs from the base body, or n^{th} body, to the tip, body 1. This is presented in literature as[39]

$$\boldsymbol{V}(k) = \phi^{\intercal}(k+1, k^{+})\boldsymbol{V}(k+1) + H^{\intercal}(k)\boldsymbol{\beta}(k) \tag{2.25}$$

where the relative velocity between bodies is the spatial hinge velocity

$$\boldsymbol{\Delta v}(k^+, k) = H^{\intercal}(k)\boldsymbol{\beta}(k) = H^{\intercal}(k)\begin{bmatrix}\boldsymbol{\omega}(\mathcal{O}_k^+, \mathcal{O}_k) \\ \boldsymbol{v}(\mathcal{O}_k^+, \mathcal{O}_k)\end{bmatrix} \tag{2.26}$$

The spatial velocity is then

$$\boldsymbol{V}(k) = \phi^{\intercal}(k+1, k^+)\boldsymbol{V}(k+1) + \boldsymbol{\Delta v}(k^+, k) \tag{2.27}$$

For a rigid body, where the $\mathcal{O}_k^+$ frame and the $\mathcal{O}_{k+1}$ frame are on the same body, as seen in Figure 2.2, $\boldsymbol{\omega}(\mathcal{O}_k^+, \mathcal{O}_k) = \boldsymbol{\omega}(\mathcal{O}_{k+1}, \mathcal{O}_k)$ and is also referred to as $\boldsymbol{\omega}(k+1, k)$. Conceptually, the spatial velocity is the body's global velocity in space, or the velocity with respect to the inertial frame, but expressed in any desired frame. The spatial acceleration similarly references the global acceleration of the body.

In this research, the position and orientation of the k^+ frame is not assumed to coincide with those of the k frame. This requires new derivation of the acceleration expressions. Additionally, a note must be made on the spatial transformation matrix in this context. In earlier definitions of the spatial transformation, the rotation between frames is also included. However, this does not guarantee consistent frame expressions for the velocity and acceleration formulations, and additional rotations are needed for correct implementation. These algorithms are currently presented here without frame dependency.

2.2.2.3 Recursive Acceleration Derivation

The spatial acceleration is derived from the spatial velocity using the spatial adaption of the Transport theorem,[28] a theorem that enables the derivation of the time derivative of a vector quantity with respect to any desired frame, as expressed in any desired frame.

$$\frac{^{\mathcal{F}}\mathrm{d}}{\mathrm{d}t}\boldsymbol{x} = \frac{^{\mathcal{G}}\mathrm{d}}{\mathrm{d}t}\boldsymbol{x} + \tilde{\boldsymbol{V}}^{\omega}(\mathcal{F}, \mathcal{G})\boldsymbol{x} \tag{2.28}$$

Where $\tilde{\boldsymbol{V}}^{\omega}$ contains only the rotation rate components of the spatial velocity and $\boldsymbol{x}$ is any spatial vector. Then the spatial acceleration can be written as

$$\begin{aligned}\boldsymbol{\alpha}(k) = \frac{{}^{k}\mathrm{d}}{\mathrm{d}t}\boldsymbol{V}(k) = \frac{{}^{k+1}\mathrm{d}}{\mathrm{d}t}\left(\phi^{\intercal}(k+1,k^{+})\boldsymbol{V}(k+1)\right) \\ - \tilde{\boldsymbol{\Delta v}}^{\omega}(k^{+},k)\phi^{\intercal}(k+1,k^{+})\boldsymbol{V}(k+1) \\ + \frac{{}^{k}\mathrm{d}}{\mathrm{d}t}\left(H^{\intercal}(k)\boldsymbol{\beta}(k)\right)\end{aligned} \tag{2.29}$$

where in this implementation, $\boldsymbol{V}(k+1)$ and $\phi^{\intercal}(k+1,k^{+})$ are expressed in the $k+1$ frame, and $H^{\intercal}(k)$ and $\boldsymbol{\beta}(k)$ are expressed in the k frame. This reveals additional rotation terms to ensure correct computation.

Expanding, the k frame derivative of the spatial velocity is

$$\begin{aligned}\frac{{}^{k}\mathrm{d}}{\mathrm{d}t}\boldsymbol{V}(k) = \frac{{}^{k+1}\mathrm{d}}{\mathrm{d}t}\phi^{\intercal}(k+1,k^{+})\boldsymbol{V}(k+1) \\ + \phi^{\intercal}(k+1,k^{+})\frac{{}^{k+1}\mathrm{d}}{\mathrm{d}t}\boldsymbol{V}(k+1) \\ - \tilde{\boldsymbol{\Delta v}}^{\omega}(k+1,k)\phi^{\intercal}(k+1,k^{+})\boldsymbol{V}(k+1) \\ + \frac{{}^{k}\mathrm{d}}{\mathrm{d}t}H^{\intercal}(k)\boldsymbol{\beta}(k) + H^{\intercal}(k)\frac{{}^{k}\mathrm{d}}{\mathrm{d}t}\boldsymbol{\beta}(k)\end{aligned} \tag{2.30}$$

The hinge map matrix is assumed to be invariant for this case and therefore $\frac{{}^{k}\mathrm{d}}{\mathrm{d}t}H^{\intercal}(k)$ is zero. Additionally, the rigid body transformation between $k+1$ and k^{+} is constant in the $k+1$ frame. The spatial acceleration can then be expressed as

$$\begin{aligned}\boldsymbol{\alpha}(k) = \phi^{\intercal}(k+1,k^{+})\boldsymbol{\alpha}(k+1) + H^{\intercal}(k)\dot{\boldsymbol{\beta}}(k) \\ - \tilde{\boldsymbol{\Delta v}}^{\omega}(k^{+},k)\phi^{\intercal}(k+1,k^{+})\boldsymbol{V}(k+1)\end{aligned} \tag{2.31}$$

Defining the Coriolis acceleration for the kth body as

$$\boldsymbol{a}(k) = -\tilde{\boldsymbol{\Delta v}}^{\omega}(k^{+},k)\phi^{\intercal}(k+1,k^{+})\boldsymbol{V}(k+1) \tag{2.32}$$

the acceleration term is then

$$\boldsymbol{\alpha}(k) = \phi^{\intercal}(k+1,k^{+})\boldsymbol{\alpha}(k+1) + H^{\intercal}(k)\dot{\boldsymbol{\beta}}(k) + \boldsymbol{a}(k) \tag{2.33}$$

and this expression also possesses a recursive structure. The Coriolis acceleration expression is then rewritten using Equation 2.25 as

$$\boldsymbol{a}(k) = -\tilde{\boldsymbol{\Delta v}}^{\omega}(k^{+}, k)\left(\boldsymbol{V}(k) - H^{\intercal}(k)\boldsymbol{\beta}(k)\right) \tag{2.34}$$

2.2.3 Framework for Complex Hinge Behavior

2.2.3.1 Hinge Mapping

The interaction of adjacent bodies in the chain are governed by the properties of the hinge connecting these bodies. The hinge map matrix, $H^{\intercal}(k)$, for a rigid body joint k defines the configuration dependence of the hinge behavior and maps the hinge velocities to the generalized spatial velocities of the body. Where $r_v(k)$ is the number of velocity degrees of freedom across the hinge, $H^{\intercal}(k) \in R^{6\times r_v(k)}$. For a free-floating rigid body in space, the hinge map matrix is a 6×6 identity matrix, I_6. Therefore, a free-floating spacecraft base-body is mapped to inertial space with $H(r) = I_6$. This mapping introduces a simple and modular way to implement velocity constraints across the hinge of two adjacent bodies without reformulation of the dynamics algorithm. Then for folding panels that are constrained to a single rotation along the fold axis of the pattern, where the fold axis is aligned with the first axis of the frame,

$$H(k) = [1, 0, 0, 0, 0, 0] \tag{2.35}$$

This only applies the hinge constraint at each connected hinge of a free serial chain. Hinge properties spanning the cut edges of a closed-chain graph are captured in loop constraints, covered in Section 2.5.1.

2.2.3.2 Internal Hinge Forces

The spatial force acting at hinge k due to the interaction with body $k+1$ is denoted $f(k)$, where $f(k)$ acts at the O_k hinge frame and an equal but opposite force $-f(k)$ acts at the O_k^{+} frame on the $k+1$ body. Then the generalized force on the k^{th} hinge, $T(k)$, is the projection of the spatial force through the hinge degrees of freedom, defined as

$$T(k) = H(k)f(k) \tag{2.36}$$

This force can be defined by the components in the hinge system. Examples of simple uncontrolled hinge forces are linear and torsion springs. Additionally, actuation components such as those used in robot arms could be installed at the hinge to control the multi-body motion. These type of actuators are not relevant to deployable folded structure research, however, due to the pursuit of a free, self-actuated deployment system. The hinges are therefore expected to contain strain or potential energy driven forces that are a function of the general coordinates. For example, a linear torsion spring with magnitude K_1 along the first rotation would be expressed in spatial coordinates for hinge k as

$$f(k) = K(k)q(k) = \begin{bmatrix} K_1 & 0 & 0 & 0 & 0 & 0 \\ 0 & 0 & 0 & 0 & 0 & 0 \\ 0 & 0 & 0 & 0 & 0 & 0 \\ 0 & 0 & 0 & 0 & 0 & 0 \\ 0 & 0 & 0 & 0 & 0 & 0 \\ 0 & 0 & 0 & 0 & 0 & 0 \end{bmatrix} \begin{bmatrix} \sigma_1 \\ \sigma_2 \\ \sigma_3 \\ l_1 \\ l_2 \\ l_3 \end{bmatrix} \tag{2.37}$$

2.2.4 Conserved Principles for Multi-body Systems

The conservation of energy and the conservation of momentum provide robust verification of dynamic systems modeling such as the approach applied here. These principles are defined for spatial notation as follows.

2.2.4.1 Energy

The energy of a body is the same regardless of the point it's measured from on the body, and therefore for a given body k, the kinetic energy of the body about its hinge frame is the same as the kinetic energy about its center of mass. In spatial coordinates, this can be expressed as

$$KE(k) = \frac{1}{2}V(k)M(k)V(k) \tag{2.38}$$

And for a hinge with linear springs, the potential energy is

$$PE(k) = \frac{1}{2} q(k) K(k) q(k) \tag{2.39}$$

Where $K(k)$ is the stiffness matrix for the kth hinge, assuming a linear spring force as a function of the hinge general coordinates. The energy calculated at a each body is invariant to the frame that it is calculated at, so the total system energy can be calculated, independent of frame as

$$E = \sum_{k=1}^{n} KE(k) + PE(k) \tag{2.40}$$

2.2.4.2 Angular Momentum

The magnitude of the angular momentum of a single body about the body center of mass, c, is conserved, where the angular momentum can be written in spatial coordinates as

$$h(c) = J(c)\omega(c) \tag{2.41}$$

where $J(c)$ is the inertial about the center of mass and $\omega(c)$ is the angular rates of body.

For a system of rigid bodies, the angular momentum of each body must be expressed in the same frame and taken about the system's center of mass, c_{sys} to demonstrate conservation. Therefore, the angular momentum of the system is calculated as

$$h = \sum_{k=1}^{n} h_{c_{\text{sys}}}(k) \tag{2.42}$$

where

$$h_{c_{\text{sys}}}(k) = J(c_k)\boldsymbol{\omega}(k) + m(k)(\boldsymbol{p}(c_{\text{sys}}, c_k) \times \boldsymbol{v}(c_k)) \tag{2.43}$$

here $J(c_k)$ is the inertia of the kth body about it's center of mass, $\boldsymbol{\omega}(k)$ is the angular velocity of the kth body, $m(k)$ is the mass of the kth body, $\boldsymbol{v}(c_k)$ is the linear velocity of the kth body center of mass, and $\boldsymbol{p}(c_{\text{sys}}, c_k)$ is the position vector from the system center of mass frame to the center of mass of the kth body. All quantities are transformed to be expressed in the inertial frame for consistency.

2.3 Folded Structure Topology Processing

2.3.1 Graph Theory Applications

A system of hinge-connected rigid bodies can be described using graph theory by treating the rigid bodies as nodes and the hinges or fold lines as edges. This representation will aid in breaking down the complex system into a form that can be efficiently analyzed. The manner in which the system of nodes is connected determines the classification of the system. For a given graph, the node from which an edge leads from is designated the parent node and the node at the destination of that edge is referred to as the child node. A node with no parent is the root node. A parent node can have multiple child nodes, and if these nodes do not share edges within the graph, the graph is referred to as a tree topology. The basis of the dynamics algorithm discussed here is written to recursively solve for a serial chain of bodies, following the branch of a tree. At initial consideration, the closed-loop patterns of a folded spacecraft structure is a multiply connected graph where multiple child nodes span from a parent node and are interconnected, and there exist paths in the graph that lead back to a given node. The first step in modeling a folded spacecraft structure is to identify edges of the system to "cut" such that the bodies are segmented into a topology where there are no closed loops, also known as a tree topology. These cut edges must then be constrained with corrections to enforce the actual closed-chain topology.

2.3.2 Tree Topology of Planar Origami Patterns

The development and analysis of origami-inspired fold patterns appropriate for use in spacecraft structures is an active area of interest. A select number of patterns have received more study due to the clear applicability to spacecraft needs. The Miura pattern,[55] illustrated in Figure 2.3, is a highly efficient folding scheme with one theoretical degree of freedom that deploys linearly in dual directions and is thoroughly studied in the literature. Similarly, the Scheel pattern illustrated in Figure 2.4 is a radially wrapped pattern that is commonly studied for spacecraft structure applications.

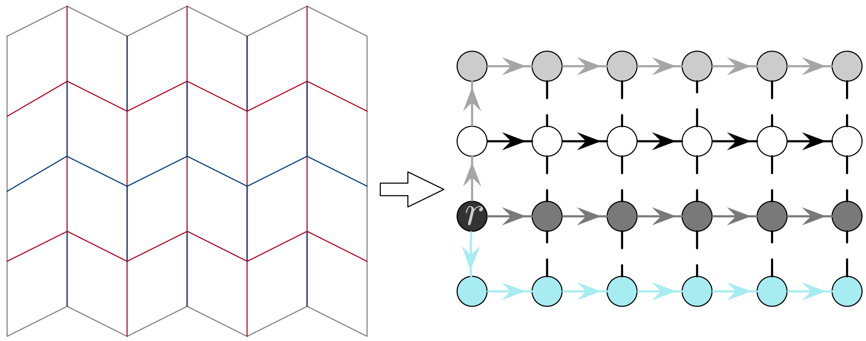

Figure 2.3: Miura folding pattern and example system graph and cut edges where r denotes the root node.

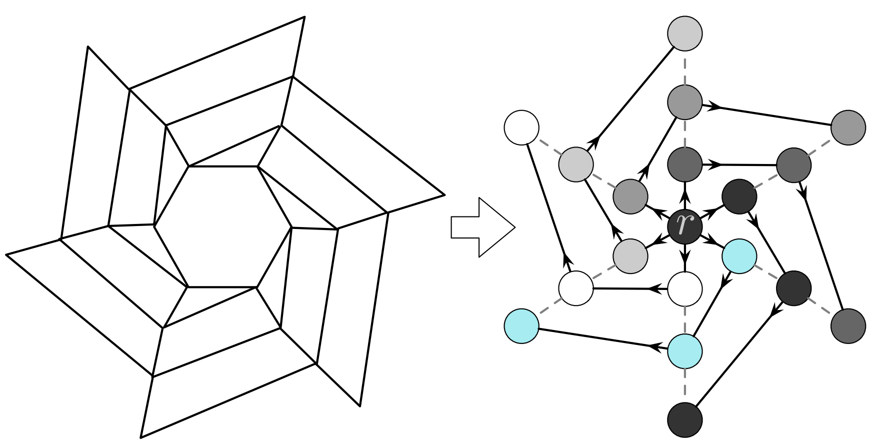

Figure 2.4: Scheel folding pattern and example graph with cut edges where r denotes the root node.

Figures 2.3 and 2.4 also display example graph patterns for their corresponding origami pattern. The patterns are segmented such that a single root parent node spawns the serial chains of the origami pattern in a manner that itself displays a repeatable and expandable pattern. These serial chains are then constrained to each other at each adjacent node of their chains. For algorithm processing, it is assumed that the root node is always the free flying spacecraft body. The pattern is then defined through declaring each chain series and defining each set of constraint nodes. For this approach, these tree topologies are assumed to be cut and defined such that they form an organized grid , as clearly seen in the graph of Figure 2.3. A graph like the Scheel pattern in Figure 2.4 can be adapted to mimic a grid with minimal adaptation, as demonstrated in Figure 2.5. The chains of the structure are laid out like a grid, and the constraint nodes are defined as the dashed lines. This system will require an additional set of closure nodes defined between the chains on the edge of the grid (represented by a repeated set of the leftmost chain).

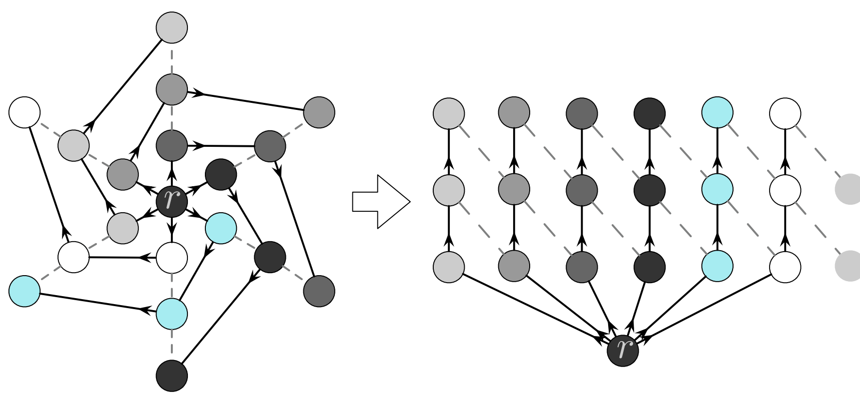

Figure 2.5: Scheel folding pattern graph adapted to a grid format, where the closed grid is represented by the closure constraints on the repeated left edge chain's nodes.

2.3.3 Constraints for Grid Adapted Tree Topologies

A given panel can have more than one constraint node, as is present where there are three or more chains in a pattern. The cut kinematic chains are defined by recording the chain sequence in terms of the named bodies in the chain from tip to base in the chain matrix κ as

$$\kappa_a = \begin{bmatrix} a(1) & ... & a(n_a) \end{bmatrix} \tag{2.44}$$

For reference, n_p are the number of constraint node pairs or number of implemented constraints, n_c are the total number of constraint nodes, n_b are the number of rigid bodies in the system, and n_h are the number of chains in the cut tree topology. Then the constraints information is stored in the $n_p \times 2$ constraint node matrix, Γ, containing the constraint node pair designations.

$$\Gamma = \begin{bmatrix} a(1) & b(1) \\ ... & \\ a(n_{b_h}1) & b(n_{b_h}2) \end{bmatrix} \tag{2.45}$$

For a given set of bodies connected in a grid format that does not close onto itself, like the Miura pattern, the total number of constraints needed to adapt the set to a tree-topology system is summarized by Equation 2.46 and the total number of constraint nodes on the system can be predicted by Equation 2.47, assuming constraint nodes are unique to a constraint pair.

$$n_p = (n_h - 1)\left(\frac{n_b}{n_h} - 1\right) \tag{2.46}$$

$$n_c = n_b - n_h \tag{2.47}$$

These are needed for constraint generating algorithms. Similar calculations can be derived for radially closed patterns by simply including the additional closure nodes.

2.3.4 Automated and Recursive Generation of Rigid Body Properties

For patterns that are built with repeating subgraphs, such as the Miura-Ori, populating the geometric definitions for the chain nodes and constraint nodes of each rigid body panel can be automated by using a uniform reference frame convention for each panel. For the numerical simulations presented here, the repeated panels of the Miura ori pattern are populated from two stock reference bodies. These provide the relative position and orientation of defined nodes of the bodies, the mass and inertia properties, and the relative position and orientation of nodes related to the inbound body on the chain. These last properties are provided through a base to tip recursive calculation. These two stock reference bodies are a "left" body and a "right body" as defined by Figure 2.6.

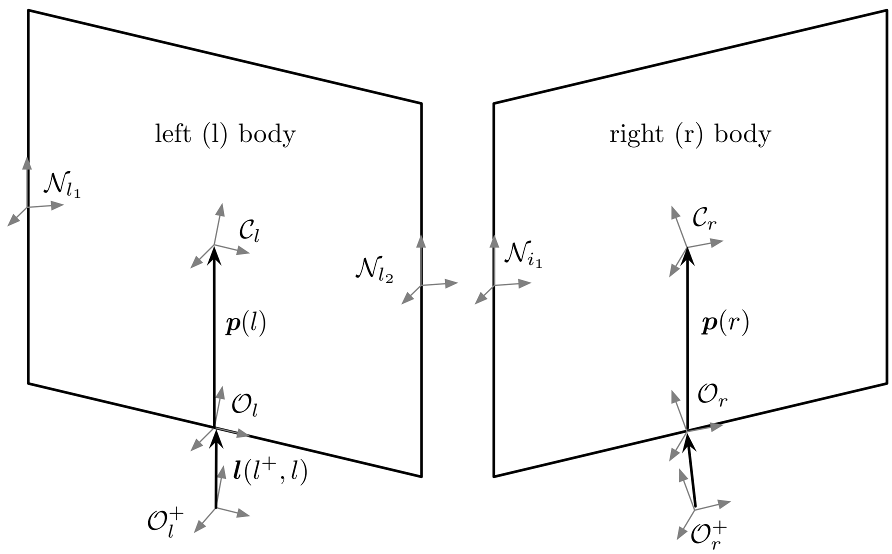

Figure 2.6: Diagram of geometric reference definitions for the two stock rigid bodies.

2.4 Multi-body Algorithm Expansions for Folded Structure Tree Topologies

2.4.1 Algorithm Summaries

The recursive forward dynamics algorithms from the literature are expanded to accommodate the generalized tree topology framework needed to handle folded structures. These expansions are suggested in the literature but are not explicitly presented. The expansions implemented in this thesis are summarized as follows. Each tip-to-base recursion formula must be converted to a tips-to-base gather recursion. Each chain outbound from a branching node is computed recursively and summed to the branching node. In Figure 2.7 the branching node is denoted as n and the chains are labeled a, b, and c, with subscript 1 denoting the tip node of each respective chain. Conversely,

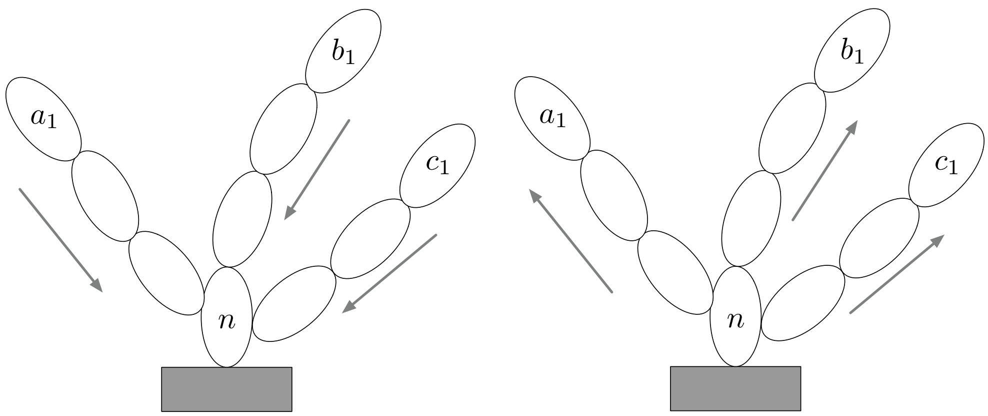

(a) Gather recursion (b) Scatter recursion

Figure 2.7: Illustrations of multiple serial chains algorithm processing schemes.

each base-to-tip recursion formula must be converted to a base-to-tips scatter recursion. The base body node behavior is calculated first and propagated through each chain. These gather and scatter algorithms present an opportunity for parallel computation, where each chain recursion can be done simultaneously apart from the final gathering or initial scattering calculations.

The following algorithms are provided as supplemental material to the literature,[39] and therefore the mathematical derivations and significance of the variables and operators are not discussed. Algorithm 1, 2, and 3 are executed sequentially. Algorithm 1 summarizes the first recursion in the dynamics framework and calculates the kinematics and velocities of the bodies. Algorithm 2 demonstrates the gather operation for the spatial inertia and spatial body forces recursions on the system. Finally, Algorithm 3 summaries adaptation for the spatial accelerations of the cut chains. For gather recursions, the algorithm expansions for multiple chains assume that for a given branching node, the chains branching from that node are processed before the chain that the branch is a member of. Similarly, for scatter recursions, chains containing branching nodes are processed before the branch chains. This ordering is contained in the algorithm frameworks here.

The variables referenced in this chapter are consistent with that in the literature[39] and previous work.[61,62] The index n references the base body and $n+1$ references the inertial frame. $\boldsymbol{V}(k)$ is the spatial velocity of a given body k, $\phi(k^+, k)$ is the spatial transformation matrix, $\boldsymbol{\Delta v}(k)$ is

Result: kinematics and velocities for each chain's bodies

$\boldsymbol{V}(n+1) = \mathbf{0}$

calculate all kinematics and velocities for the root body, n

for $m = 1$ **to** $n_{\mathbf{h}}$ **do**

  for $j = n_{\mathbf{b}}(m) - 1$ **to** 1 **do**

    set k to be the $m(j)$th body

    set l to be the next body, $m(j+1)$ in the m chain

$$
\begin{aligned}
\phi(k^{+}, k) &= f(\boldsymbol{q}(k), \text{body geometry}) \\
\Delta\boldsymbol{v}(k) &= H^{\intercal}(k)\boldsymbol{\beta}(k) \\
\Delta\boldsymbol{v}^{\omega}(k) &= [\Delta\boldsymbol{\omega}(k), 0, 0, 0] \\
\boldsymbol{V}(k) &= \phi^{\intercal}(k^{+}, k)\boldsymbol{V}(l) + \Delta\boldsymbol{v}(k) \\
\boldsymbol{a}(k) &= -\tilde{\Delta\boldsymbol{v}}^{\omega}(k)(\boldsymbol{V}(k) - \boldsymbol{\beta}(k)) \\
\boldsymbol{b}(k) &= \boldsymbol{V}\bar{(}k)M(k)\boldsymbol{V}(k) \\
\boldsymbol{T}(k) &= f(\boldsymbol{q}(k), H(k))
\end{aligned}
$$

  end

end

Algorithm 1: articulated body spatial velocities algorithm for multiple chains the relative spatial velocity of a body with respect to the next body in the chain, $\boldsymbol{a}(k)$ is the Coriolis spatial acceleration, $\boldsymbol{b}(k)$ is the gyroscopic spatial acceleration, $\boldsymbol{T}(k)$ is the internal spatial force acting at the hinge, and $H(k)$ is the hinge map matrix that defines the configuration dependence of the hinge behavior and maps the hinge velocities to the generalized spatial velocities of the body.

Algorithm 2 contains the sequence for recursively calculating the articulated body spatial inertia $P(k)$ and the articulated body forces $\boldsymbol{\zeta}(k)$. This requires the definition and reference of several spatial operators, and these can be reviewed in the literature. The articulated body spatial inertia represents the inertia of all the bodies connected outbound of a given body, and similarly the articulated body force represents the cumulative body force of all the bodies outbound in the chain. The superscript $^+$ denotes the transition of a value to the inboard reference frame defined in Figure 2.2. The spatial inertia of just body k is denoted $M(k)$, $D(k)$ is the articulated body hinge inertia, $G(k)$ is the articulated body Kalman gain operator, $\bar{\tau}(k)$ is the complement of the articulated body projection operator, $\boldsymbol{\epsilon}(k)$ is the articulated body inertia innovations generalized force, and $\boldsymbol{\eta}(k)$ is the articulated body inertia innovations generalized acceleration. For the gather recursion, n_r is the number of root bodies in the cut tree topology, or bodies that have chains branching from them.

Algorithm 3 provides the accelerations of the generalized coordinates, $\dot{\boldsymbol{\beta}}(k)$, and the spatial accelerations, $\boldsymbol{\alpha}(k)$, from the spatial operators listed in the previous algorithms. At this point, the equations of motion for the cut tree-topology of the structure is obtained, and the constraints for enforcing the closed-chain topology must be implemented.

2.4.2 Numerical Demonstration of General Tree Topology Dynamics Simulations

A numerical demonstration is designed to verify the correct implementation of the general tree topology algorithms from Section 2.4.1. An adequate system to serve as a demonstration of this is a 3 by 3 grid of rigid bodies, where this requires the ability to process more than two bodies on a chain, and to process more than two chains attached to a base body or spacecraft. An illustration of the configuration of each body is shown in Figure 2.8. Each panel is attached to the

Result: serial chain articulated body spatial inertia and articulated body forces for each chain's bodies

$P^{+}(0) = \mathbf{0}$, $\zeta^{+}(0) = \mathbf{0}$, $T(0) = \mathbf{0}$, $\bar{\tau}(0) = \mathbf{0}$

for $m = 1$ **to** n_h **do**

  for $j = 1$ **to** $n_b(m) - 1$ **do**

    set k to be the $m(j)$th body

    set i to be the previous body, $m(j-1)$ in the m chain

$$
\begin{aligned}
P(k) &= \phi(k,i)P^{+}(i)\phi^{\intercal}(k,i) + M(k) \\
D(k) &= H(k)P(k)H^{\intercal}(k) \\
G(k) &= P(k)H^{\intercal}(k)D^{-1}(k) \\
\bar{\tau}(k) &= \boldsymbol{I} - G(k)H(k) \\
P^{+}(k) &= \bar{\tau}(k)P(k) \\
\boldsymbol{\zeta}(k) &= \phi(k,i)\boldsymbol{\zeta}^{+}(i) + P(k)\boldsymbol{a}(k) + \boldsymbol{b}(k) \\
\boldsymbol{\epsilon}(k) &= \boldsymbol{T}(k) - H(k)\boldsymbol{\zeta}(k) \\
\boldsymbol{\eta}(k) &= D^{-1}(k)\boldsymbol{\epsilon}(k) \\
\boldsymbol{\zeta}^{+}(k) &= \boldsymbol{\zeta}(k) + G(k)\boldsymbol{\epsilon}(k)
\end{aligned}
$$

  end

end

for $n = 1$ **to** n_r **do**

  initialize $P(n) = M(n)$

  for $m = 1$ **to** n_h **do**

    set j to be the node of chain m connecting to that chain's root body

$$P(n) = P(n) + \phi(n,j)P^{+}(j)\phi^{\intercal}(n,j)$$

  end

  calculate $D(n)$, $G(n)$, $K(n)$, and $\psi(n^{+}, n)$

  initialize $\boldsymbol{\zeta}(n) = P(n)\boldsymbol{a}(n) + \boldsymbol{b}(n)$

  for $m = 1$ **to** n_h **do**

    set j to be the node of chain m connecting to the root body

$$\boldsymbol{\zeta}(n) = \boldsymbol{\zeta}(n) + \phi(n,j)\boldsymbol{\zeta}^{+}(j)$$

  end

end

calculate $\boldsymbol{\epsilon}(n)$ and $\boldsymbol{\eta}(n)$

Algorithm 2: articulated body spatial inertia and articulated body forces algorithm for multiple chains

Result: serial chain relative coordinate accelerations and spatial accelerations for multiple chains

$\boldsymbol{\alpha}(n+1) = \mathbf{0}$

calculate accelerations for the root body, n

for $m = 1$ **to** n_h **do**

  for $j = n_b(m) - 1$ **to** 1 **do**

    set k to be the $m(j)$th body

    set l to be the next body, $m(j+1)$ in the m chain

$$\begin{aligned}\boldsymbol{\alpha}^+(k) &= \phi^\intercal(k^+, k)\boldsymbol{\alpha}(l)\\ \dot{\boldsymbol{\beta}}(k) &= \boldsymbol{\eta}(k) - G^\intercal(k)\boldsymbol{\alpha}^+(k)\\ \boldsymbol{\alpha}(k) &= \boldsymbol{\alpha}^+(k) + H^\intercal(k)\dot{\boldsymbol{\beta}}(k) + \boldsymbol{a}(k)\end{aligned}$$

  end

end

Algorithm 3: articulated body spatial accelerations and general coordinate accelerations algorithm previous body in the chain with only a single rotation degree of freedom, θ_i, and an internal torsion spring acting at that rotation. The panels are treated as identical through the pattern definitions as discussed in Section 2.3.4, and their geometric relationships are generated using the described recursion approach. A RK4 integrator is used for numerical integration with a time step of 0.001 seconds, and the Matlab simulation takes 6 minutes and 36 seconds to complete.

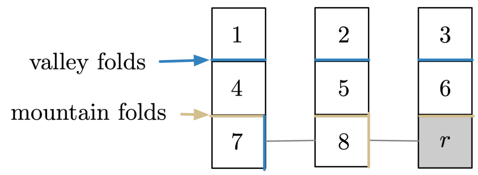

Figure 2.8: Diagram of the 3 by 3 grid tree topology system for the numerical demonstration.

Table 2.1: Mass properties of the rigid root body and panel bodies.

body	$m(k)$ (kg)	$K(k)$ (N/m)	**width** (m)	**thickness** (m)	**inertia** (kg m^2)
r	100	0	2	1	diag $(66.7, 66.7, 66.7)$
1-8	1	0.01	2	0.01	diag $(0.3342, 0.3342, 0.0017)$

2.5 Closed-Chain Forward Dynamics

As discussed in Section 2.3.2, capturing the closed-chain behavior is achieved by cutting an edge of a closed-chain system and treating each leg of the cut as an open serial chain, emulating a tree topology. Then the cut edges are treated as motion constraints imposed on the free dynamics of the tree. There are several approaches to enforcing the closure constraints. The augmented approach compensates for the cut edge by including a correction acceleration, resulting in additional motion constraint equations and a non-minimal coordinate set. This approach faces issues with error drift that must be compensated for with error control techniques. The direct approach uses matrix solvers and absolute coordinates, resulting in a much larger system and greater computational complexity. This approach also shares similar issues as the augmented approach, and therefore is not considered, as the augmented approach is more desirable for this application. A new technique

Table 2.2: Geometry properties of the rigid bodies.

body	$\theta(c_k, k-1^+)$ (rad)	$\boldsymbol{p}(c_k, k-1^+)$ (m)	$\boldsymbol{p}(k, c_k)$ (m)
r	[π/2,0,0]	[1,0,0]	[0,0,0]
1-6	[0,0,0]	[1,0,0]	[1,0,0]
7	[0,π/2,0]	[1,0,0]	[0,0,-1]
8	[0,π/2,0]	[1,0,0]	[0,0,-1]

Table 2.3: Initial conditions of the numerical simulation.

body	θ (rad)	$\dot{\beta}$ (rad/s)
r	[0,0,0]	[0,0,0]
mountain folds, 4,5,6,8	π	0
valley folds, 1,2,3,7	$-\pi$	0

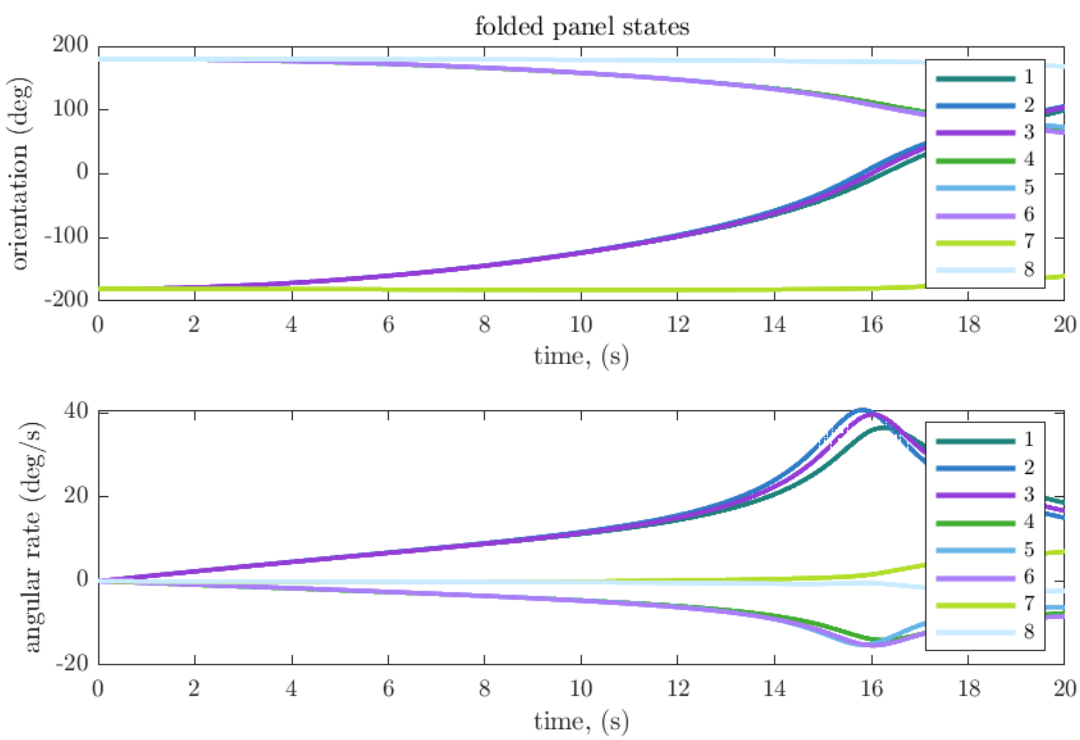

Figure 2.9: Angular orientation and rates of the eight panel bodies.

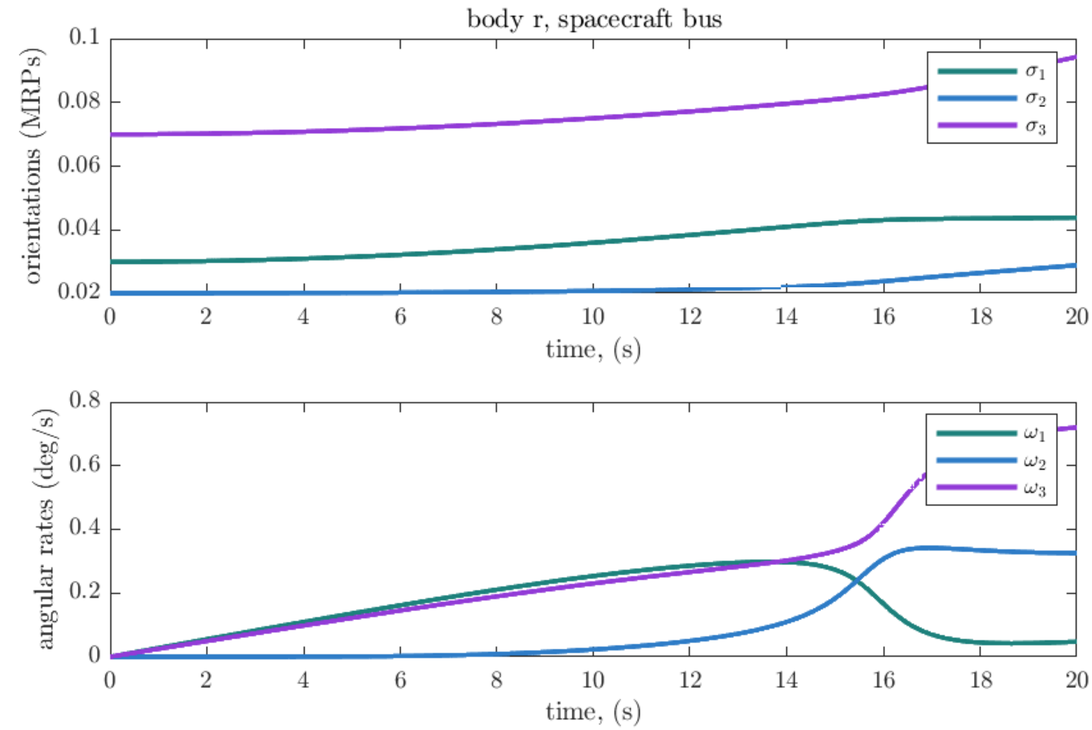

Figure 2.10: Angular orientation and rates of the spacecraft body in three dimensional space.

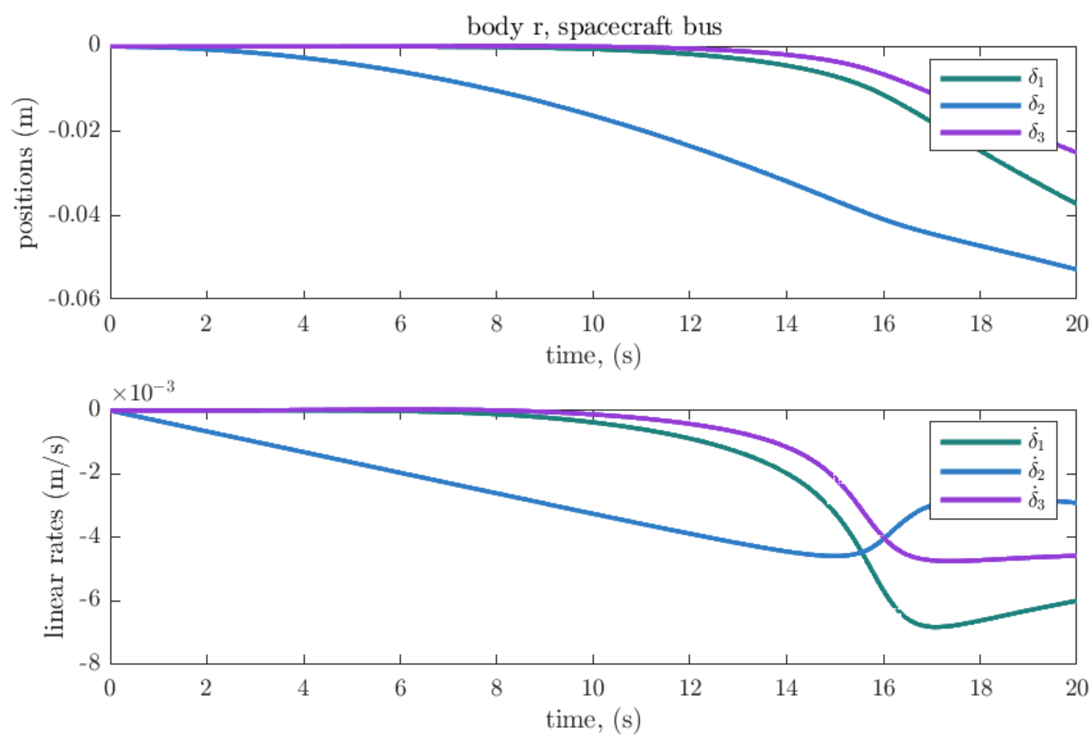

Figure 2.11: Linear orientation and rates of the spacecraft body in three dimensional space.

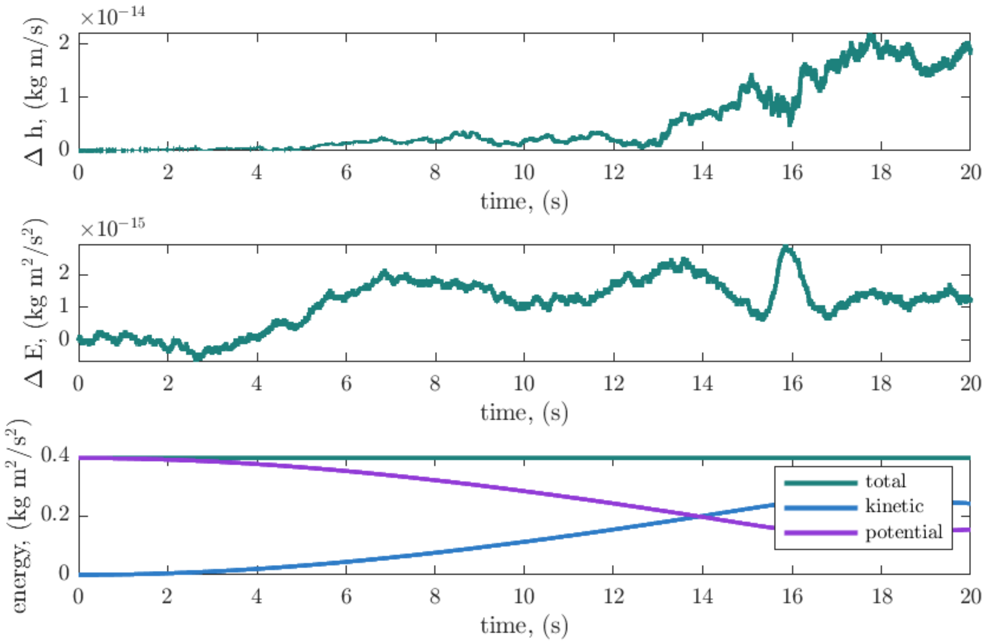

Figure 2.12: Change in total system angular momentum, total system energy, and the kinetic and potential energy over time.

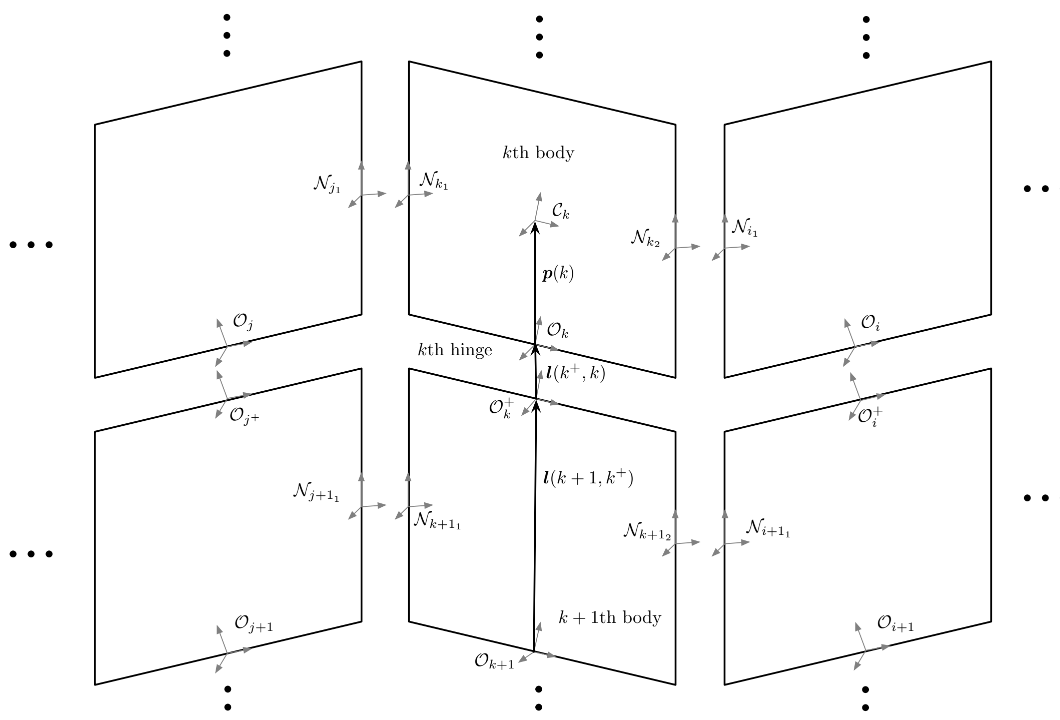

Figure 2.13: Vector and frame notation between multiple serial chains subject to multiple closure constraints.

that provides a minimal coordinate set is the constraint embedding approach. In this approach, the non-tree graph is transformed into a tree topology by aggregating the closed-chain structures of the topology into a representative node. This is suitable for systems with a clear tree-like structure surrounding the closed-chain elements. The folded structures of interest contain multiple dependent systems of closed loops, as demonstrated in Figures 2.3 and 2.4, and therefore this approach is not well suited to the problems of interest and is not currently considered. Therefore, the tree-augmented approach is selected and developed for the general origami-folded spacecraft structure. Custom algorithms are developed specifically to handle the large number of rigid bodies subjected to closed-chain constraints across multiple serial chains, as depicted in Figure 2.13, and are presented.

2.5.1 Tree-Augmented Approach to Closed Chain Structures

Implementing the correction terms to account for the motion constraints is captured in the system equations of motion by introducing the Lagrange Multipliers,[39] denoted as λ, to represent the constraint forces. Additionally, a new set of equations must be considered to include the constraint expression. The generalized acceleration is then defined as

$$\dot{\beta} = \dot{\beta}_f + \dot{\beta}_c \tag{2.48}$$

where $\dot{\beta}_f$ are the free unconstrained accelerations and $\dot{\beta}_c$ are the correction accelerations. The correction acceleration is derived from the constraint expression, and is expressed in terms of global system spatial operators as

$$\dot{\beta}_c = [I - H\phi K]D^{-1}H\phi\mathcal{B}Q^{\intercal}\lambda \tag{2.49}$$

where H is the global hinge map matrix, ϕ is the $6n_b \times 6n_b$ global spatial transformation matrix, K is the $6n_b \times 6n_b$ spatial operator referred to in literature as the shifted Kalman gain operator, D is the $6n_b \times 6n_b$ articulated body hinge inertia, and $\mathcal{B}$ is th $6n_b \times 6n_c$ node pick-off operator that transforms information from the body frame to the relevant constraint nodes on the body. Q is the

$n_{c_{\mathrm{DOF}}} \times 6n_b$ constraint matrix that defines the constrained spatial degrees of freedom between nodes where $n_{c_{\mathrm{DOF}}}$ are the total number of constrained node pair degrees of freedom. For a node that is rigidly constrained to another, the corresponding entry in Q is a 6×6 identity matrix. Finally, λ is the $n_{c_{\mathrm{DOF}}} \times 1$ Lagrange Multipliers. These are defined for loop constraints as

$$\lambda = -[Q\underline{\Lambda}Q^{\intercal}]^{-1}\ddot{\boldsymbol{\Phi}} \tag{2.50}$$

where $\underline{\Lambda}$ is the operation space compliance matrix

$$\underline{\Lambda} = \mathcal{B}^{\intercal}\Omega\mathcal{B} \tag{2.51}$$

and Ω is the extended operational space compliance matrix. Additionally, $\ddot{\boldsymbol{\Phi}}(\beta, t)$ is the derivative of a Pfaffian form constraint equation, $\dot{\boldsymbol{\Phi}}(\beta, t)$.

2.5.1.1 Spatial Constraint Equations for Folded Structures

For any set of two closure nodes for a single closed loop in the system, up to six constraint equations can be written in the global spatial coordinates, three for position and three for rotations. For a rigorous derivation of the constraints, these will be considered separately and then interpreted to a general spatial format for implementation. First considering the position of the closure nodes, a constraint equation that defines the two nodes must be in the same place is written as

$$\boldsymbol{\Phi}^{\boldsymbol{v}} = \boldsymbol{l}(1_{nd}) - \boldsymbol{l}(2_{nd}) = \mathbf{0} \tag{2.52}$$

Where the location of the nodes can be written in terms of the hinge frames as

$$\boldsymbol{\Phi}^{\boldsymbol{v}} = (\boldsymbol{l}(1) + \boldsymbol{l}(1, 1_{nd})) - (\boldsymbol{l}(2) + \boldsymbol{l}(2, 2_{nd})) = \mathbf{0} \tag{2.53}$$

Taking the first time derivative

$$\dot{\boldsymbol{\Phi}}^{\boldsymbol{v}} = \frac{\mathrm{d}}{\mathrm{d}t}(\boldsymbol{l}(1) + \boldsymbol{l}(1, 1_{nd})) - \frac{\mathrm{d}}{\mathrm{d}t}(\boldsymbol{l}(2) + \boldsymbol{l}(2, 2_{nd})) = \mathbf{0} \tag{2.54}$$

Using the Transport theorem and the shorthand from Equation 2.24,

$$\dot{\boldsymbol{\Phi}}^{\boldsymbol{v}} = (\boldsymbol{v}(1) + \boldsymbol{\omega}(1) \times \boldsymbol{l}(1, 1_{nd})) - (\boldsymbol{v}(2) + \boldsymbol{\omega}(2) \times \boldsymbol{l}(2, 2_{nd})) = \mathbf{0} \tag{2.55}$$

Then recognizing the relationship with the node pick-off operator, the velocity form of the position loop constraint is

$$\dot{\boldsymbol{\Phi}}^{\boldsymbol{v}} = \boldsymbol{v}(1_{nd}) - \boldsymbol{v}(2_{nd}) = \boldsymbol{0} \tag{2.56}$$

Taking the second derivative,

$$\ddot{\boldsymbol{\Phi}}^{\boldsymbol{v}} = \frac{\mathrm{d}}{\mathrm{d}t}(\boldsymbol{v}(1) + \boldsymbol{\omega}(1) \times \boldsymbol{l}(1, 1_{nd})) - \frac{\mathrm{d}}{\mathrm{d}t}(\boldsymbol{v}(2) + \boldsymbol{\omega}(2) \times \boldsymbol{l}(2, 2_{nd})) = \boldsymbol{0} \tag{2.57}$$

$$\begin{aligned}\ddot{\boldsymbol{\Phi}}^{\boldsymbol{v}} = (\boldsymbol{\alpha}^{\boldsymbol{v}}(1) + (\dot{\boldsymbol{\omega}}(1) \times \boldsymbol{l}(1, 1_{nd})) + \boldsymbol{\omega}(1) \times (\boldsymbol{\omega}(1) \times \boldsymbol{l}(1, 1_{nd}))) - \\ (\boldsymbol{\alpha}^{\boldsymbol{v}}(2) + (\dot{\boldsymbol{\omega}}(2) \times \boldsymbol{l}(2, 2_{nd})) + \boldsymbol{\omega}(2) \times (\boldsymbol{\omega}(2) \times \boldsymbol{l}(2, 2_{nd}))) = \boldsymbol{0}\end{aligned} \tag{2.58}$$

$$\ddot{\boldsymbol{\Phi}}^{\boldsymbol{v}} = (\boldsymbol{\alpha}^{\boldsymbol{v}}(1_{nd}) + \boldsymbol{\omega}(1) \times (\boldsymbol{\omega}(1) \times \boldsymbol{l}(1, 1_{nd}))) - (\boldsymbol{\alpha}^{\boldsymbol{v}}(2_{nd}) + \boldsymbol{\omega}(2) \times (\boldsymbol{\omega}(2) \times \boldsymbol{l}(2, 2_{nd}))) = \boldsymbol{0} \tag{2.59}$$

where $\boldsymbol{\alpha}^{\boldsymbol{v}}(k)$ is the free, unconstrained linear acceleration of body k, and $\boldsymbol{\alpha}^{\boldsymbol{v}}(k_{nd})$ is the free, unconstrained linear acceleration of the constraint node points on body k.

Now considering the constraint derivation for the rotational components of the nodes, in order to avoid complications due to the choice of non-integrable rates $\boldsymbol{\omega}(k)$ for the generalized coordinates, a non-holonomic Pffafian constraint is written as a function of those rates. This use of rate-based constraints will introduce error control concerns.

$$\dot{\boldsymbol{\Phi}}^{\boldsymbol{\omega}} = \boldsymbol{\omega}(1_{nd}) - \boldsymbol{\omega}(2_{nd}) = \boldsymbol{\omega}(1) - \boldsymbol{\omega}(2) = \boldsymbol{0} \tag{2.60}$$

Taking the time derivative

$$\ddot{\boldsymbol{\Phi}}^{\boldsymbol{\omega}} = \dot{\boldsymbol{\omega}}(1) - \dot{\boldsymbol{\omega}}(2) = \boldsymbol{0} \tag{2.61}$$

$$\ddot{\boldsymbol{\Phi}}^{\boldsymbol{\omega}} = \boldsymbol{\alpha}_{\boldsymbol{\omega}}(1) - \boldsymbol{\alpha}_{\boldsymbol{\omega}}(2) = \boldsymbol{0} \tag{2.62}$$

where $\boldsymbol{\alpha}^{\boldsymbol{\omega}}(k)$ is the free, unconstrained rotational acceleration of body k, and $\boldsymbol{\omega}(k_{nd}) = \boldsymbol{\omega}(k)$ because these points are on the same rigid body.

Now considering the spatial operator format of the algorithms discussed thus far, the constraint formulation is restructured into a single spatial expression as

$$\ddot{\mathbf{\Phi}} = \phi^{\mathsf{T}}(1,1_{nd})\boldsymbol{\alpha}(1) - \phi^{\mathsf{T}}(2,2_{nd})\boldsymbol{\alpha}(2) + \begin{bmatrix} \mathbf{0} \\ \boldsymbol{\omega}(1)\times(\boldsymbol{\omega}(1)\times\boldsymbol{l}(1,1_{nd})) - \boldsymbol{\omega}(2)\times(\boldsymbol{\omega}(2)\times\boldsymbol{l}(2,2_{nd})) \end{bmatrix} = \mathbf{0} \quad (2.63)$$

Expanding to include the constraint matrix formulation for constraint design flexibility,

$$\ddot{\mathbf{\Phi}} = [Q]\begin{bmatrix} \phi^{\mathsf{T}}(1,1_{nd})\boldsymbol{\alpha}(1) + \begin{bmatrix} \mathbf{0} \\ \boldsymbol{\omega}(1)\times(\boldsymbol{\omega}(1)\times\boldsymbol{l}(1,1_{nd})) \end{bmatrix} \\ \phi^{\mathsf{T}}(2,2_{nd})\boldsymbol{\alpha}(2) + \begin{bmatrix} \mathbf{0} \\ \boldsymbol{\omega}(2)\times(\boldsymbol{\omega}(2)\times\boldsymbol{l}(2,2_{nd})) \end{bmatrix} \end{bmatrix} = \mathbf{0} \quad (2.64)$$

which can be written in a general compact form as

$$\ddot{\mathbf{\Phi}} = Q\left(\mathcal{B}^{\mathsf{T}}\boldsymbol{\alpha} + \mathcal{U}\right) \quad (2.65)$$

This two node derivation is applicable to multiple closed chain constraints within a system by simply considering the formatting of the Q and $\mathcal{B}$ matrices in those cases. Special care must be applied to generating the $\mathcal{U}$ vector appropriately for this expanded case.

2.5.1.2 Baumgarte Stabilization of Constraint Enforcement

The forward dynamics problem for rigid bodies subject to closure constraints is unstable in numerical computation and the bodies in the system quickly deviate from the constraint manifold over time. Initial numerical demonstrations were found to be very unstable on the time scales of interest and under the actuation of internal forces of deployable space structures. The most popular approach to removing this instability is to use Baumgarte Stabilization,[63] and this method is implemented here. A correction gain is included to the constraint equation, $\mathfrak{f}$, such that instead of writing

$$\mathfrak{f} = \ddot{\mathbf{\Phi}} = \mathbf{0} \quad (2.66)$$

the constraint equation is defined as

$$\mathfrak{f} = \ddot{\mathbf{\Phi}} + 2\mathfrak{a}\dot{\mathbf{\Phi}} + \mathfrak{b}^2\mathbf{\Phi} = \mathbf{0} \tag{2.67}$$

where Φ is stable for any positive values of $\mathfrak{a}$ and $\mathfrak{b}$, which are tuned uniquely for each system they are implemented in.

2.5.1.3 Computation of the Operational Space Compliance Matrix for Folded Space Structures

The diagonal terms of Ω are computed directly using a recursion for free-flying system from the literature[39] as

$$\Omega(k,k) = \Upsilon(k) = [P(k) + S(k)]^{-1} \tag{2.68}$$

for all bodies k, where $\Upsilon(k)$ is known as the operational space compliance kernel. The compliance properties of a free-flying system enables these terms to be expressed in terms of the articulated body inertia and what is referred to as the dual articulated body inertia, $S(k)$. The difference between these two inertias is simply whether the base or tip body is treated as hinged to free inertial space, and each is calculated using the recursive algorithm defined in Algorithm 4. Spatial operator expressions are identical to those defined for Algorithm 2, with subscript dl indicating the dual inertia distinction.

The diagonal terms of Ω are computed directly using Equation 2.68. Then, where for two bodies k and j

$$\Omega(k,j) = \Omega(j,k)^{\intercal} \tag{2.69}$$

the off diagonal terms are computed by propagating through the root node, r, as

$$\Omega(j,k) = \Omega(j,j)\psi(j,r)\psi(r,k) \tag{2.70}$$

where $\psi(r,k)$ represents the articulated body transformation matrix and is calculated from the articulated body projection operator and the spatial transformation matrix $\psi(r,k) = \phi(r,k)\bar{\tau}(k)$.

Result: serial chain dual spatial inertia for each chain's bodies
$P^{+}(0) = \mathbf{0}$, $\bar{\tau}(0) = \mathbf{0}$
for $m = 1$ **to** n_h **do**
  for $j = n_b(m) - 1$ **to** 1 **do**
    set k to be the $m(j)$th body
    set l to be the next body, $m(j+1)$ in the m chain

$$
\begin{aligned}
S^{+}(k) &= \phi^{\intercal}(i,k)(S(i) + M(i))\phi(i,k) \\
D_{dl}(k) &= H(k)S^{+}(k)H^{\intercal}(k) \\
G_{dl}(k) &= -S^{+}(k)H^{\intercal}(k)D_{dl}^{-1}(k) \\
\bar{\tau}_{dl}(k) &= \boldsymbol{I} - G_{dl}(k)H(k) \\
S(k) &= \bar{\tau}_{dl}(k)S^{+}(k)
\end{aligned}
$$

  end
end

Algorithm 4: articulated body dual spatial inertia algorithm for multiple chains

This property enables all of the operational space matrix terms to be computed from the diagonal terms, and in turn from the recursive articulated body inertias.

To populate the operational space matrix, $\underline{\Lambda}$, only the diagonal terms and cross-diagonal terms of the extended operational space matrix that correspond with the constraint nodes are needed due to the structure of $\mathcal{B}$. The node pick off operator $\mathcal{B}$ is a $6n \times 6n_c$ sparse spatial operator matrix that contains the spatial rigid body transformation matrix from a given body frame to the constraint node frame at that body's row and that node's column, for example $\phi^{\intercal}(k, \mathcal{N}_{k_2})$. Then $\underline{\Lambda}$ is populated using the shortcut expression provided by[39]

$$\underline{\Lambda}(\mathcal{N}_{k_2}, \mathcal{N}_{j_1}) = \phi^{\intercal}(k, \mathcal{N}_{k_2})\Omega(k, j)\phi(j, \mathcal{N}_{j_1}) \tag{2.71}$$

when using the node frame definitions demonstrated in Figure 2.13, and k is shorthand for $\mathcal{O}_k$.

2.5.1.4 Transformation of Constraint Equations to Acceleration Corrections

This reviews the mathematical background needed to generate the node constraint expressions, and the steps are implemented in Algorithm 5. The Lagrange multipliers λ are now interpreted into a constraint force that is applied to the rigid body system. The constraint force is defined as

$$f_c = -Q^{\intercal}\lambda \tag{2.72}$$

and is converted into constraint correction body force at each hinge degree of freedom through Algorithm 6, an algorithm that is adapted here for any general case of multiple serial chains subject to multiple constraints. The constraint correction body forces are then used to calculate the constraint correction accelerations $\dot{\beta}_c$ in Algorithm 7. Here, $\zeta(k)$ and $\eta(k)$ are not related to those used in previous algorithms but are representing similar roles.

Result: internal forces due to closure constraints

(1) Generate the extended operational space compliance matrix Ω using Equation 2.70 for all constraint node bodies in the system

(2) Project this into the operational space compliance matrix $\underline{\Lambda}$ for all constraint nodes using Equation 2.71

(3) Calculate the Lagrange multipliers λ in Equation 2.50

(4) Express the constraint force f_c using Equation 2.72

Algorithm 5: Converting constraint node information to constraint forces

2.5.2 Origami-Folded Deployable Spacecraft Structure Algorithm

The complete algorithm for solving the dynamics of a set of rigid bodies subject to any number of closure constraints is summarized in Figure 2.14. The connections between information obtained and required at multiple steps in the algorithm are depicted by arrows. This algorithm is written to only apply to multiple closed-chain constraints within a free-flying spacecraft system, but can be applied to any system that resembles the folding-structure topologies described in this chapter. While the ABFD framework provides an $\mathcal{O}(\mathcal{N})$ solution to the free serial chain dynamics in Algorithm 3, the overall computational efficiency of the Algorithm summarized in 2.14 is less. The matrix inversion of Equation 2.50 represents an $\mathcal{O}({n_c}^3)$ operation that dramatically slows down the simulation as more constraint nodes of the origami pattern are introduced. Unfortunately the non-square structure of the Q matrices and the fully populated structure of the $\underline{\Lambda}$ matrix indicates that further decomposition of the matrices will not yield a convenient property as the Innovations Factorization Method lends to the articulated body model. Therefore, the overall computation efficiency of this algorithm is $\mathcal{O}({n_c}^3)$.

2.5.3 Four-Body Closed Loop Structure Case

The closed-chain theory is now demonstrated in detail for the four-body structure case. Using the notation displayed in Figure 2.15, the cut edge is selected at the internal edge connecting nodes l and m, where the root parent node is selected as node r. Due to the non-integrable spatial

Result: constraint correction body forces for multiple serial chains
$\boldsymbol{\alpha}(n+1) = \mathbf{0}$
for $m = 1$ **to** n_h **do**
  for $j = 1$ **to** $n_b(m) - 1$ **do**
    set k to be the $m(j)$th body
    if $j = 1$ **then**

$$\boldsymbol{\zeta}(k) = -\phi(\mathcal{B}_k, \mathcal{N}_k^i) f_c(k)$$

    else
      set i to be the previous body, $m(j-1)$ in the m chain

$$\boldsymbol{\zeta}(k) = \psi(k,i)\boldsymbol{\zeta}(i) - \phi(\mathcal{B}_k, \mathcal{N}_k^i) f_c(k)$$

    end

$$\boldsymbol{\eta}(k) = -D^{-1}(k) H(k) \boldsymbol{\zeta}(k)$$

  end
end
initialize $\boldsymbol{\zeta}(n) = \mathbf{0}$
for $m = 1$ **to** n_h **do**
  set j to be the node of chain m connecting to the root body

$$\boldsymbol{\zeta}(n) = \boldsymbol{\zeta}(n) + \phi(n,j)\boldsymbol{\zeta}^+(j)$$

end

Algorithm 6: Constraint correction body forces for multiple serial chains

Result: constraint correction accelerations for multiple serial chains
$\boldsymbol{\alpha}(n+1) = \mathbf{0}$
calculate accelerations for the root body, n
for $m = 1$ **to** n_h **do**
  for $j = n_b(m) - 1$ **to** 1 **do**
    set k to be the $m(j)$th body
    set l to be the next body, $m(j+1)$ in the m chain

$$\lambda(k) = \psi^{\mathsf{T}}(l,k)\lambda(l) + H^{\mathsf{T}}(k)\boldsymbol{\eta}(k)$$
$$\dot{\boldsymbol{\beta}}_c(k) = \boldsymbol{\eta}(k) - K^{\mathsf{T}}(k)\lambda(l)$$

  end
end

Algorithm 7: Constraint correction accelerations for multiple serial chains

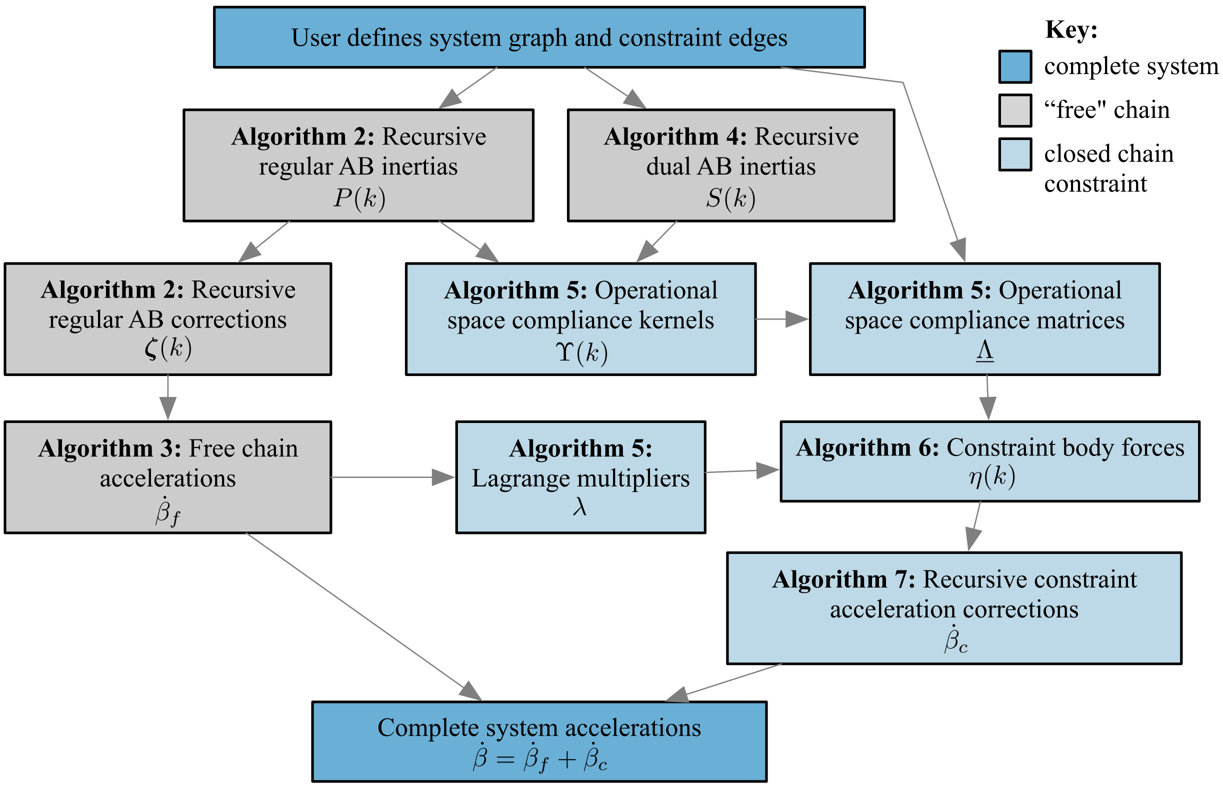

Figure 2.14: Diagram of full closed-chain dynamics algorithm flow.

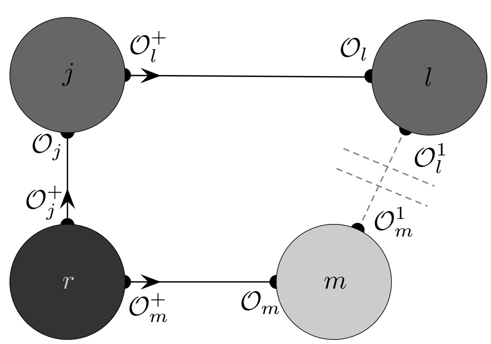

Figure 2.15: Frame notation of 4 body closed-chain structure.

velocities, the closure constraint is better expressed as a non-holonomic constraint, expressed in the Pfaffian form, as derived in Section 2.5.1. The points on the body where the constraint is to be applied must first be defined. Where frame $\mathcal{O}_m$ denotes the m^{th} link hinge frame connecting to the body's predecessor in the chain, the single outboard frame where the closure is connected is denoted as $\mathcal{O}_m^1$. Similarly, the outboard frame of the l^{th} link's closure point is denoted as $\mathcal{O}_l^1$, as illustrated in Figure 2.15. Then the spatial velocity at these closure nodes, V_{nd}, can be mapped from the global spatial velocity at the body hinges using the pick-off spatial operator, $\mathcal{B}$,

$$V_{nd} = \mathcal{B}^{\intercal} V \tag{2.73}$$

where $\mathcal{B}$ is $\in R^{6n \times 6n_{nd}}$, and contains the corresponding spatial transformation matrices. For this four-body example,

$$V = \begin{bmatrix} \boldsymbol{V}(m) & \boldsymbol{V}(l) & \boldsymbol{V}(j) & \boldsymbol{V}(r) \end{bmatrix}^{\intercal} \in R^{6n \times 1} \tag{2.74}$$

and

$$V_{nd} = \begin{bmatrix} \boldsymbol{V}(m^1) & \boldsymbol{V}(l^1) \end{bmatrix}^{\intercal} \in R^{6n_{nd} \times 1} \tag{2.75}$$

Following this order structure,

$$\mathcal{B} = \begin{bmatrix} \phi(\mathcal{O}_m, \mathcal{O}_m^1) & 0_6 \\ 0_6 & \phi(\mathcal{O}_l, \mathcal{O}_l^1) \\ 0_6 & 0_6 \\ 0_6 & 0_6 \end{bmatrix} \tag{2.76}$$

Using this notation, the Pfaffian constraint is then expressed as:

$$\dot{\boldsymbol{\Phi}}(\beta, t) = QV_{nd} = \begin{bmatrix} Q(m^1) & -Q(l^1) \end{bmatrix} \begin{bmatrix} V(m^1) \\ V(l^1) \end{bmatrix} = \mathbf{0} \tag{2.77}$$

where Q is the constraint matrix relating rigidly constrained velocity degrees of freedom between nodes l and k. A fully constrained node would have an identity matrix for the corresponding constraint matrix. For this case, bodies l and m are permitted to rotate about their hinge axes, so

$$Q(m^1) = Q(l^1) = \begin{bmatrix} 0 & 1 & 0 & 0 & 0 & 0 \\ 0 & 0 & 1 & 0 & 0 & 0 \\ 0 & 0 & 0 & 1 & 0 & 0 \\ 0 & 0 & 0 & 0 & 1 & 0 \\ 0 & 0 & 0 & 0 & 0 & 1 \end{bmatrix} \tag{2.78}$$

The Lagrange multipliers for this case are derived as follows. To derive the operational space matrix, $\underline{\Lambda}$, only the diagonal terms and cross-diagonal terms of the extended operational space matrix that correspond with the constraint nodes are needed due to the structure of $\mathcal{B}$. Then

$$\underline{\Lambda} = \mathcal{B}^{\mathsf{T}} \begin{bmatrix} \Omega(m,m) & \Omega(m,l) & \times & \times \\ \Omega(l,m) & \Omega(l,l) & \times & \times \\ \times & \times & \times & \times \\ \times & \times & \times & \times \end{bmatrix} \mathcal{B} \tag{2.79}$$

The diagonal terms are computed directly using Equation 2.68. Then, where $\Omega(l,m) = \Omega(m,l)^{\mathsf{T}}$, the off diagonal terms are computed by propagating through the root node, as

$$\Omega(m,l) = \Omega(m,m)\psi(m,r)\psi(r,l) \tag{2.80}$$

where ψ represents the articulated body transformation matrix and is calculated from the articulated body inertia and the rigid body transformation matrix. This enables the direct calculation of the constraint force and constraint acceleration using the Algorithms from Section 2.5.1. These calculations will now be implemented in a numerical demonstration.

2.5.3.1 Numerical Demonstration of a Constrained Four-Bar Mechanism

A physical case of a four-bar mechanism with only in plane motions is now implemented in a numerical demonstration for initial assessment of the closure constraint approach. The numerical integration is run with an RK4 integrator using a 0.001 second time step, over a 5 second simulation, and the computational clock time for the integration is 38.7 seconds. Each bar is defined with geometric and mass properties as defined in Tables 2.4, 2.5, and 2.6. One hinge joint is equipped with a torsion spring that creates an internal force to open the mechanism. The initial condition of the system, reported in Table 2.7, flattens the four bar mechanism so the spring actuated joint is closed to 45 deg and the free joint angles are 135 deg. The constraint is set to a rigid closure constraint in this demonstration for clear state evaluation. In Figure 2.16 it is seen that the bars are actuated, and in Figures 2.17 and 2.18, the free-flying root bar is seen to do the same. Under these conditions, the conservation of angular momentum and kinetic energy is expected to hold, and in Figure 2.19 this is true under an allowable numerical tolerance. The energy is seen to drift at a higher order of magnitude than the angular momentum and this is attributed to the use of the Baumgarte Stabilization technique on the constraint equation. A primary challenge of this approach is determining an acceptable numerical tolerance for conservation drift for the system, a metric that is heavily influenced by the tuning of the Baumgarte parameters. For this case, $\alpha = 1400$ and $\beta = 0$, where only the Pfaffian form is available for all of the constraint equations. The values of the constraint equations is shown over time in Figure 2.20, where it is shown to stabilize at magnitudes around $10 \times E^{-6}$, which is considered numerically acceptable for this analysis. The internal constraint forces and torques are shown in Figure 2.21, and are shown to have notable forces as required to counter the internal spring forces. This simulation provides the first validation of the constraint enforcement performance for an in-plane dynamics case.

Table 2.4: Mass properties of the rigid root body and bar bodies.

body	$m(k)$ (kg)	$K(k)$ (N/mm)	**length** (mm)	**inertia** (kg mm^2)
r	0.96	0	100	diag $(344.3, 12.1, 344.3)$
1	0.72	0	75	diag $(809.9, 16.0, 809.9)$
2	0.96	0	100	diag $(344.3, 12.1, 344.3)$
3	0.72	1000	75	diag $(809.9, 16.0, 809.9)$

Additionally, a comparison study is done to assess performance against a known simulation tool. The four bar simulation is replicated in the Abaqus 6.14 software using simple beam elements to represent the bars and single degree of freedom hinge connectors to represent the hinge nodes,

Table 2.5: Geometry properties of the rigid bodies.

body	$\theta(c, k-1^+)$ (rad)	$\boldsymbol{p}(c, k-1^+)$ (m)	$\boldsymbol{p}(k, c)$ (m)
r_1	$[0, 0, 0]$	$[0, -50, 0]$	$[0, 0, 0]$
r_2	$[0, 0, 0]$	$[0, 50, 0]$	$[0, 0, 0]$
1	$[0, 0, 0]$	$[0, -37.5, 0]$	$[0, 0, 0]$
2	$[0, 0, 0]$	$[0, 50, 0]$	$[0, 0, 0]$
3	$[0, 0, 0]$	$[0, 37.5, 0]$	$[0, 37.5, 0]$

Table 2.6: Geometry properties of the constraint nodes.

i	$\theta(k, \mathcal{N}_{k_i})$ (rad)	$\boldsymbol{p}(k, \mathcal{N}_{k_i})$ (m)
1	$[0, 0, 0]$	$[0, -75, 0]$
2	$[0, 0, 0]$	$[0, 100, 0]$

Table 2.7: Initial conditions of the numerical simulation.

body	q	$\dot{\beta}$
r	$[0, 0, 0, 0, 0, 0]$	$[0, 0, 0, 0, 0, 0]$
1	$-3\pi/4$	0
2	$3\pi/4$	0
3	$\pi/4$	0

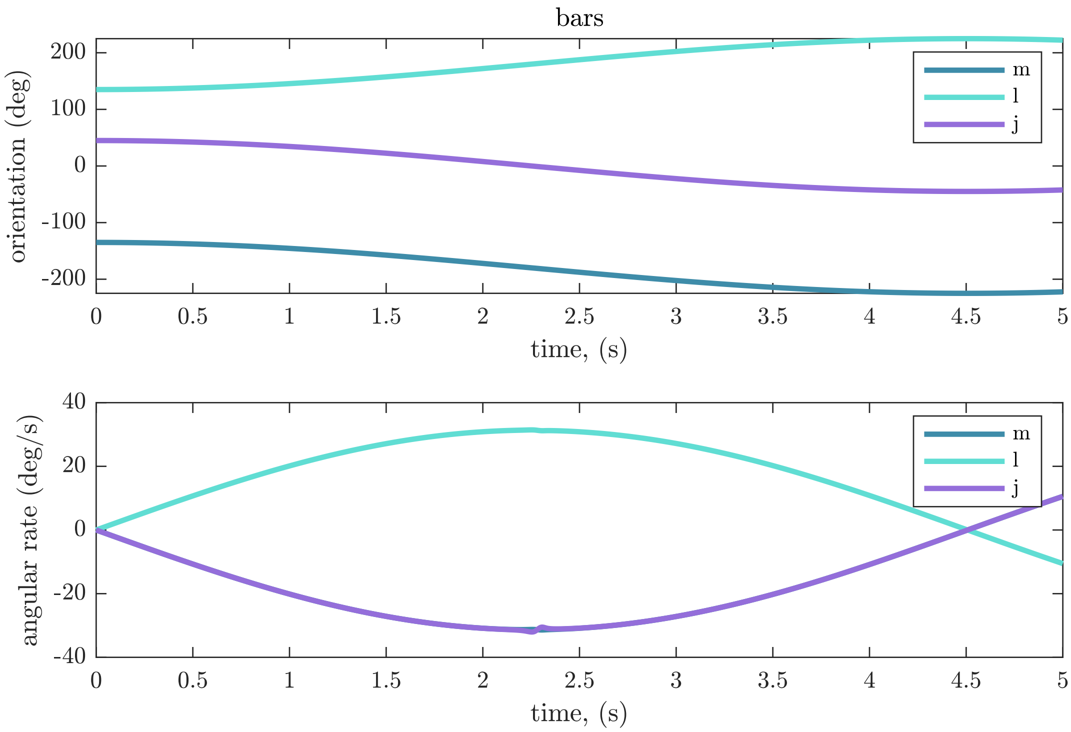

Figure 2.16: Angular orientation and rates of the three bar bodies.

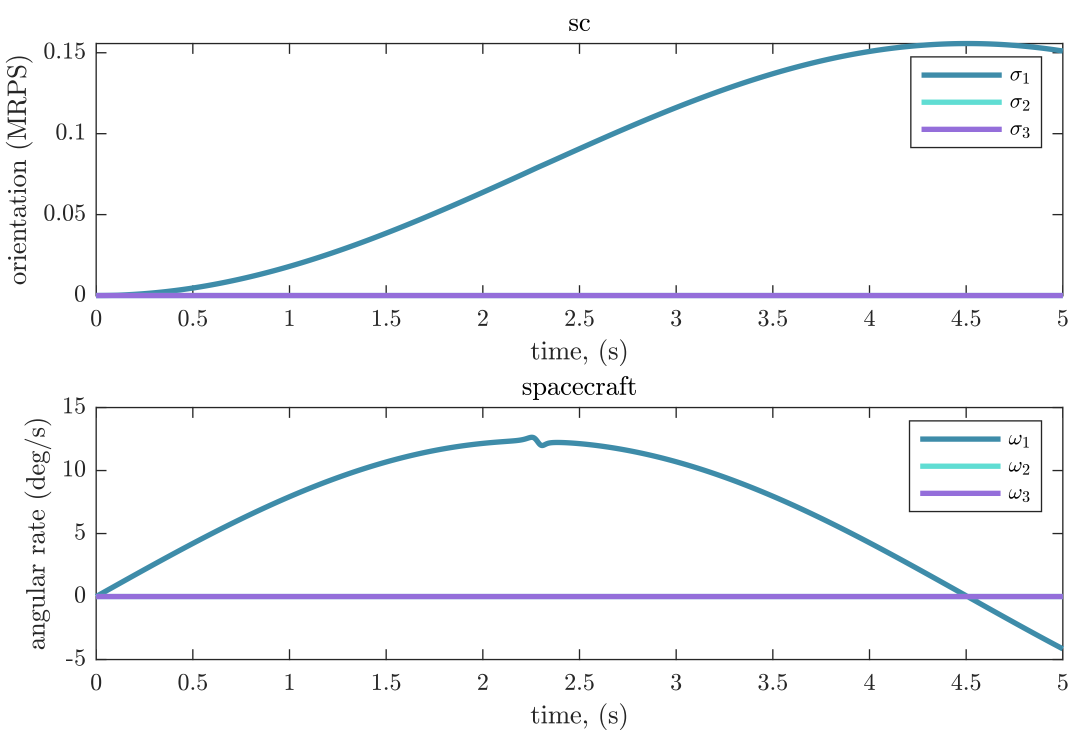

Figure 2.17: Angular orientation and rates of the free-flying root bar in three dimensional space.

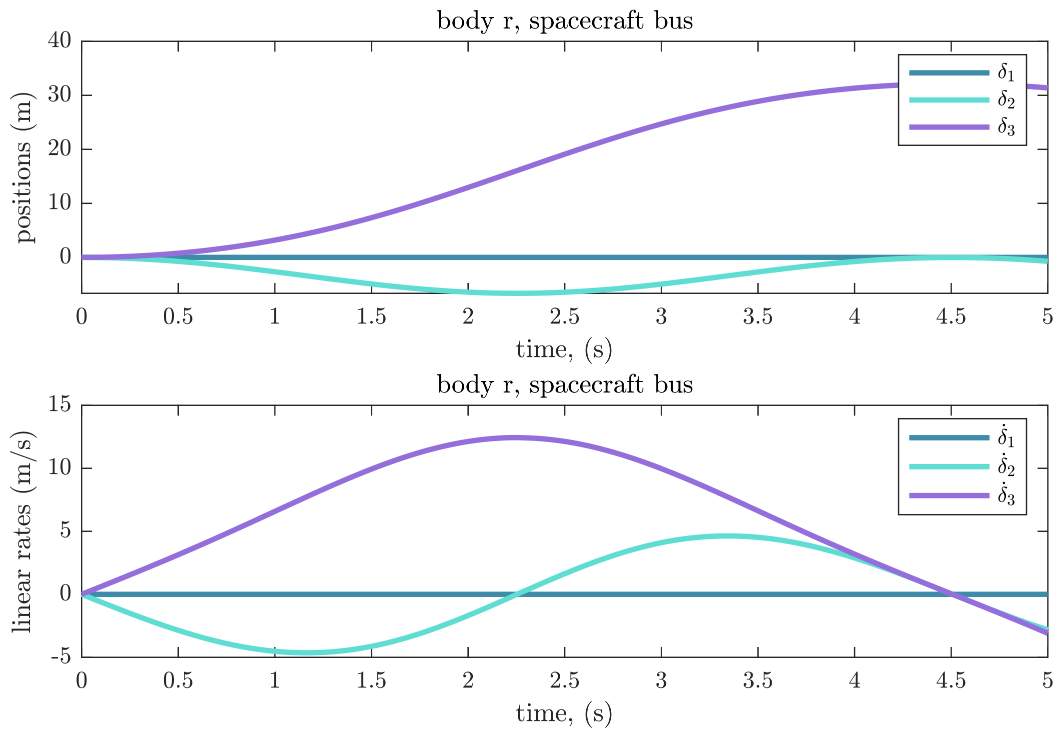

Figure 2.18: Linear orientation and rates of the free-flying root bar in three dimensional space.

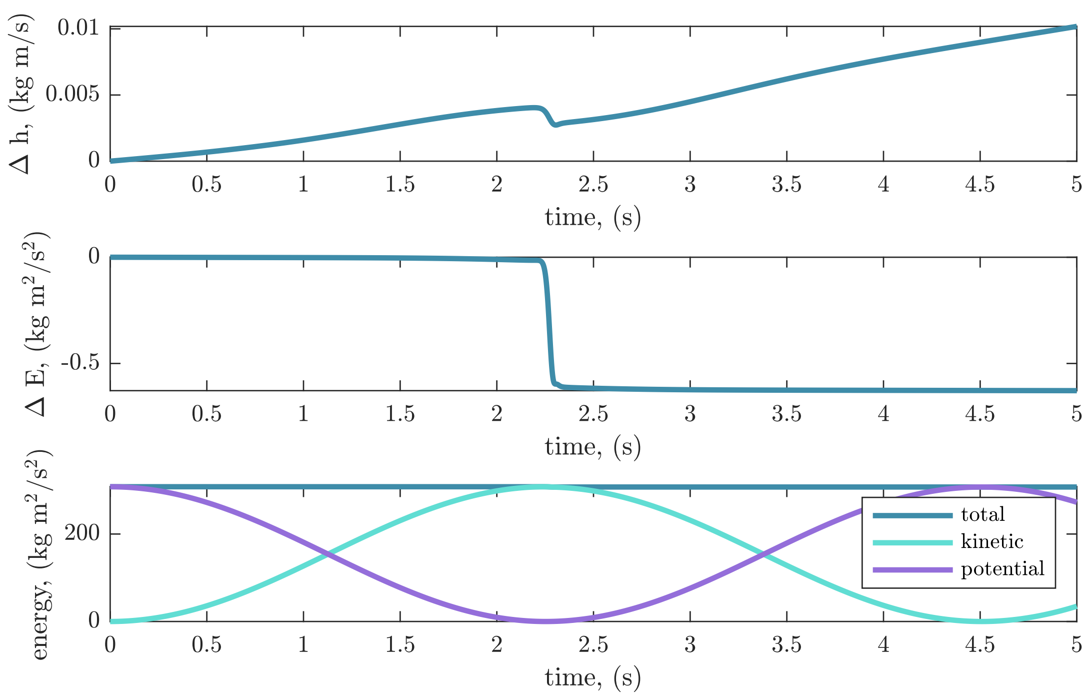

Figure 2.19: Change in total system energy and total system angular momentum.

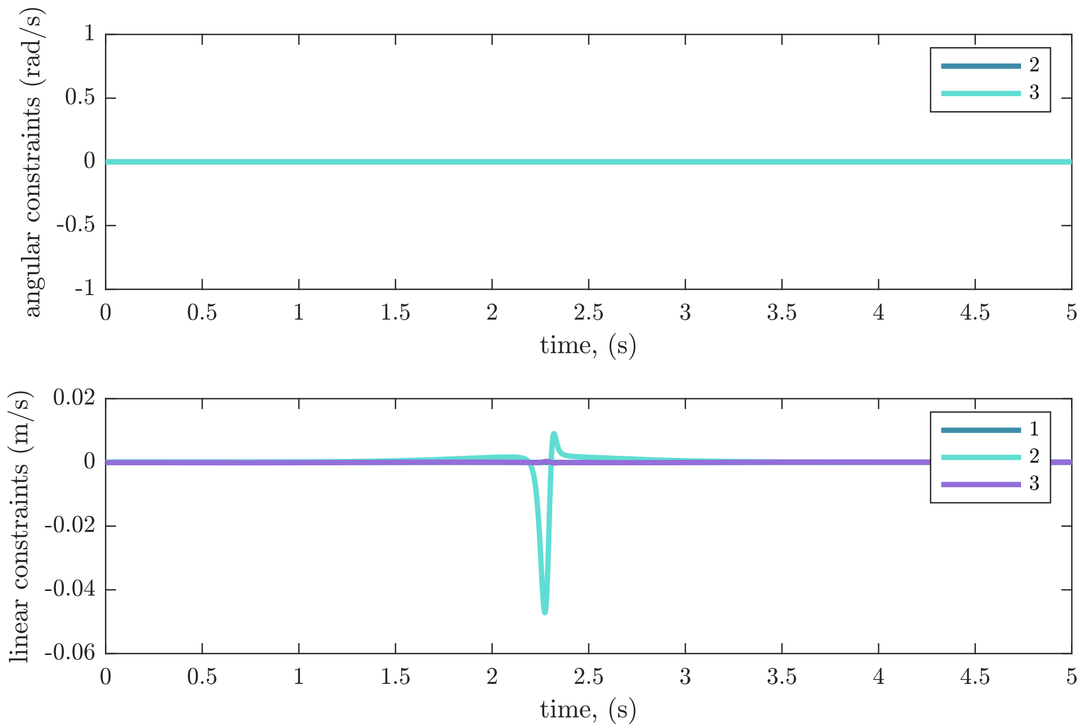

Figure 2.20: Change in the velocity form of the constraint equations.

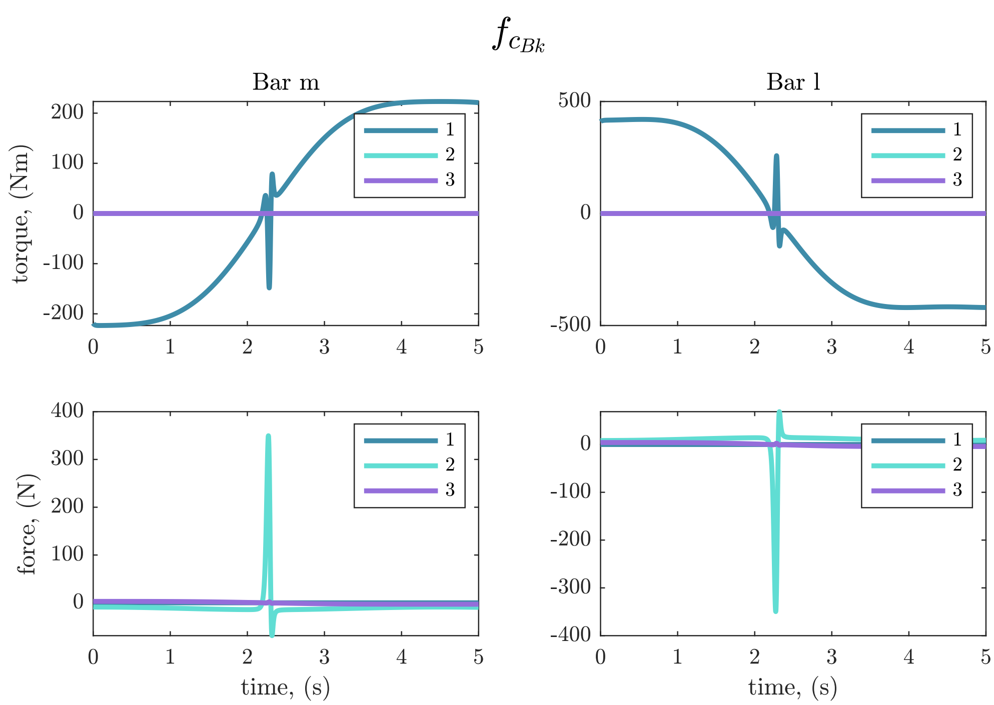

Figure 2.21: Internal forces and torques to enforce the constraint equations.

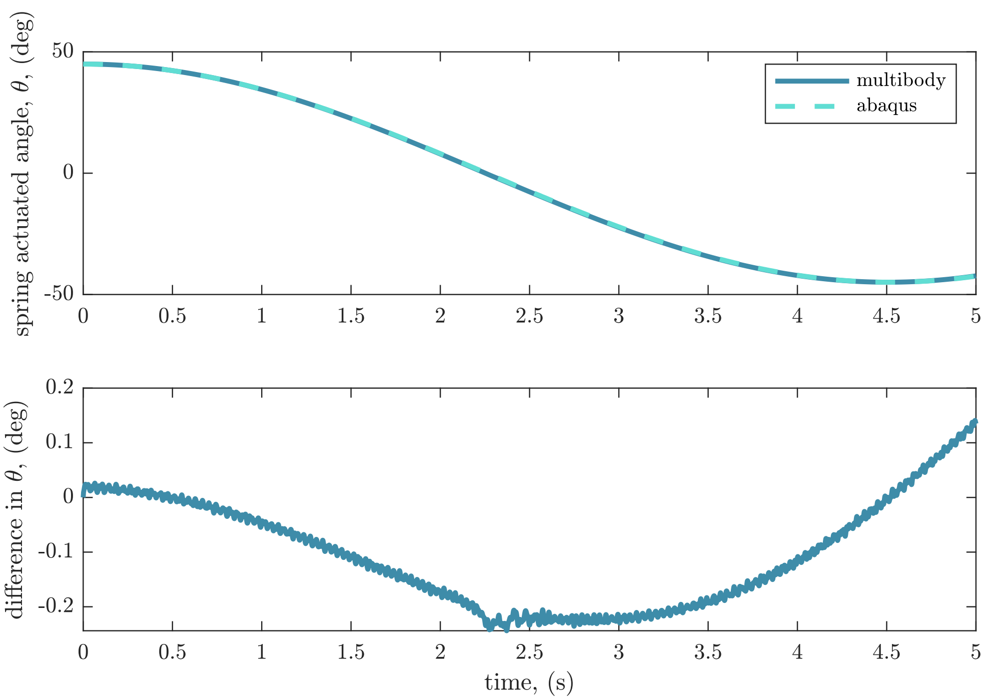

Figure 2.22: Comparison of results between a 4-bar simulation done in Abaqus and in the multibody dynamics framework.

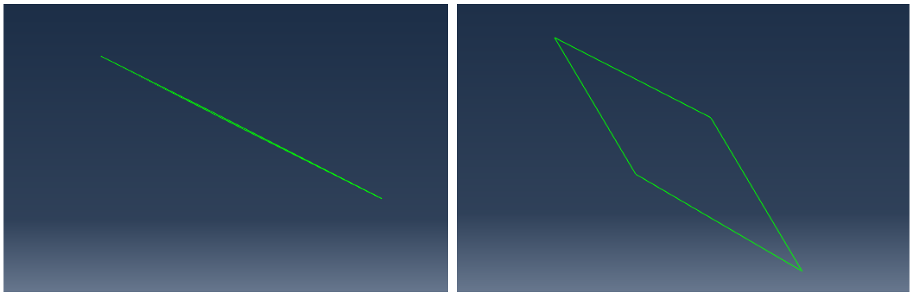

(a) flat zero energy configuration

(b) open configuration

Figure 2.23: Graphics representing the 4-bar simulation done in Abaqus.

and the graphic representation of this from the software GUI is shown in Figure 2.23. An elastic property is given to one of the hinges to replicate the torsion spring and identical mass and inertia properties are assigned to the bars. The time history of the angular coordinate between bar 3 and 4, where the torsion spring is applied, is shown with the prediction found with the multi-body simulation in Figure 2.22, as well as the difference between the two simulations at each point in time. Each simulation is run with the same time step, $\mathrm{d}t = 0.001$ seconds, and the Abaqus simulation takes 13.5 minutes to compute where the multi-body simulation is complete in 38 seconds. This indicates a significant time savings, however the difference between the two results shows slight variation. The variation is possibly due to shortcomings in the constraint enforcement of the multi-body simulation, and so this indicates a trade off between accuracy and speed in the two approaches, which is expected.

2.5.3.2 Numerical Demonstration of a Constrained Map Folded Structure

The next numerical demonstration considers a folded structure with planar panels and three dimensional spatial motions. This structure is representative of a map-folded four body structure, or a single base unit of the Miura pattern where the pattern angle is 90 deg, and a diagram of how this structure folds is displayed in Figure 2.24. The structure is flat folded and assembled with only a single rotational degree of freedom on the hinge joints, captured in the initial conditions in Table 2.11. A RK4 integrator is implemented and a simulation of 10 seconds is run with a time increment

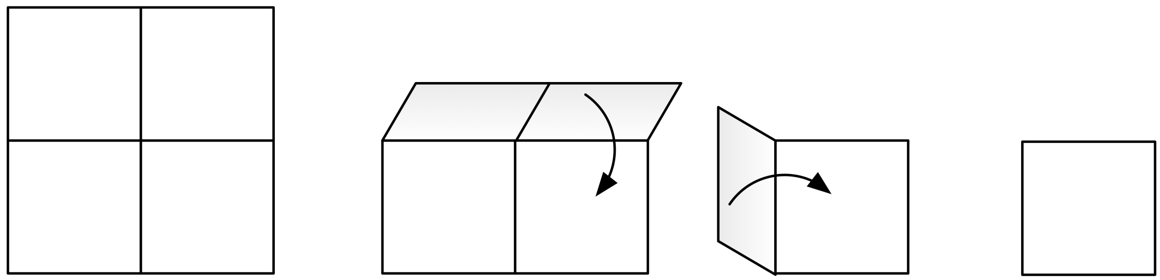

Figure 2.24: Stages of a four body planar map from unfolded to folded configurations.

of 0.001 seconds, resulting in a computational clock time of 281.5 seconds for the integration. Each panel body is defined with identical geometric and mass properties as defined in Tables 2.8, 2.9, and 2.10. The panel motions in Figure 2.25 show the unfolding of the hinge at panel j, but because of the geometry of the map fold, the hinges at l and j do not unfold, where the first hinge would need to stabilize in a flat configuration before these hinges could unfold. The free-flying host body motion in shown in Figure 2.26. The constraint violations are captured in Figure 2.28, where $\dot{\Phi}^{\intercal}\dot{\Phi}$ is the square of the spatial magnitude of the applied constraint equations and does not have physical units, and are shown to behave nonlinearly around $\theta_j = 0$. The internal constraint forces and torques are seen in Figure 2.29 to be highly nonlinear around this value as well. This point is suspected to be a numerically singular configuration of the system, and special consideration must be taken for the constraint violations around these points. In comparison to the static planar case in Section 2.5.3.1, the numerical accuracy of the constraint enforcement for this case, with spatial motion, is reduced by orders of magnitude. Taking the physical system in to account, the constraint violations are sub-millimeter and are considered acceptable for capturing the bulk deployment motion for the system. However these results highlight the need for special consideration of acceptable numerical performance of the dynamics approach for deployable systems.

Table 2.8: Mass properties of the rigid root body and panel bodies.

body	$m(k)$ (kg)	$K(k)$ (N/m)	**length** (m)	**inertia** (kg m^2)
r	1	0	2	diag $(0.3342, 0.3342, 0.0017)$
1	1	0.1	2	diag $(0.3342, 0.3342, 0.0017)$
2	1	0.1	2	diag $(0.3342, 0.3342, 0.0017)$
3	1	0.1	2	diag $(0.3342, 0.3342, 0.0017)$

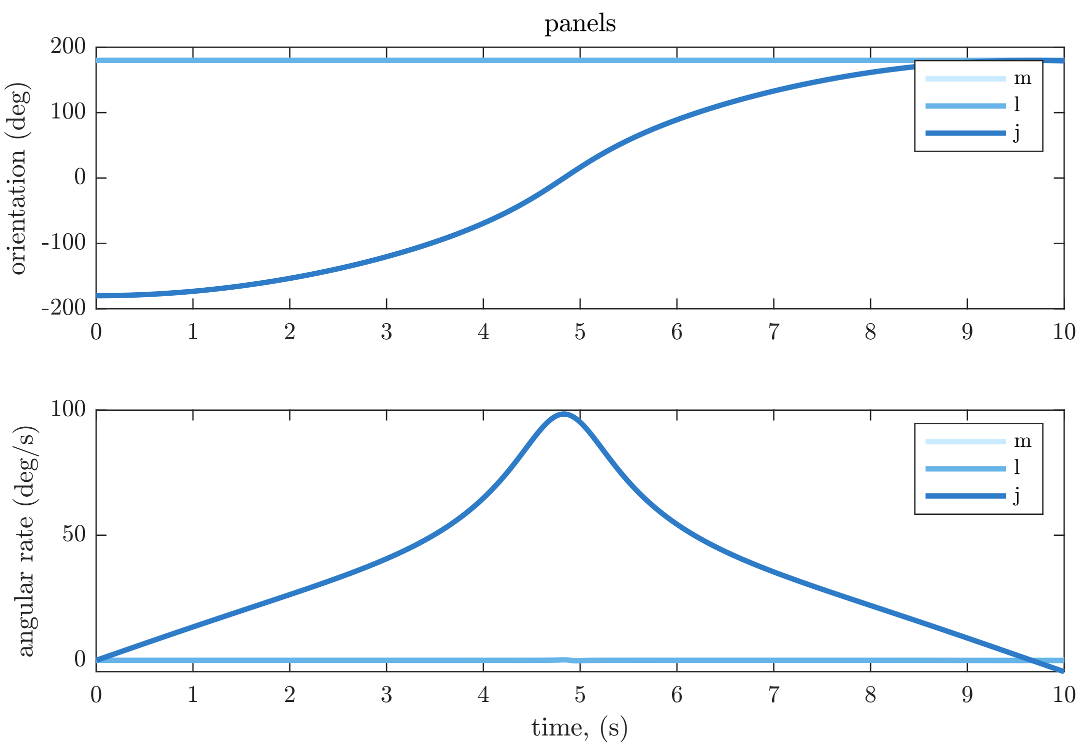

Figure 2.25: Angular orientation and rates of the three panel bodies.

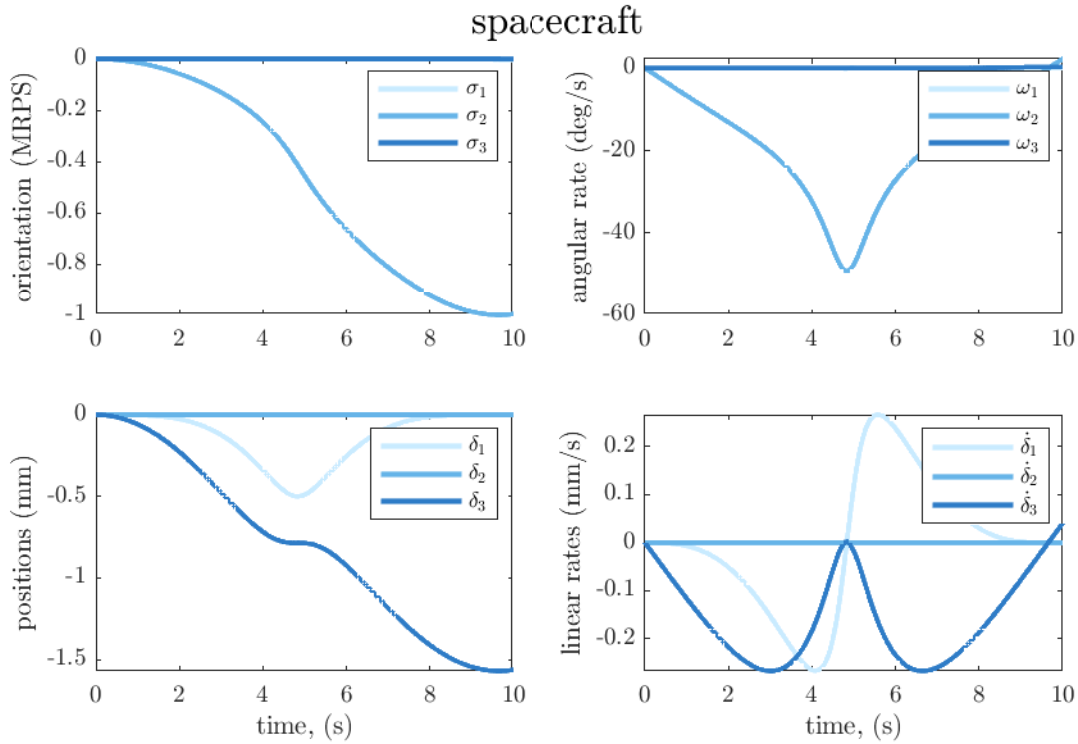

Figure 2.26: States and rates of the spacecraft body in three dimensional space.

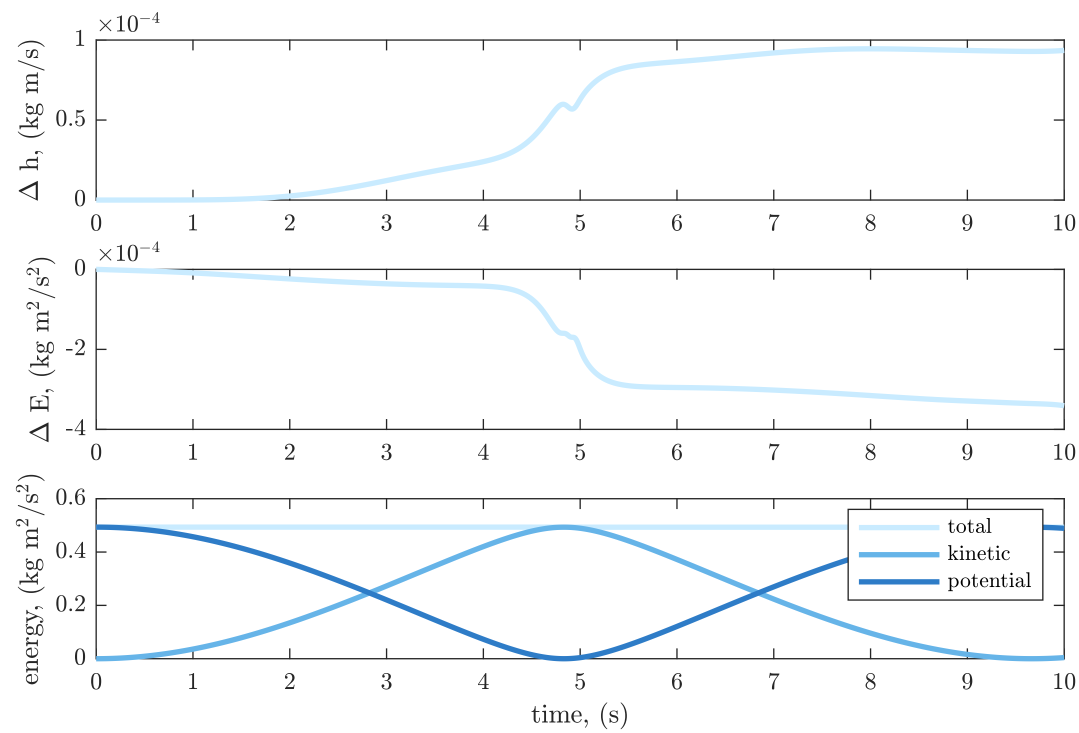

Figure 2.27: Change in total system energy and total system angular momentum.

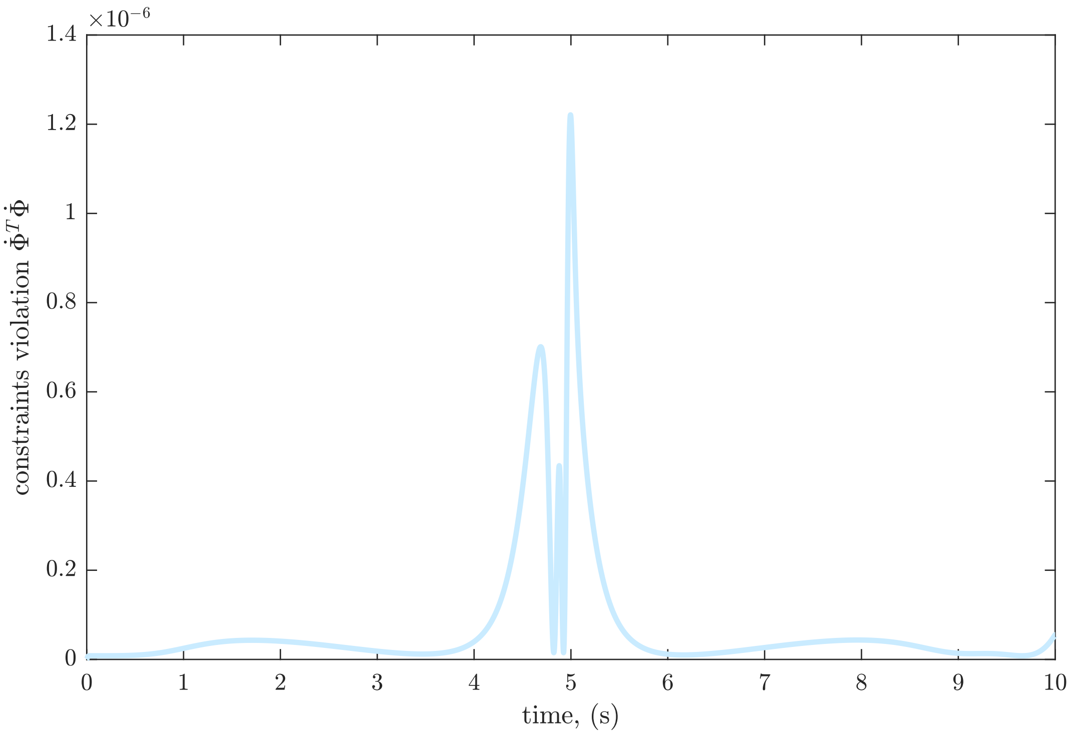

Figure 2.28: Change in the velocity form of the constraint equation.

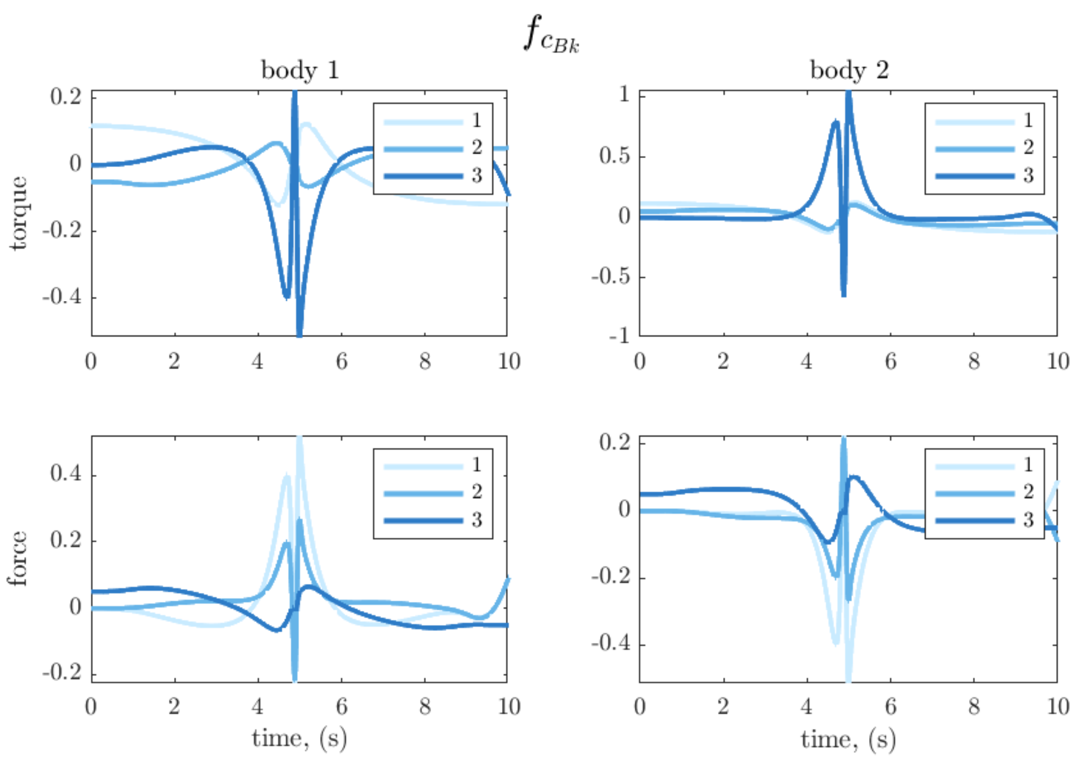

Figure 2.29: Internal forces and torques to enforce the constraint equations.

Table 2.9: Geometry properties of the rigid bodies.

body	$\theta(c, k-1^+)$ (rad)	$\boldsymbol{p}(c, k-1^+)$ (m)	$\boldsymbol{p}(k, c)$ (m)
r_1	$[0, 0, 0]$	$[0, 1, 0]$	$[0, 0, 0]$
r_2	$[0, 0, \pi/2]$	$[1, 0, 0]$	$[0, 0, 0]$
1	$[0, 0, 0]$	$[0, 1, 0]$	$[0, 0, 0]$
2	$[0, 0, 0]$	$[0, 1, 0]$	$[0, 0, 0]$
3	$[0, 0, \pi/2]$	$[1, 0, 0]$	$[0, -1, 0]$

2.5.4 Multiple Constraint Enforcements

Numerical test cases are developed to investigate the algorithm performance as it has been adapted for enforcing multiple constraints across multiple chains in a cut tree topology. Two cases in particular are of interest. The first is the case where there is more than one pair of constrained bodies between two chains of the cut tree topology for a system graph. The second case of interest is when there are more than two chains in the cut tree, and a single body is subjected to more than one constrained node pair. Figure 2.30 displays the graphs of the two example cases designed for this study. The goal of this section is to assess the performance of the current approach as it is scaled up for larger folding space structures.

2.5.4.1 Numerical Demonstration of Multiple Constrained Bodies

The first test case considers a system of eight bodies in two chains, with bodies referenced by number in the illustration of this dynamical system in Figure 2.30. The configuration properties of the bodies are listed in Tables 2.13 and 2.12. Each fold representative hinge is constrained to a single rotation θ about the 3rd axis, is given the same linear torsional spring stiffness, and the geometry is designed such that each panel is identical. The root node, r, does not have a force

Table 2.10: Geometry properties of the constraint nodes.

i	$\theta(k, \mathcal{N}_{k_i})$ (rad)	$\boldsymbol{p}(k, \mathcal{N}_{k_i})$ (m)
1	$[0, 0, \pi/2]$	$[0, -2, 0]$
2	$[0, 0, \pi/2]$	$[0, 2, 0]$

Table 2.11: Initial conditions of the numerical simulation.

body	q	$\dot{\beta}$
r	$[0,0,0,0,0,0]$	$[0,0,0,0,0,0]$
1	$-\pi$	0
2	$-\pi$	0
3	π	0

acting between it and the six degree of freedom hinge to inertial space, representing a free-flying spacecraft root body. The inertia is calculated from the height, width, and thickness assuming all bodies are square. The orthogonal rotations of the $\theta(c_k, k-1^+)$ orientations represents the fold lines of a square fold and are reported in 321 Euler angles for quick physical interpretation. Changing this value and the inertia definitions would adapt the simulation from a square map fold to Miura map folds or other desired patterns. The initial conditions of the numerical demonstration are listed in Table 2.15 and are designed to mimic a flat folded map fold with no initial rates. Positive angle folds are representative of mountain folds and negative angle folds of valley folds. A 2×8 grid of rigid bodies is set up using the relative coordinate frame approach shown in Figure 2.13. The root body r is the branching node of the chains as shown in Figure 2.3. Table 2.14 contains the relative position and orientation of the constraint nodes illustrated in Figure 2.13, where the frames are rotated such that the unconstrained axis is along the fold axis. Using a time step of $dt = 0.001$ seconds, the 10 second simulation of 14 degrees of freedom takes 11 minutes to compute using an RK4 integrator.

From Figure 2.31 the states of the folded panels are seen to begin the unfolding process, where

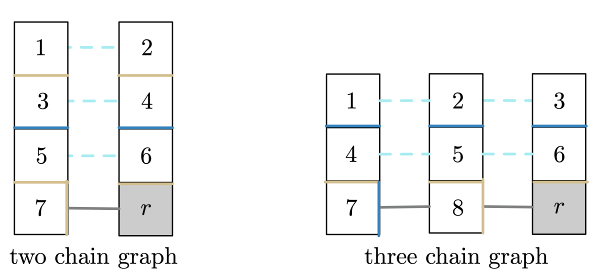

Figure 2.30: Diagrams for the two and three chains in a cut tree topology.

Table 2.12: Mass properties of the rigid root body and panel bodies.

body	$m(k)$ (kg)	$K(k)$ (N/m)	**width** (m)	**thickness** (m)	**inertia** (kg m^2)
r	100	0	2	1	diag $(66.7, 66.7, 66.7)$
1-6	1	0.01	2	0.01	diag $(0.3342, 0.3342, 0.0017)$
7	1	0.03	2	0.01	diag $(0.3342, 0.3342, 0.0017)$

Table 2.13: Geometry properties of the rigid bodies.

body	$\theta(c_k, k-1^+)$ (rad)	$\boldsymbol{p}(c_k, k-1^+)$ (m)	$\boldsymbol{p}(k, c_k)$ (m)
r	[$\pi/2$,0,0]	[1,0,0]	[0,0,0]
1-6	[0,0,0]	[1,0,0]	[1,0,0]
7	[0,$\pi/2$,0]	[1,0,0]	[0,0,-1]
8	[0,$\pi/2$,0]	[1,0,0]	[0,0,-1]

Table 2.14: Geometry properties of the constraint nodes.

i	$\theta(k, \mathcal{N}_{k_i})$ (rad)	$\boldsymbol{p}(k, \mathcal{N}_{k_i})$ (m)
1	[0,$\pi/2$,0]	[1,0,-1]
2	[0,$-\pi/2$,0]	[1,0,1]

Table 2.15: Initial conditions of the numerical simulation.

body	q	$\dot{\beta}$
r	[0,0,0,0,0,0]	[0,0,0,0,0,0]
mountain folds, 1,2,5,6,7	π	0
valley folds, 3,4	$-\pi$	0

the fold between Panel 7 and the spacecraft body r must unfold first to then allow the z-folded pairs (Panels $1-2$, $3-4$, and $5-6$) to then release near the 20 second mark. Due to the design of the system, the z-folded pairs are expected to unfold with identical states, and this kinematic behavior is verified in the dynamics simulation by the states in Figure 2.31. The unfolding process of the z-folded pairs is not representative of a physical structure however, as the model does not include contact. Therefore, the internal force from sets $1-2$ unfolding causes the sets $3-4$ and $5-6$ to fold beyond 180 degrees, as seen from Figure 2.31. The host spacecraft states during the deployment, shown in Figures 2.32 and 2.33, show a general tumble and small linear perturbations are created. Most notable is the change in the system total energy over the course of the simulation, shown in Figure 2.34, which grows significantly around 20 seconds, the point where the deployment transitions to the second stage. This non-conservative energy behavior is due to the Baumgarte constraint stabilization method implemented and is a compromise for using this modeling approach. The constraint violations are plotted as the square of the magnitude of all constraint violations at a node in Figure 2.35, and it is noted that the violations have significant peaks at the deployment transition point. These violations are 4 orders of magnitude smaller than the state motions they are applied to, which can be considered acceptable for this demonstration but may need further improvement for future implementation. The magnitude of the constraint violations is suspected to be a function of the number of system constraints, and this relationship is explored in the next section. For a single demonstration of the internal forces applied at the panel body frames due to the constraint, the constraint forces and torques between Panels 1 and 2 is reported in Figure 2.36. These are shown to be complex internal behaviors of significant magnitude.

2.5.4.2 Constraint Violations for Multiple Constraints

Comparing the results of Section 2.5.4.1 to those obtained for a single constraint node in Section 2.5.3, the magnitude of the constraint violations is suspected to be influenced by the number of constraints in a system. A numerical demonstration for the second test case of the three chain graph is also conducted, and the constraint violation errors are significant enough to invalidate

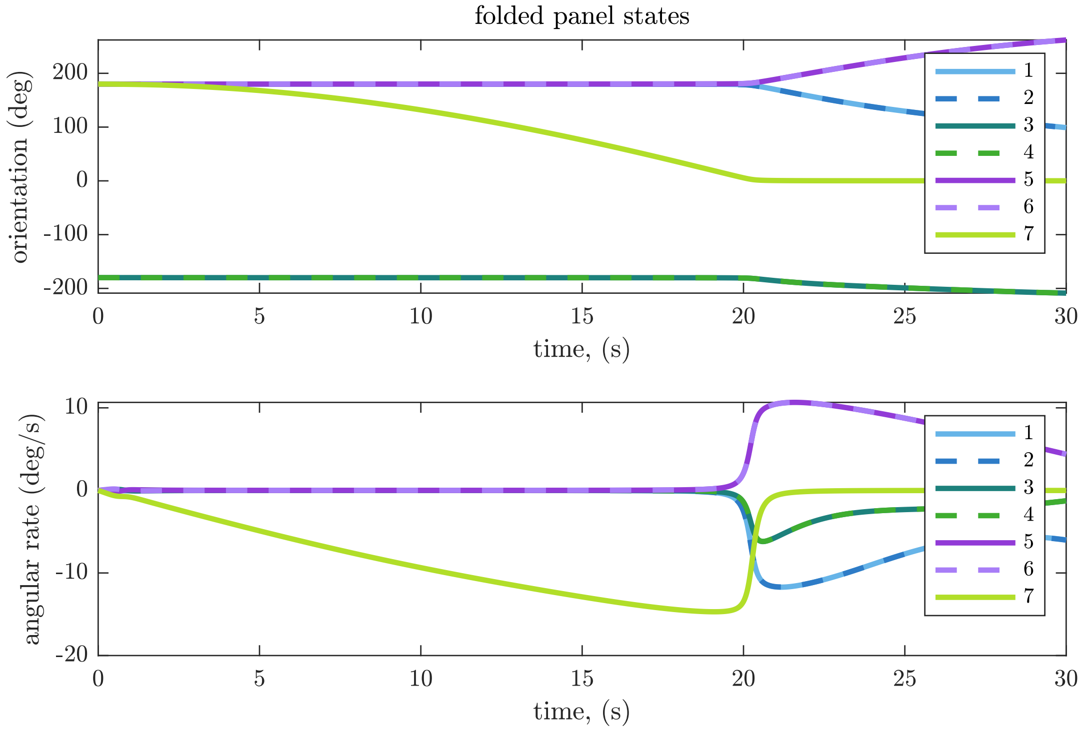

Figure 2.31: Angular orientation and rates of the three panel bodies.

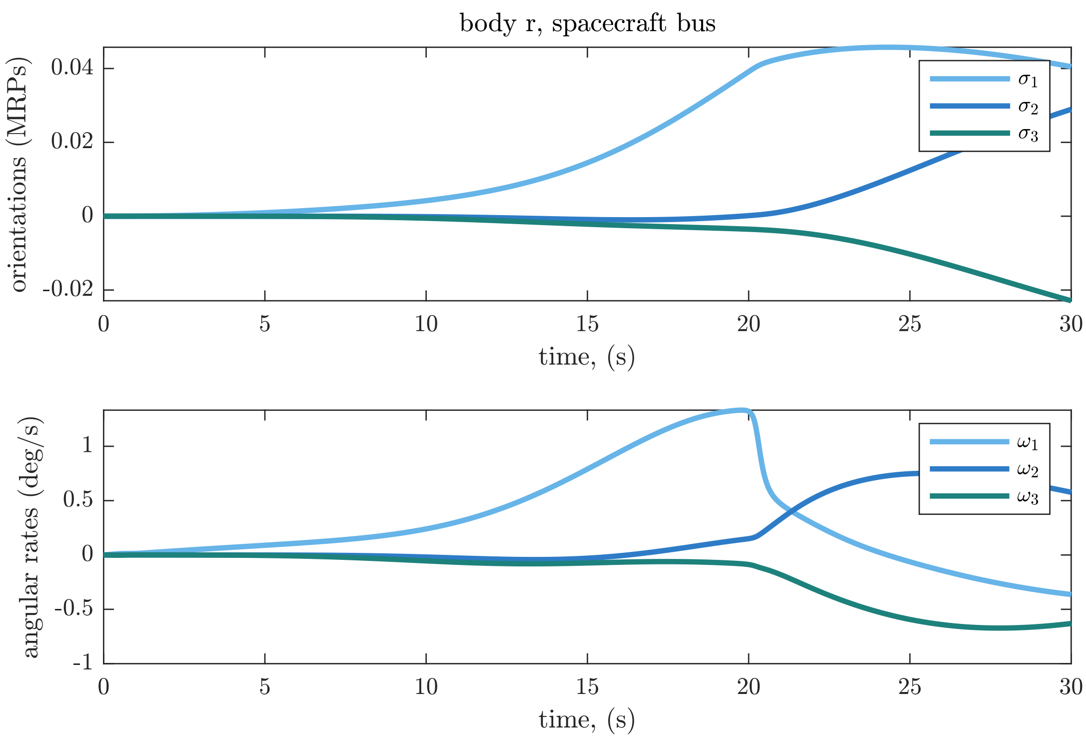

Figure 2.32: Angular orientation and rates of the spacecraft body in three dimensional space.

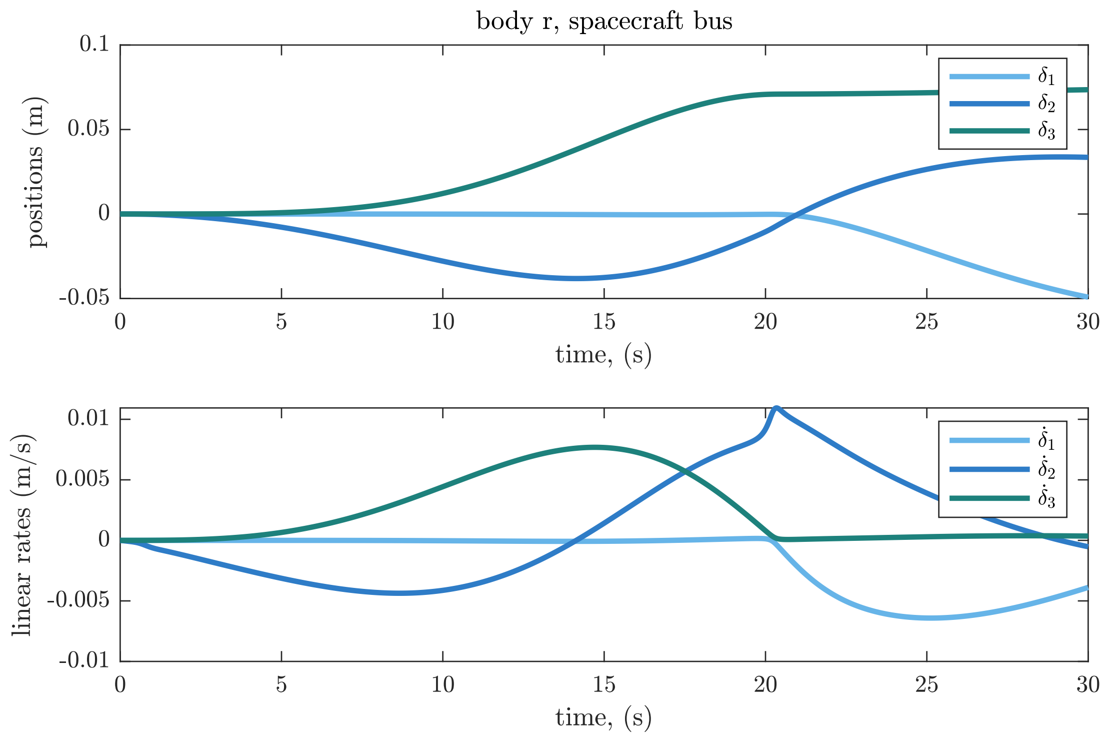

Figure 2.33: Linear orientation and rates of the spacecraft body in three dimensional space.

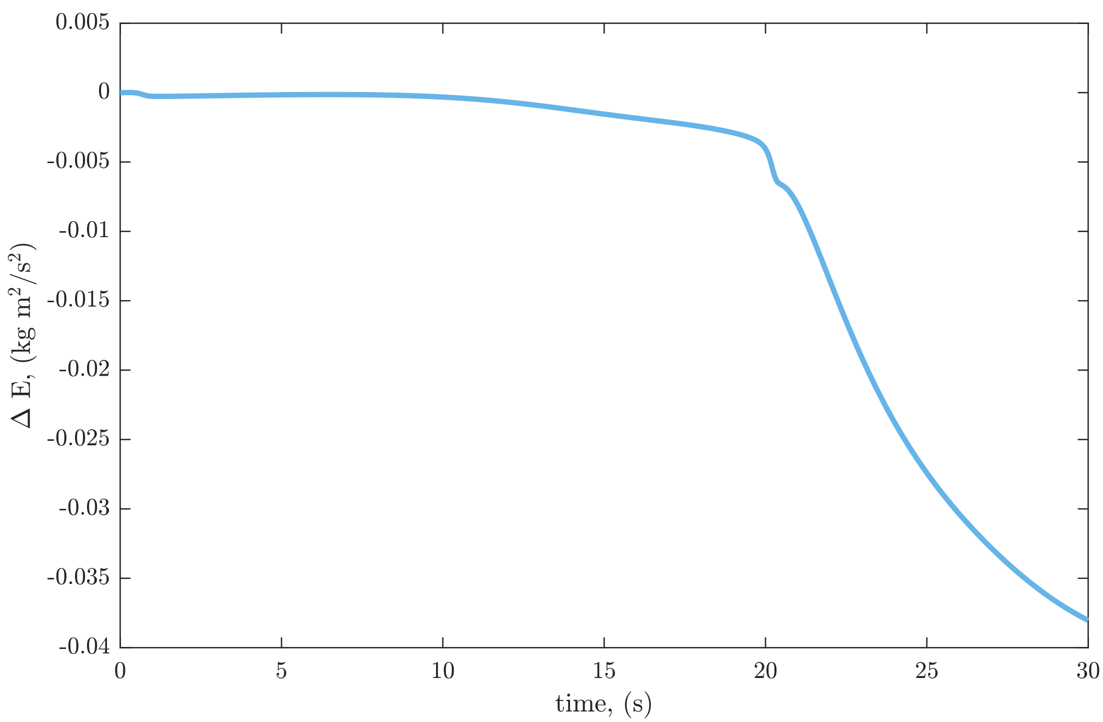

Figure 2.34: Change in total system energy and total system angular momentum.

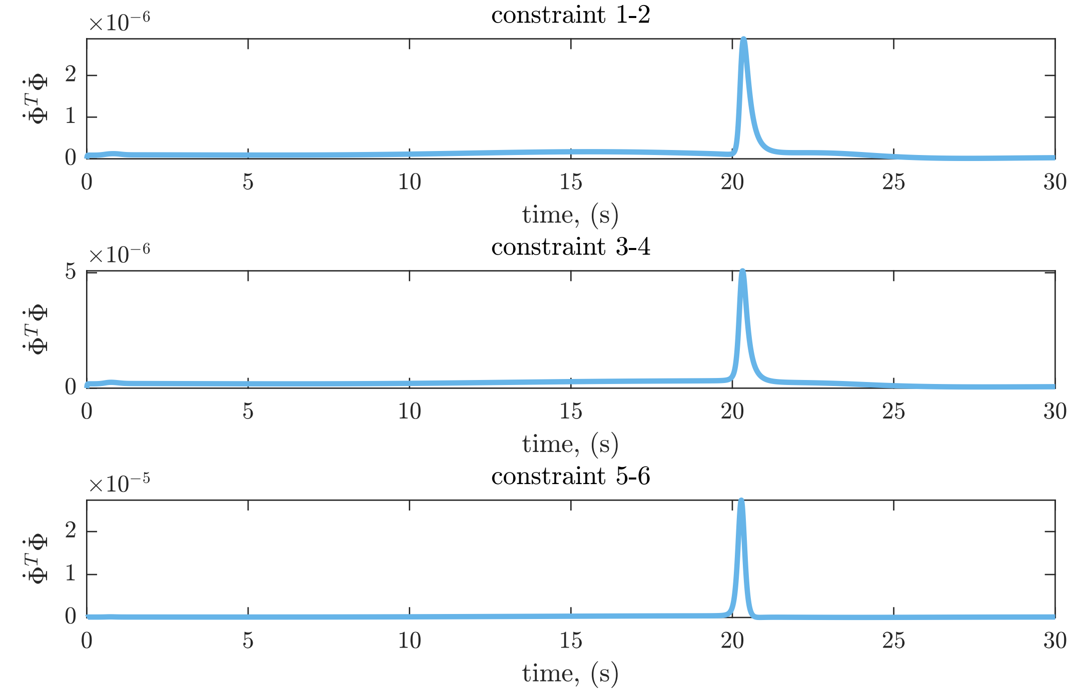

Figure 2.35: Change in the velocity form of the constraint equation.

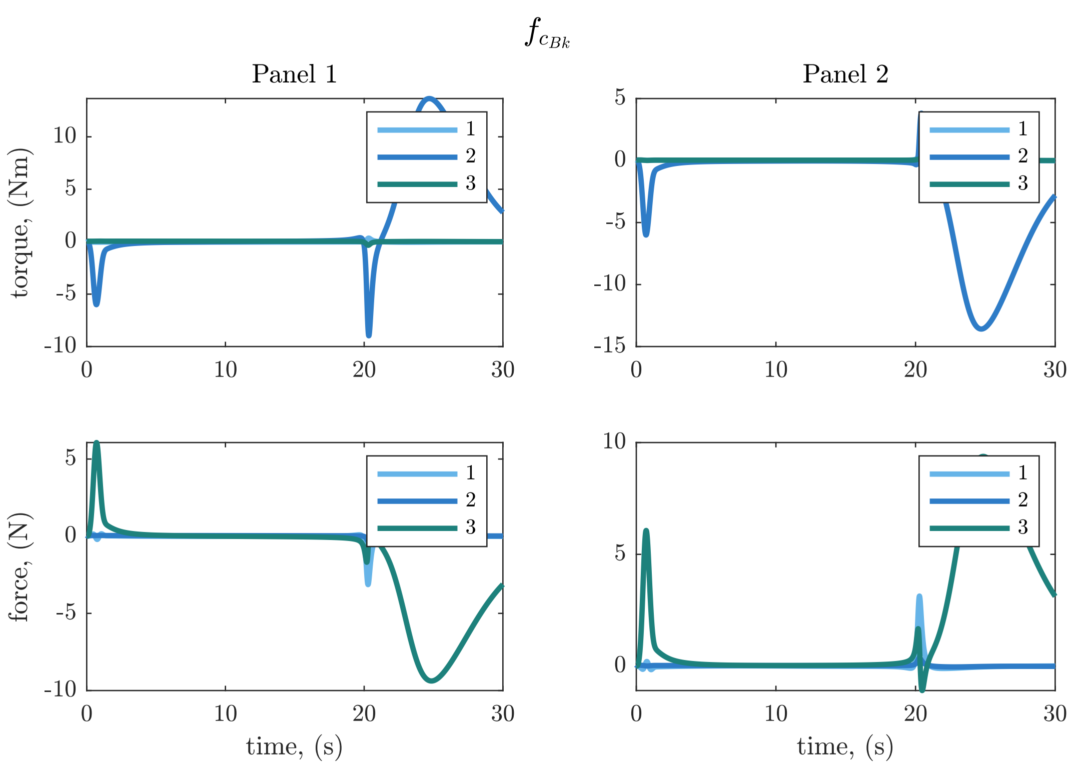

Figure 2.36: Internal forces and torques to enforce the constraint equations.

the results of the demonstration. To investigate the constraint violation trends, numerous runs of the two test cases are conducted with different constraints enforced. The results of the two chain graph case are shown in Figure 2.37, which shows the squared magnitude of all the constraint violations for instances of 1, 2, and 3 constraints applied on a log scale. There is clearly an increase in violations as the number of constraints are increased, and the violations are shown to stabilize over the simulation with a peak at the point where the deployment stage transitions as discussed previously.

For the second test case where there are instances of a single rigid body subjected to two constraint node pairs, the jump in constraint violation behavior is much more significant. Additionally, the simulation is not stable for long integration times, and tuning the Baumgarte stabilization parameters, $\mathfrak{a}$ and $\mathfrak{b}$, is difficult. In Figure 2.38, the square of the magnitude of all constraint violations in the system is shown for just the closure between $5-6$ and for closures on body 5 between $5-6$ and $4-5$, as well as the additional two constraints in the 3×3 grid structure. The cases of more than one constraint do not contain stabilization corrections as the tuning did not yield good results for this case. This study demonstrates that the Baumgarte Stabilization technique is not sufficient when applying multiple constraints to a single rigid body. For a large scale folding structure architecture, there are many instances of a single rigid body subject to two constraint nodes as seen in the pattern graphs of Figures 2.3 and 2.4. Therefore, more advanced constraint stabilization techniques are required for scaling the multi-body dynamics approach to larger folding structure architectures. This point is left for future work in the field.

2.6 Conclusions and Future Work

A self-actuated folded deployable spacecraft structure presents a novel modeling challenge due to free-flying spacecraft dynamics coupled with a complexly constrained multibody system. An approach that blends several SOA articulated body-derived robotics dynamics algorithms together is presented to address the multibody folded structure problems. The articulated body forward dynamics algorithm is outlined as the basis for the approach, and derivations that generalize the

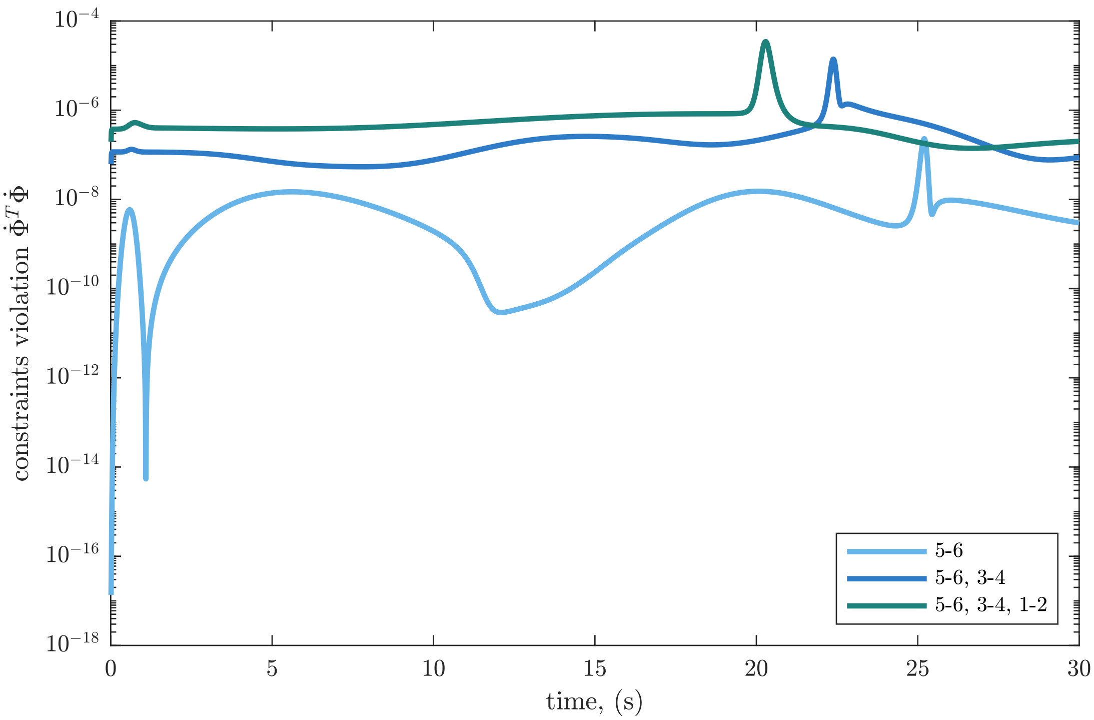

Figure 2.37: Constraint violations of cases of multiple constraints for the two chain graph.

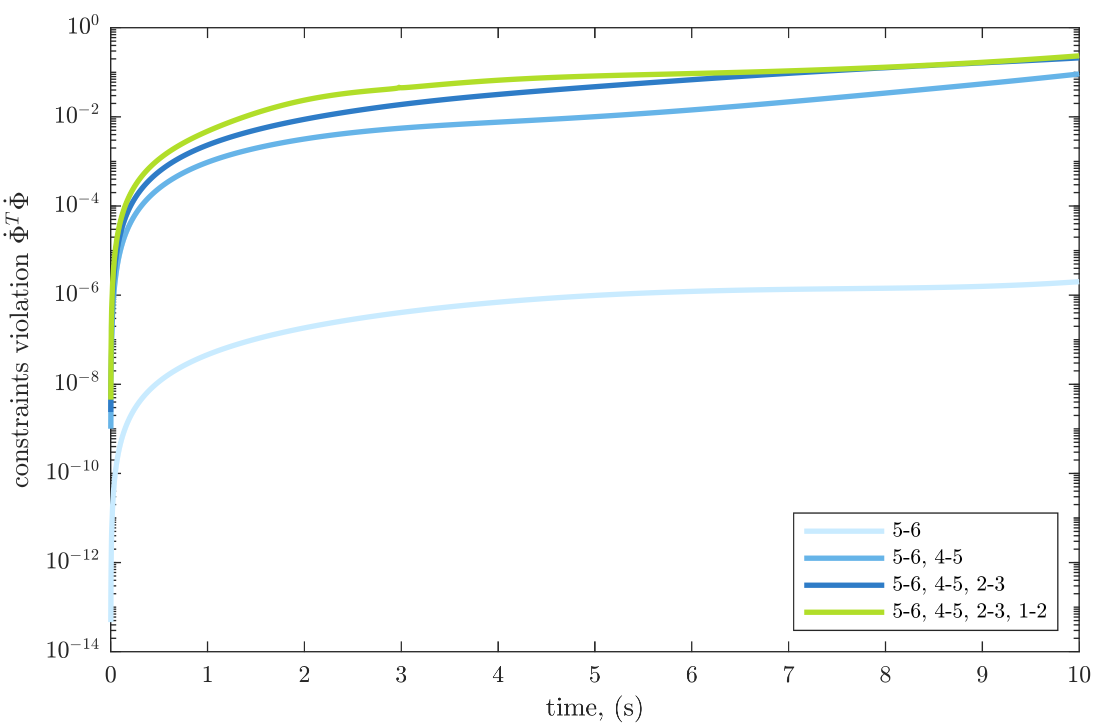

Figure 2.38: Constraint violations of multiple constraints for the three chain graph.

ABFD algorithm to the spacecraft folded deployable structure scenario are provided. The tree augmented approach is developed for any grid formatted spacecraft structure. It is found that this approach provides significant value over the Lagrangian approach or Kane's equations. This is due to the computation gains of the recursive structure of the equations of motion and that the algorithm provides a framework for working with a high volume of rigid bodies and rigid body constraints. Origami-folded structure topology is studied and interpreted for dynamics analysis using graph theory, and two forms of a 4 body architecture, the four-bar mechanism and a map fold unit, are analyzed for algorithm demonstration. Origami-inspired folding topologies with large number of bodies are shown to have algorithm gains for recursively calculated loop constraints, however constraint violations are a significant concern, as demonstrated on two cases of multiple constraint configurations. Future work in the field should focus on developing robust constraint correction and stabilization tools for systems with a large number of constraints as well as multiple constraints applied to a given body in the system.

Chapter 3

Research Goal 2: Elastic Hinge Modeling

3.1 Introduction

A central challenge for folded deployable structures is the deployment dynamics and deployment actuation of the folded structure and spacecraft system. A novel lightweight solution is to integrate strain energy hinges to facilitate folding and actuate the deployment.[25] Compared to standard piano hinges, these hinges are lightweight, eliminate rotational mechanical contact surfaces, and are self-actuating. In this thesis, the system deployment dynamics are studied using multi-body dynamics and a simplified hinge representation. In this approach, fold panels are treated as rigid bodies and the flexible joints are represented by internal forcing functions. In this Chapter, a model to represent the hinge mechanics is designed as a function of the hinge's full degrees of freedom, relative position and orientation states. Data containing reaction forces and torques at the hinge body connection points are obtained from FEA simulation and experimental studies for hinge configurations containing non-symmetric displacements, and they are compared for validation purposes. A nonlinear regression is applied to fit the simulated data to polynomials and the efficacy of this fit is assessed. The approach is shown to provide an approximation that may enable sufficient deployment dynamics simulation accuracy without a full FEA simulation of the system. The approach is applied to develop a hinge model for a two hinge system that is used in an assessment in a folded deployable structure in Chapter 5.

Several research studies characterize the moment-curvature behavior of tape spring hinges for various materials assuming the hinge folds symmetrically, meaning through only one rotational

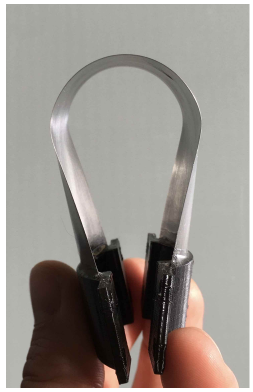

(a) equal sense

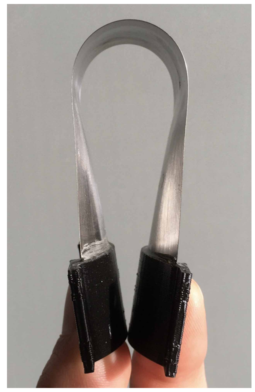

(b) opposite sense

Figure 3.1: Fold orientations of a high strain tape spring hinge.

degree of freedom (DOF). Typically, the equal-sense and opposite-sense bending moment is characterized through theoretical analysis and experimental testing.[43,44] Here, equal-sense refers to a fold where the open cross sections face each other and opposite-sense is a fold where the open cross sections face away, as is consistent with the tape spring literature, and can be viewed in Figure 3.1. There has been further interest in characterizing the behavior of a diagonally folded hinge.[45] These studies provide fundamental understanding of a hinge's structural mechanics behavior, focusing on failure and stiffness, and demonstrate their correlation with mechanics theory. However, here, the objective is to reframe the hinge as a dynamic actuator and capture the deployment behavior of a system as actuated by the hinge. The tape spring introduces unique challenges from this perspective. A typical fold joint is treated as a single DOF revolute joint where the attachment points on each connected body are coincident and have one relative rotation. Under certain assumptions, the symmetric behavior of the tape spring hinge can be modeled as a single rotation where the moment-curvature behavior describes the internal torque due to the hinge. However, the connection points are separated by the length of the hinge and will be displaced from each other over the deployment. The actual force and torque response of the hinge will depend on the loading of either side of the hinge, and small displacements from the nominal configuration may introduce significant force and torque responses. Therefore, the established moment-curvature approach is not sufficient for the modeling fidelity desired here, and a study of force and torque responses due to non-symmetric behavior is conducted.

The phenomenon of undesirable non-symmetric configurations in the tape spring hinge fold is not well studied. Here, non-symmetric behavior refers to any change in position and orientation that does not follow the nominal fold rotation, as is illustrated in Figure 3.2. To guarantee symmetric behavior, additional components must be included in a hinge assembly to constrain the hinge, which can add mass and complexity where lightweight simplicity is desired. Such solutions are not addressed here. Inclusion of multiple independent state variables in this study makes it difficult to approach the problem with classical theory, therefore, to study this phenomenon, numerical and experimental techniques are employed.

3.2 Rigid Body Dynamics and the 6 State Hinge Model

The tape spring hinge is represented in the rigid body dynamics simulations as an internal forcing function in terms of the position and orientation of the hinge connection points. This concept is illustrated in Figure 3.2, where the fixed end points of the hinge are each assigned a reference frame, $\mathcal{A}_0$ and $\mathcal{A}_1$, the reaction forces from the hinge are denoted $\boldsymbol{N}_0$ and $\boldsymbol{N}_1$, and the reaction moments are denoted as $\boldsymbol{M}_0$ and $\boldsymbol{M}_1$. These mechanics are modeled as functions of the relative position, $\boldsymbol{\delta}$, and orientation of frame $\mathcal{A}_0$ with respect to $\mathcal{A}_1$.

The hinge model is developed to be compatible with a preexisting multi-body dynamics framework based on the Spatial Operator Algebra multi-body dynamics approach[39] reviewed in Chapter 2. This approach de-constructs a system of linked rigid bodies by defining the interactions across the hinge connecting an outbound body to an inbound body through relative coordinates, and selecting these as the generalized coordinates of the dynamics model. The framework of the algorithm then calculates the system dynamics having only needed the relative hinge definitions and rigid body properties. To provide consistency with this, the generalized coordinates are selected to

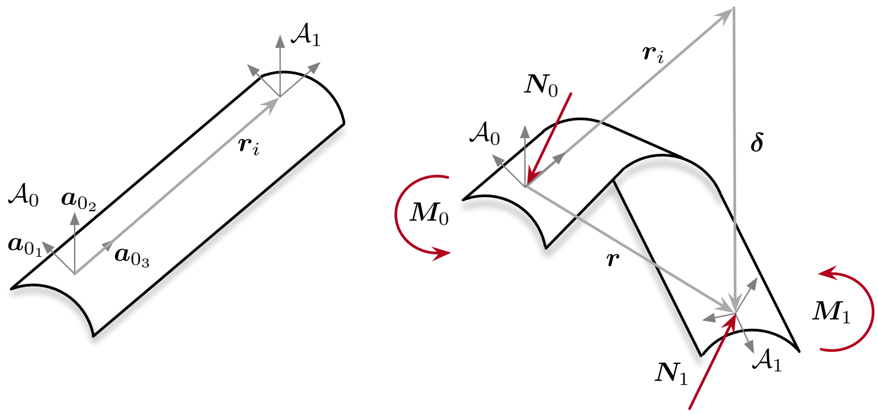

Figure 3.2: Definitions for a tape spring hinge in deployed (left) and non-symmetric (right) configurations.

be the displacement of the relative hinge frame coordinates and the relative orientation

$$\boldsymbol{q} = \begin{bmatrix} \boldsymbol{\theta}(\mathcal{A}_0, \mathcal{A}_1) \\ \boldsymbol{\delta}(\mathcal{A}_0, \mathcal{A}_1) \end{bmatrix} \tag{3.1}$$

For this analysis, all dynamics quantities are expressed with respect to the hinge origin frame defined as the inbound frame, $\mathcal{A}_0$. This lends insight into how the hinge affects any inbound body directly, and how an outbound body is affected relative to the inbound body. This information can be easily transformed to desired frames as needed. The hinge origin frame is oriented on the hinge such that the third axis, $\boldsymbol{a}_{0_3}$ is pointed down the length of the hinge, $\boldsymbol{a}_{0_2}$ is normal to the hinge cross section, and $\boldsymbol{a}_{0_1}$ completes the right hand convention. The relative orientation $\boldsymbol{\theta}(\mathcal{A}_0, \mathcal{A}_1)$ contains $3-2-1$ Euler Angles for ease of interpretation and because the second axis, where the 90 degree Euler angle singularity resides, can be oriented with an axis which does not accommodate significant relative deflection. The $\mathcal{A}_1$ frame is oriented identically to the $\mathcal{A}_0$ frame when the hinge is deployed in the zero energy state. The displacement of the relative hinge frame coordinates, $\boldsymbol{\delta}$, is selected over the relative position, $\boldsymbol{r}$, to better correlate the physical behavior with the numerical fit. The relation of these vectors is displayed in Figure 3.2, defined as

$$\boldsymbol{\delta} = \boldsymbol{r} - \boldsymbol{r}_i \tag{3.2}$$

Then the generalized forces and torques acting at frame $\mathcal{A}_0$ are written as a function of the relative coordinates across the hinge frames, in spatial notation, as

$$\boldsymbol{f}_0(\boldsymbol{q}) = \begin{bmatrix} \boldsymbol{M}_0 \\ \boldsymbol{N}_0 \end{bmatrix} = \begin{bmatrix} M_{0_1} \\ M_{0_2} \\ M_{0_3} \\ N_{0_1} \\ N_{0_2} \\ N_{0_3} \end{bmatrix} \tag{3.3}$$

The common assumption for hinge force and torque models is that the force and torque are acting in equal but opposite direction on each of the connected rigid bodies at the connection frames. While a quick free body analysis of Figure 3.2 verifies this to be true for the force, the moment balance introduces another term. The summation of moments at either frame will require the torque due to the reaction force and the relative position of the frames be included. Therefore, the spatial force at frame $\mathcal{A}_1$ is written in terms of only the force and torque at frame $\mathcal{A}_0$ as

$$\boldsymbol{f}_1(\boldsymbol{q}) = \begin{bmatrix} \boldsymbol{M}_1 \\ \boldsymbol{N}_1 \end{bmatrix} = \begin{bmatrix} -\boldsymbol{M}_0 - \boldsymbol{r} \times \boldsymbol{N}_0 \\ -\boldsymbol{N}_0 \end{bmatrix} \tag{3.4}$$

3.3 Model Estimation and Nonlinear Regression

Equation 3.4 indicates that the force and torque applied to the rigid bodies can be determined for both sides of the hinge using a model of only one set of forces and torques. Therefore, the objective is to determine adequate models for the six entries of $\boldsymbol{f}_0(\boldsymbol{q})$. There are several options for determining response functions that include large multi-variable data sets. Simple approaches include using a look-up table or interpolation between data points. However, these will not necessarily provide insight into predictor variable relationships and cannot be further manipulated. Therefore, a function fit is desired. A polynomial containing both first order and second order coupled polynomials is first proposed for capturing the non-symmetric relationships.

$$p(\boldsymbol{q}) = \sum_{i=1}^{6} a_i q_i + \sum_{j=1}^{6} \sum_{k=1}^{6} b_{jk} q_j q_k \tag{3.5}$$

Equation 3.5 contains 27 unknown coefficients. In this approach, each of the force and torque data sets is first fit using the full polynomial, and the resulting coefficients are then analyzed to eliminate expressions that have insignificant contributions. The objective is to reduce the polynomial to the smallest, and therefore computationally most efficient, expression while still providing an adequate fit to the data. Additionally, the coefficients for these second order cross-coupled terms can be used to interpret the significance of the generalized state variables. It's suggested from the literature that the nominal fold produces a pure moment in the symmetric case, and this moment can be represented using a 7th order polynomial.[43] Then for the moment about $\boldsymbol{a}_{0_1}$, the initial polynomial includes higher order terms for the nominal rotation, as in

$$M_{0_1} = p(\boldsymbol{q}) + \sum_{i=3}^{7} c_i q_1^i \tag{3.6}$$

A non-linear regression approach is best suited for the nonlinear, multivariate model functions in Equations 3.5 and 3.6. The Statistics and Machine Learning Toolbox published for Matlab is used to fit and evaluate the models. The quality of the fit is evaluated by several means. The toolbox is further used to acquire an R-squared estimate, the root mean squared error (RMSE), and the histograms of the raw residuals. The coefficient of determination, R-squared, is meant to indicate how much of the variation in the response is captured by the model and is expressed on a scale of 0 to 1 where the fit is better the closer it is to 1. For a non-linear regression, the R-squared value is not entirely trustworthy but is considered here as for initial evaluations. The root mean squared error is the average standard deviation of the fit and the histograms provide a full picture of how variable the fit is. The effectiveness of each coefficient is evaluated by calculating the coefficient's p-value, a measure that reflects how much the function is influenced by the inclusion of the coefficient. Coefficients and their corresponding polynomial terms are eliminated using this measure and the effect on the R-squared and RMSE values are monitored for improvements.

3.4 High Strain Composite Tape Spring Hinge Study

High strain composites are a novel class of flexible material with great potential for spacecraft deployable structures. The material is able to accommodate large deflections and experience high strain without failure or plastic deformation, while providing high structural stiffness for low mass. Additionally, when compared to metallics, composites are able to achieve thinner shells as well as tighter bending ratios, resulting in mass and packaging efficiencies for deployable structures. However there are challenges to implementing these materials. Modeling and predicting the behavior is difficult due to nonlinearity, manufacturing variability, and complex geometry. For these reasons, an experimental test is needed for qualification of the numerical simulation data and is included in this study. Example hinge coupons for the materials used in this study are shown in Figure 3.3.

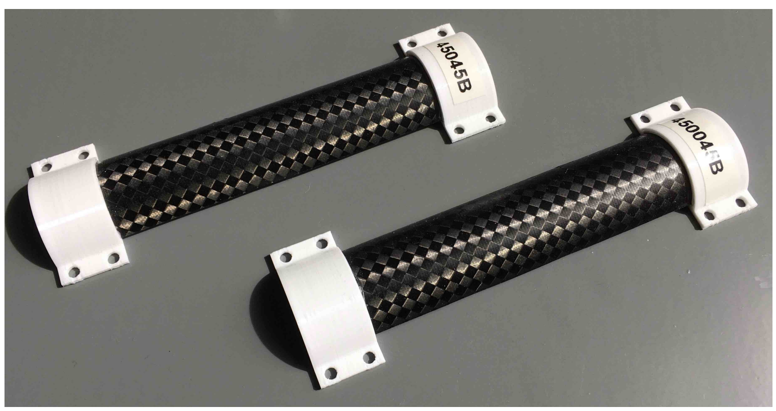

Figure 3.3: Example high strain composite tape spring coupons used for this study.

3.4.1 Tape Spring Hinge Properties and Geometry

The geometry of the structure in the folded and unfolded state is determined by the parameters of the tape spring geometry. The material thickness t, radius of cross sectional curvature R, and cross section arc length a are free design parameters that are fixed to specific material samples in this study. Two hinge material samples are provided in this study, and the parameters of the samples are recorded in Table 3.1. The first material sample is a high strain composite with a single layer of 0 deg unidirectional fibers sandwiched between 45 deg plain weave carbon fiber, a material

Table 3.1: Hinge geometry for tested samples and matching FEA models.

sample	**x-section radius** R, (mm)	**arc length** a, (mm)	**thickness** t, (mm)	**length** L, (mm)
$[45PW_{12}/0_{12}/45PW_{12}]$	15.875	35	0.20	150

recently developed for high strain composite spacecraft deployable booms. The properties of this material is derived from tensile test data and classical laminate theory and are provided by the NASA Langley Research Center. The tape spring length, L, is designed to minimize fold profile and non-symmetric fold range or flexibility. The capacity for non-symmetric fold behavior increases as the length of the flexible hinge section is increased. However, the hinge must be long enough for the cross section to transition from the stable c-shape to the flat fold without material failure. Therefore, the minimum allowable length of the tape spring must be determined. The high strain materials applied here were observed to have a maximum tensile strain of 1.7%, and a maximum allowable strain is set to 1.2% to allow for some factor of safety. A quick study is conducted to observe the maximum principle strains occurring in the tape spring for various lengths when the hinge undergoes a nominal fold to 90 deg using an FEA simulation. The results are shown in Figure 3.4 for both materials undergoing an equal sense fold, and a length of 150 mm is selected for this study. This is done for a tape spring with 20 mm long clamps attached at each end point, resulting in a shorter effective composite hinge section.

3.4.2 Asymmetry Definitions

The space of all possible hinge configurations is intractable at initial consideration, and so a subspace of most likely configurations that is also observable is identified. Three primary asymmetric configurations are identified as deviations from the symmetric case. The deviations considered ranged from 5-10 degrees, deviations that are too large to be negligible but small enough that they are feasible. Each deviation from the symmetric case is observed separately, and not compounded, in attempt to isolate the independent variables from each other. The bounds for these cases are listed in Table 3.2 for both the simulation and experimental cases, in both the equal

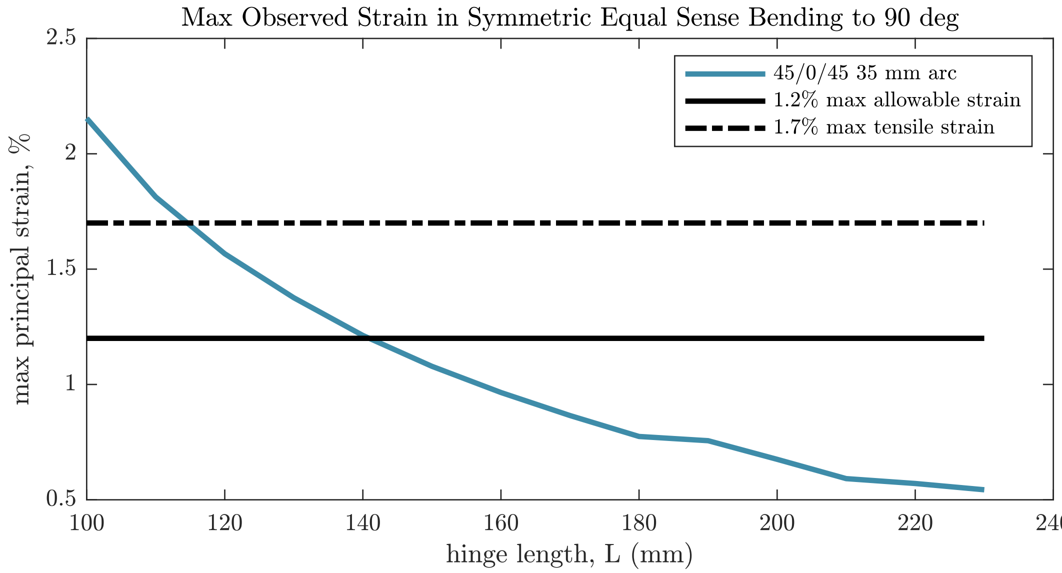

Figure 3.4: Maximum principle strain in the HSC tape spring as a function of length.

and opposite sense fold directions. A shorthand notation for the configurations is also introduced and defined in this Table.

Identifying these bounds is the primary challenge to studying the asymmetric behavior and strongly dictates the outcome of the model fits. Three primary displacement cases are selected for this study based on the obvious configurations and are not representative of all possible configurations. The bounds for the non-symmetric configurations are designed to approach the physical bounds of the hinge. The experimental fixture is designed to implement these measured deviations in a single system, therefore limiting the number of possible configurations. The resulting design is described in detail in Section 3.4.4. Future work could investigate measuring additional asymmetries through multiple fixtures. These deviations are expressed with respect to the $\mathcal{A}_0$ frame as described in previous sections. The tape spring behavior is subject to a few physical constraints that are used to define these bounds and the relationships within the states. For example, the relationship between the orientation about $\boldsymbol{a}_{0_1}$ and the displacement δ_3 can be expressed generally, for any non-symmetric relative angles by considering the law of cosines and by assuming the radius of curvature over the fold bend is known.

Table 3.2: Asymmetric configuration constraints used to generate Abaqus (A) and experimental (S) data sets in both equal (E) and opposite (O) folds.

Case	θ_1 sym (deg)	θ_1 offset (deg)	θ_2 (deg)	θ_3 (deg)	δ_1 (mm)	δ_2 (mm)	δ_3 (mm)
AE0	$0-180$	0	0	0	0	0	free
AE1	$30-180$	±10	0	0	0	0	free
AE2	$30-180$	0	0	±10	0	0	free
AE3	$30-180$	0	±10	0	$f(\theta_3)$	$f(\theta_3)$	free
SE0	$0-140$	0	0	0	0	0	$f(\theta_1)$
SE1	$100-140$	±10	0	0	0	0	$f(\theta_1)$
SE2	$100-140$	0	0	±10	0	0	$f(\theta_1)$
AO0	$0-180$	0	0	0	0	0	free
AO1	$90-180$	±10	0	0	0	0	free
AO2	$90-180$	0	0	±5	0	0	free
SO0	$0-140$	0	0	0	0	0	$f(\theta_1)$
SO1	$90-140$	±10	0	0	0	0	$f(\theta_1)$
SO2	$90-140$	0	0	±10	0	0	$f(\theta_1)$

3.4.3 Finite Element Model Overview

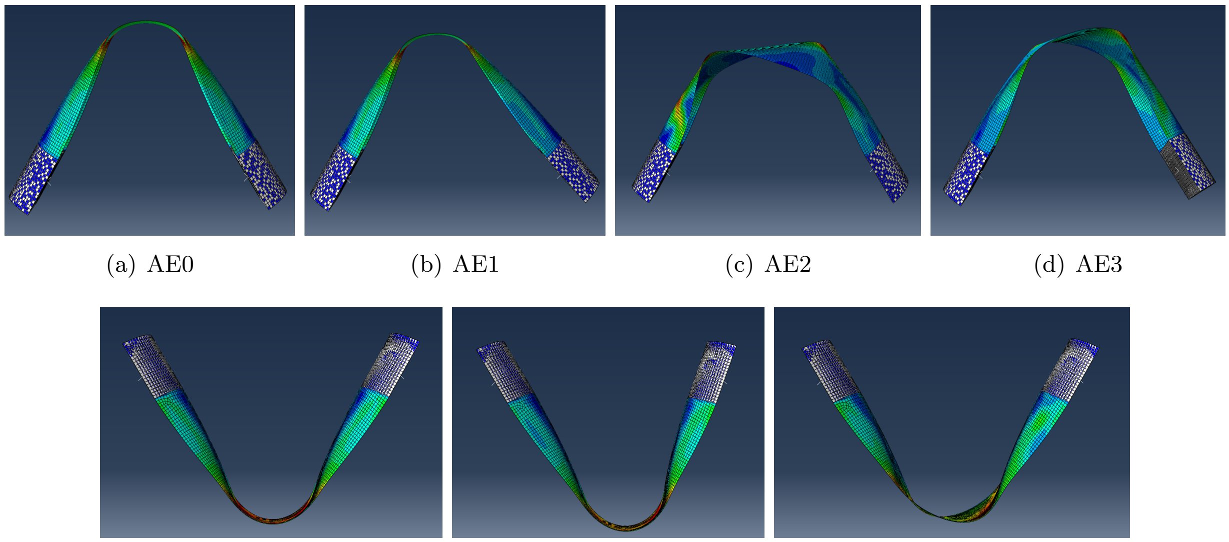

(a) AE0 (b) AE1 (c) AE2 (d) AE3

(e) AO0 (f) AO1 (g) AO2

Figure 3.5: Examples of displacements implemented in ABAQUS where the symmetric angle is ± 60 deg.

Finite element analysis simulations of the asymmetric hinge displacements are built in Abaqus 6.14. The hinge is represented as a shell with elastic behavior defined by engineering constants. The fixtures are represented as discrete rigid parts, are 20 mm in length, and are assembled and constrained using tie constraints. Four node shell (S4R) elements are meshed on the hinge shell using a 1 mm mesh. The asymmetric configurations are implements as displacement and rotation boundary conditions in static/general steps. Each range of asymmetric configurations is explored as a separate step enforced on an initially symmetric configuration. An asymmetric data set is generated for each primary fold angle, θ_1, at increments of 5 degrees, resulting in 16 equal sense and 10 opposite sense data sets for each material. Figure 3.5 shows example profiles for the equal sense and opposite sense cases and with non-symmetric deviations, with a no added deformation scaling.

Designing the displacement and rotation boundary conditions such that the simulations converge without error is not trivial and not easily automated. The approach here is to fix the inbound hinge frame to zero displacements and to apply displacements and necessary degrees of freedom to the outbound frame. Then the reaction forces, reaction moments, displacement, and rotational displacements are reported for the reference points representative of the hinge reference frames. The hinge reference frame is centered on the hinge endpoint fixture, and is mirrored in the design of the experiment. The opposite sense simulation required an additional step to bring the hinge pass the initial snap through phase. This was done by first pressing the shell flat with a rigid pin, and then removing the pin and continuing to the symmetric fold configurations. These steps are excluded from the data. The full range of symmetric fold angle data is acquired despite the pin by stepping through the fold angle constraints in reverse, from fully folded to fully deployed.

3.4.4 Experimental Testbed Overview

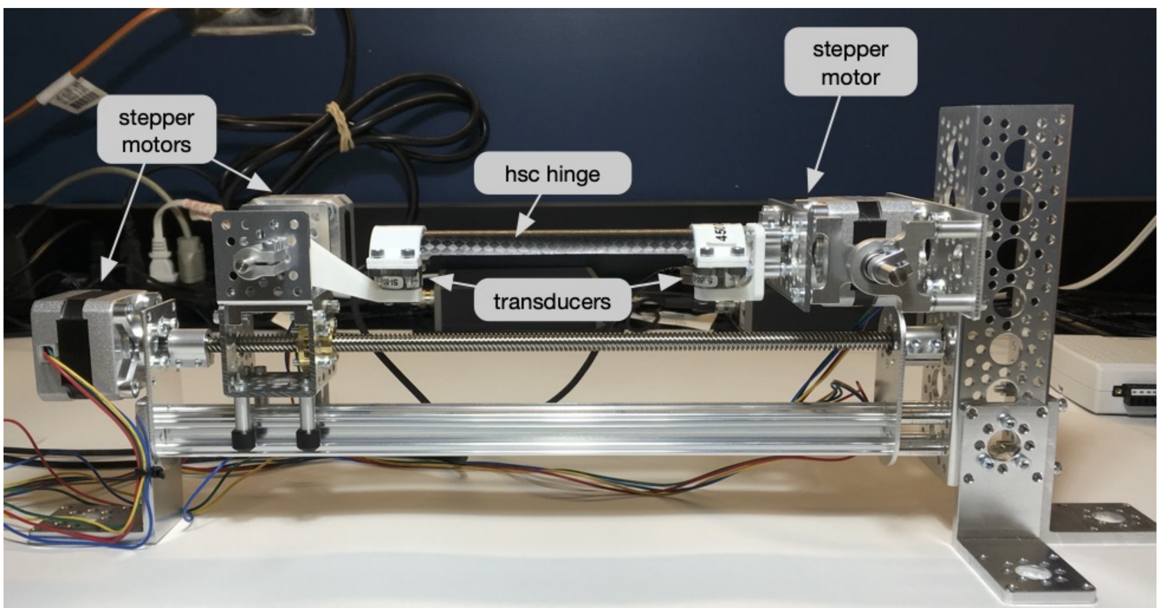

Figure 3.6: Components of the experiment testbed set up.

A mechanical testbed is designed to configure and control the asymmetric displacements, and a diagram of this design is presented in Figure 3.6. Two ATI six-axis force/torque transducers are used at the reference frames on the hinge to directly measure the full force/torque profile. The transducers are calibrated for torque measurements of 500 N-mm with 1/16th N-mm resolution and forces of 50 N in plane and 70 N out of plane with 1/80th N resolution. These sensors are aligned with the hinge such that the measurement frame of the sensor is coincident and orthogonally aligned to the hinge reference frames $\mathcal{A}_0$ and $\mathcal{A}_1$. The data from these hinges are then transformed into the frame alignments defined in Figure 3.2. An NI Labview program is used to interface with the transducers through an NI USB-6218 data acquisition card. The hinge configuration is controlled using multiple stepper motors and a SparkFun RedBoard, also interfaced through the Labview program with identical timing. The hinge configuration is not observed through external means, but is derived through the stepper motor count. The stepper motors are controlled using microstepping, with a resolution of 0.225 degrees per step. The left reference point of the hinge is mounted to a cart controlled through a smooth linear rail and the rotation about $\boldsymbol{a}_{0_1}$ is controlled by an additional motor. The right reference point is mounted to a freely rotating axis parallel to $\boldsymbol{a}_{0_1}$, and the twist about the hinge length axis is controlled with a third motor. A fourth motor is available to twist the hinge point along the $\boldsymbol{a}_{1_1} - \boldsymbol{a}_{1_2}$ plane to acquire data on relative translation, but is not implemented in the presented data. A system of precision shafts, ball bearing mounts, and standardized hardware provide smooth rotation, and this hardware is entirely manufactured by Actobotics. The tape spring hinges are each fixed at each end to 3D printed PLA plastic clamps using epoxy, and custom 3D printed mounts affix the hinge to the transducers. Custom mounting brackets are also 3D printed in PLA to mount the transducer assemblies to the testbed.

The experimental procedure is as follows. The hinge configuration is incremented into the symmetric configuration and data is sampled statically. Then each non-symmetric displacement is configured and sampled statically, reseting back to the symmetric configuration between each sample. Examples of the non-symmetric configurations are displayed in Figure 3.7. The geometry of the fixture must be taken into account when transforming the relative position and orientation data. The fixture creates an offset of the rotation axis from $\boldsymbol{a}_{0_1}$ of 42.5 mm at both sides of the testbed. The opposite sense configuration is achieved by using a modified mounting bracket, such that the hinge frames remain in the same position relative to the motor hubs. Several data samples are collected for a given configuration and averaged to provide one sample per configuration.

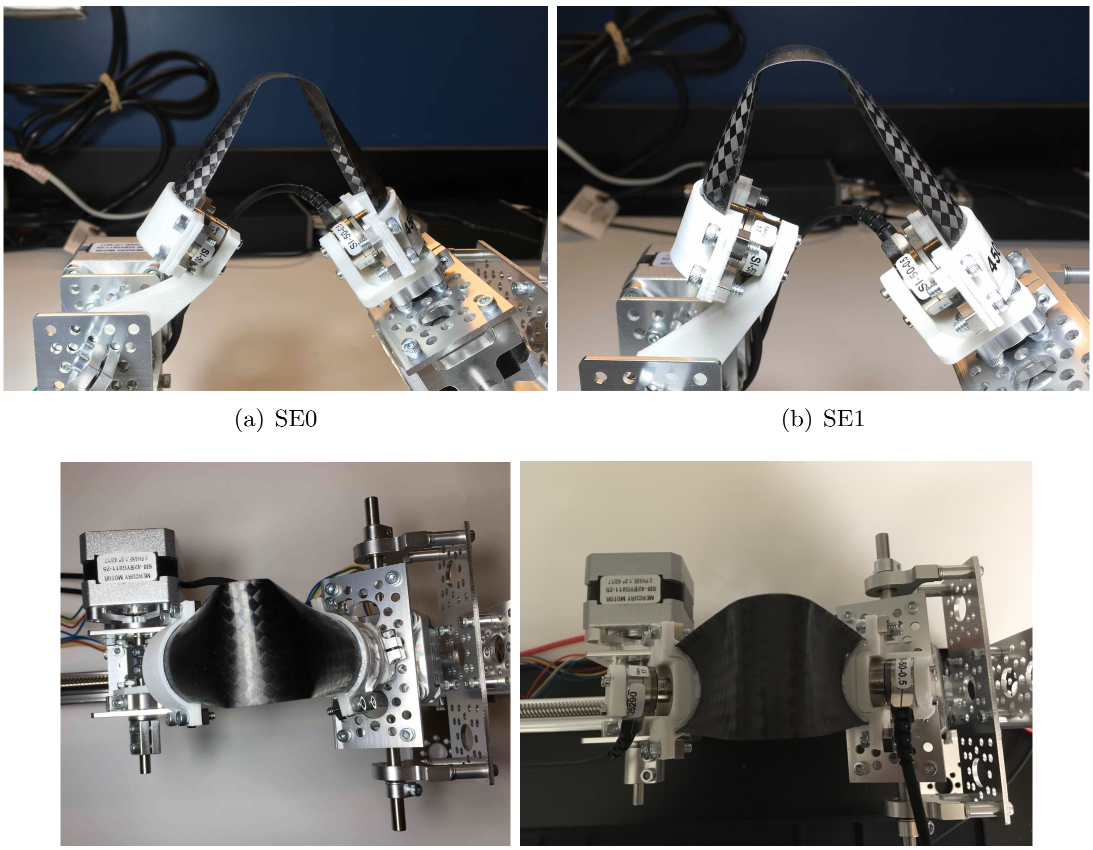

(a) SE0 (b) SE1

(c) SE2 (d) SO0

Figure 3.7: Examples of symmetric and non-symmetric displacements implemented in the experiments.

3.4.5 Results

3.4.5.1 Symmetric Data Comparison

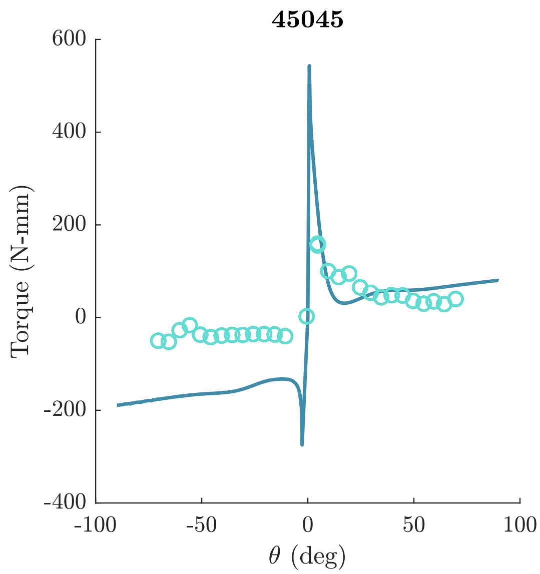

Figure 3.8: Moment response for the symmetric, 1 DOF moment-rotation.

Visualization of the fit is difficult due to the high number of independent state variables in the estimation. For an initial comparison, the symmetric case is considered due to its simplicity of visual and quantitative evaluation. The first axis moment is plotted in Figure 3.8 for both the experimental and simulated cases in both materials, where θ is the rotation from the initial position to the current position of the hinge frame. The experimental approach is not able to capture the moment peak at the initial fold, possibly due to small flexibilities in the testbed preventing the truly rigid response found in the simulations, and the trends do not strongly mimic each other. In particular, the opposite sense experimental data is significantly smaller an the general trend also deviates from the prediction. This indicates there will be notable variation in the numerical and experimental models. Additionally, the experimental data shows significant third axis, or hinge normal, moments generated in this configuration, where no moment is expected. This is suspected to be due to imperfections in the layup construction, where the outer 45 degree plain weave plies are not truly aligned, and may also be due to unperceived misalignment of the testbed. This may imply that hinge performance relies heavily on hinge construction and undesired forces and torques are easily introduced to the system.

3.4.5.2 Non-Symmetric Data Trends

The non-symmetric FEA numerical data predicts significant forces and torques generated from the hinge, suggesting that a slightly non-symmetric configuration can have significant impacts on deployment behavior. For certain cases, the forces are observed to be on the order of tens of Newtons and torques in the hundreds of Newton-millimeters, on the same order of magnitude as the symmetric torque. This trend is consistently observed in all the equal-sense and opposite-sense numerical FEA data sets. In Figure 3.9, the forces and torques for non-symmetric configurations of the 45/0/45 hinge are plotted for both the experimental and simulation data for the same symmetric angle cases, where only the boundary point of the simulated data is recorded. The simulation data shows large torques on all axes are possible, and large forces are predicted for some equal sense bends.

Comparing the experimental data with the simulation data reveals the experimental data does not exhibit any of the large force and torque behaviors. This is an unexpected result and warrants further study into the high strain composite hinge modeling and testing. The discrepancy suggests there are limitations of predicting the behavior of high strain materials undergoing large complex displacements using the material model implemented here, or that there is an unknown error in the simulation. The experimental data has further discrepancies, where for the third axis force, forces are observed where they were not predicted. These forces are suspected to be due to inconsistencies in the composite sample and the model assumptions, and warrant an investigation into the material construction.

3.4.6 Material Construction Uncertainty in the Spatial Force Profile

A major source of uncertainty is represented by the composite material fabrication. The material model of the composite is developed from Classical Laminate Theory and tensile testing.

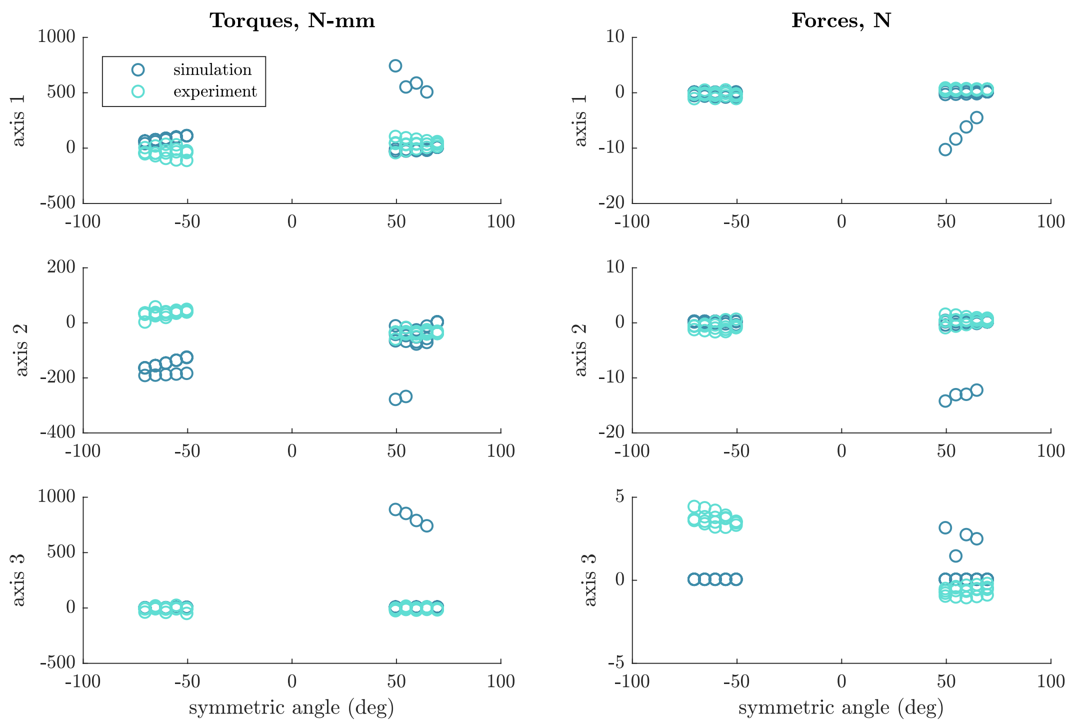

Figure 3.9: Forces and torques from non-symmetric configurations, recorded from both the experimental and simulated data of the 45/0/45 hinge. The symmetric angle is expressed as the hinge orientation from the initial flat configuration.

Classical Laminate Theory assumes the laminates are perfectly aligned, however modern fabrication techniques cannot guarantee perfect alignment and can have non-negligible imperfections. Additionally, fabrication of the tape spring hinges is not guaranteed to be perfectly aligned with the longitudinal hinge axis. Small deviations from the tape spring hinge axis are shown to introduce significant off-axis torques for the symmetric fold case and cannot be ignored. In Figure 3.10, the predicted forces and torques for a symmetric fold are shown for varying angles of fabrication error of the longitudinal hinge axis, and plotted with measurements. The fabrication error for this sample was estimated to be 1.1 deg, and the measured forces and torques are seen to waiver near the off-axis predictions. This motivates further investigation into how robust the hinge model is in terms of manufacturing uncertainty, and motivates more refined testing of the materials. This is left to future work.

3.4.7 FEA Nonlinear Regression Model

3.4.7.1 Nominal Data Results

The nonlinear regression approach is not currently applied to the experimental data due to the low sample size of the data. The nonlinear regression is applied to the FEA data set and a reduced polynomial is iterated towards by evaluating the p-value of each coefficient for the full 45/0/45 material set with both equal and opposite sense folds. The statistical results for each material are reported in Table 3.3, and the corresponding estimated coefficients are reported in Table 3.6 for completeness. The results show that the polynomial fits are not improved, but are also not greatly reduced, by reducing the number of polynomial terms. The statistics indicate that the fit is able to capture the majority of the trends, but is by no means a perfect fit. The histograms in Figure 3.11 show that the data is not normally distributed and there are large residual outliers. This is true for both the force and torque cases. The large force and torque profiles from the asymmetries highlighted in Figure 3.9 are likely contributors to the difficulty of fitting this data. It's possible that the experimental data, or an FEA model that is reconciled with the data, would

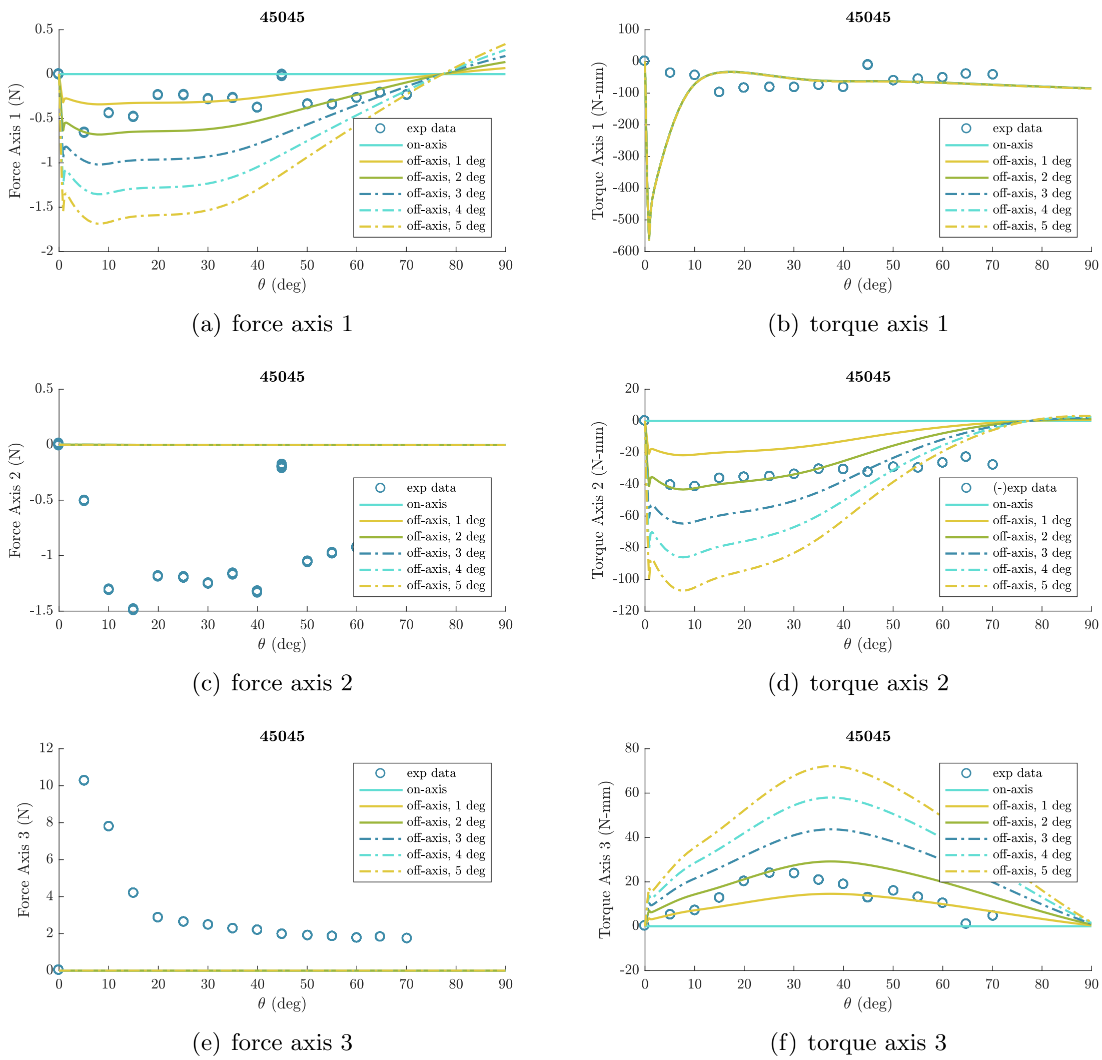

(a) force axis 1

(b) torque axis 1

(c) force axis 2

(d) torque axis 2

(e) force axis 3

(f) torque axis 3

Figure 3.10: Force and Torque for off-axis layup cases and experimental data.

provide better results, where the experimental data did not measure these large force and torque responses. Fitting the primary deployment moment, M_{0_1}, is difficult to capture when including the asymmetric data. Evaluation of the coefficient p-values reveals that the higher order polynomial terms of Equation 3.6 do not contribute to improving the regression fit, and that $p(\boldsymbol{q})$ provides an equivalent fit. Therefore, these additional coefficients are removed and only $p(\boldsymbol{q})$ coefficients are reported in Table 3.6.

Table 3.3: Statistics for the 45/0/45 FEA model fit functions.

statistic	M_{0_1}	M_{0_2}	M_{0_3}	N_{0_1}	N_{0_2}	N_{0_3}
full R-Squared	0.81	0.80	0.88	0.82	0.89	0.82
full RMSE	181	238	202	4.01	3.24	0.43
reduced R-Squared	0.81	0.79	0.88	0.81	0.88	0.79
reduced RMSE	182	240	203	4.05	3.25	0.46
num of coefficients	18	19	17	17	18	20

3.4.7.2 Additional Nonlinear Regressions

Attempts to improve the regression fit are made by examining alternative data sets, and two approaches are recommended. First, model improvements can be made by fitting the equal-sense and opposite-sense data individually and by using piecewise functions to join the models. The statistics for such a case are shown in Table 3.4, where all RMSE values are decreased and the opposite-sense fits have greatly improved RMSE and R-squared values. The second approach to improving the model is to consider smaller asymmetric displacements for the data set. A numerical data set is generated in Abaqus for cases where AE0 and AE1 are the same, but AE2 and AE3 are reduced to boundaries of $\theta = 5\,\mathrm{deg}$. Table 3.5 shows that the RSME and R-Squared values improve for both materials with this reduction. This improvement is as expected, where approximations are generally more accurate for smaller deviations. In addition to these approaches, expansions of Equation 3.5 beyond polynomial terms are explored. However, additions of trigonometric functions, logarithmic functions, or inverse polynomials are not found to significantly improve the fits, and therefore this approach is not currently recommended.

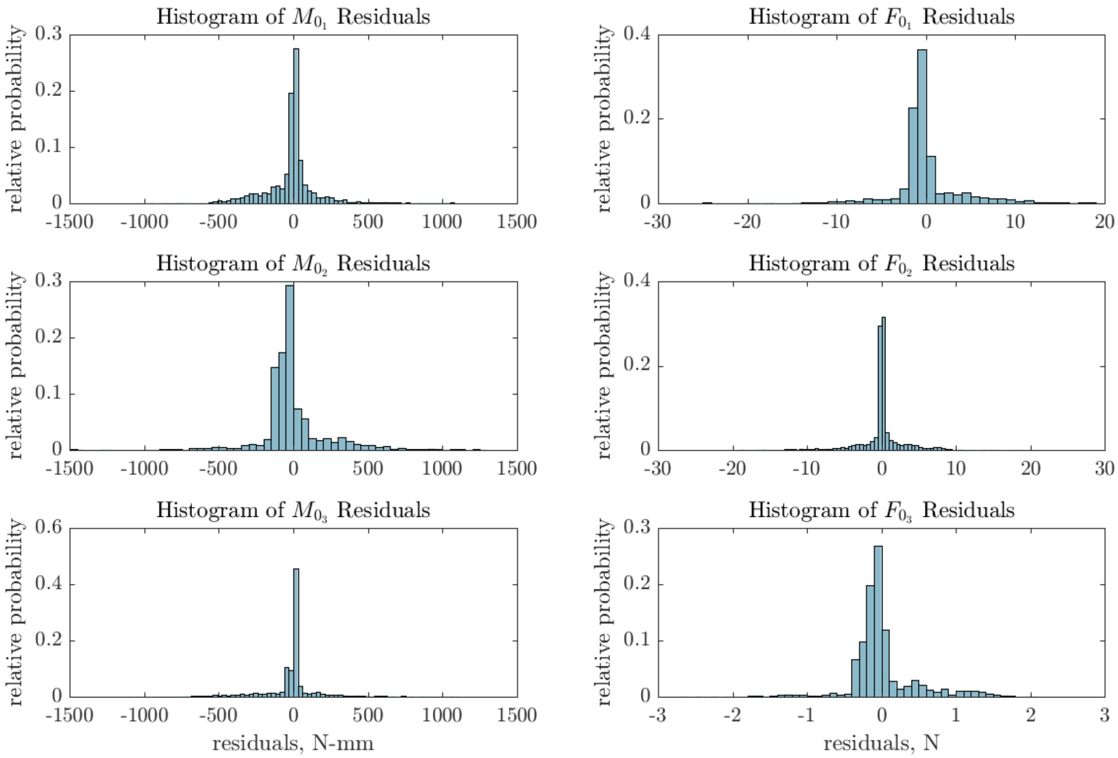

Figure 3.11: Fit function histograms for the 45/0/45 numerical simulations.

Table 3.4: Statistics for the 45/0/45 FEA model fit functions with full 27 coefficient polynomials using only equal or opposite sense data.

statistic	M_{0_1}	M_{0_2}	M_{0_3}	N_{0_1}	N_{0_2}	N_{0_3}
Equal R-Squared	0.84	0.88	0.93	0.90	0.92	0.91
Equal RMSE	127	191	121	3.12	1.89	0.29
Opposite R-Squared	0.98	0.97	0.99	0.97	0.99	0.98
Opposite RMSE	87.9	78.7	96.6	1.52	1.73	0.14

Table 3.5: Statistics for the fit functions with full 27 coefficient polynomials using non-symmetric boundaries of $\theta = 5\,\mathrm{deg}$ for AE2 and AE3 Abaqus data sets.

statistic	M_{0_1}	M_{0_2}	M_{0_3}	N_{0_1}	N_{0_2}	N_{0_3}
45/0/45 R-Squared	0.85	0.93	0.93	0.93	0.92	0.93
45/0/45 RMSE	145	130	138	2.29	2.44	0.21

Table 3.6: Reduced coefficients for the 45/0/45 FEA model.

coefficient	M_{0_1}	M_{0_2}	M_{0_3}	N_{0_1}	N_{0_2}	N_{0_3}
a_1	-75.23	81.11	-10.95	0.5636	-	-0.1072
a_2	-	-15720	3964	-292.68	-44.10	-
a_3	-9706	14460	-10920	236.58	138.6	-2.215
a_4	453.3	-1122	565.5	-18.617	-7.337	-
a_5	-	803.8	-244.0	11.997	3.507	-
a_6	-	-	-	-	-	-0.01040
$b_{1,1}$	-	-	-	0.718	-	-
$b_{1,2}$	10850	10640	8842	175.3	-151.7	-
$b_{1,3}$	2192	-4310	5370	-71.58	-82.83	-
$b_{1,4}$	-131.9	-132	-	-2.224	-	0.0718
$b_{1,5}$	14.83	-	177.7	-	-2.988	0.1051
$b_{1,6}$	-0.7309	0.6111	-	-	-	-1.584E-3
$b_{2,2}$	-3590	19050	-	165.4	100.4	201.8
$b_{2,3}$	-	-	-10340	-	165.5	51.32
$b_{2,4}$	1004	-482.9	861.8	-8.875	-12.64	-2.091
$b_{2,5}$	-615.5	-	-467.3	-	8.655	3.075
$b_{2,6}$	178.1	141.25	173.5	2.845	-3.333	-0.08831
$b_{3,3}$	18140	-	-	-	-	-57.94
$b_{3,4}$	-	-	-	-	-	-1.499
$b_{3,5}$	396.7	-182.1	-	-	-1.551	-3.501
$b_{3,6}$	-101.7	157.3	110.0	2.843	1.312	-0.1451
$b_{4,4}$	11.47	3.916	-11.59	0.07821	0.1422	8.22E-3
$b_{4,5}$	10.42	-	5.962	-	-0.1010	-0.08333
$b_{4,6}$	1.777	-14.77	6.614	-0.2523	-0.08466	3.949E-3
$b_{5,5}$	-	-1.411	-	-	-	0.01146
$b_{5,6}$	-	9.077	1.981	0.1383	-0.04249	-
$b_{6,6}$	-	-0.008314	-	-6.74E-4	-	-1.087E-4

3.4.8 Conclusions and Future Work

This chapter presents an approach for capturing the full six degree of freedom force and torque behavior of a tape spring hinges in symmetric and non-symmetric configurations as a function of the hinge's six relative coordinates. Non-symmetric behavior is demonstrated to have significant force and torque profiles and therefore should be included in a robust dynamics model. Numerical predictions for force and torque are generated in Abaqus for three non-symmetric cases in the equal-sense fold and two non-symmetric cases for the opposite-sense fold. A non-linear regression is applied to the full data set assuming a simple second order polynomial, and the resulting fits are evaluated. Fits for the numerical data are not conclusively good, and therefore interpolation methods or a look-up table may be more appropriate for capturing these data trends, depending on needs. The regression is found to improve if smaller asymmetry ranges are used, or if the equal and opposite fold regimes are fit separately, so using a piecewise switching function is another possible solution. Experimental and numerical data predicting the hinge behavior in symmetric and non-symmetric folding are obtained. The results from these databases do not correlate and are not able to conclusively validate each other. This may be due to differences in the fabrication of the composite tape spring configuration and the assumptions of the material model, but it may also be influenced by bias and shortcomings in the experimental set up. This highlights a potential issue in implementing composites, where each batch is uniquely manufactured and earlier models must be considered carefully before applying them to later units. Recommendations for iterating on these results are to improve the testbed design to eliminate possible biases influencing the experimental data and to search for better candidate model functions for regression fits. A simpler test bed to investigate the symmetric data discrepancies only would be a good first step towards better understanding the results. Additionally, vetting the test bed with a simple flat plate with known material properties, such as a steel plate, would provide confidence for the validity of the asymmetric test bed results.

Chapter 4

Research Goal 3: Folding Structure with Tape Spring Hinges Deployment Testing

The objective of this research goal is to design and build a folding structure that can be used to evaluate the effectiveness of the modeling approach developed in Chapters 2 and 3. A prototype structure is developed and a deployment testing campaign is conducted. In Chapter 5, a full system model is developed that integrates the hinge model with the closed-chain multi-body dynamics algorithms. The simulated dynamics is compared with the measured dynamics and model performance is evaluated. A concept illustration of the deployment test system is displayed in Figure 4.1, where a four-body structure is shown suspended by gravity offload lines and a gravity compensation system of counter masses. The deployment tests include two sets of trials, one in the "cup down" configuration, where the folded structure creates a "cup" that faces the ground during deployment, and a "cup up" orientation, where this cup is facing towards the ceiling. These two sets of data will be used to approximate any residual influence of gravity remaining beyond what is offset by the gravity compensation system.

4.1 Four-Body Prototype Design and Build

The prototype is developed for the simplest closed-chain system case, the four-body structure case. The panel pattern is modeled after the base unit of the Miura-ori pattern, where the fold line geometry of the theoretical pattern is designed such that there is only one degree of freedom through folding and unfolding. This makes the pattern ideal for space structures applications. Two

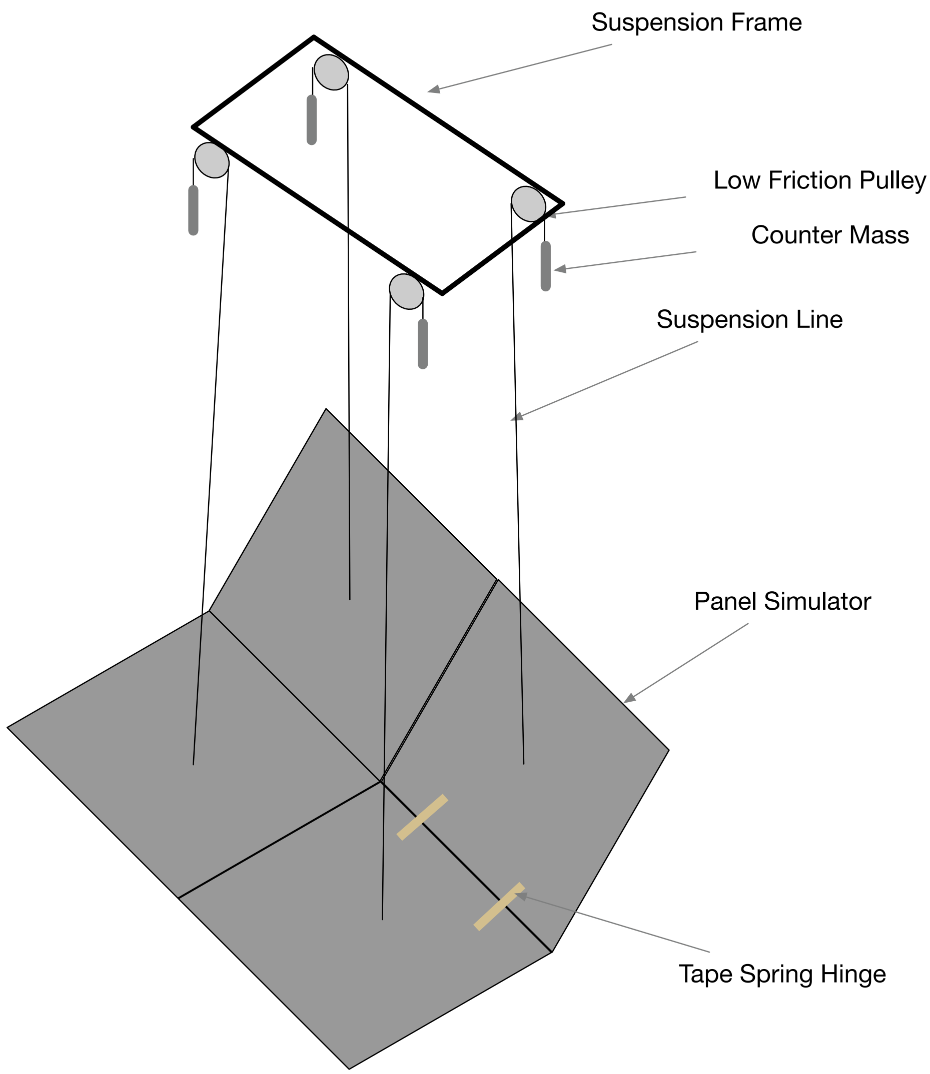

Figure 4.1: Concept illustration of the gravity offloading system and structure prototype, not to scale.

tape spring hinges are implemented across a single fold line of the pattern, where spring steel tape spring hinges are used in the prototype build and are modeled using the methodology developed in Chapter 3. The prototype structure is shown in the deployed configuration in Figure 4.2, where several features are observed. A 60 deg Miura fold angle is chosen for the fold panels to maximize the stability of the folds and to have a symmetric design of the panel geometry. The edges of the panels are chamfered to reduce the influence of contact dynamics in the deployment. These edges are attached using thin, 0.0025 inch kapton such that the fold axis of the edge is approximated as the physical edge of the panels. As thicker material is used for these fold lines, the influence of the material as it curves may become a concern. The tape spring hinges are observed on the lowest panels, where the mounting fixtures are manufactured from 3D printed PLA. Additional physical properties are listed in Table 4.1.

Table 4.1: Properties of the prototype parts.

Part	**Material**	**Mass** (g)	**Thickness** (mm)	**Length** (mm)
Panel	cast acrylic	$350 - 369$	3.2	292 along edge
Hinge Plate	PLA	7.8	NA	NA
Tape Spring	spring steel	4.6	0.15	150

The physical separation of the two panels along the fold line is a novel advantage for an origami inspired structure. This opens the possibility of a flat-folded origami pattern, where the thickness of the panels would require extensive design of the fold line placements to ensure flat-foldability.[64,65] Using segmentation to enable physical implementation of an origami-inspired pattern due to material thickness is demonstrated by the novel Slipping Fold design presented by Arya[66] for membrane structure applications. The hinge design presented here offers an alternative approach to this challenge as applied to rigid or semi-rigid folded structures, and a basic diagram of this concept is shown in Figure 4.3. Figure 4.4 displays the prototype structure in the folded configuration and suspended in the cup down orientation. From the hinge facing view, the multi-DOF status of the tape spring hinge edge is revealed. The panels are able to separate completely, and their relative orientation demonstrates multiple-DOF offsets. The structure is not compressed into a fully flat

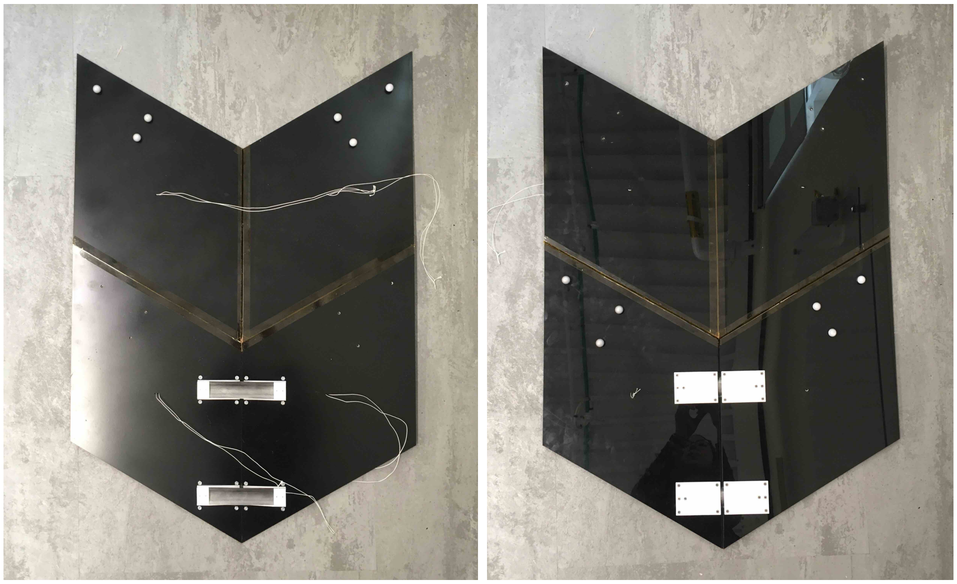

(a) cup up side (b) cup down side

Figure 4.2: Prototype structure in deployed configuration.

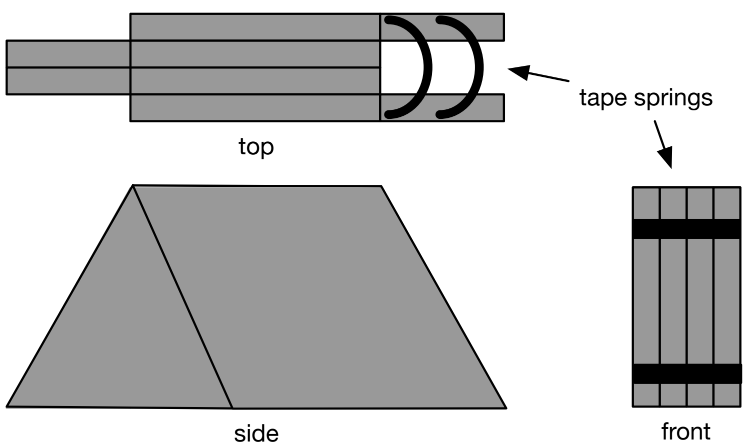

Figure 4.3: Three view illustration of a thick flat-folded Miura pattern unit with tape spring hinges embedded.

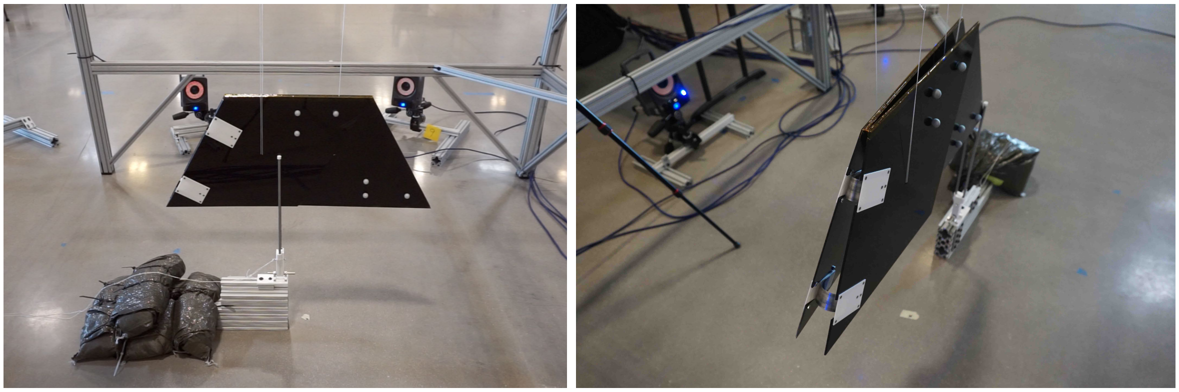

(a) side view (b) hinge view

Figure 4.4: Prototype structure in folded configuration in test bed.

folded configuration due to limitations of the steel tape springs, which cannot be folded to the flat folded radius without plastic deformation.

4.2 Four-Body Prototype Deployment Test Bed

Along with the prototype, a deployment test bed is developed. Deployment testing of the prototype must provide gravity compensation, measure each panel body's positions in 3D space through the deployment duration, and operate at sufficient resolution through the deployment duration. These requirements are met by developing two systems, a suspension system that provides gravity off-loading, and a metrology system that is capable of taking the desired measurements. Previous work completed through wide collaboration, developed a similar system for a CubeSat deployable boom,[49] and this experience has provided many insights for the project.

The approach for gravity compensation for the deployment testing is designed as follows. Each panel of the system is treated as a rigid body. The attachment points of the gravity compensation lines are placed at the center of mass of each rigid body using a line tie point. The center of mass of each flat panel is determined from the panel geometry using mass property evaluation tools in SolidWorks. The placement of these points determine that the deployment must be tested in either the "cup-up" or "cup-down" configurations. A concept diagram of a gravity off-loading system and

(a) offload frame

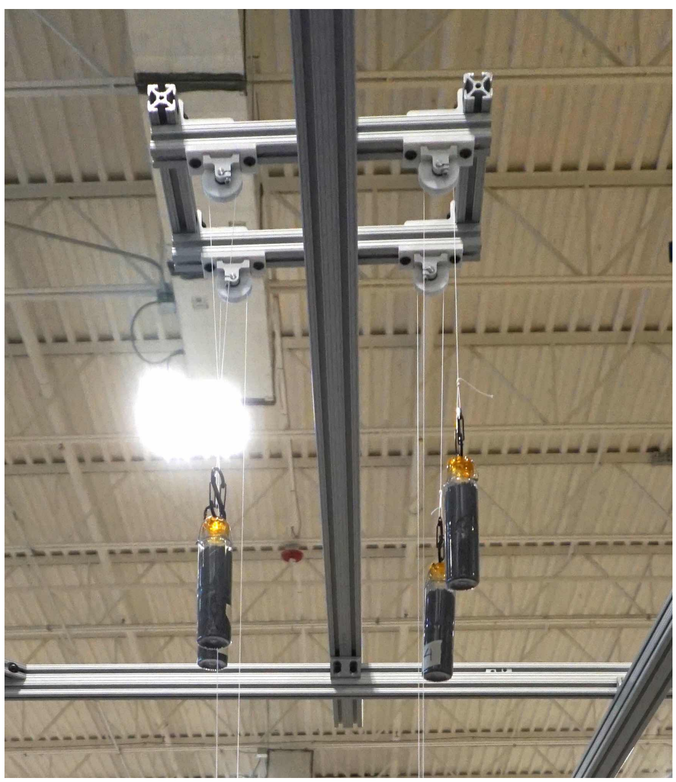

(b) offload pulleys

Figure 4.5: Gravity compensation system frames.

four-body prototype is shown in Figure 4.1, and examples of the system as implemented are shown in Figures 4.4 and 4.5. The mass of each panel is compensated using a counter mass, which is shown in Figure 4.5, made from narrow bottles of lead shot. The counter masses are calibrated carefully by hand, such that a small angular or linear velocity perturbation along any axis of the structure is not restored by the compensation system, and the velocity is not damped over acceptably small motion ranges. This insures the gravity compensation system is not significantly influencing the dynamic response of the deployment. Each gravity compensation line is made from braided Spectra and is approximately 6 feet long, where the length is limited by the offload frame. The braided Spectra line is selected to eliminate dynamic flexing from the lines. The influence of the static offload pulley point through the deployment is considered negligible, where at this height the translation difference is an order of magnitude smaller than the suspension length, and due to the symmetry of the deployment. Finally, a detached clamp system is designed to hold the structure in the folded state at the initialization of the test, and is displayed in Figure 4.4. This clamp is activated using a pull-pin to release and a stiff torsion spring to quickly open the clamp and move the clamp arms out of range of the structure as it deploys.

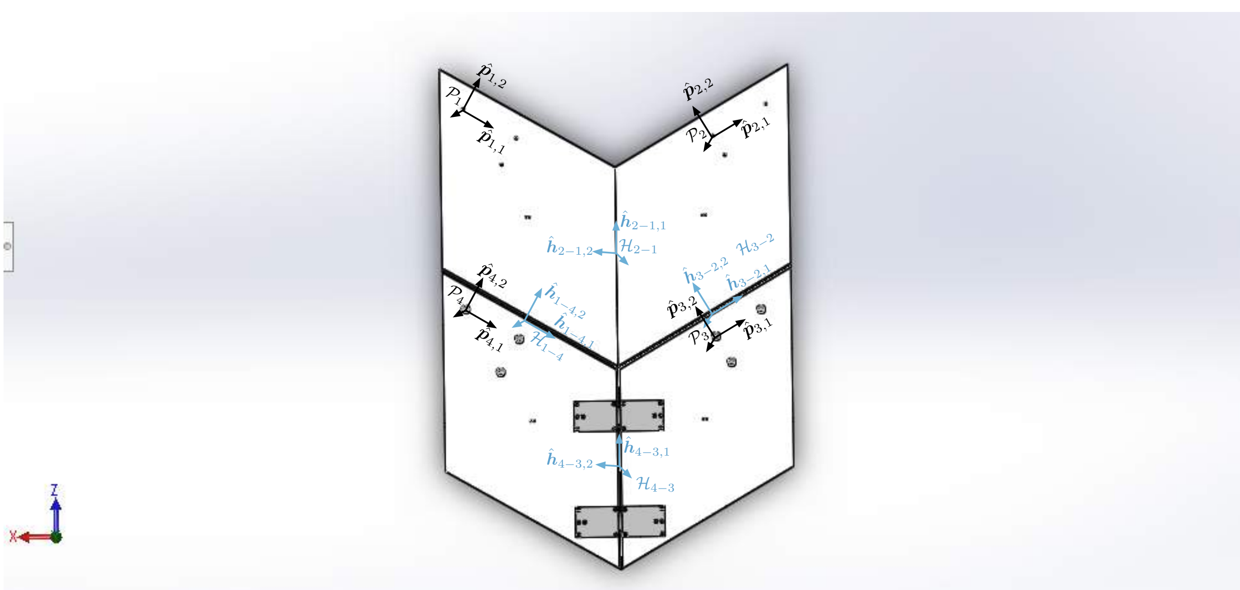

Figure 4.6: Reference frames defined in Vicon are denoted as $\mathcal{P}$ and hinge frames are denoted by $\mathcal{H}$.

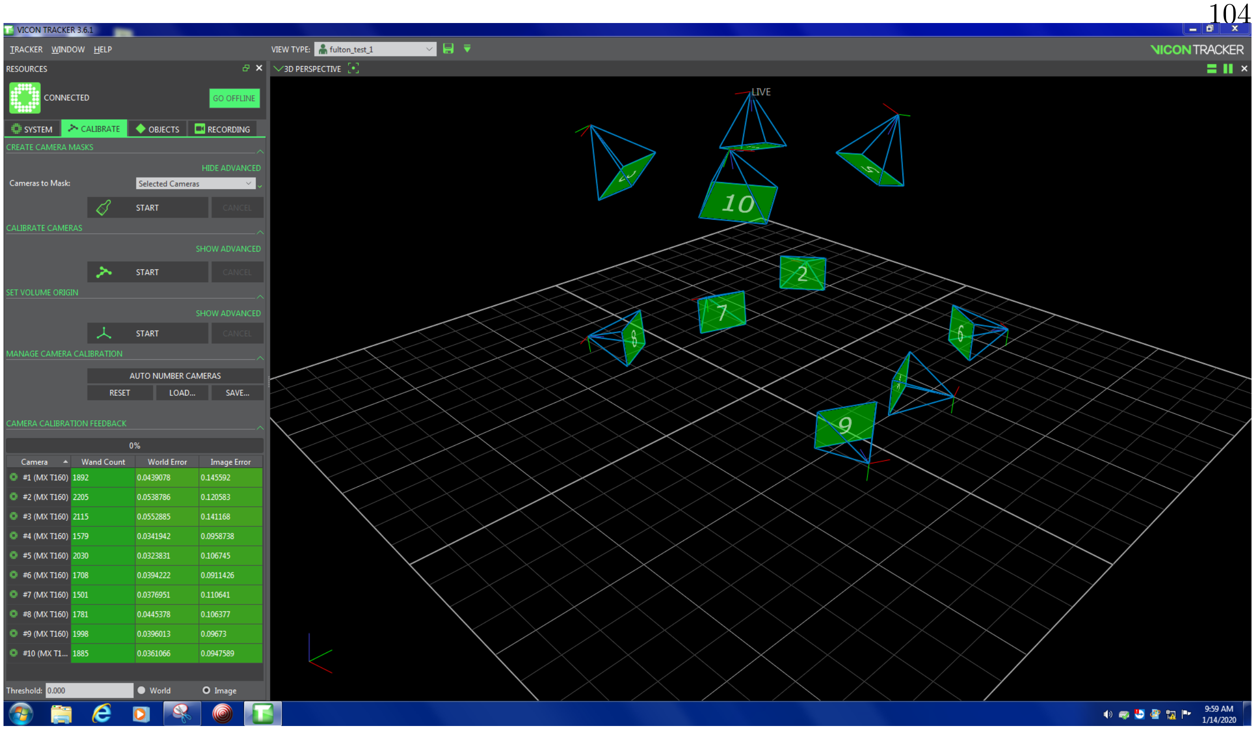

Figure 4.7: Vicon camera calibration results in Tracker 3 software.

The metrology system selected for this testing implements the Vicon MX T-Series cameras and Tracker 3 software by Vicon Motion Systems. This is a motion capture system that is designed to track discrete targets in three dimensional space. Ten Vicon cameras are installed around the gravity offload frame, as shown in Figure 4.5. These cameras are calibrated using a precision calibration tool that enables the Tracker 3 software to learn the camera's position in space. The results of the calibration used in the test trials is displayed in Figure 4.7, and state that each camera has an error in knowledge of a target's position in the camera frame of less than 60 micrometers. High precision spherical targets of 14 mm diameter are installed on the prototype and are visible in Figure 4.2. This system is designed such that each target is visible by at least two cameras at all times during the trial, and the multiple simultaneous images of the same target are processed to determine the target's position in space. Three targets are required at minimum to define an object for tracking, and these three targets are further used to define a reference frame for each object. These reference frames are defined to be on the plane of the cup up side of the prototype, where the tape spring hinges are visible. The notation of these frame definitions is defined in Figure 4.6

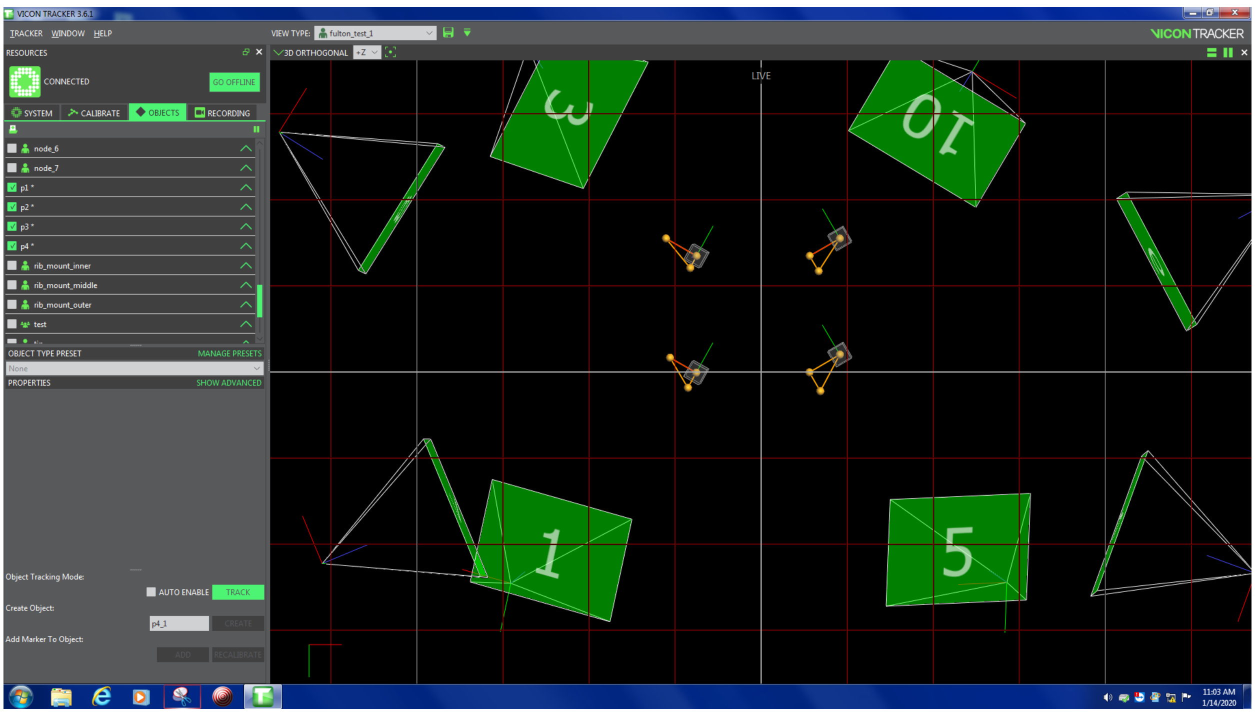

Figure 4.8: Vicon reference frame definitions using prototype target definitions.

with the panel numbering for reference. The corresponding frame and object tracking in Vicon's Tracker 3 software is displayed in Figure 4.8. Data is collected at a frame rate of 100 frames per second (fps), providing sufficient resolution to observe the dynamic response well. A selection of camera frames from the deployment are shown in Figure 4.9 to illustrate the deployment behavior of a single trial.

4.3 Four-Body Prototype Deployment Test Initial Data and Results

The raw global tracking data is processed to describe the behavior across each hinge connection of the system. These hinge frames are defined in the same convention as described in Chapters 2 and 3. These definitions require a hinge frame at the hinge attachment point for each rigid body in the system. These hinge definitions are shown in Figure 4.10 along with their relative relationship with the panel tracking reference frames. The positions of the hinge frames relative to the tracking frame are known from the prototype model CAD, and therefore position and orientation transformations are completed for each rigid body. Then, the relative states across the hinge are calculated. The results are printed for all the data sets together for an initial first evaluation of the data and test campaign quality. Two trial sets of fifteen trials were completed, one set in each the cup up and cup down orientations. The results of the trials are discussed in the following section. All data sets have been treated with a five point moving average smoothing algorithm on the raw measurements to reduce the appearance of noise. The initial conditions of each trial is not absolutely the same for each case, due to the limitations of the fold clamp and the flexibility of the tape spring hinges. Generally, the cup up trials have a slightly deployed initial angle of 177 deg versus a more closed 179 deg of the cup down cases. This limits the direct comparison capabilities of the following discussion.

4.3.1 Relative Orientation Results for all Data Sets

The behavior responses of the relative orientations across each hinge are shown in Figures 4.11, 4.12, 4.13, and 4.14. Orientations are described in 1-2-3 Euler angles for intuitive clarity, and

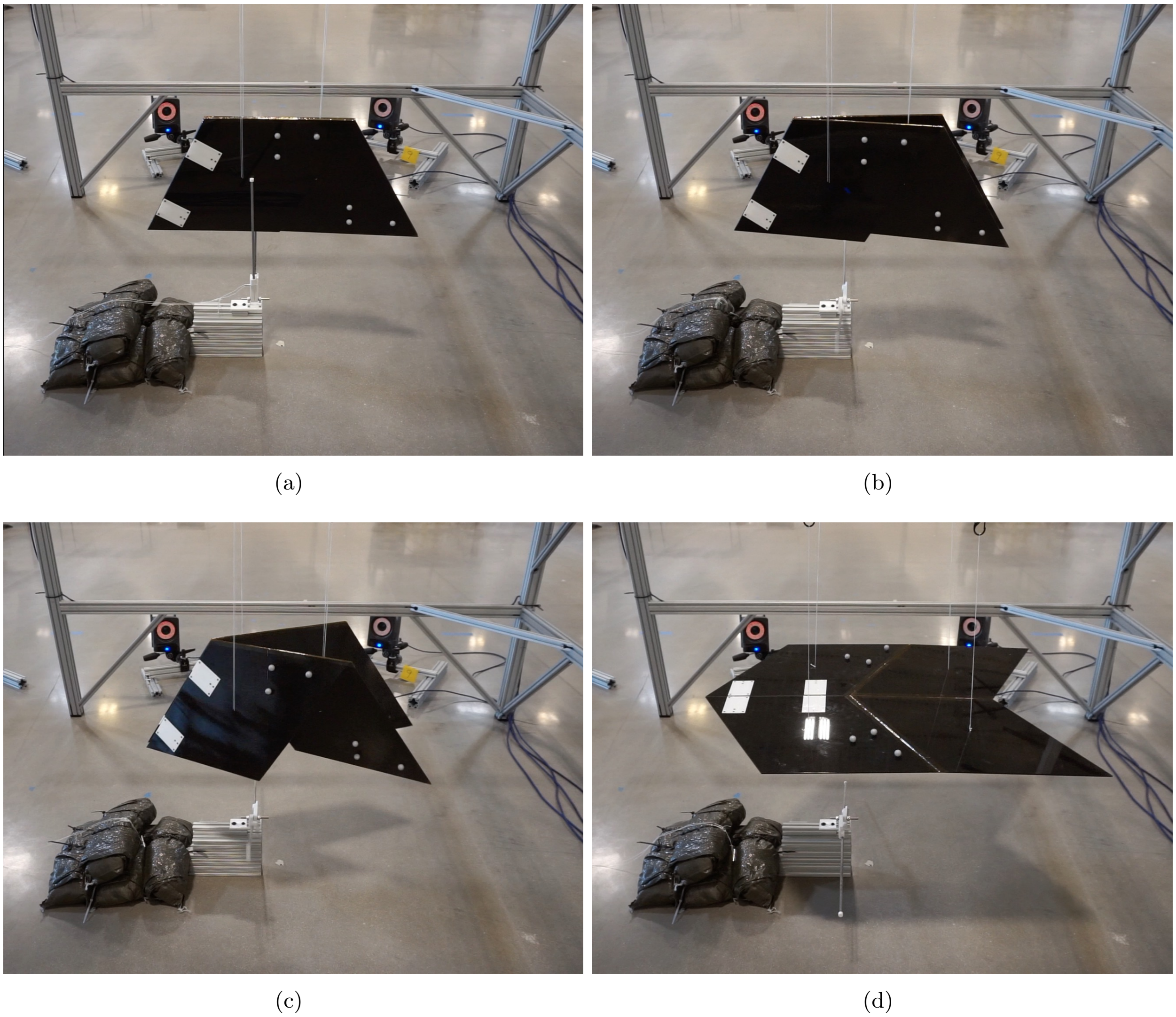

(a) (b) (c) (d)

Figure 4.9: Prototype structure through deployment sequence.

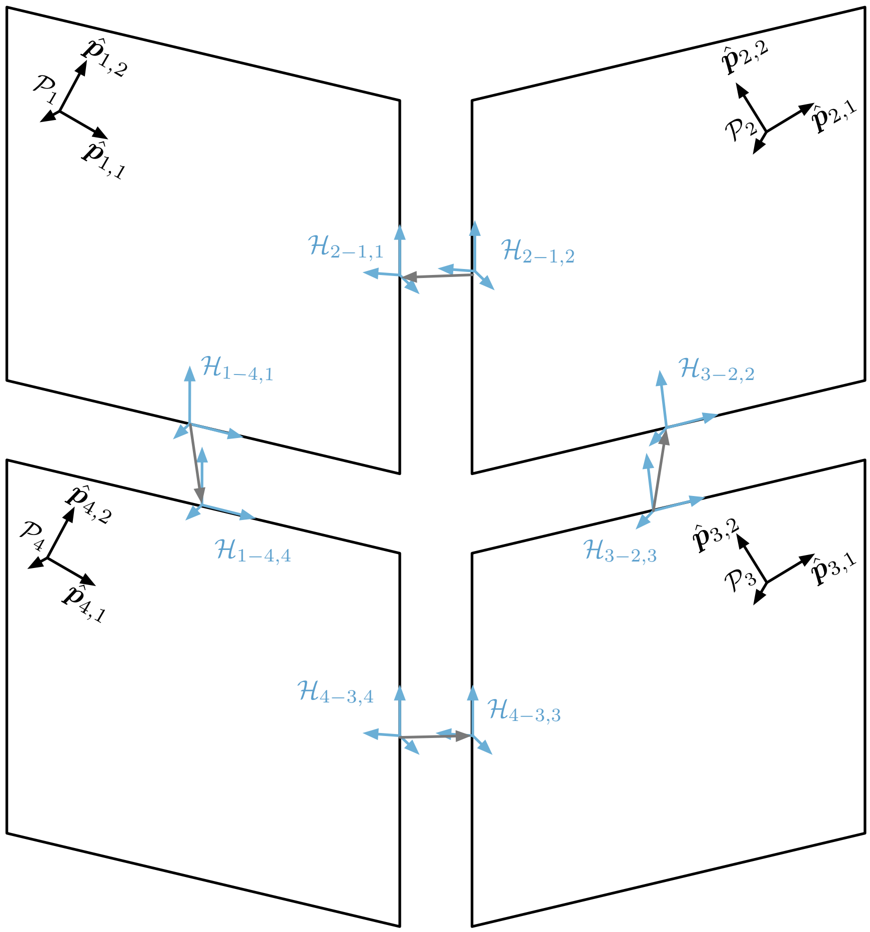

Figure 4.10: Reference frames defined in Vicon are denoted as $\mathcal{P}$ and hinge frames are denoted by $\mathcal{H}$.

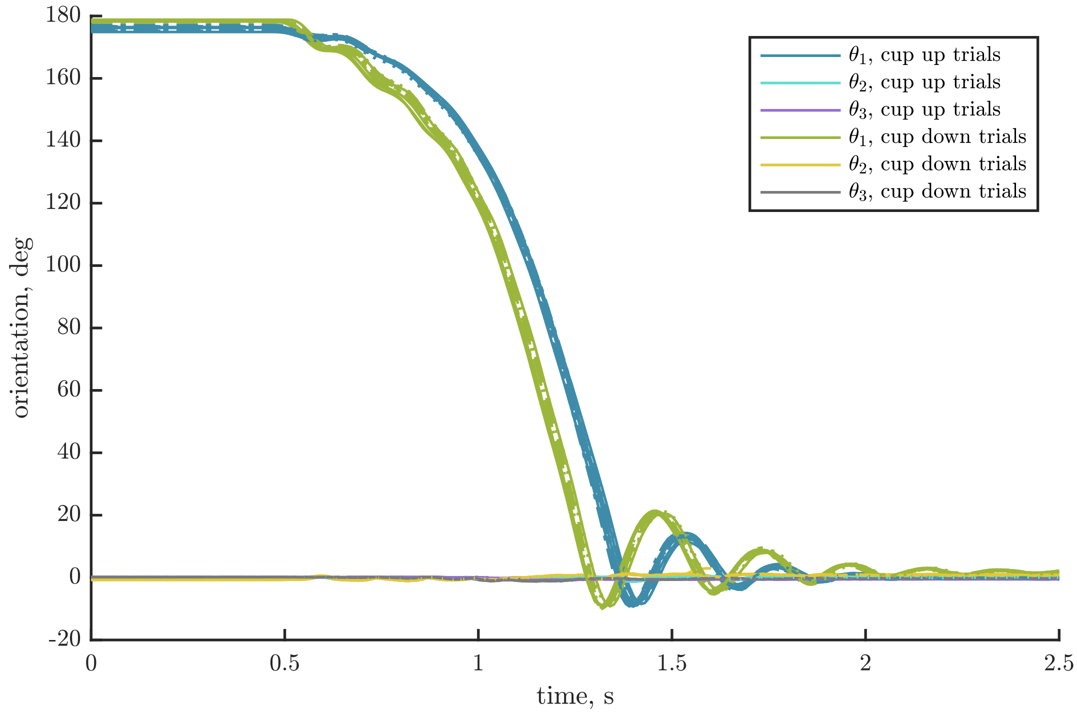

Figure 4.11: Measured relative orientation for hinge 4-1.

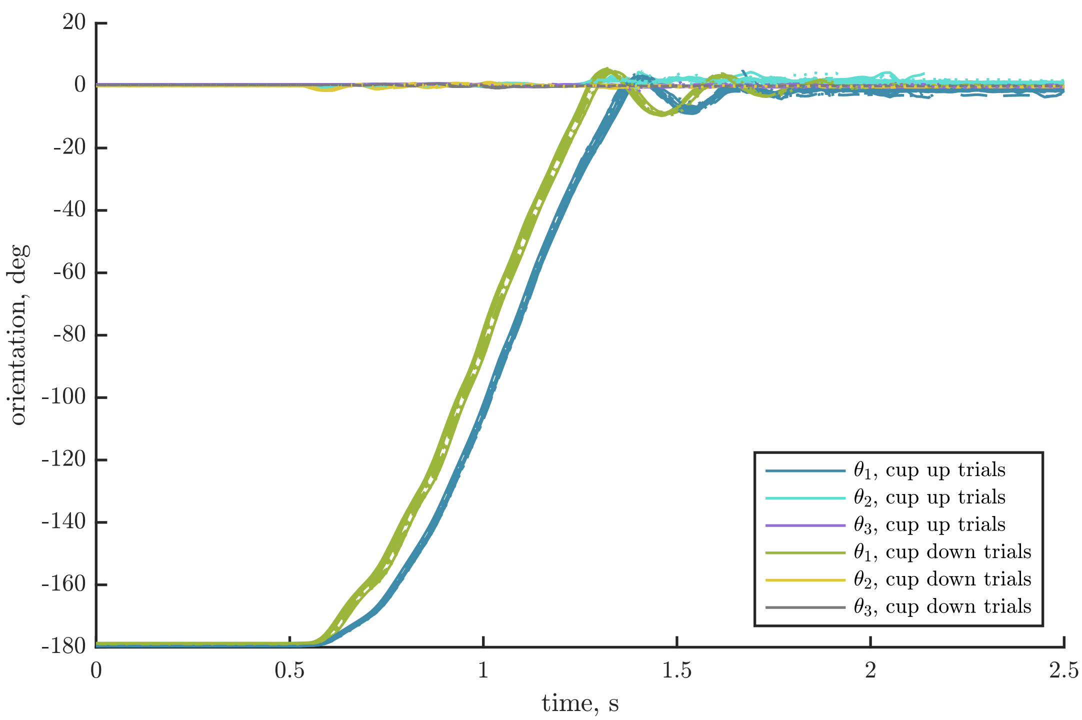

Figure 4.12: Measured relative orientation for hinge 2-1.

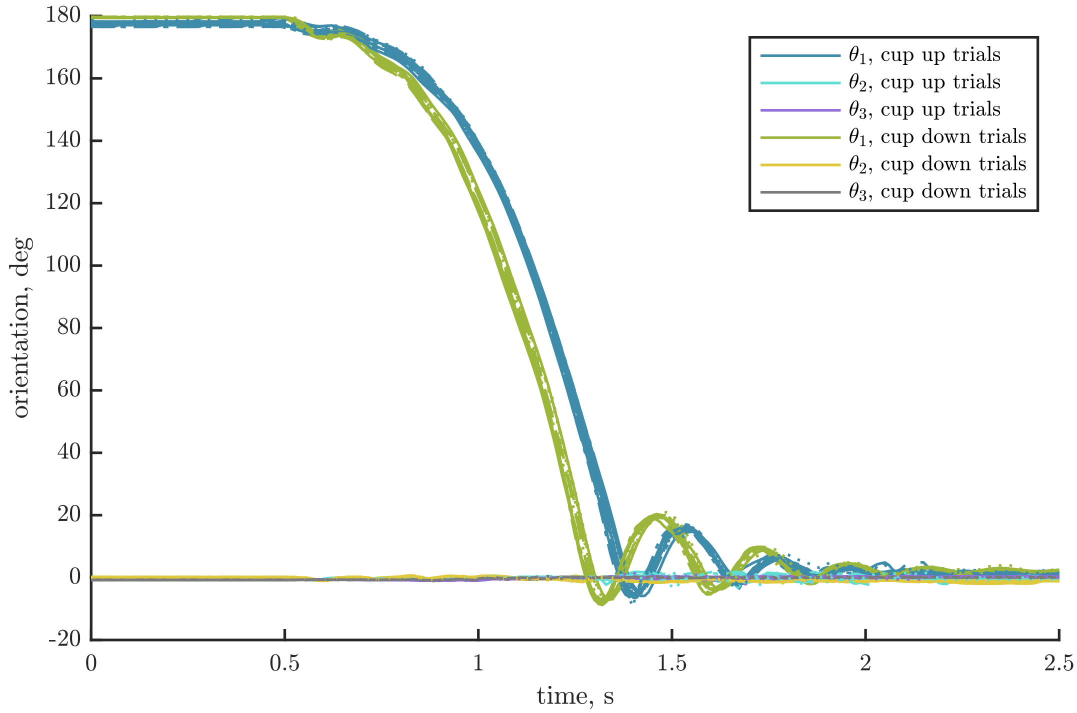

Figure 4.13: Measured relative orientation for hinge 3-2.

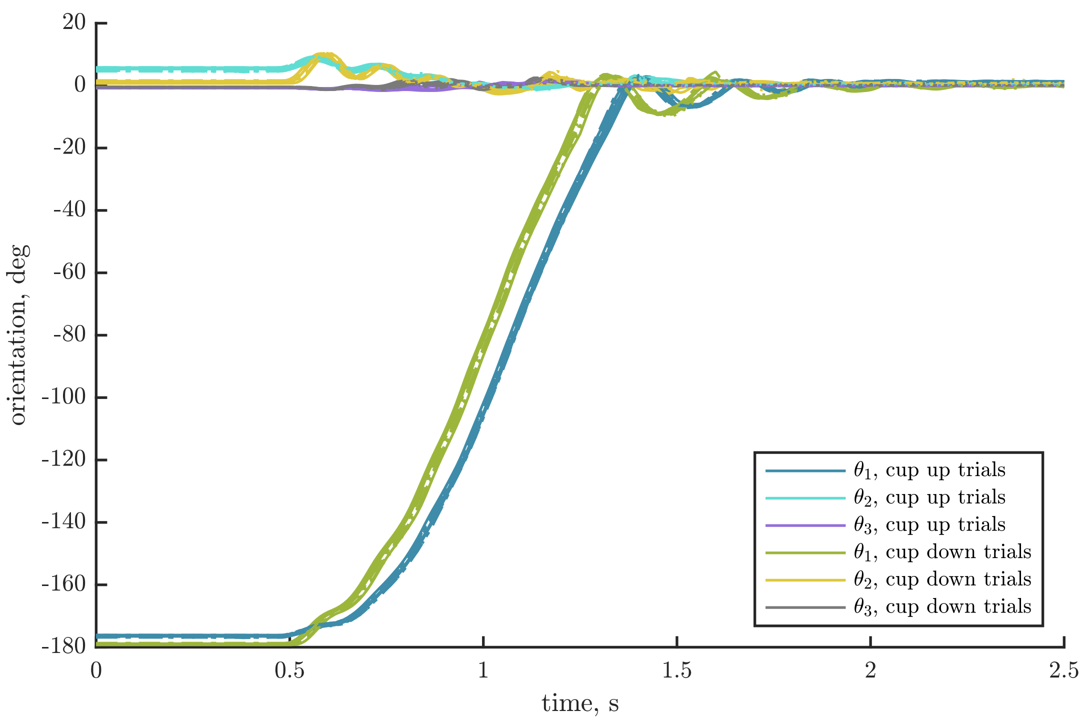

Figure 4.14: Measured relative orientation for hinge 4-3.

because the angle ambiguity of this Euler set, when $\theta_2 = 90\,\text{deg}$, will not be encountered in the response behavior. Each hinge is described by the two rigid bodies that it attaches, and in order of what the relative states are defined. For example, hinge 4-1 describes the relative states between bodies 4 and 1, expressed in the 4 frame, measured from 4 to 1. For hinges 4-1, 2-1, and 3-2, all degrees of freedom but the primary fold axis have been restricted. Therefore, only the first angle, θ_1, should have non-zero behavior, and this is what is observed in Figures 4.11, 4.12, and 4.13. The fold angles θ_1 for each hinge are shown to have a vibration response at full deployment, where the fold over shoots beyond the ideal deployed angle of $0\,\text{deg}$ and settles down over a few oscillations. This behavior is observed for both the cup up and cup down trials, although the cup up trials observe a smaller peak and dampens out a little faster than the cup down cases. This may be due to slight variation in the initial conditions or due to a slight influence of the gravity offloading system in one orientation versus the other. However, the response profiles are close enough to evaluate these effects as minimal. The time of each trial is standardized such that $\theta_1 = 160\,\text{deg}$ at the same time increment, allowing initial variation at the release time to be visible as well as peak deployment responses. The restricted states of θ_2 and θ_3 are shown to become more noisy as the deployment progresses, and this suggests a limited ability of the metrology system to accurately track fast moving objects as expected.

For the flexible hinge states, on hinge 4-3, the small orientation offset of θ_2 is observed in both the cup up and cup down cases. There is relatively large variation in this angle for the two trial cases, and this is a product of that angle's initial condition not being controlled by the clamp directly. The flexible tape spring hinges determine the initial condition of the configuration.

4.3.2 Relative Position Results for all Data Sets

The behavior responses of the relative positions across each hinge are shown in Figures 4.15, 4.16, 4.17, and 4.18. For hinges 4-1, 2-1, and 3-2, these relative positions, δ_1, δ_2, and δ_3 should remain at 0 mm for the duration of the trials. However, this is not what is observed from the data. While the initial condition of the relative positions are all within a 1 mm boundary, during and

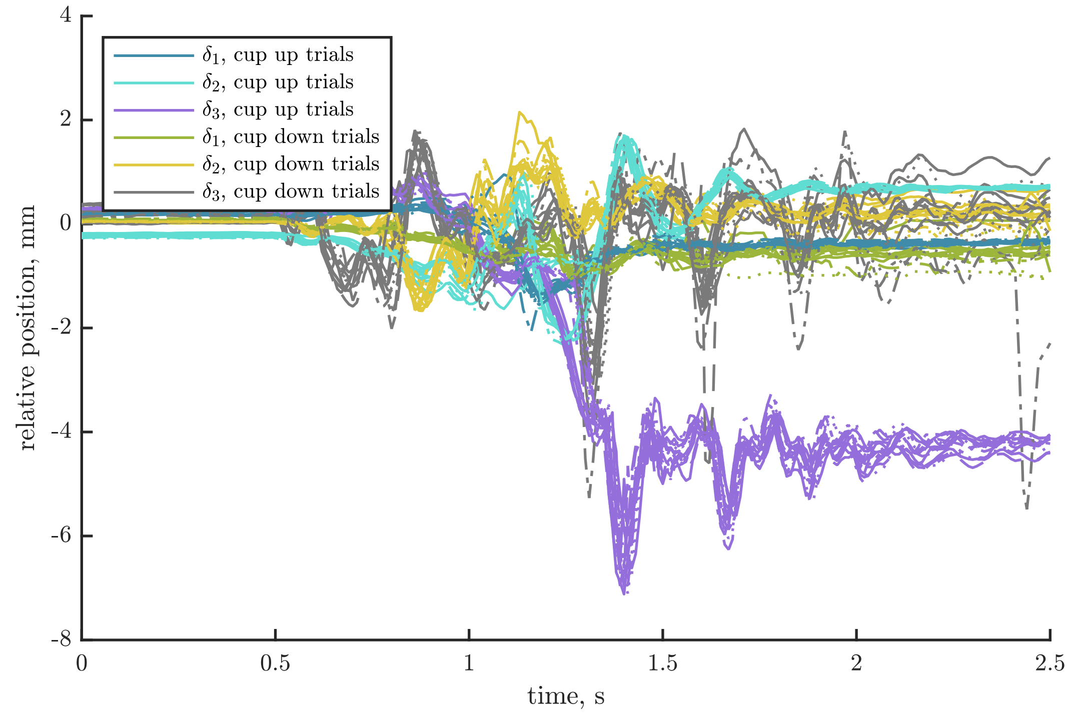

Figure 4.15: Measured relative position for hinge 4-1.

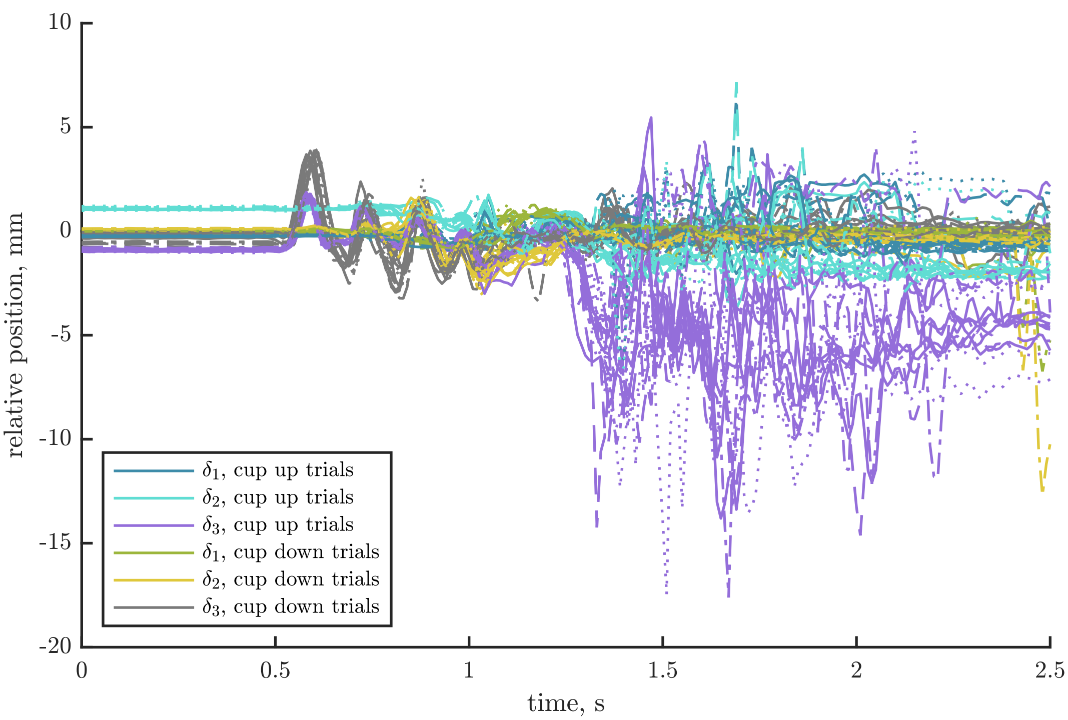

Figure 4.16: Measured relative position for hinge 2-1.

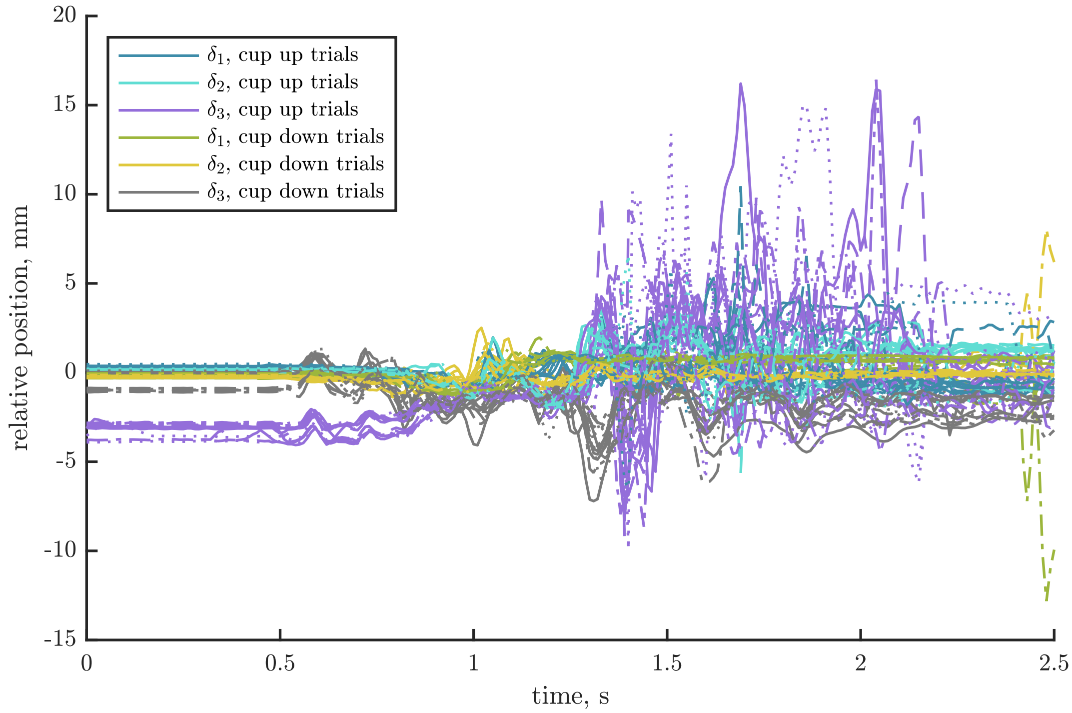

Figure 4.17: Measured relative position for hinge 3-2.

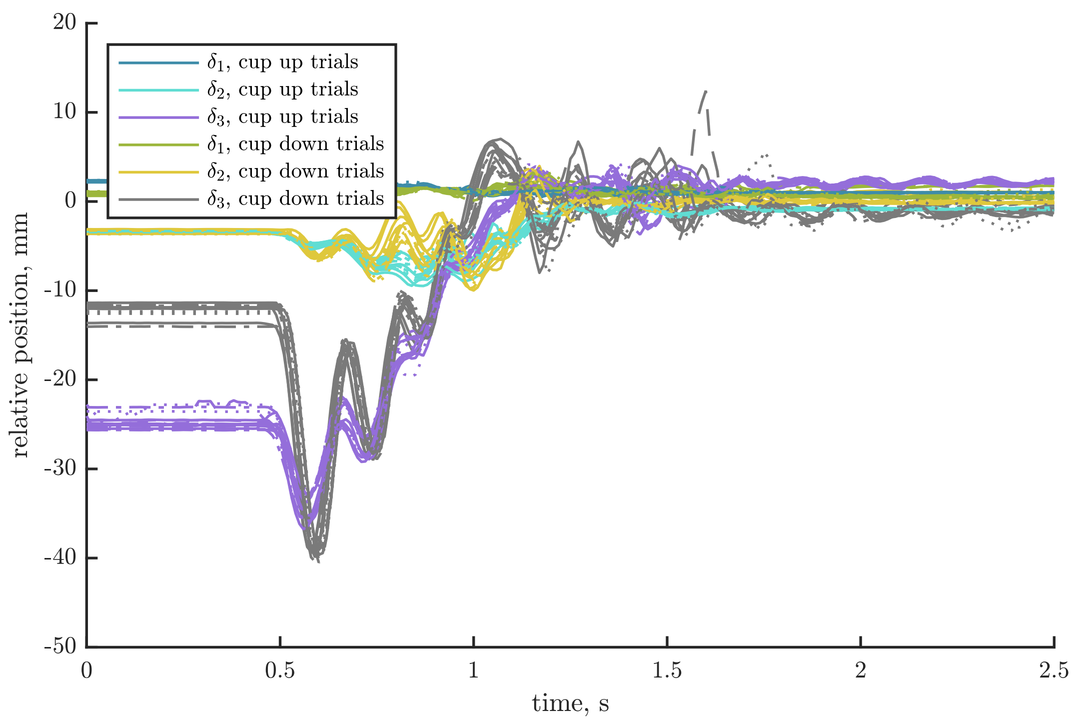

Figure 4.18: Measured relative position for hinge 4-3.

after deployment these relative positions become noisy and exhibit large variation. This can be indicative of a few things. First, that the rigid body assumption of the acrylic panels is a strong assumption, and variations of a few millimeters are possible. Second, it can indicate a compounding error due to the use of rotational transformations informed by the angular data to translate the panel information into relative hinge information. Finally, poor knowledge of the final assembled shape of the prototype may be influencing the results. The relative position between the tracking frames and the hinge frames may be off by a few millimeters due to construction.

Looking at the behavior of the flexible, multi-DOF tape spring hinge states, in Figure 4.18, the initial offsets due to the separation of the hinges are shown to be quite different for the cup up and cup down trials in the δ_3 states. This is again due to the unconstrained and flexible nature of the hinge when the structure is folded and constrained by the clamp mechanism. The deployment responses of both cases shown very similar magnitude in the oscillations and major deployment behaviors despite the difference in initial offsets. The δ_2 offsets are shown to be identical however and indicate this relative state is not strongly influenced by the initial condition of δ_3.

4.3.3 Measured Frame State versus CAD Geometry Error

The results of the previous sections indicate a more rigorous evaluation of the state error contributions is required if the relative position data is to be used. To address this, three inquiries into the measured geometry of the prototype are conducted, and are done for the cup up and cup down cases separately while only evaluating a single typical trial. The error is the difference in relative position of two panels frames, compared between what the perfect CAD deployed configuration is predicted to be, versus the measured result from the trials. The measured states are evaluated after a 13 second settling period post-deployment to measure if the deployed states achieve the theoretical geometry of the structure. The first evaluation shows the error norm of the relative positions between panel frames, denoted in Figures 4.19 and 4.22 by the panel frames in question. Figures 4.19 and 4.22 show a sub-millimeter accuracy in this metric for each rigid body pair except for panels 3 and 2, where the error hovers between $2.3 - 2.4$ mm for both the cup up and cup down orientations. This indicates a notable manufacturing error in either the target placement or the panel geometry that must be factored in to the relative position evaluations. To further understand the relative geometry error, the error is evaluated for each axis component and displayed in Figures 4.20 and 4.23. From these plots, the offsets in each x and y are revealed. An additional revelation from these Figures is a notable offset between panel z, or in the norm of the panel direction, for panels 1 and 4 in the cup down case. This indicates that the panels are not fully deployed to an ideal 0 deg orientation. To investigate this hypothesis, the error in deployed relative angle is shown in Figures 4.21 and 4.24. These plots do reveal a non-trivial rotation of $\theta_1 = 1.7$ deg for the relative fold on panels 1 and 4 that would account for a 10 mm additional offset in the z component.

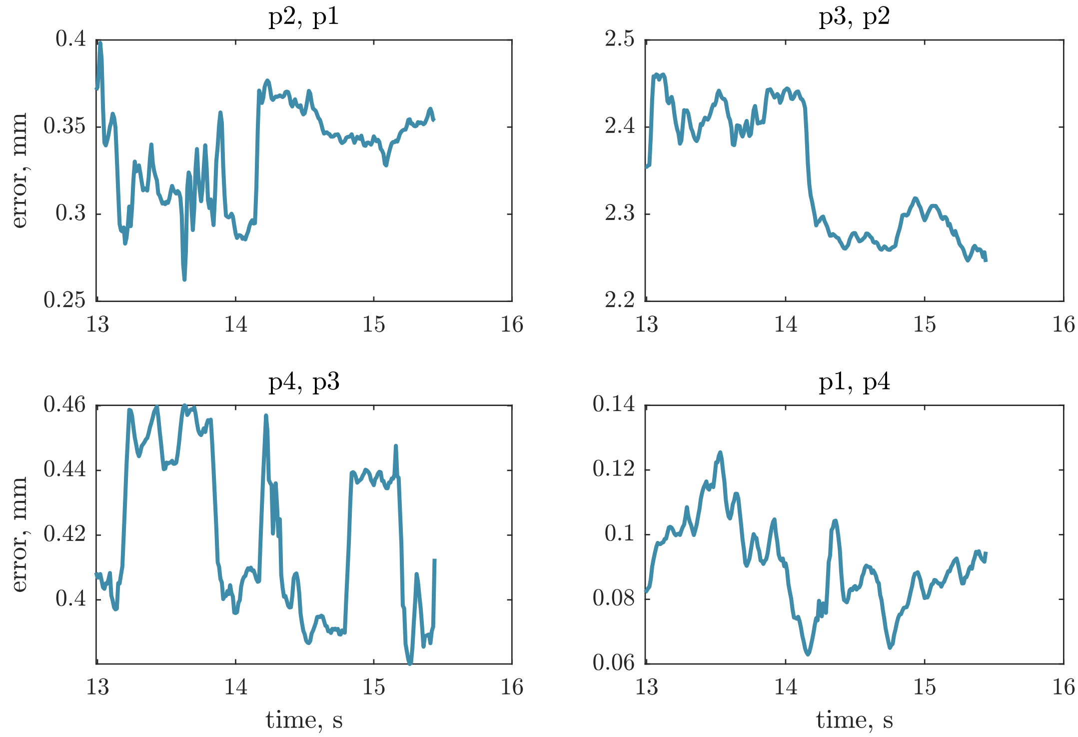

Figure 4.19: Norm of the error in a cup up trial.

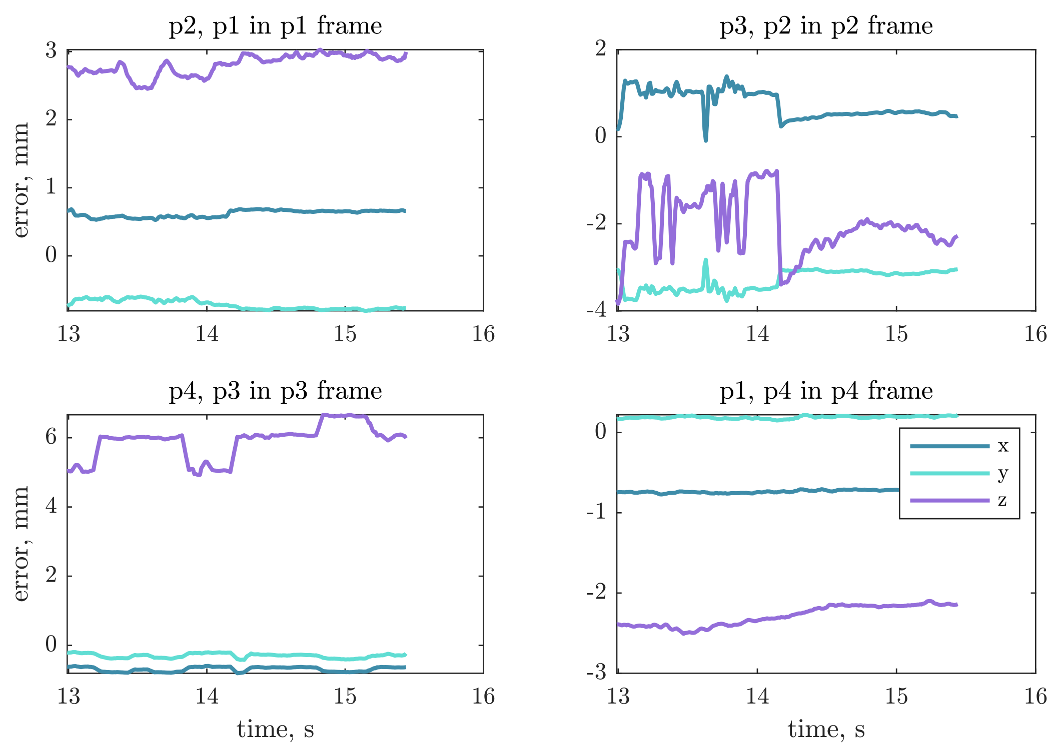

Figure 4.20: Positions error in a cup up trial.

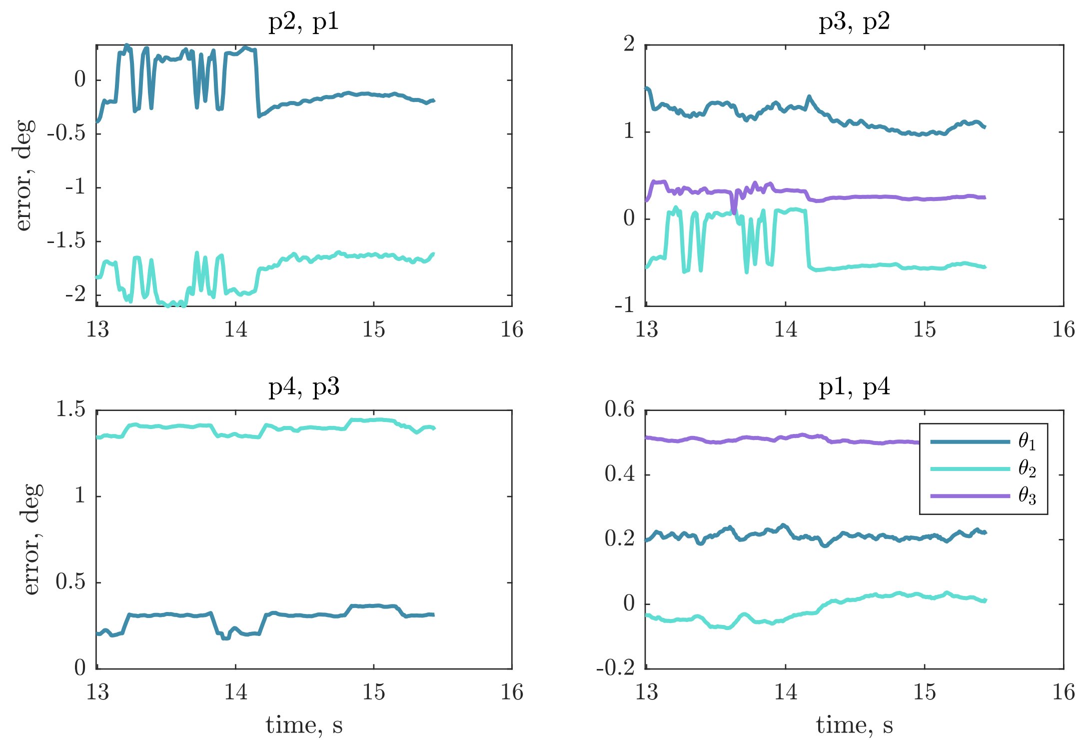

Figure 4.21: Orientations error in a cup up trial.

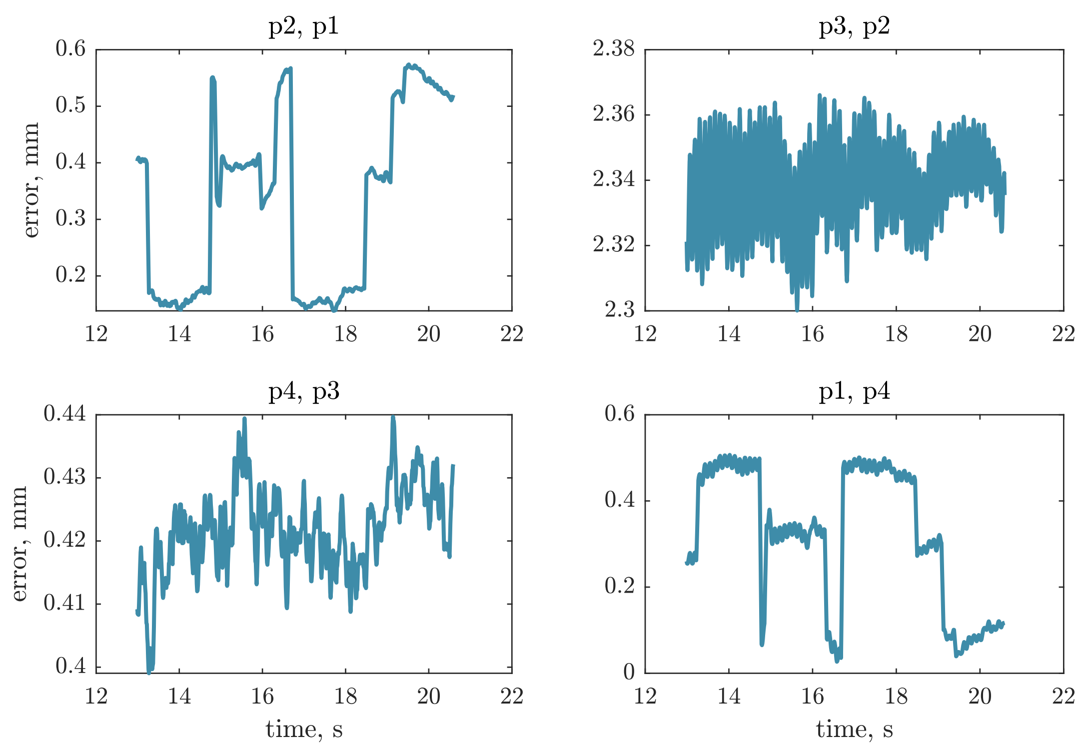

Figure 4.22: Norm of the error in a cup down trial.

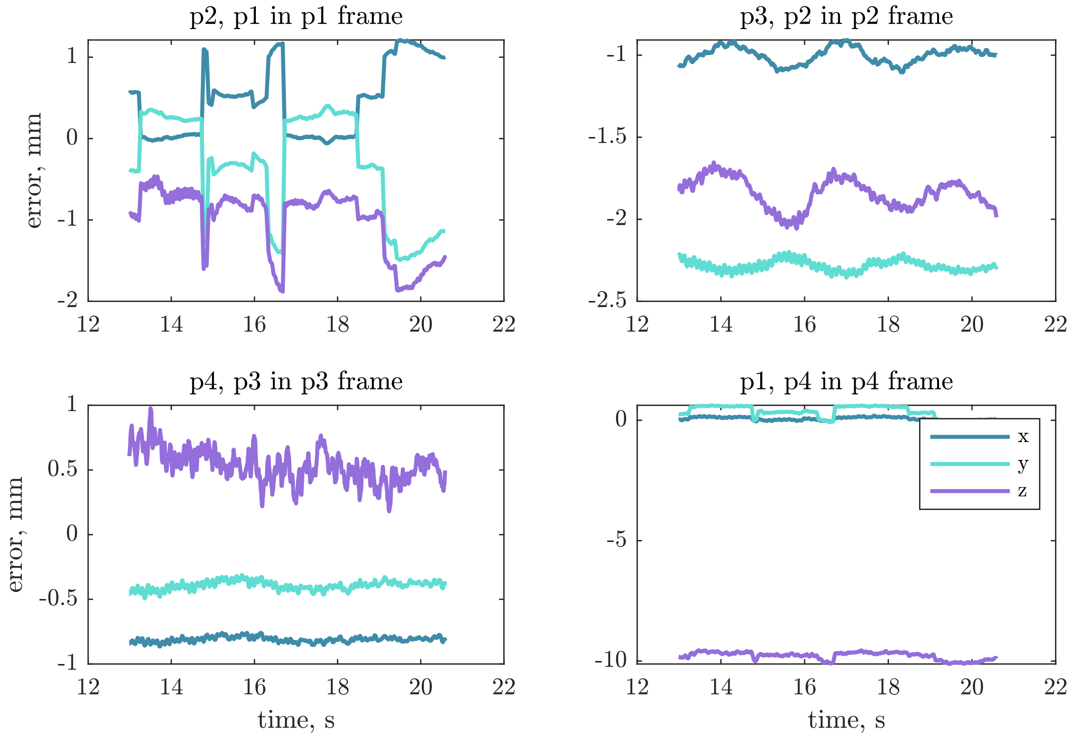

Figure 4.23: Positions error in a cup down trial.

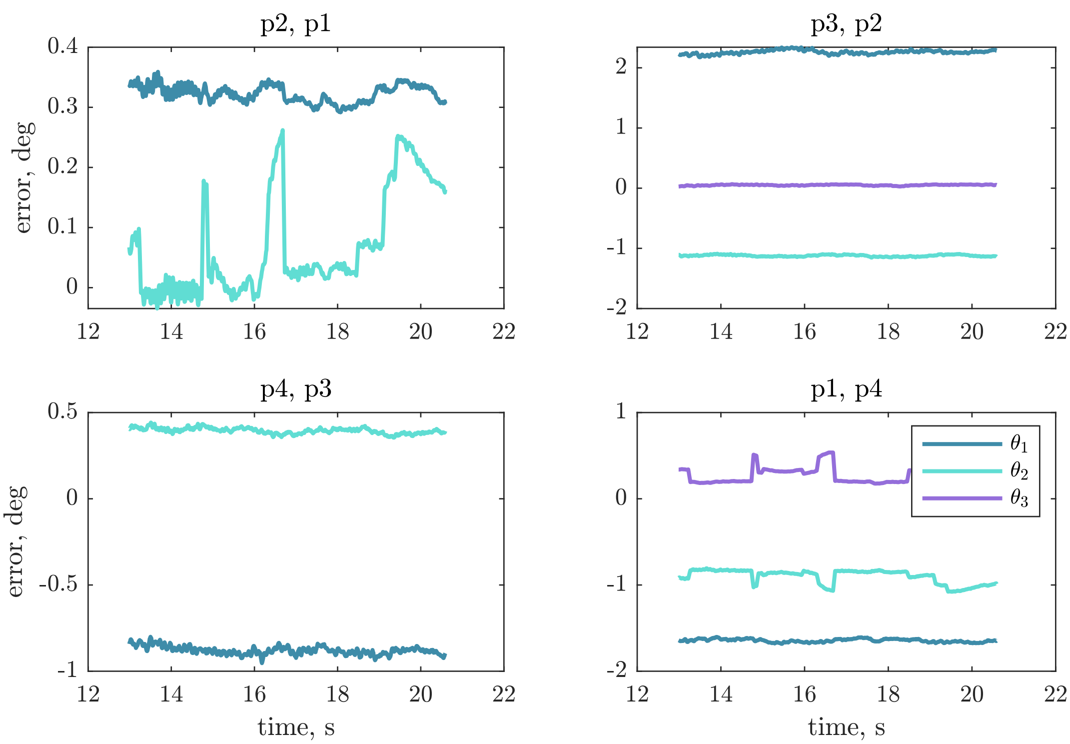

Figure 4.24: Orientations error in a cup down trial.

Chapter 5

Research Goal 4: Model Integration and Relative Validation

The two models developed in Chapters 2 and 3 are integrated to provide a complete deployable structure model based on the prototype developed in Chapter 4. The approach to developing the high strain tape spring hinge descriptions was designed for direct use in the multi-body dynamics algorithms, and the integration of these models is critical to completing the approach put forward in this thesis. First, a simulation of the prototype case is developed under the assumption that the elastic tape spring hinges are operating on a single degree of freedom. A single degree of freedom hinge model is developed by fitting torque response data for the symmetric fold case. Following this, the full six degree of freedom hinge case is built. From observation of the experimental deployment data and hinge model fits, two of the degrees of freedom are seen to have no off-nominal motion or observable contribution to the deployment, and therefore are removed from the hinge map matrix to simplify the model. The deployment prediction of the one degree of freedom hinge model is 0.70 seconds, where as the multi-DOF hinge case predicts a peak deployment time of 0.82 seconds and 0.92 seconds for the cup-down and cup-up initial conditions. The average experimental time to peak deployment is 0.83 seconds for the cup-down trials and 0.93 seconds for the cup-up trials, indicating good correlation.

5.1 Steel Tape Springs Hinge Model

For implementation in a proof of concept deployable structure, the significant challenges and uncertainties uncovered in the composite tape spring hinge study are undesirable. To eliminate this, spring steel tape springs are selected for the folded deployable structure study. The behavior of this material is well known and the simulation of the behavior in a finite element software is more reliable. Therefore, the following study implements lessons learned from the initial study to create a model of the hinge configuration of the desired prototype structure. Data is generated from a finite element model for this study and is considered sufficient due to the well established properties of the hinge materials and therefore a hinge experiment is not conducted for the spring steel tape springs. This section provides the details of the hinge data library generation, the nonlinear regression models, and a statistical evaluation of the model fits.

5.1.1 Prototype Tape Spring Actuated Hinge Design

The folded deployable structure prototype design is presented and reviewed in Chapter 4. For this study, only the fold line where tape spring hinges are embedded is of immediate interest. Two tape springs are embedded to provide stability, to reduce the degrees of freedom, and to provide sufficient torque for deployment. This configuration of this hinge design is displayed in Figure 5.1, as depicted in the Abaqus 6.14 user interface. The tape springs are identical and their relevant geometry and material properties are reported in Table 5.1.

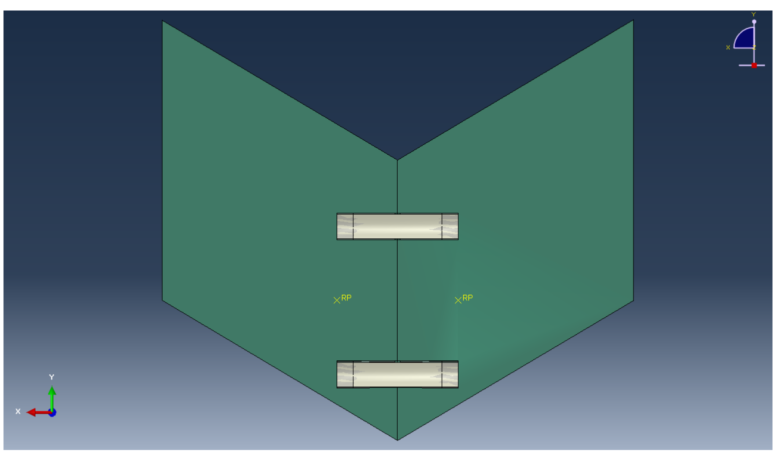

Figure 5.1: Implementation of two tape spring hinges on a single fold line of two panels.

Table 5.1: Hinge geometry for spring steel tape springs as measured and implemented in the FEA models.

material	**elastic modulus** (GPa)	**x-section radius** R, (mm)	**arc length** a, (mm)	**thickness** t, (mm)	**length** L, (mm)
spring steel	200	22.46	29.21	0.15	150

5.1.2 FEA Model Construction

The finite element analysis simulations are built in Abaqus 6.14. The hinge is represented as a shell with elastic behavior defined by the elastic modulus and a Poisson's ratio of 0.3. The hinge mounting plates and panel assembly is represented as a discrete rigid part, and the tape springs are constrained to them using tie constraints. Four node shell (S4R) elements are meshed on the hinge shell using a 2 mm mesh, as this is the largest mesh size that results in successful folding of the prototype due to the large deformation of the fold radius on the tape springs, where element deformations above 20 degrees is not desirable. The asymmetric configurations are implements as displacement and rotation boundary conditions in static/general steps. Each range of asymmetric configurations is explored as a separate step enforced on an initially symmetric configuration. An asymmetric data set is generated for each primary fold angle, θ_1, at increments of 5 degrees from $100 - 180$ degrees of fold, resulting in 9 equal sense data sets. Asymmetries on smaller fold angles are excluded due to Abaqus convergence issues. Figure 5.2 shows example profiles for the equal sense and opposite sense cases and with non-symmetric deviations, with a no added deformation scaling. The same approach for designing the displacement and rotation boundary conditions such that the simulations converge without error that was implemented in Section 3.4.3 is implemented here.

5.1.2.1 Asymmetric Definitions

The configuration of the hinge within the prototype design informs the definition of the asymmetric configurations. From inspection, three degrees of freedom from the six state hinge model defined in Section 3.2 can excluded for this study. This is due to the fact that the prototype has single degree of freedom hinges on the other fold lines, constraining linear motion in the x and y axes and rotations about the y axis. Therefore, the configuration constraints in the model simulation contain three asymmetric configurations beyond the nominal fold. These are defined in Table 5.2, where the first asymmetry is on the primary degree of freedom, and the second asymmetry captures the remaining observed degrees of freedom on the fold line. Considering the opposite sense behavior of this hinge, all potential asymmetries are eliminated due to the constraining design of the panels when folded in this direction. Therefore, only the nominal fold data in the opposite sense is needed from the simulation.

Table 5.2: Asymmetric boundary conditions used to generate Abaqus (A) data sets in both equal (E) and opposite (O) folds of the prototype structure hinge, defined in an inertially fixed frame.

Case	θ_1 sym (deg)	θ_1 offset (deg)	θ_2 (deg)	θ_3 (deg)	δ_1 (mm)	δ_2 (mm)	δ_3 (mm)
AE0	$0-180$	0	0	0	0	0	free
AE1	$100-180$	± 10	0	0	0	0	free
AE2	$100-180$	0	5	0	free	free	free
AO0	$0-30$	0	0	0	0	0	free

5.1.2.2 Importance of Directional Fold Modeling

A notable feature of tape spring hinges is that they can display different moment-curvature behaviors depending on the direction that the fold is taking place in. This is not referring to how the fold may be in the equal or opposite direction in terms of the cross-section's configuration, as discussed in Section 1.2.2 and displayed in Figure 3.1. Instead, this refers to if the trajectory of the fold is going into the closed or open configuration, and can be applied to either an equal or opposite sense fold. The moment-curvature changes due to hysteresis effects and should be included in a robust hinge model. To do this, an additional piecewise function layer would be added, where the velocity direction of the hinge would be checked to determine which hinge model to implement at that state. For the prototype hinge, the moment curvature data for both the folding and unfolding trajectories of the equal sense fold is displayed in Figure 5.3. The asymptotic peak, at $\theta = 2.64$ degrees, is shown to be much lower in the unfolding direction, but the behavior is otherwise identical.

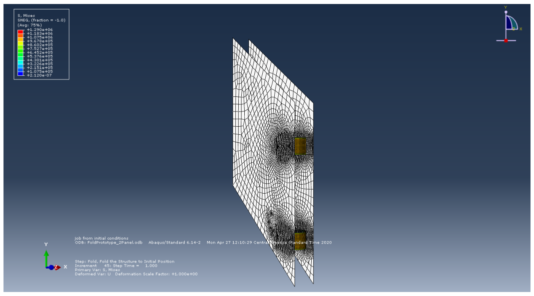

(a) AE0

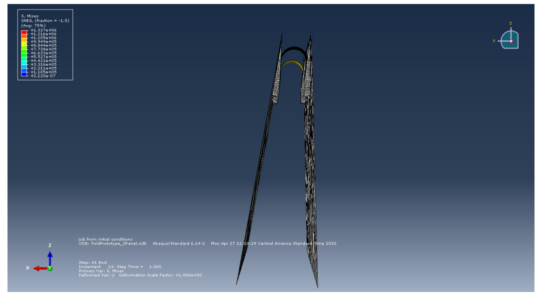

(b) AE1

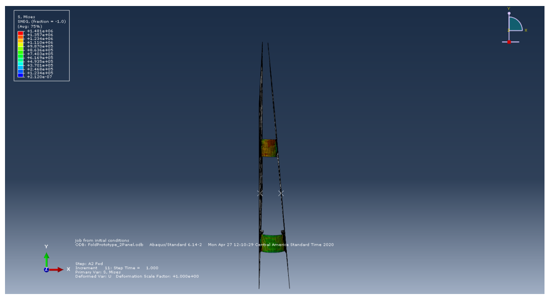

(c) AE2

Figure 5.2: Examples of displacements implemented in Abaqus where the symmetric angle is ±90 deg.

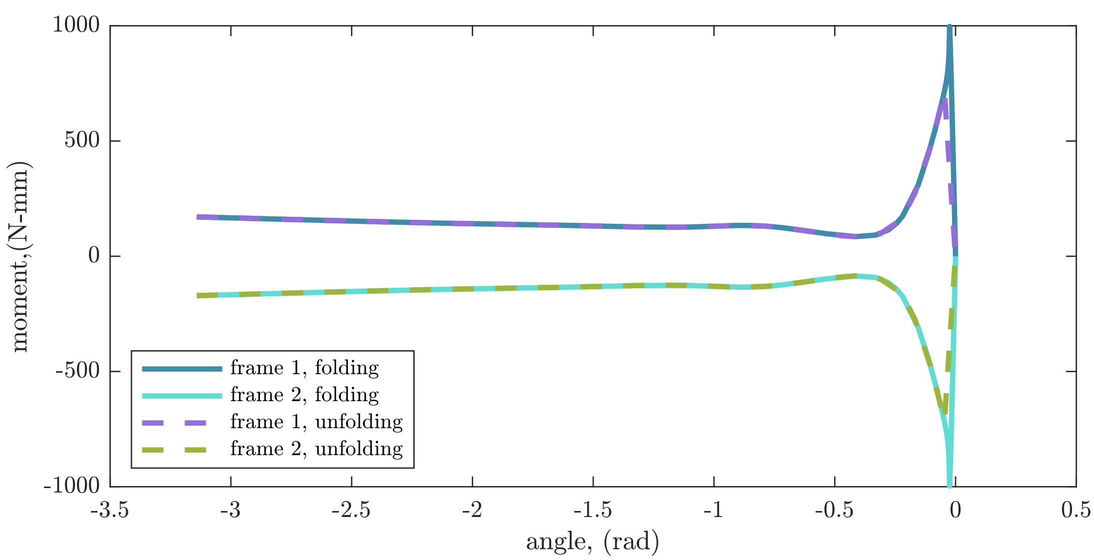

Figure 5.3: Moment curvature data for the prototype hinge, as predicted for the folding direction and unfolding direction.

Due to computational and numerical issues that are observed around the asymptotic peak, only the unfolding direction is applied in the model implemented here. However, if higher fidelity is required and the numerical issues are addressed, it is recommended that a directionally sensitive model be used.

5.1.3 Nonlinear Regression Models

The hinge profile data is fit to polynomial expressions using the nonlinear regression techniques from Section 3.3. Two models are created for use in the prototype deployment model. The first model is for the nominal fold torque and is only a function of the nominal fold angle. This provides an idealized model for initial evaluation of the deployment characteristics. The second model considers the full spatial force and torque profile from the asymmetric profiles of the prototype hinge. For both models, a piecewise function is designed for the primary moment such that the equal sense and opposite sense behavior is modeled independently. This provides a much more accurate behavior model, where the opposite sense fold behavior is significantly different due to the presence of the rigid body panels and restricted freedoms due to contact with the panels.

5.1.3.1 Nominal Fold Moment

For the nominal fold moment behavior, the best fit regression model is determined to be a piecewise nonlinear function of the form

$$M_{0_1} = \begin{cases} \sum_{i=2}^{6} a_i \theta_1^i + \sum_{i=1}^{4} b_i \frac{1}{(\theta_1+\epsilon)^i} & \theta_1 > 0 \\ c_1\theta_1 + c_2\theta_1^2 & \theta_1 < 0 \end{cases} \tag{5.1}$$

Where the inclusion of the inverse polynomial terms in Equation 5.1 greatly increases the fitting performance for the theoretical peak moment due to snap through of a tape spring hinge, as seen in Figure 5.4. In this expression, θ_1 is the nominal fold angle on the primary hinge axis, $\epsilon, = 0.001$ is a small numerical buffer to prevent numerical issues at 0, and a_i, b_i, and c_i are the coefficients to be determined through regression techniques. The resulting coefficients are reported in Table

5.3, and the fit function is plotted over the source data in Figure 5.4. Additionally, the statistic evaluation of these regressions are reported in Table 5.4 and the histograms and normal probability are shown in Figure 5.5. The non-linear regression model for the nominal fold data is seen to be a strong fit in both the equal and opposite sense cases. The model histograms show a near Gaussian distribution with no outliers and the normal probability is approximately linear as expected. This model therefore provides a sufficient representation of the hinge behavior when restricted to a single degree of freedom deployment demonstration.

Table 5.3: Equal and opposite sense nominal fold non-linear regression coefficients. Coefficients have units of N-mm in this table.

a_2	a_3	a_4	a_5	a_6	b_1	b_2	b_3	b_4	c_1	c_2
2.24e2	1.43e2	0	-18.54	-3.43	-21.26	4.08	0.16	-1.62e-4	-3.10e5	1.02e5

Table 5.4: Nonlinear regression fit statistics for the nominal fold of the prototype hinge.

statistic	equal sense	opposite sense
R-Squared	0.99	1
RMSE (N-mm)	11.3	814

5.1.3.2 Six DOF Models of Forces and Torques

The proposed polynomial from Section 3.2, Equation 3.5, is also implemented for the secondary forces and torques of the steel tape springs prototype hinge model using the asymmetric data library. As seen in Table 5.5, the coefficient sets are not reduced for this model, where the RSME is observed to grow for each removal of a coefficient despite no change in the R-squared assessment. The primary moment, M_{0_1}, is found to be sufficiently modeled with just the expression of Equation 5.1 using the steel spring hinge data library as well, and the coefficients for this case are recorded in Table 5.6. The opposite sense behavior of the hinge is modeled with the same data of the one-DOF model in Section 5.1.3.1. The RSME and R-squared values for each fit is shown in Table 5.7, and the fits are for all but the second axis force are all in high percentile with relatively small RSME compared to the force and torque magnitudes. The histograms in Figure 5.6 reflect

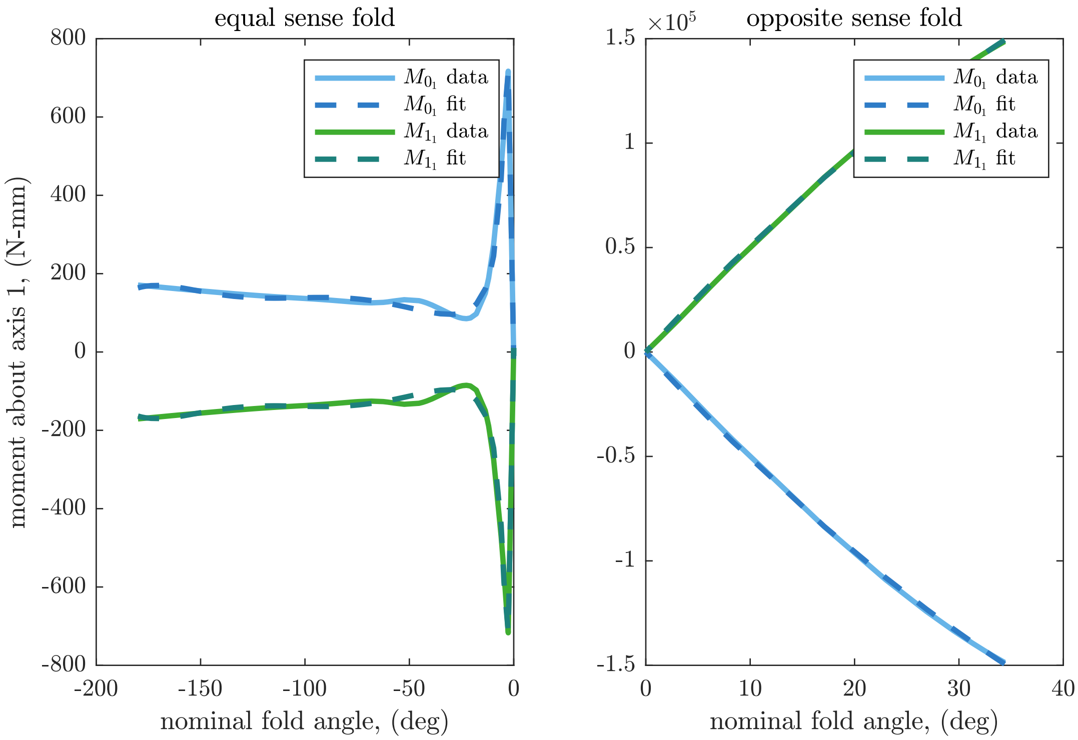

Figure 5.4: Nonlinear regression fit curves for the nominal fold hinge data.

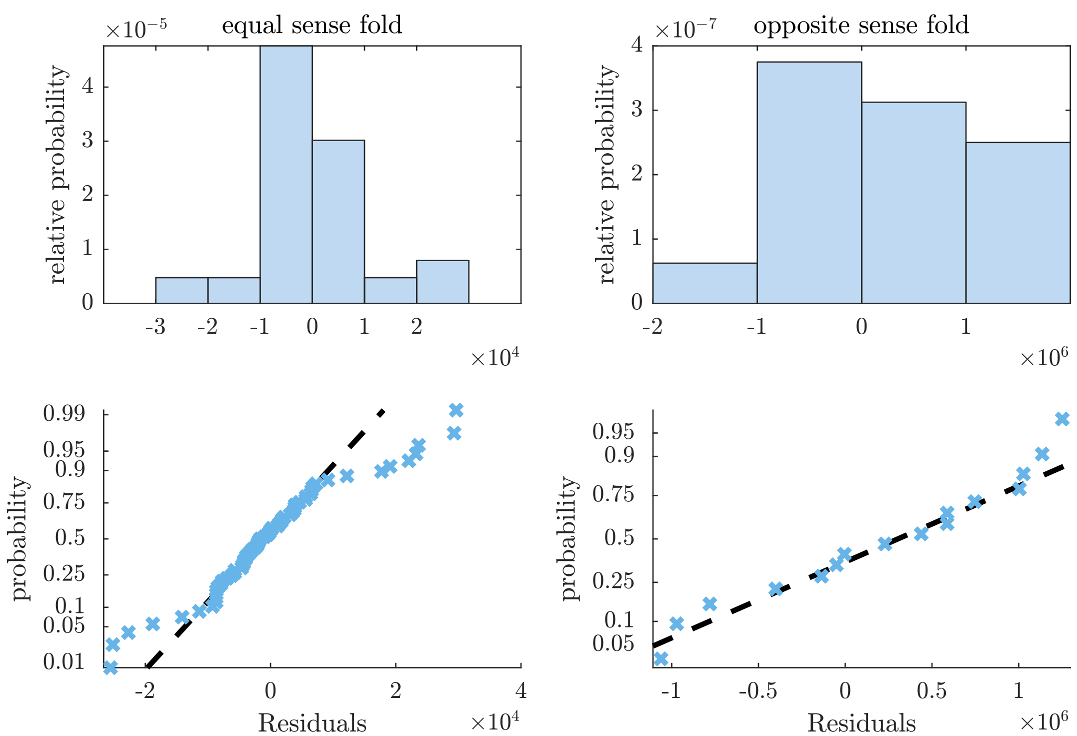

Figure 5.5: Fit function histogram and normal probability for the nominal fold simulation data.

this, where the fits follow a normal distribution with few outliers. These force and torque models are therefore sufficient for use in the demonstration of a multi-DOF hinge actuated deployment.

5.2 Prototype Model Properties

The mass, inertia, and geometry properties of the prototype structure are estimated from the CAD model, as presented in Chapter 4. Each body's properties are recorded in that body's hinge located reference frame, as defined in Figure 4.10. Table 5.8 records the mass and inertia, and it's noted that each panel contains unique non-symmetric inertia properties. Table 5.9 presents the relevant geometry of the panels and enforces the Miura-ori pattern. Table 5.10 contains the geometry properties of the constraint nodes, which are the node frames of Panels 1 and 2 from Figure 4.10. The closed-chain dynamics topography and implementation of the model is a direct adaptation of the model in Section 2.5.3, where here, body r is panel 4, body m is panel 1, body l is panel 2, and body j is panel 3. This notation is changed for consistency with the prototype testing notation. Relative hinge states are referenced in order of their definition, i.e., hinge 4-3 measures from panel 4 to panel 3 and is expressed in the hinge 4 frame, also for continuity with Chapter 4.

5.3 Results: Deployment Dynamics Prediction

Two deployment simulations are presented with the current model, absent of contact or damping effects. The first simulation implements the 1-DOF hinge model in an idealized 1-DOF fold. The second simulation implements a 4-DOF hinge definition with a multi-DOF hinge force and torque model. The idealized 1-DOF simulation shows a smooth deployment behavior with a predicted time to peak deployment at 0.70 seconds. The multi-DOF model, on the other hand, shows behaviors curve that more closely tracks the experimental models, exhibits small oscillations, and a peak deployment at 0.76 seconds. Both models exhibit unstable constraint violations at peak deployment that can be attributed to the asymptotic behavior of the hinge model around this state.

Table 5.5: Reduced coefficients for the prototype hinge assembly FEA model.

coefficient	M_{0_2}	M_{0_3}	N_{0_1}	N_{0_2}	N_{0_3}
a_1	105.29e-3	-69.86	-129.75e-3	-768.48e-3	723.68e-3
a_2	-318.17e3	-123.21e3	207.75	-94.46	173.97
a_3	-18.99e3	-207.82e3	-890.34	288.94	-528.02
a_4	22.12e3	15.40e3	60.89	-4.33	3.10
a_5	7.75	14.29	-7.19e-3	151.34e-3	-164.95e-3
a_6	-17.48	-32.86	-23.56e-3	-334.97e-3	333.49e-3
$b_{1,1}$	91.77	34.04	-109.58e-3	343.78e-3	-599.31e-3
$b_{2,2}$	-4.20e6	-3.60e6	-2.08e3	1.25e3	-1.97e3
$b_{3,3}$	-1.83e6	-1.71e6	-481.68	557.51	-1.07e3
$b_{4,4}$	-15.33e3	-13.44e3	-5.83	3.59	-5.80
$b_{5,5}$	216.17e-3	-11.03e-3	178.22e-6	656.73e-6	4.58e-3
$b_{6,6}$	208.16e-3	-104.07e-3	61.87e-6	1.41e-3	2.54e-3
$b_{1,2}$	-198.66e3	-105.69e3	-292.91	61.40	-89.76
$b_{1,3}$	6.30e3	-95.52e3	-397.31	133.37	-248.77
$b_{1,4}$	10.26e3	5.02e3	27.98	-2.49	500.11e-3
$b_{1,5}$	-7.34	418.17e-3	547.87e-6	-5.14e-3	-49.82e-3
$b_{1,6}$	-707.44e-3	-15.65	-18.69e-3	-143.05e-3	85.93e-3
$b_{2,3}$	5.46e6	4.99e6	2.03e3	-1.31e3	2.34e3
$b_{2,4}$	497.43e3	431.36e3	220.90	-127.77	200.22
$b_{2,5}$	6.37e3	2.49e3	9.77	-3.78	5.16
$b_{2,6}$	12.70e3	14.99e3	18.64	-3.34	7.30
$b_{3,4}$	-342.40e3	-314.80e3	-106.69	85.12	-157.63
$b_{3,5}$	-2.15e3	-288.38	-7.46	-480.06e-3	1.35
$b_{3,6}$	-2.42e3	-2.48e3	1.55	-1.22	1.84
$b_{4,5}$	-251.78	-13.29	-601.34e-3	65.04e-3	80.53e-3
$b_{4,6}$	-644.11	-698.39	-384.07e-3	89.92e-3	-219.37e-3
$b_{5,6}$	-334.05e-3	395.28e-3	812.43e-6	2.64e-3	-1.33e-3

Table 5.6: Equal sense primary fold model non-linear regression coefficients with asymmetric configuration data. Coefficients have units of N-mm in this table.

a_2	a_3	a_4	a_5	a_6	b_1	b_2	b_3	b_4
194.77	120.18	0	-14.78	-2.66	-23.93	3.70	0.15	-1.50e-4

Table 5.7: Statistics for the fit functions of the prototype hinge assembly model.

statistic	M_{0_1}	M_{0_2}	M_{0_3}	N_{0_1}	N_{0_2}	N_{0_3}
Hinge Asm R-Squared	0.96	1	1	0.99	0.87	0.93
Hinge Asm RMSE	14.3	5.6	4.5	0.005	0.01	0.02

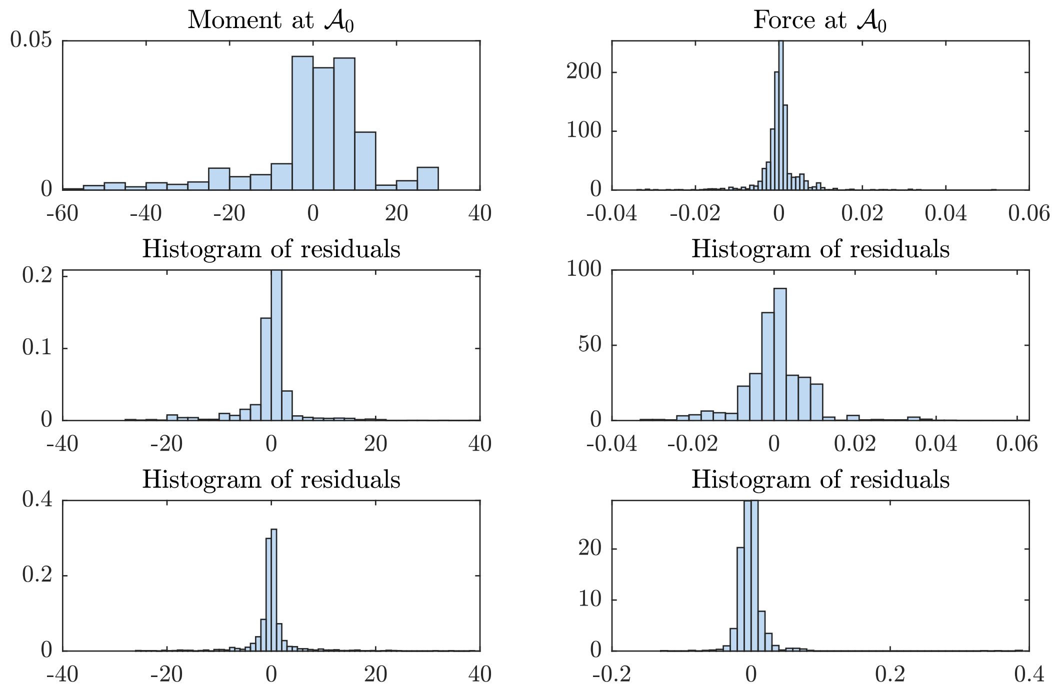

Figure 5.6: Fit function histograms for the asymmetric hinge fold simulation data.

Table 5.8: Mass properties of the rigid root body and panel bodies of the prototype structure, expressed in respective body frames.

body	**1**	**2**
m (kg)	0.3748	0.3748
J_c (kg mm^2)	$\begin{bmatrix} 2642.62 & -1546.55 & 3.66 \\ -1546.55 & 4408.84 & -2.60 \\ 3.66 & -2.60 & 7050.26 \end{bmatrix}$	$\begin{bmatrix} 2644.47 & 1547.90 & -3.66 \\ 1547.90 & 4409.29 & -2.72 \\ -3.66 & -2.72 & 7052.56 \end{bmatrix}$
body	**3**	**4**
m (kg)	0.3735	0.3735
J_c (kg mm^2)	$\begin{bmatrix} 2103.52 & -1242.75 & 3.20 \\ -1242.75 & 3577.07 & -0.55 \\ 3.20 & -0.55 & 5679.61 \end{bmatrix}$	$\begin{bmatrix} 2637.78 & -1544.42 & -1.75 \\ -1544.42 & 4358.84 & 2.34 \\ -1.75 & 2.34 & 6995.27 \end{bmatrix}$

Table 5.9: Geometry properties of the rigid bodies of the prototype folded structure, expressed in respective body frames.

body	$\theta(c, k-1^+)$ (deg)	$\boldsymbol{p}(c, k-1^+)$ (mm)	$\boldsymbol{p}(k, c)$ (mm)
4_1	$[0, 0, 0]$	$[-88.49, 147.69, 0]$	$[0, 0, 0]$
4_2	$[0, 0, 120]$	$[166.13, 0.68, 0]$	$[0, 0, 0]$
1	$[0, 0, 0]$	$[0, 0, 0]$	$[-84.91, 147.193, 0]$
2	$[0, 0, 0]$	$[0, 0, 0]$	$[86.81, 147.96, 0]$
3	$[0, 0, -60]$	$[170.75, -2.03, 0]$	$[81.78, -144.98, 0]$

Table 5.10: Geometry properties of the constraint nodes expressed in respective body frames.

i	$\theta(k, \mathcal{N}_{k_i})$ (deg)	$\boldsymbol{p}(k, \mathcal{N}_{k_i})$ (mm)
1	$[0, 0, 120]$	$[85.972, 147.637, 0]$
2	$[0, 0, 60]$	$[-82.67, 148.27, 0]$

Table 5.11: Initial conditions of the numerical simulation.

body	q	$\dot{\beta}$
4	$[0, 0, 0, 0, 0, 0]$	$[0, 0, 0, 0, 0, 0]$
1	180	0
2	180	0
3	-180	0

5.3.1 1-DOF Hinge Deployment Model

The initial conditions for the simulation are provided in Table 5.11 and are selected for the idealized, flat folded relative angles. The hinge between panels 4 and 3 is restricted to a single degree of freedom rotation about the first axis. The simulation is shown in Figure 5.7 to predict a smooth deployment behavior with peak deployment occurring at 0.7 seconds. After the structure reaches a fully deployed configuration however, the structure enters a difference folding mode, where only the folds at hinge 2-1 and 4-3 are changing, and folds 3-2 and 4-1 remain open. This can be interpreted as the structure folding in half, and is not observed during the testing. This discrepancy is attributed to the presence of unmodeled contact in the prototype. In Figure 5.8, the states of the root body with respect to inertial space show there is a significant general tumble introduced to the system in response to the deployment. The effect of the deployment to the system states in an actual implementation of this structure would rely heavily on energy damping and contact within the structure as well as energy management techniques within the spacecraft. Figure 5.9 reveals a significant constraint violation at the peak deployment and indicates that better constraint management techniques are needed for accurate prediction of deployment behavior as the system crosses this state. Constraint management such as the Baumgarte Stabilization used here balances tuning the correction gains and the integration time step. This is in direct opposition to the asymptotic nature of the hinge behavior close to the deployed configuration, $\theta_1 = 0$, where smaller time steps will generate more data points along the asymptotic legs of the curve, producing a more erratic, and therefore unstable, behavior that is difficult to correct with a simple linear gain. Therefore, future work should focus heavily on stabilizing constraints under these forcing conditions. Additionally, future work should focus on determining the true moment peak of the hinge behavior, where the theoretical peak may be much greater than what is observed, and reducing this asymptotic peak from the hinge model would greatly improve model stability.

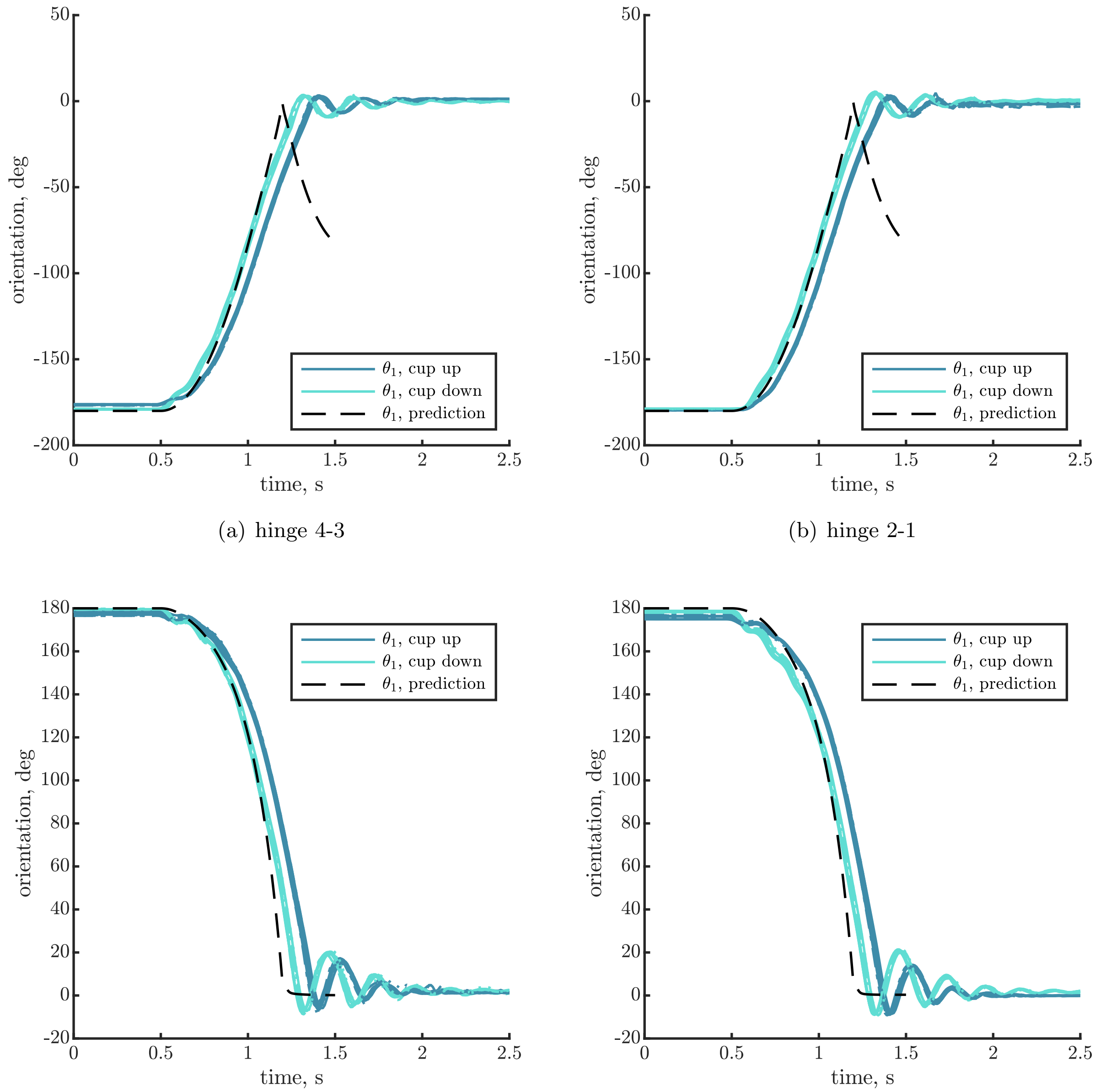

(a) hinge 4-3 (b) hinge 2-1

(c) hinge 3-2 (d) hinge 4-1

Figure 5.7: Deployment actuation predictions of a 1-DOF hinge simulation and the experimental behavior from cup up and cup down trials.

Table 5.12: Initial conditions of the cup up and cup down numerical simulations. All initial rates are set to zero.

body	q cup up	q cup down
4	$[0, 0, 0, 0, 0, 0]$	$[0, 0, 0, 0, 0, 0]$
1	176.1 deg	179.6 deg
2	177.5 deg	178.5 deg
3	$[-176.4\,\text{deg}, 5.4\,\text{deg}, -3.5\text{ mm}, -24.6\text{ mm}]$	$[-179.0\,\text{deg}, 1.0\,\text{deg}, -3.3\text{ mm}, -12.1\text{ mm}]$

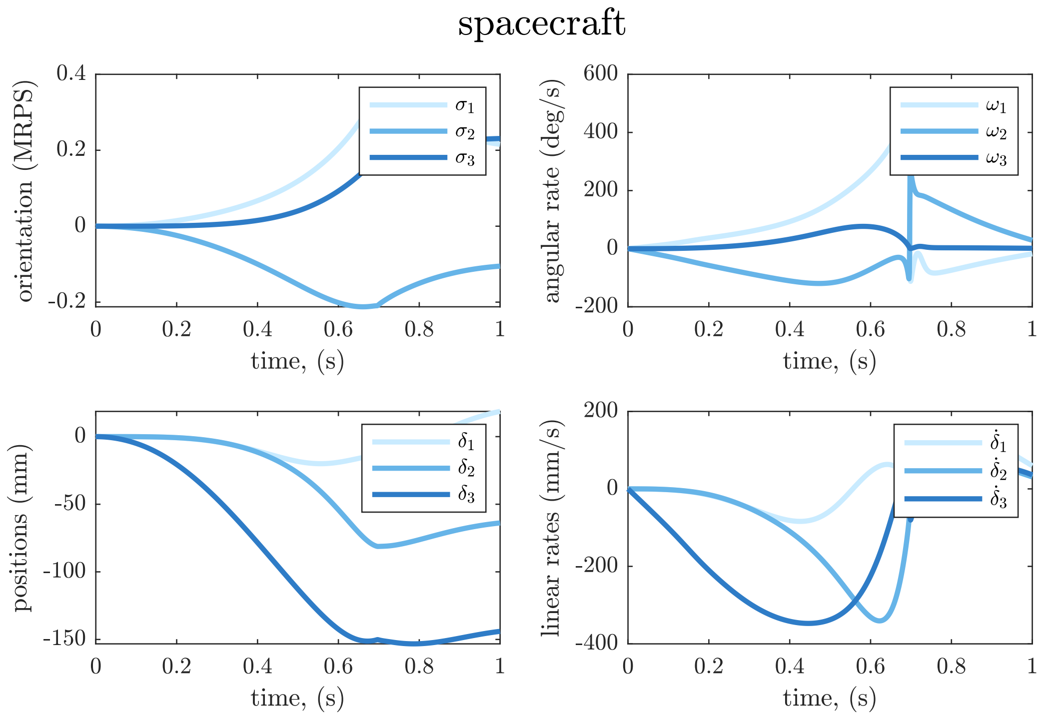

Figure 5.8: Angular orientation and rates of the spacecraft body in three dimensional space.

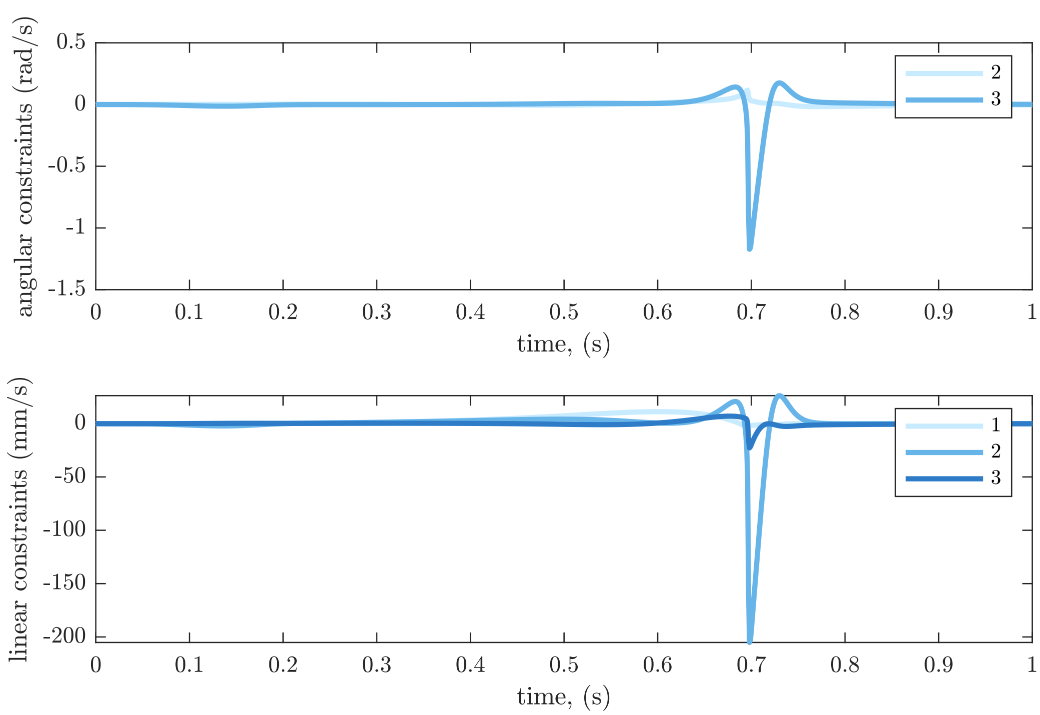

Figure 5.9: Constraint violations during the 1DOF prototype numerical simulation peak as the simulation enters the asymptotic range of the hinge behavior.

5.3.2 4-DOF Hinge Deployment Model

The initial conditions of the two numerical simulations for the 4-DOF case, shown in Table 5.12, are set to emulate the non-ideal, actual conditions of the average deployment from the cup up and cup down trials. The non-ideal initial conditions were not implemented in Section 5.3.1 because these initial conditions do not satisfy the constraint conditions of a 1-DOF hinged structure, and therefore were not stable. From the design of the prototype, the tape spring hinge fold line between panels 4 and 3, hinge 4-3, is constrained due to the configuration of the other three hinges and therefore two of the degrees of freedom can be removed, such that the generalized coordinates are

$$q = \begin{bmatrix} \theta_1 & \theta_2 & \delta_2 & \delta_3 \end{bmatrix}^\intercal \tag{5.2}$$

and the hinge map matrix is

$$H = \begin{bmatrix} 1 & 0 & 0 & 0 & 0 & 0 \\ 0 & 1 & 0 & 0 & 0 & 0 \\ 0 & 0 & 0 & 0 & 1 & 0 \\ 0 & 0 & 0 & 0 & 0 & 1 \end{bmatrix} \tag{5.3}$$

From Figure 5.10, the numerical simulation of these four states shows good correlation of the primary fold, however the three asymmetric states are not well predicted. The observed oscillatory behavior has a much lower frequency and greater magnitude than what is predicted for θ_2 and δ_3, and the δ_2 simulation does not predict the oscillation observed. The experimental behavior may be due to further unmodeled effects from the hinge or may be influenced by unknown perturbations from the gravity compensation system. The primary angle θ_1 is observed to better track the observed behavior curve than the 1-DOF model, and the deployment peak times are closer to the observed, at 0.82 seconds and 0.92 seconds for the cup-down and cup-up initial conditions compared to the 0.83 and 0.93 seconds of the cup up and cup down trials, respectively. However the predicted behavior at and after the snap through at the peak deployment is observed to quickly go unstable for these simulations. The constraint violations for the cup up simulation in Figure 5.13 show the simulation is not able to resolve the constraints near this point and therefore the results are not reliable. This is also attributed to the hinge function issues highlighted in Section 5.3.1, where the instability then influences multiple forcing functions across several states and therefore yields more erratic behavior. Further investigation into the hinge model approach will yield better predictions for structure behavior. The states of the other fold lines, seen in Figure 5.11, show good tracking of the observed behavior for the simulations. The predicted behavior for all fold angles is seen to accelerate at a greater rate near the deployed state than what is observed, and this is attributed again to the theoretical peak moment of the tape springs. The prediction does not settle out due to a lack of contact and damping in this model. The inertial states of the root body in Figure 5.12 shows very similar behavior as that in Figure 5.8, predicting a general inertial tumble of the system.

5.4 Finite Element Model Comparison

A matching finite element simulation-based model provides an additional analysis that complements the research demonstrated in this goal. A model of the prototype is constructed in Abaqus to generate deployment dynamics data and is compared to both the experimental data and the folding system multi-body dynamics model. The finite element model is expected to capture more subtle behaviors in the system than the multi-body model, however the computation time is expected to reach exceeding long times. Additionally, development of a working model in the software is not a simple task. Complex, high deformation simulations are known to have issues, and the architecture of the prototype is not simple to reconstruct. The prototype is composed of two tape spring hinges in a system subject to closure constraints in full three-dimensional space, creating additional computational complexity. This simulation provides a point of comparison for the performance of the multibody model with another approach seen in the deployable structures field for studying this kind of system. The literature lacks demonstration of FEA modeling for folding deployable structures, and therefore this study provides insights for the greater community on it's relative use and performance with respect to a multibody model.

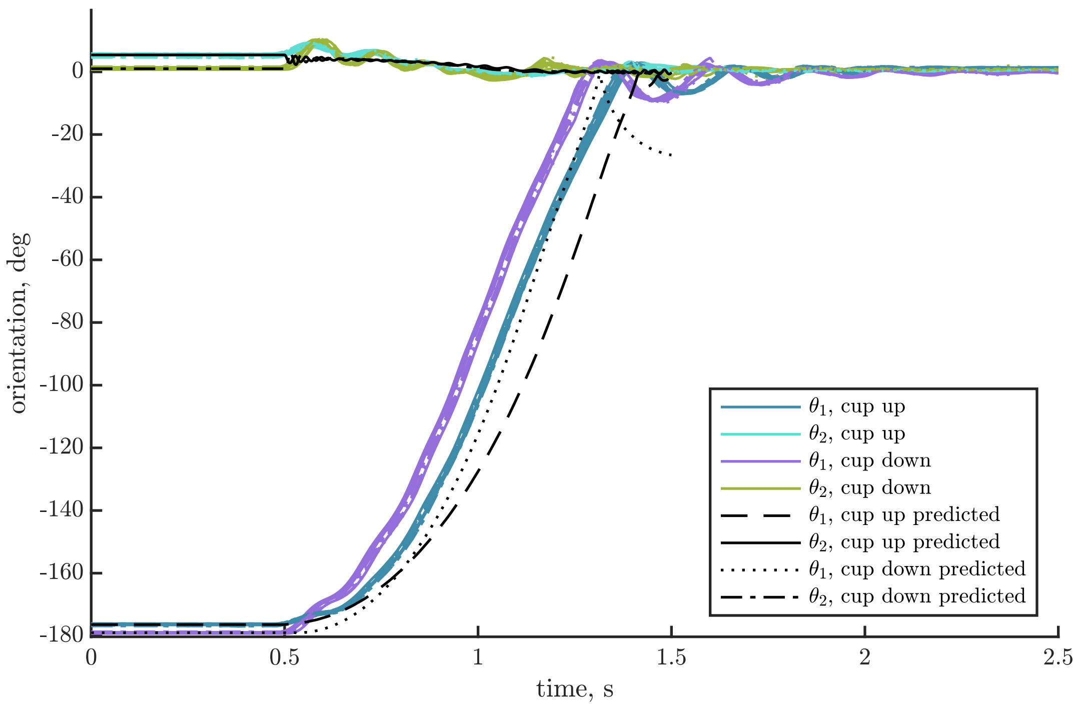

(a) hinge 4-3 orientations

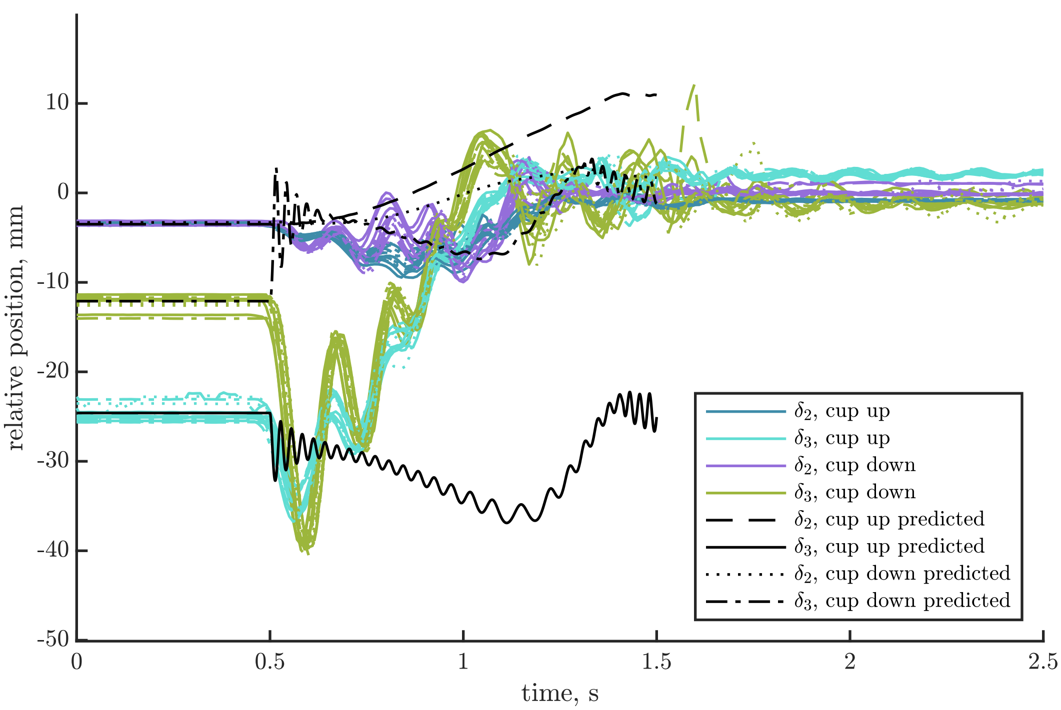

(b) hinge 4-3 positions

Figure 5.10: Deployment actuation predictions of the four states of hinge 4-3 and their experimental counterparts from all trials.

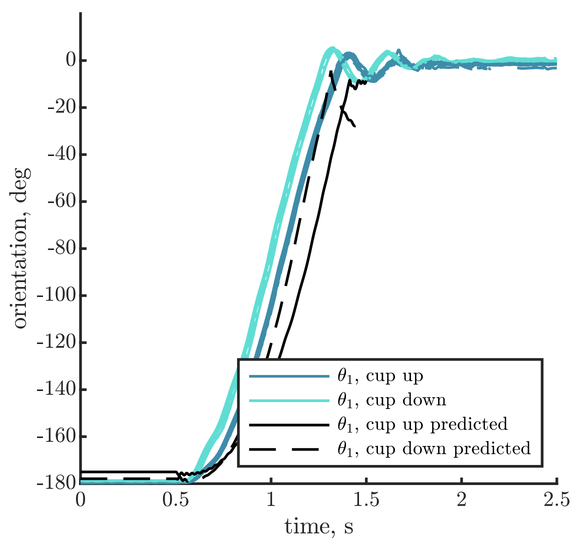

(a) hinge 2-1

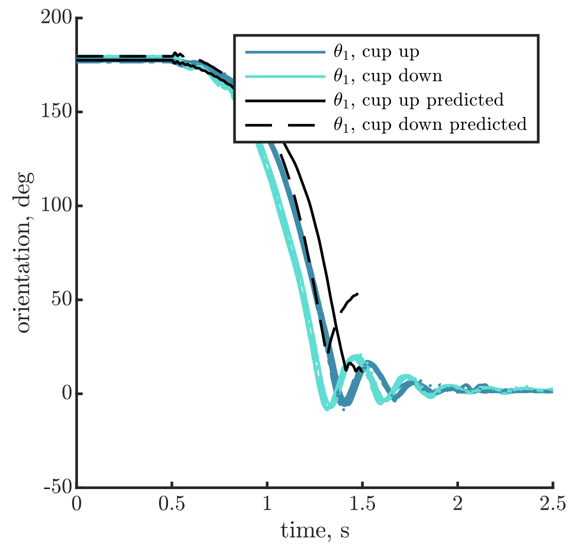

(b) hinge 3-2

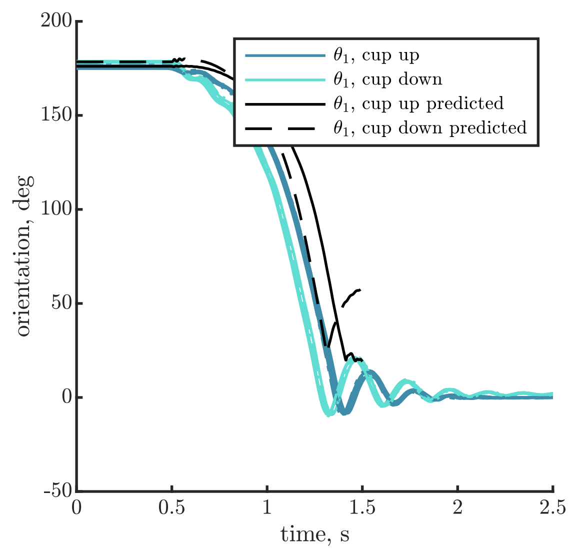

(c) hinge 4-1

Figure 5.11: Deployment actuation predictions of the three 1-DOF hinges and their experimental counterparts from all trials.

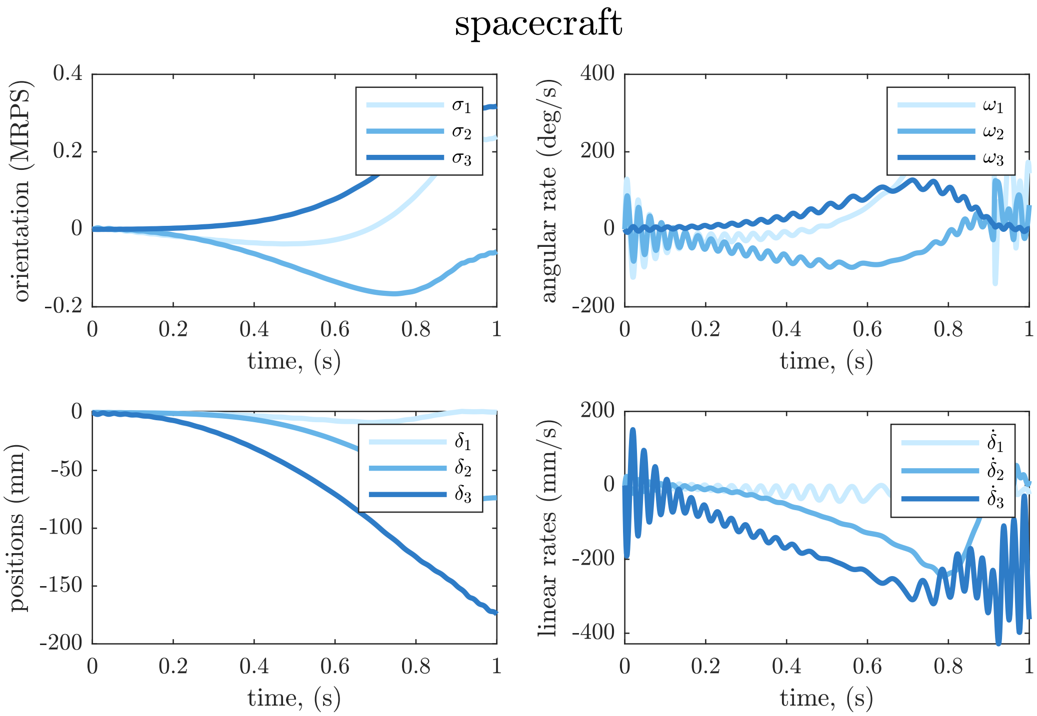

Figure 5.12: States of the root body in three dimensional space for cup up initial conditions.

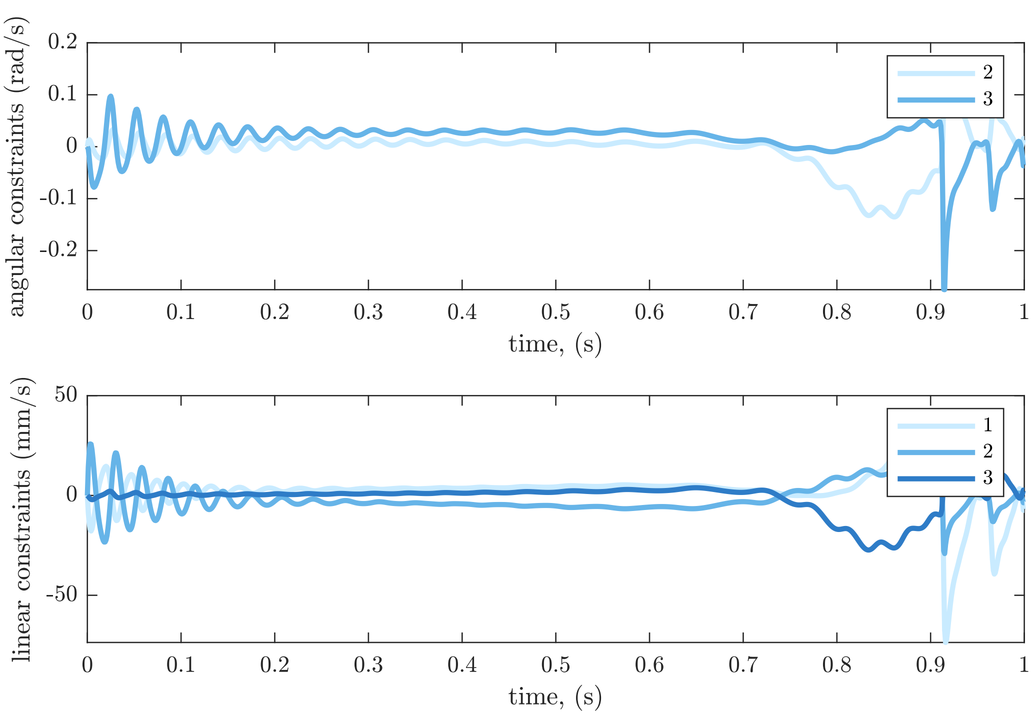

Figure 5.13: Constraint violations during the 4DOF prototype numerical simulation peak as the simulation enters the asymptotic range of the hinge behavior for cup up initial conditions.

5.4.1 Abaqus Model Construction

Finite element analysis (FEA) has been applied extensively to deployable spacecraft structure problems and represents the industry standard for understanding complex deformable and deployable systems. An FEA model of the prototype structure is created to provide an additional point of reference for the expected deployment behavior. FEA modeling capabilities are required in addition to multi-body modeling due to the large deformation behavior of the two tape spring hinges in the system. The behavior of these tape springs as they work together in a closed chain system is not possible to capture without the full FEA analysis. The model is developed using the Abaqus/CAE 6.14 program. The program architecture of Abaqus heavily influences and limits the construction of the model and will now be discussed in detail. The discussion will be formatted to follow the module design of Abaqus to provide continuity for familiar users.

5.4.1.1 Abaqus\Standard and Abaqus\Explicit

First, the two Abaqus software packages used, Abaqus\Standard and Abaqus\Explicit, are discussed. These two packages are designed by Abaqus as two complementary analysis tools to be applied as appropriate to a wide variety of problems. While the tools are used for similar problems, they are designed with fundamental differences in the theories applied. Abaqus\Standard provides good static analysis tools by solving for true static equilibrium in structural analysis. It also contains Dynamic\Implicit analysis, which is well suited for slow and stable dynamics problems. Implicit analysis uses the current information available at the current time to calculate the unknown values and requires iterations and convergence checks, which is implemented in Abaqus using the Hilber-Hughes-Taylor operator (an extension of the trapezoidal rule). Conversely, the Dynamic\Explicit analysis in the Abaqus\Explicit package obtains unknown values at the current time step using the information obtained from the previous time step, in what is known as an explicit dynamic integration method (or forward dynamics). Abaqus uses the forward Euler or central difference algorithm, and adjusts the time increment to be small enough that the result lies on the curve.

Abaqus\Explicit is best for dynamic problems that are high speed, have large nonlinear behavior, or are highly discontinuous. For the context of this research, the large nonlinear deformations of the tape spring hinges combined with the use of a complex system assembly requires that a Dynamic\Explicit analysis be used for the free deployment simulation. Therefore, the analysis is set up in two main phases. The first phase creates a pre-load condition on the system to replicate the stowed configuration of the structure, and this is completed in Abaqus\Standard. Then, the results are imported to an Abaqus\Explicit model as the initial state and a full Dynamic\Explicit step is run.

5.4.1.2 Parts, Material Properties, and Assembly

The physical structure is represented using ten parts with the following attributes. Each panel assembly, including the Vicon targets, hinge assemblies, and hardware, is represented by a unique deformable trapezoidal shell part. This is required to minimize the complexity of the mesh and reduce computation time of the analysis. The full panel assembly is then represented by the user input inertia properties. The properties are generated by the solid CAD model approximation, where physically measuring the inertia properties was not an option. The inertia properties are applied at the center of mass location of each panel for correct geometric representation. The panels are assigned elastic mechanical properties and set with the Young's modulus for cast acrylic, as this is the material of the panels and additional assemblies are represented by rigid bodies. Then four rigid body hinge attachment plates are used to interface between the folding panels and the tape spring hinges. These parts are geometrically simplified versions of the hinge attachment plates and are modified to provide the best mesh and constraint surface definitions in the analysis. Finally, the tape springs are represented by deformable extruded shell parts with a Young's modulus for spring steel. The details of this construction are summarized in Table 5.13. The mesh size of the tape springs is set to 2 mm, as this is the largest mesh size that results in successful folding of the prototype due to the large deformation of the fold radius on the tape springs, where element deformations above 20 degrees is not desirable. Then for successful interactions between the tape spring and the attachment plate, the same mesh size is applied to the attachment plate. The mesh of the panels is set to the recommended size of 33 mm, but is refined to 2 mm at the region that interacts with the attachment plate, again for interaction purposes. No additional mesh refinement is achieved due to the sensitivity of the simulation to the mesh, however it's acknowledged that a more optimal mesh may yield different results and faster computation time.

Table 5.13: Abaqus model part properties.

Part	**Type**	**Material**	**Modulus** (GPa)	**Shell Thickness** (mm)	**Instances**
P1	deformable	cast acrylic	3	3.175	1
P2	deformable	cast acrylic	3	3.175	1
P3	deformable	cast acrylic	3	3.175	1
P4	deformable	cast acrylic	3	3.175	1
Hinge Plate	rigid body	spring steel	180	NA	4
Tape Spring	deformable	NA	NA	0.1	2

The full assembly of the prototype is shown in Figure 5.14 for reference. The four panels are named following the convention established in the deployment test campaign of Chapter 4. This figure shows the local frame definitions of the panels and the center of mass reference points (RP) of the panels that are needed for the inertia properties.

5.4.1.3 Interactions and Constraints

Determining the best implementation of the interactions and constraints is a central challenge to the application of Abaqus to folded deployable structures. First consider the constraints. The initial approach concept strove to represent the panels as rigid bodies to reduce the computational complexity of the simulation. However, the interconnected nature of the panels proved to make this infeasible using the Abaqus framework. The primary way to connect the panels would be through either constraints or connector elements. A tie constraint between the mesh nodes of the edge of the panel can represent this behavior if the rotational degrees of freedom are not included in the constraint between the nodes. This is the method used in this analysis. However, Abaqus is not capable of enforcing a tie constraint between two rigid bodies. The rigid body tools have

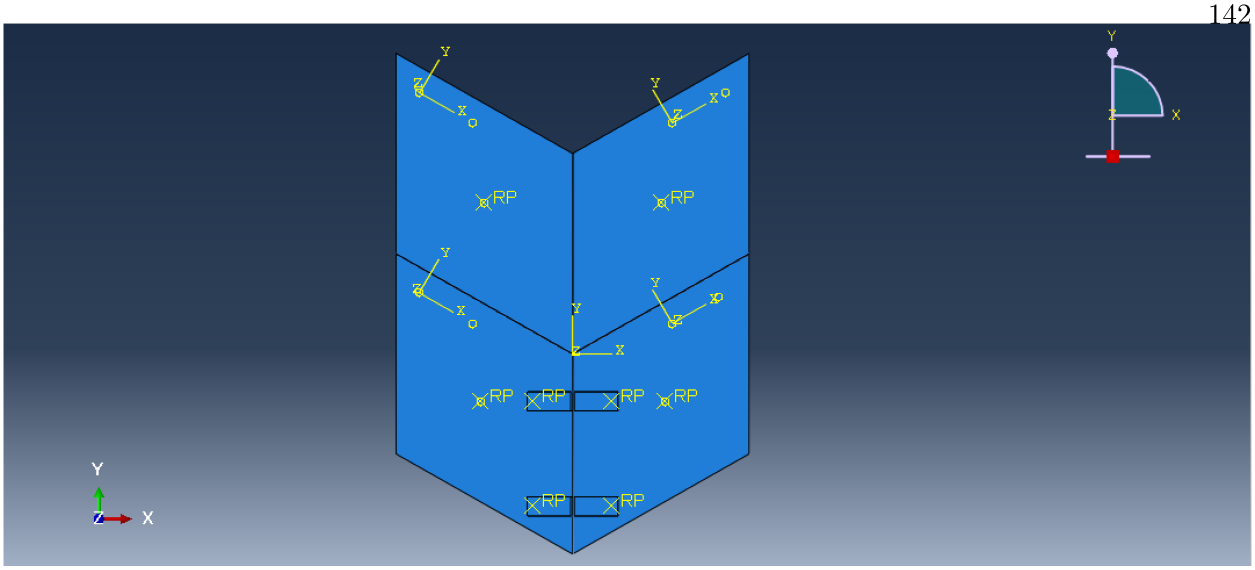

Figure 5.14: Graphic representation of system assembly in Abaqus CAE with center of mass reference points (RP) and local coordinate systems shown for the panels.

been developed to represent interactions between test coupons and their fixtures, and therefore are not well suited to create this kind of model. Therefore, the panels are represented by deformable parts and are also given accurate material properties to capture the real system's flexibility. The tape springs are attached to the hinge attachment plates using a surface-to-surface tie constraint between the overlapping surfaces. Finally, the hinge attachment plates are constrained to the panels at their attachment points using coupling constraints. Coupling constraints require that a set of slave nodes follow the behavior of a master point. The master point is set to a reference point on the hinge plates. In the full assembly, each panel is subject to either a master or slave tie constraint designation for the fold line. This reduces the available nodes for the slave nodes, and therefore a small radius of influence, set to 60 mm, is dictated for the coupling constraint slave node designation. A summary of all constraints needed to capture the prototype Miura unit structure is provided in Table 5.14.

Considering the interactions, there are a few primary concerns to address. These are all due to the presence of contact in the stowed step of the simulation. Obtaining the stowed configuration requires the tape springs contact with the attachment plates, while not self-intersecting when they

Table 5.14: Abaqus model constraint definitions.

Constraint	Type	Master	Slave
H21	Tie	Panel 2 Edge Nodes	Panel 1 Edge Nodes
H32	Tie	Panel 3 Edge Nodes	Panel 2 Edge Nodes
H14	Tie	Panel 1 Edge Nodes	Panel 4 Edge Nodes
P3-Hinge 1	Kinematic Coupling	Hinge Plate 1	Panel 3
P3-Hinge 2	Kinematic Coupling	Hinge Plate 2	Panel 3
P4-Hinge 3	Kinematic Coupling	Hinge Plate 3	Panel 4
P4-Hinge 4	Kinematic Coupling	Hinge Plate 4	Panel 4
Tape 1-Hinge 1	Tie	Hinge Plate 1	Tape Spring 1
Tape 1-Hinge 2	Tie	Hinge Plate 2	Tape Spring 1
Tape 2-Hinge 3	Tie	Hinge Plate 3	Tape Spring 2
Tape 2-Hinge 4	Tie	Hinge Plate 4	Tape Spring 2

are brought together in the final configuration. Additionally, the shell representations of the panels may intersect in the fully stowed configuration. The panel contact interactions are considered negligible due to their thin shell designation, where at a full 180 deg fold they would be occupying the same plane. Additionally, the expected behavior of the system does not include panel to panel contact through deployment. A basic "hard contact" property is defined for all contact interactions. Contact interactions are defined between each of the attachment plates and the tape springs. These contact interactions are found to be a primary influence on the deployment behavior, where a "hard contact" definition results in a failed deployment, but a staged, multi-step defined separation results in the expected deployment behavior. No experiments were conducted to model this contact surface, so these results must be taken with a grain of salt. Future work must be careful in modeling any contact surfaces within the structure. Additionally, self contact interactions are defined for the tape springs to prevent self-intersection in the fully deployed configuration. A general self-contact designation for the full model is not used as it is unnecessary and computationally infeasible.

5.4.1.4 Loads and Boundary Conditions

To obtain the free deployment dynamics behavior, the system must first be preloaded into the high strain initial condition and then released for deployment. The Loads and Boundary Conditions modules provide tools to manipulate the model into the desired initial conditions for the dynamic analysis. The limitations of the software requires this to be a multi-step process. The specific sequential implementation of these loads and boundary conditions is outlined in the next section. The first boundary condition fixes the position of the P4 panel by applying encastre boundary conditions at each of the reference points of the hinge attachment plates. These plates are selected because the rigid bodies control both the panel behavior and the tape spring behaviors. Similarly, the primary fold-enforcing boundary condition is applied at the hinge attachment plate RPs that are mounted to the P3 panel. A small initial fold is introduce to the $2-1$ hinge fold line to ensure the fold starts in the correct direction, but is otherwise uncontrolled. The boundary conditions of the static general analysis are applied over a linear ramp on an arbitrary time step, and simultaneously controlling more than one fold line is not recommended over the full course of the folding step. A final adjustment is applied after the major fold is implemented to best replicate the physical test campaign. Additionally, a loading condition is applied to the tape springs to help initialize the folding behavior. This is a pressure load applied uniformly across the tape springs to press them flat against the panels at the initial fold. This is necessary because of the high stiffness condition of the tapes close to the initial buckling in folding. After the initial fold, the pressure is reduced for the duration of the folding. After folding, the pressure is deactivated. All boundary conditions and loads are summarized in Tables 5.15 and 5.16, and are removed for the free deployment step.

Table 5.15: Abaqus model boundary conditions.

Boundary Condition	**Type**	**Location**
P4	Encastre	RPs on P4 Rigid Bodies
P3	Rotation	RPs on P3 Rigid Bodies
h21 Nodes	Rotation	Fold line nodes on h21

Table 5.16: Abaqus model load conditions.

Load Condition	**Type**	**Location**
Press Tapes	Pressure	Tape Spring surfaces

5.4.1.5 Step Sequence

The step sequence is outlined in detail in Table 5.17 and references the same loads and boundary conditions defined in Tables 5.16 and 5.15. The complexity of the multi-step approach to creating the desired preloaded condition of this structure illustrates the difficulty of this approach for folded deployable spacecraft structures. This prototype only contains one fold pattern unit structure and is the minimum pattern case, where in practice, tens to hundreds of unit structures are desired. Analysis clock time for the preloaded condition steps is 45 minutes.

Table 5.17: Abaqus model step specifications.

Step	BC P4	BC P3	BC H21	BC Adjust	Press Tapes
Initial					
Initial Fold	encastre	$\begin{bmatrix} - & 0 & 0 & 0 & 0.1 & 0 \end{bmatrix}$	UR2 = 0.1	-	2000
Full Fold	encastre	$\begin{bmatrix} - & 0 & - & 0 & 3 & 0 \end{bmatrix}$	inactive	-	1000
Release Press	encastre	$\begin{bmatrix} - & 0 & - & 0 & 3 & 0 \end{bmatrix}$	inactive	-	inactive
Deploy	encastre	inactive	inactive	inactive	inactive

5.4.2 Abaqus Deployment Trial Results and Comparison to Measured Tests

The Abaqus \Explicit deployment simulation results are displayed over the experimental deployment data in Figure 5.16, and show the bulk deployment behavior is well predicted. Two seconds of simulation requires approximately 22 hours of user clock time to compute using Windows 10 on a Parallels Virtual Machine, with 4 GB of memory and 2 processors. Clock time can be significantly improved with more advanced computer hardware. Additionally, an optimization study to provide a refined mesh may also improve the simulation time. Looking at the secondary behaviors, such as the oscillations and motion trends, it's possible the discrepancies between the experimental and Abaqus simulation are due to test environment effects, such as aeroeffects and gravity. While these effects can be simulated in Abaqus, this is not done due to challenges with defining the relative orientation of these effects, and is left to future work. The predicted deployment time is seen to be 0.88 seconds, midway between the cup up and cup down trials. The result is suspected to be due to the initial conditions of the simulation, and the imperfect modeling of the contact behavior between the tape springs and their attachment plates. Over all, the simulation is able to predict the bulk behaviors and the settling of the structure in the deployed state well.

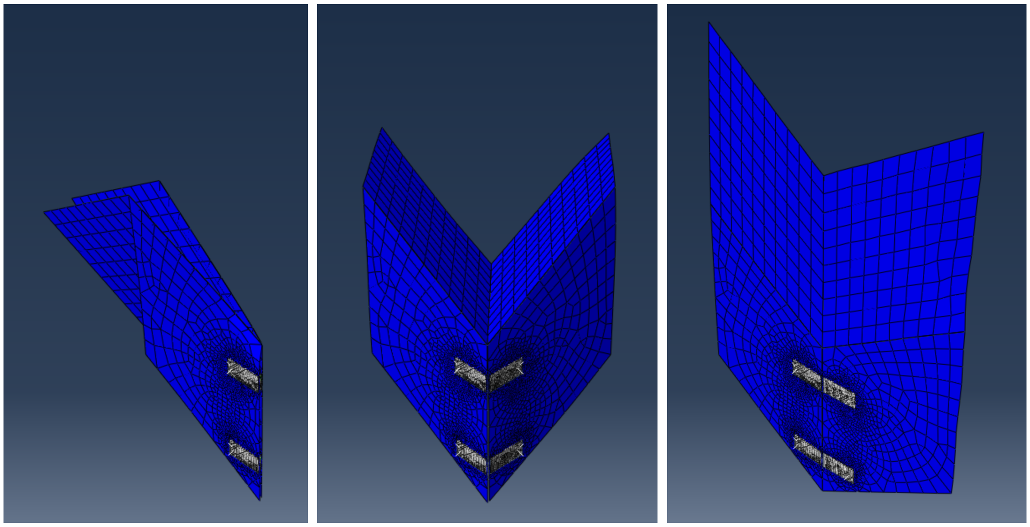

(a) folded (b) deploying (c) deployed

Figure 5.15: Graphic representation of the deployment stages from the Abaqus simulation GUI.

In conclusion, this Abaqus modeling effort quantifies the time and effort commitment of creating a high fidelity deployment model, and highlights the limitations of the multibody dynamics modeling approach. In practice, it's recommended that the multibody modeling approach be implemented for large scale fold patterns of many bodies and for early design iterations of the geometry, mass, and hinge properties. The fast computation speed of the multibody framework increases feasibility of large parameter design studies and the accuracy of the deployment model is shown to be sufficient for informing early design evaluations. A high fidelity FEA deployment model should also be studied, but is primarily recommended for validation phases of the project. The FEA model is best able to capture the secondary behaviors of the flexible panels, the lock out of the hinges, and contact behaviors. Deployment testing of a prototype provides context for expected performance and should also be conducted during the design cycle of the project. All three data sets confirm the prototype folded structure will successfully self-deploy with the tape spring actuated hinge design.

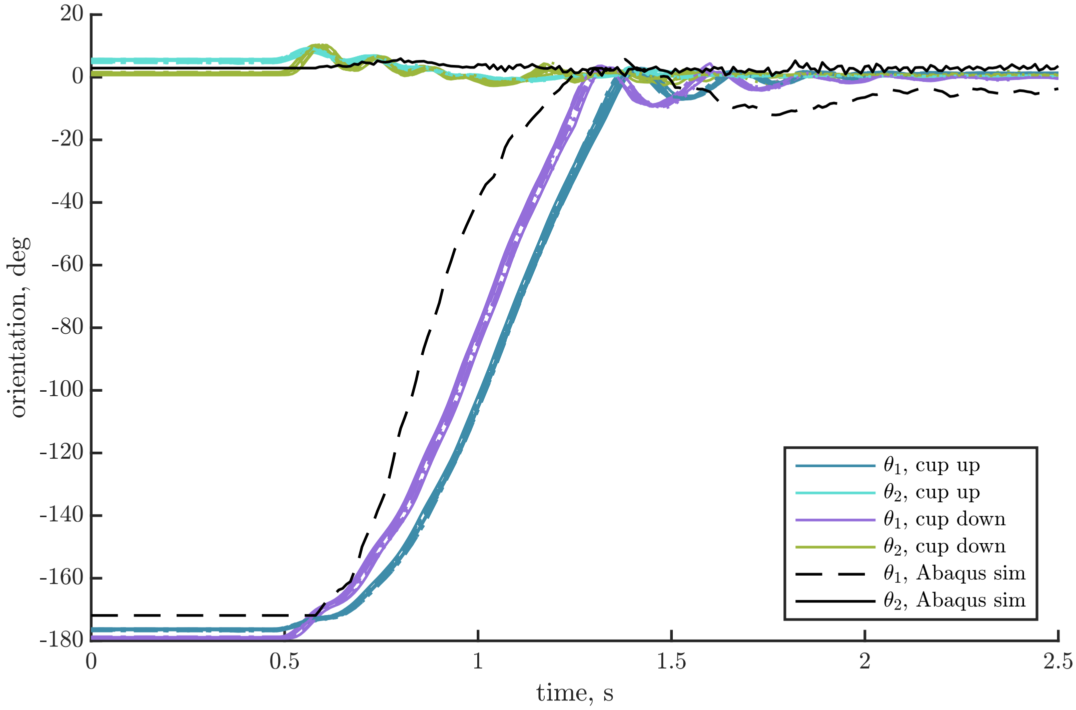

(a) hinge 4-3 orientations

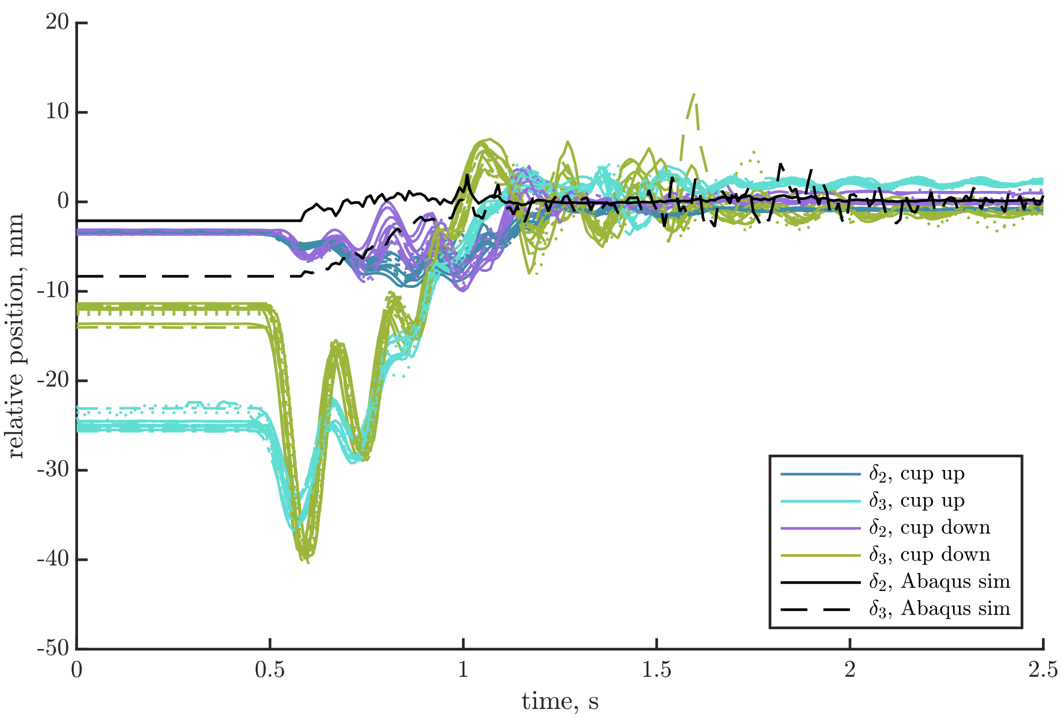

(b) hinge 4-3 positions

Figure 5.16: Deployment actuation predictions from the Abaqus FEA model of the four states of hinge 4-3 and their experimental counterparts from all trials.

Chapter 6

Conclusions and Future Work

6.1 Summary and Conclusions

This dissertation presents a method for simulating the deployment dynamics of a novel, self-actuated folded deployable spacecraft structure. Origami folded architectures are gaining interest in the field of deployable structures for many applications. The development of deployment actuation techniques for these structures is an active area of interest, and the simulation of the deployment dynamics of such architectures has not been discussed in detail. In this thesis, high strain tape spring hinges are studied for deployment actuation in a folded structure, presenting a novel challenge due to the multi-DOF behavior of the hinges within the architecture. Several commercial tools for multibody dynamics models and finite element models exist, but evaluation of their application to the specific challenges of these deployable systems has not been presented. Full context of where the current state of the art is for deployable structures modeling is presented in Chapter 1. In this thesis, the application of a general dynamics framework to this problem is presented. A method of capturing the nonlinear multi-DOF behavior of the tape spring hinges is presented and testing is conducted to validate the method. Additionally, a prototype folded structure is designed and manufactured, and deployment tests are conducted. These tests provide a measure for comparing the predicted behavior generated by the dynamics modeling approach and shows good performance for deployment time and behavior prediction. Therefore, this thesis contributes a novel method for deployment actuation of folded deployable structures, outlines the applicability and challenges of current dynamics modeling approaches for these systems, and furthers the understanding of flexible hinge behaviors within these systems. Highlights of each chapter are identified as follows.

A self-actuated folded deployable spacecraft structure presents a novel modeling challenge due to free-flying spacecraft dynamics coupled with a complexly constrained multibody system. An approach that blends several SOA articulated body-derived robotics dynamics algorithms together is presented in Chapter 2 to address the multibody folded structure problems. The articulated body forward dynamics algorithm is outlined as the basis for the approach, and derivations that generalize the ABFD algorithm to the spacecraft folded deployable structure scenario are provided. The tree augmented approach is developed for any grid formatted spacecraft structure. It is found that this approach provides significant value over the Lagrangian approach or Kane's equations. This is due to the computation gains of the recursive structure of the equations of motion and that the algorithm provides a framework for working with a high volume of rigid bodies and rigid body constraints. Origami-folded structure topology is studied and interpreted for dynamics analysis using graph theory, and two forms of a 4 body architecture, the four-bar mechanism and a map fold unit, are analyzed for algorithm demonstration. Origami-inspired folding topologies with large number of bodies are shown to have algorithm gains for recursively calculated loop constraints, however constraint violations are a significant concern, as demonstrated on two cases of multiple constraint configurations. Future work in the field should focus on developing robust constraint correction and stabilization tools for systems with a large number of constraints as well as multiple constraints applied to a given body in the system.

Chapter 3 presents an approach for capturing the full six degree of freedom force and torque behavior of a tape spring hinges in symmetric and non-symmetric configurations as a function of the hinge's six relative coordinates. Non-symmetric behavior is demonstrated to have significant force and torque profiles and therefore should be included in a robust dynamics model. First, numerical predictions for force and torque are generated in Abaqus for three non-symmetric cases in the equal-sense fold and two non-symmetric cases for the opposite-sense fold for two materials. These two materials are found to display similar behavior in both experimental and numerical data. A non-linear regression is applied to the full data set of each material assuming a simple second order polynomial, and the resulting fits are evaluated. Fits for the numerical data are not conclusively good, and therefore interpolation methods or a look-up table may be more appropriate for capturing these data trends, depending on needs. The regression is found to improve if smaller asymmetry ranges are used, or if the equal and opposite fold regimes are fit separately, so using a piecewise switching function is another solution. Experimental and numerical data predicting the hinge behavior in symmetric and non-symmetric folding are obtained. The results from these databases do not correlate and are not able to conclusively validate each other. This is primarily due to differences in the fabrication of the composite tape spring configuration and the assumptions of the material model. This highlights a major issue in implementing composites, where each batch is uniquely manufactured and earlier models must be considered carefully before applying them to later units.

In Chapter 4, a prototype folded deployable structure is designed to represent a base unit of the Miura-ori pattern. The deployment for this structure is self-actuated by the use of two high strain tape spring hinges on one of the fold lines. These tape springs are embedded within a segmented fold line, presenting a novel solution to the implementation of a tape spring actuated folded structure. Deployment tests of the structure are conducted with videogrammetry, data is reduced to the relative spatial hinge states, and the precision of the deployment as well as structure manufacturing is discussed.

In Chapter 5, simulations of the prototype are constructed from models presented in Chapters 2 and 3. The simulations are compared to the data collected in 4 and performance is evaluated. The simulations of both a 1-DOF and a 4-DOF hinge model show good prediction of the deployment time, however deployment behavior past the peak deployment is not well predicted due to a lack of contact and damping in the model. Issues due to constraint violations are also acknowledged. An additional simulation is constructed using a full finite element analysis, and the deployment time is also well predicted, as well as the settling period. The overall deployment behavior is also captured across multiple degrees of freedom, however the simulation takes 22 hours of computation time to complete. This confirms the original motivation of designing a more computationally efficient method of deployment dynamics modeling, and demonstrates that multibody dynamics modeling is able to predict deployment behavior with similar accuracy. In practice, it's recommended that the multibody modeling approach be implemented for large scale fold patterns of many bodies and for early design iterations of the geometry, mass, and hinge properties. The fast computation speed of the multibody framework increases feasibilty of large parameter design studies and the accuracy of the deployment model is shown to be sufficient for informing early design evaluations. A high fidelity FEA deployment model should also be studied, but is primarily recommended for verification and validation phases of the project. The FEA model is best able to capture the secondary behaviors of the flexible panels, the lock out of the hinges, and contact behaviors. Deployment testing of a prototype provides context for expected performance and should also be conducted during the design cycle of the project. All three data sets confirm the prototype folded structure will successfully self-deploy with the tape spring actuated hinge design.

6.2 Recommendations for Future Work

There are several key areas to develop to improve the simulation capabilities of folded deployable spacecraft structures. Some of the recommendations for future work in the area of multi-body dynamics modeling for folded structures include

(1) The development of robust constraint enforcement for multiple constraints applied to an individual rigid body in a cut-tree topology multi-body dynamics model. Multiple constraints on a single body can be interpreted as conflicting correction calculations, resulting in poor constraint enforcement for both sets. A method for resolving these coupled constraints simultaneously is needed to ensure correct constraint enforcement.

(2) The development of robust constraint enforcement at the system level for multiple rigid body constraints. Multiple constraints within the system, regardless of if they are on the same body, can also cause correction conflicts as the folded structure is highly coupled through many interconnected loops. A constraint enforcement technique that solves for

constraints across coupled loops is needed.

(3) Creating base unit models that can be used to quickly create full system folding structure models. The prototype model in this thesis represents a single base unit of the Miura pattern, for example. A framework for copying and connecting several units of this base unit model would enable faster design and evaluation cycles for structure development.

Some recommendations for implementing high strain tape spring hinges in folded deployable structures include

(1) Improving the quality and repeatability of high strain composite tape spring manufacturing, which in turn will improve the predictability of the hinge behavior modeling.

(2) Improve material testing techniques for high strain composite tape spring hinges.

(3) Develop tape spring hinge geometries to eliminate or reduce asymmetric fold behavior, therefore eliminating complex force and torque behaviors that are difficult to predict.

(4) Developing an approach to model the damping in the tape spring hinge behavior, particularly around the snap-through state of the hinge.

Some recommendations for improving FEA applications to folded deployable spacecraft structure simulations include

(1) Development of boundary condition enforcement in terms of relative coordinates. The Abaqus finite element software is designed for small systems simulation and is currently not capable of applying loads or boundary conditions in a relative frame manner. This is very restrictive for origami folding structures, where the fold pattern may induce complex spatial motion.

Bibliography

[1] Jeremy Banik. Frontiers of Engineering: Reports on Leading-Edge Engineering from the 2015 Symposium, chapter Realizing Large Structures in Space. the National Academies Press, 2015.

[2] Malcolm Macdonald. Advances in Solar Sailing. 01 2014.

[3] P.-A. Lindqvist, G. Olsson, R. B. Torbert, B. King, M. Granoff, D. Rau, G. Needell, S. Turco, I. Dors, P. Beckman, J. Macri, C. Frost, J. Salwen, A. Eriksson, L. Åhlén, Y. V. Khotyaintsev, J. Porter, K. Lappalainen, R. E. Ergun, W. Wermeer, and S. Tucker. The spin-plane double probe electric field instrument for mms. Space Science Reviews, 199(1):137–165, 2016.

[4] Jenkins Christopher H. Banik, Jeremy A. American Institute of Aeronautics and Astronautics, 2017.

[5] Zhi-Quan Liu, Hui Qiu, Xiao Li, and Yang Shu-Li. Review of large spacecraft deployable membrane antenna structures. Chinese Journal of Mechanical Engineering = Ji xie gong cheng xue bao, 30(6):1447–1459, 2017.

[6] B. R. Spence, S. White, M. LaPointe, S. Kiefer, P. LaCorte, J. Banik, D. Chapman, and J. Merrill. International space station (iss) roll-out solar array (rosa) spaceflight experiment mission and results. In 2018 IEEE 7th World Conference on Photovoltaic Energy Conversion (WCPEC) (A Joint Conference of 45th IEEE PVSC, 28th PVSEC 34th EU PVSEC), pages 3522–3529, 2018.

[7] S. Pellegrino and S. D. Guest, editors. IUTAM-IASS Symposium on Deployable Structures: Theory and Applications. Springer Netherlands, 2000.

[8] C. Gantes, J.J. Connor, and R.D. Logcher. Combining numerical analysis and engineering judgment to design deployable structures. Computers and Structures, 40(2):431 – 440, 1991.

[9] ATK. Atk demonstrates high-power megaflex solar array for nasa, 2014. [Online; accessed April 14, 2020].

[10] Brigham Young University. Origami in space: Byu-designed solar arrays inspired by origami, 2013. [Online; accessed April 14, 2020].

[11] Giulia E Fenci and Neil GR Currie. Deployable structures classification: A review. International Journal of Space Structures, 32(2):112–130, 2017.

[12] Sergio Pellegrino. Deployable Structures. Springer-Verlag Wien, 2001.

[13] Esther. Rivas, Adrover. Deployable Structures. Laurence King Publishing, 2015.

[14] C. J. Gantes. Deployable Structures: Analysis and Design. Southampton : WIT Press ; Billerica, MA : Computational Mechanics, Inc., 2001.

[15] Andrea Del Grosso. Deployable structures. Advances in Science and Technology, 83:122–131, 09 2012.

[16] Shannon A. Zirbel, Brian P. Trease, Mark W. Thomson, Robert J. Lang, Spencer P. Magleby, and Larry H. Howell. HanaFlex: a large solar array for space applications. In Thomas George, Achyut K. Dutta, and M. Saif Islam, editors, Micro- and Nanotechnology Sensors, Systems, and Applications VII, volume 9467, pages 179 – 187. International Society for Optics and Photonics, SPIE, 2015.

[17] David Murphy. MegaFlex - The Scaling Potential of UltraFlex Technology.

[18] Sungeun K. Jeon and Joseph N. Footdale. Scaling and design of a modular origami solar array. In AIAA SciTech Spacecraft Structures Conference, 2018.

[19] Sungeun Jeon and Thomas Murphey. Fundamental Design of Tensioned Precision Deployable Space Structures Applied to an X-Band Phased Array.

[20] Nathan A. Pehrson. Folding approaches for tensioned precision planar shell structures. In AIAA SciTech Spacecraft Structures Conference, 2018.

[21] Mark Thomson, Douglas Lisman, Richard Helms, Phil Walkemeyer, Andrew Kissil, Otto Polanco, and Siu-Chun Lee. Starshade design for occulter based exoplanet missions. Space Telescopes and Instrumentation 2010: Optical, Infrared, and Millimeter Wave, 2010.

[22] Whitney Reynolds, Sungeun Jeon, and Jeremy Banik. Advanced folding approaches for deployable spacecraft payloads. In Proceedings fo the ASME 2013 International Design Engineering Technical Conference and Computers and Information in Engineering Conference, Portland, OR, USA, August 4-7 2013.

[23] Daniel Kling, Sungeun Jeon, and Jeremy Banik. Novel folding methods for deterministic deployment of common space structures. In 3rd AIAA Spacecraft Structures Conference, 2016.

[24] Shannon A. Zirbel, Brian Trease, Spencer P. Magleby, and Larry L. Howell. Deployment methods for an origami-inspired rigid-foldable array. 2014.

[25] Thomas W. Murphey and Sergio Pellegrino. A novel actuated composite tape-spring for deployable structures. In 45th AIAA/ASME/ASCE/AHS/ASC Structures, Structural Dynamics and Materials Conference, 2004.

[26] Sir Isaac Newton. Mathematical Principles of Natural Philosophy. 1728.

[27] Anil Vithala Rao. Dynamics of particles and rigid bodies. Cambridge University Press, 2006.

[28] Hanspeter Schaub and John L. Junkins. Analytical Mechanics of Space Systems. American Institute of Aeronautics and Astronautics, Inc., 1801 Alexander Bell Drive, Reston, Virginia, 20191-4344, 3rd edition, 2014.

[29] JoAnna Fulton and Hanspeter Schaub. Dynamic modeling of folded deployable space structures with flexible hinges. In 2017 AAS/AIAA Astrodynamics Specialist Conference, Stevenson, WA, 2017.

[30] JoAnna Fulton and Hanspeter Schaub. Dynamics and control of the flexible electrostatic sail deployment. 26th AAS/AIAA Space Flight Mechanics Meeting, 2016.

[31] JoAnna Fulton and Hanspeter Schaub. Sensitivity analysis of the electric sail deployment dynamics parameters. In The Fifth International Conference on Tethers in Space, 2016.

[32] JoAnna Fulton and Hanspeter Schaub. Fixed-axis electric sail deployment dynamics analysis using hub-mounted momentum control. Acta Astronautica, 144:160 – 170, 2018.

[33] Thomas R. Kane and David A. Levinson. Dynamics: Theory and Applications. McGraw-Hill, Inc., New York, 1985.

[34] A Purushotham and Mr. J.Anjeneyulu. Kane's method for robotic arm dynamics: a novel approach. IOSR Journal of Mechanical and Civil Engineering (IOSR-JMCE), 6(4):7–13, May-June 2013.

[35] Cody Allard. Modular Software Architecture for Complex Multi-Body Fully-Coupled Spacecraft Dynamics. PhD thesis, University of Colorado at Boulder, 2018.

[36] Roy Featherstone. The calculation of robot dynamics using articulated-body inertias. The International Journal of Robotics Research, 2(1):13–30, Spring 1983.

[37] Guillermo Rodriguez. Recursive forward dynamics for multiple robot arms moving a common task object. IEEE Transactions on Robotics and Automation, 5(4):510–521, August 1989.

[38] Abhinandan Jain. Unified formulation of dynamics for serial rigid multibody sytems. Journal of Guidance, Control, and Dynamics, 14(3):531–542, May-June 1991.

[39] Abhinandan Jain. Robot and Multibody Dynamics. Springer Science+Business Media, LLC, 2011.

[40] Roy Featherstone. Rigid Body Dynamics Algorithms. Springer Science+Business Media, LLC, 2008.

[41] David A. Huffman. Curvature and creases: A primer on paper. IEEE Transactions on Computers, c-25(10):1010–1019, 1976.

[42] Kyeongsik Woo and Christopher H. Jenkins. Effect of crease orientation on wrinklecrease interaction for thin membranes. Journal of Spacecraft and Rockets, 50(5):1024–1034, 2013.

[43] K. A. Seffen and S. Pellegrino. Deployment dynamics of tape springs. Proceedings of The Royal Society of London, 1998.

[44] Omer Soykasap. Analysis of tape spring hinges. International Journal of Mechanical Sciences, 2007.

[45] Scott J. I. Walker and Guglielmo Aglietti. Study of the dynamics of three-dimensional tape spring folds. AIAA Journal, 42(4):850–856, April 2004.

[46] Thomas W. Murphey, Michael E. Peterson, and Mikhail M. Grigoriev. Four point bending of thin unidirectional composite laminas. In 54th AIAA/ASME/ASCE/AHS/ASC Structures, Structural Dynamics, and Materials Conference, Boston, Massachusetts, April 2013.

[47] Jonathan Sauder, Nacer Chahat, Richard E. Hodges, Eva Peral, Yahya Rahmat-Samii, and Mark Thomson. Lessons learned from a deployment mechanism for a ka-band deployable antenna for cubesats. 2018.

[48] Joseph N. Footdale and Jeremy Banik. Design and Deployment Testing of the Multi-Arm Radial Composite (MARCO) Reflector Antenna.

[49] JoAnna Fulton, Sungeun Jeon, and Thomas W. Murphey. Flight qualification testing of a meter-class cubesat deployable boom. In 4th AIAA Spacecraft Structures Conference, Kissimmee, FL, January 2017.

[50] Mehran Mobrem and Douglas S. Adams. Deployment analysis of the lenticular jointed antennas onboard the mars express spacecraft. Journal of Spacecraft and Rockets, 46(2):394–402, 2009.

[51] Douglas Adams and Mehran Mobrem. MARSIS Antenna Flight Deployment Anomaly and Resolution.

[52] Gina Olson, Thomas Murphey, and Grant Thomas. Free deployment dynamics of a z-folded solar array. 04 2011.

[53] Nathan A. Pehrson, Samuel P. Smith, Daniel C. Ames, Spencer P. Magleby, and Manan Arya. Self-deployable, self-stiffening, and retractable origami-based arrays for spacecraft. In AIAA SciTech Spacecraft Structures Conference, San Diego, CA, 7-11 January 2019.

[54] Joseph R. Blandino, Brant Ross, Nelson Woo, Zachary Smith, and Eric McNaul. Simulating cubesat strucure deployment dynamics. In AIAA SciTech Spacecraft Structures Conference, 2018.

[55] Koryo Miura. Folding a plane- scenes from nature technology and art, symmetry. In Symmetry of structure, interdisciplinary symposium, Budapest, Hungary, August 13-19 1989.

[56] S.D. Guest and Sergio Pellegrino. Inextensional wrapping of flat membranes. In Proceedings of the First International Seminar on Structural Morphology, 1992.

[57] Marco B. Quadrelli, Adrian Stoica, Michel Ingham, and Anubhav Thakur. Flexible electronics-based transformers for extreme environments. In AIAA SPACE 2015 Conference and Exposition, 2015.

[58] T. F. Wiener. Theoretical Analysis of Gimballess Inertial Reference Equipment Using Delta-Modulated Instruments. PhD thesis, Massachusetts Institute of Technology, 1962.

[59] S. R. Marandi and V. J. Modi. A preferred coordinate system and the associated orientation representation in attitude dynamics. Acta Astronautica, 15(11):833843, 1987.

[60] M. D. Shuster. A survey of attitude representations. Journal of the Astronautical Sciences, 41(4):439517, 1993.

[61] JoAnna Fulton and Hanspeter Schaub. Closed-chain forward dynamics modeling of a four-panel folding spacecraft structure. In International Astronautical Congress, Bremen, Germany, Oct 1-5 2018.

[62] JoAnna Fulton and Hanspeter Schaub. Forward dynamics algorithm for origami-folded deployable spacecraft structures. In International Astronautical Congress, Washington, D.C., Oct 2019.

[63] J. Baumgarte. Stabilization of constraints and integrals of motion in dynamical systems. Computer Methods in Applied Mechanics and Engineering, 1:1 – 16, 1972.

[64] Tomohiro Tachi. Rigid-foldable thick origami. 5, 06 2011.

[65] Erik D. Demaine and Joseph O'Rourke. Geometric Folding Algorithms. Cambridge University Press, 2007.

[66] Manan Arya, Nicolas Lee, and Sergio Pellegrino. Crease-free biaxial packaging of thick membranes with slipping folds. International Journal of Solids and Structures, 108:24 – 39, 2017.

[67] JoAnna Fulton and Hanspeter Schaub. Non-symmetric behavior of high strain composite tape spring hinges for folding structures. In Spacecraft Structures Conference, AIAA SciTech Forum, 2019.

[68] Mark Schenk. Folded Shell Structures. PhD thesis, University of Cambridge, 2011.

[69] Hiraku Sakamoto, Yoji Shirasawa, Daisuke Haraguchi, Hirotaka Sawada, and Osamu Mori. A spin-up control scheme for contingency deployment of the sailcraft ikaros. In 52nd AIAA/ASME/ASCE/AHS/ASC Structures, Structural Dynamics, and Materials Conference, 2011.

[70] Jessica Morgan, Spencer P. Magleby, and Larry L. Howell. An approach to designing origami-adapted aerospace mechanisms. Journal of Mechanical Design, 138(5):052301–052311, March 2016.

[71] Hiroshi Furuya, Osamu Mori, Nobukatsu Okuizumi, Yoji Shirasawa, M. C. Natori, Yasuyuki Miyazaki, and Saburo Matanaga. Manufacturing and folding of solar sail 'ikaros'. In 52nd AIAA/ASME/ASCE/AHS/ASC Structures, Structural Dynamics and Materials Conference, 2011.

[72] Whitney D. Reynolds and Thomas W. Murphey. Elastic spiral folding for flat membrane apertures. In Spacecraft Structures Conference, 2014.

[73] M. C. Natori, Hiraku Sakamoto, Nobuhisa Katsumata, Hiroshi Yamakawa, and Naoko Kishimoto. Conceptual model study using origami for membrane space structures – a perspective of origami-based engineering. Mechanical Engineering Reviews, 2(1):1–15, 2015.

[74] Hiraku Sakamoto, M. C. Natori, Shogo Kadonishi, Yasutaka Satou, Yoji Shirasawa, Nobukatsu Okuizumi, Osamu Mori, Hiroshi Furuya, and Masaaki Okuma. Folding patterns of planar gossamer space structures consisting of membranes and booms hiraku. Acta Astronautica, 94:34–41, 2014.

[75] Jeremy A. Banik, Thomas W. Murphey, and Hans-Peter Dumm. Synchronous deployed solar sail concept demonstration. In 49th AIAA/ASME/ASCE/AHS/ASC Structures, Structural Dynamics, and Materials, Schaumburg, IL, April 2008.

[76] M. C. Natori, Nobuhisa Katsumata, Hiroshi Yamakawa, Hiraku Sakamoto, and Naoko Kishimoto. Conceptual model study using origami for membrane space structures. In Proceedings fo the ASME 2013 International Design Engineering Technical Conference and Computers and Information in Engineering Conference, 2013.

[77] Taketoshi Nojima. Origami modeling of functional structures based on organic patterns. Master's thesis, Graduate School of Kyoto University, Kyoto, Japan, 2002.

[78] Kazuya Saito, Akira Tsukahara, and Yoji Okabe. New deployable structures based on an elastic origami model. Journal of Mechanical Design, 137, 2015.

[79] Koryo Miura and Tomohiro Tachi. Synthesis of rigid-foldable cylindrical polyhedra. Symmetry: Art and Science, 2010.

[80] Robert Connelly. The rigidity of polyhedral surfaces. Mathematics Magazine, 52(5):275–283, 1979.

[81] Friedrich Bös, Max Wardetzky, Etienne Vouga, and Omer Gottesman. On the incompressibility of on the incompressibility of cylindrical origami patterns. Journal of Mechanical Design, 139, 2017.

[82] Yuchen Wei and Sergio Pellegrino. Modular foldable surfaces: a novel approach based on spatial mechanisms and thin shells. 4th AIAA Spacecraft Structures Conference, 2017.

[83] L. Puig, A. Barton, and N. Rando. A review on large deployable structures for astrophysics missions. Acta Astronautica, 2010.

[84] Sungeun K. Jeon and Thomas W. Murphey. Design and analysis of a meter-class cubesat boom with a motor-less deployment by bi-stable tape springs. 52nd AIAA/ASME/ASCE/AHS/ASC Structures, Structural Dynamics and Materials Conference, 2011.

[85] Whitney D. Reynolds, Thomas W. Murphey, and Jeremy A. Banik. Highly compact wrapped-gore deployable reflector. 52nd AIAA/ASME/ASCE/AHS/ASC Structures, Structural Dynamics and Materials Conference, 2011.

[86] David Webb, Brian Hirsch, Vinh Bach, Jonathan Sauder, Case Bradford, and Mark Thomson. Starshade mechanical architecture and technology effort. In 3rd AIAA Spacecraft Structures Conference, 2016.

[87] Whitney D. Reynolds and Thomas W. Murphey. Elastic spiral folding for flat membrane apertures. In AIAA SciTech Spacecraft Structures Conference, 2014.

[88] Jason S. Ku and Erik D. Demaine. Folding flat crease patterns with thick materials. CoRR, abs/1601.05747, 2016.

[89] Mark Schenk, Andrew D. Viquerat, Keith A. Seffen, and Simon D. Guest. Review of inflatable booms for deployable space structures: Packing and rigidization. Journal of Spacecraft and Rockets, 51(3):762–778, 2014.

[90] Witold M. Sokolowski and Seng C. Tan. Advanced self-deployable structures for space applications. Journal of Spacecraft and Rockets, 44(4):750–754, 2007.

[91] Fabio Santoni, Fabrizio Piergentili, Serena Donati, Massimo Perelli, Andrea Negri, and Michele Marino. An innovative deployable solar panel system for cubesats. Acta Astronautica, 95:210 – 217, 2014.

[92] Antonio Alessandro Deleo, James ONeil, Hiromi Yasuda, Marco Salviato, and Jinkyu Yang. Origami-based deployable structures made of carbon fiber reinforced polymer composites. Composites Science and Technology, 191:108060, 2020.

[93] Omer Soykasap, Sergio Pellegrino, Phil Howard, and Mike Notter. Tape Spring Large Deployable Antenna.

[94] Gina Olson, Sergio Pellegrino, Joseph Costantine, and Jeremy Banik. Structural Architectures for a Deployable Wideband UHF Antenna.

[95] A. Jain, G. Rodriguez, and K. Kreutz-Delgado. Multi-arm grasp and manipulation of objects with internal degrees of freedom. 1990.

[96] A. Jain, G. Rodriguez, and K. Kreutz-Delgado. Recursive dynamics of multiarm robotic systems in loose grasp of articulated task objects. 1990.

[97] Filipe Marques, Antnio P. Souto, and Paulo Flores. On the constraints violation in forward dynamics of multibody systems. Multibody System Dynamics, 39:385 – 419, 2017.

[98] Paulo Flores, Rui Pereira, Margarida Machado, and Eurico Seabra. Investigation on the baumgarte stabilization method for dynamic analysis of constrained multibody systems. M. Ceccarelli (ed.), Proceedings of EUCOMES 08, pages 305 – 312, 2009.

[99] H. M. Y. C. Mallikarachchi and S. Pellegrino. Quasi-static folding and deployment of ultrathin composite tape-spring hinges. Journal of Spacecraft and Rockets, 48(1):187198, 2011.

Appendix A

Lagrangian Approach to Dynamics Model Derivation

A.1 Introduction

Modeling the dynamics of deployable structure and spacecraft systems using a more efficient approach has not been investigated due to the complexity and lack of approach precedence in the literature. The deployment dynamics of complex deployable systems must be understood to verify deployment and to ensure mission success, and should be available early in the design process to enable more efficient and reliable designs. In this chapter, modeling the hinge behaviors in folded deployable structures as functions of the translational and rotational displacement is investigated using the Lagrangian dynamics method. This approach is applied to a prototypical single panel and a three panel folded structure on a host spacecraft. The system is studied and described using dynamics techniques traditionally developed for attitude dynamics and control to better understand how the structure's motion affects the spacecraft motion.

A.2 Modeling Approach

A simple example of a folded space structure is a z-folded solar array, where the fold pattern extends the structure linearly through single axis rotations. For the applications mentioned above, more complex patterns are needed, where panels are folded on multiple edges and undergo full three dimensional rotations through the fold. Therefore, these problems must be approached using full three dimensional rotational and translational descriptions, and will not be simplified to single degree of freedom kinematic chains. Additionally, the coupling of the panel behaviors and

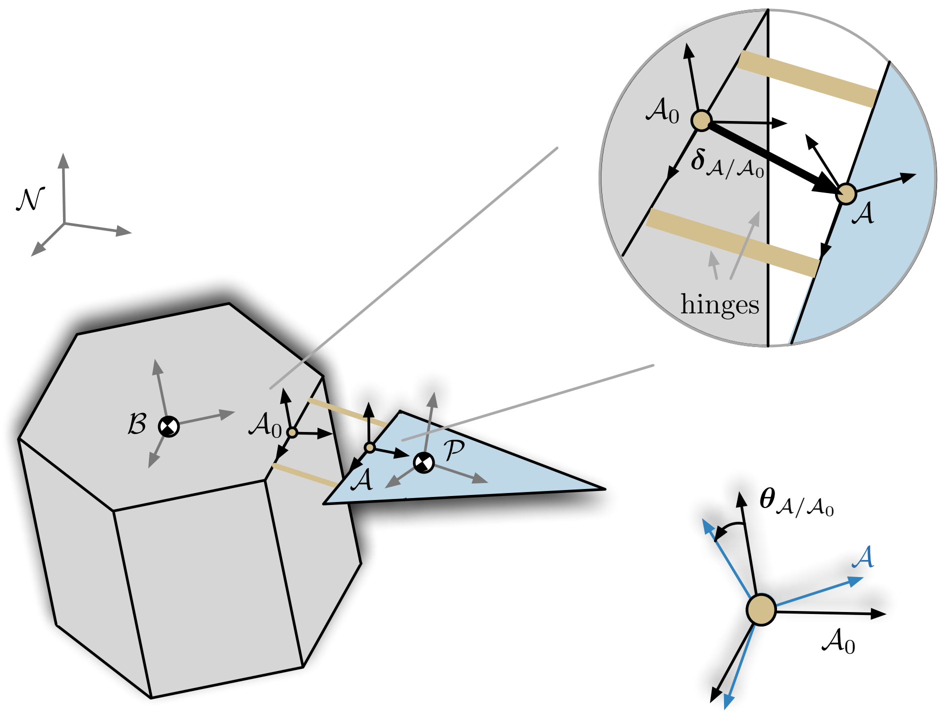

Figure A.1: Reference frame and relative coordinate definitions of one panel.

the spacecraft attitude are of primary concern. Therefore, intuitive relations between the panel descriptions and the hub descriptions are pursued. The modeling approach is developed using energy-based dynamics modeling methods, particularly Lagrange's Equations, to create full multi-body dynamics models. This method works well for derivations of n-body problems such as this, where energy can be described in general coordinates for each panel set. The equations of motion as found through Lagrange's Equation is expressed generally as

$$\frac{\partial}{\partial t}\frac{\partial T}{\partial \dot{q}_i} - \frac{\partial T}{\partial q_i} = Q_i \tag{A.1}$$

where Q_i is the generalized force and can represent conservative and non-conservative forces and torques, T is the kinetic energy of the system, and q_i are the generalized coordinates. There are many ways to describe these three components, and the formulation will become less trivial as the model expands across larger structure flashers. The generalized coordinates of each rigid sub-component contains 6 degrees of freedom, which are best described in either global position and orientations or relative position and orientations. The trade here is due to kinetic energy being a function of global terms, and the generalized forces being a function of the relative terms. The definition of the relative terms, $\boldsymbol{\delta}_{\mathcal{A}/\mathcal{A}_0}$ and $\boldsymbol{\theta}_{\mathcal{A}/\mathcal{A}_0}$, are illustrated in Figure A.1 on a single panel example. The body-fixed $\mathcal{A}_0$ frame represents the position and orientation at which there are no restorative forces or torques acting between the two bodies. The panel-fixed $\mathcal{A}$ frame represents the actual position and orientation of the panel relative to this reference, and when these two frames are aligned, there are no internal hinge forces or torques in the system.

In this approach, the relative term descriptions are needed for integrating empirical models of flexible hinge behaviors into the multi-body dynamics simulation. Experiments on hinge force and torque responses can be conducted on a single hinge test article for all possible combinations of displacement and orientation. A mathematical approximation of the hinge behavior as a function of the relative coordinates would be ideal, however even without a mathematical fit, a interpolation over a look up table would also provide this. Therefore, the generalized forces are written in terms of the relative position displacement and relative orientation of the attached panel. All forces are modeled as generalized forces Q_i, instead of using potential functions, as this study is interested in developing a framework where any forces written as functions of the hinge displacement and orientation relative to the body can be applied.

A.3 Spacecraft Bus and Single Panel Model Derivation

A.3.1 Equations of Motion Development

A single panel case is first considered to develop the hinge representation expressions. This case is set up as two general bodies representing a spacecraft bus and a rigid panel. The spacecraft bus center of mass position, $\boldsymbol{R}_{\mathcal{B}/\mathcal{N}}$, and orientation, $\boldsymbol{\theta}_{\mathcal{B}/\mathcal{N}}$, are unconstrained and tracked through inertial space. For this study the body orientation is parameterized using 3-2-1 Euler Angles, but any attitude parameterization can be applied. The spacecraft bus kinetic energy is then determined through

$$T_B = \frac{1}{2}\boldsymbol{\omega}_{\mathcal{B}/\mathcal{N}}[I_{\mathcal{B}}]\boldsymbol{\omega}_{\mathcal{B}/\mathcal{N}} + \frac{1}{2}m_B\dot{\boldsymbol{R}}_{\mathcal{B}/\mathcal{N}} \cdot \dot{\boldsymbol{R}}_{\mathcal{B}/\mathcal{N}} \tag{A.2}$$

Where the $\mathcal{B}$ frame is a body fixed frame and $\mathcal{N}$ indicates an inertial frame. A diagram of the required reference frames is shown in Figure A.1. Additionally, $\boldsymbol{\omega}_{\mathcal{B}/\mathcal{N}}$ is the rotation rate of the body with respect to the inertial frame, $[I_B]$ is the body inertia tensor, m_B is the body mass, and $\dot{\boldsymbol{R}}_{\mathcal{B}/\mathcal{N}}$ is the inertial velocity of the body. Similarly, the kinetic energy of the panel is written in a general form, for a panel fixed frame $\mathcal{P}$, as

$$T_P = \frac{1}{2}\boldsymbol{\omega}_{\mathcal{P}/\mathcal{N}}[I_P]\boldsymbol{\omega}_{\mathcal{P}/\mathcal{N}} + \frac{1}{2}m_P\dot{\boldsymbol{R}}_{\mathcal{P}/\mathcal{N}} \cdot \dot{\boldsymbol{R}}_{\mathcal{P}/\mathcal{N}} \tag{A.3}$$

Where $\boldsymbol{\omega}_{\mathcal{P}/\mathcal{N}}$ is the rotation rate of the panel with respect to the inertial frame, $[I_P]$ is the panel inertia tensor, m_P is the panel mass, and $\dot{\boldsymbol{R}}_{\mathcal{P}/\mathcal{N}}$ is the inertial velocity of the panel.

Then the total kinetic energy of the system is the sum of these two contributions. The generalized coordinates are selected to include the spacecraft states as expressed in the spacecraft body frame, and the panel relative coordinates as expressed in the zero-orientation $\mathcal{A}_0$ frame,

$$\boldsymbol{q} = \begin{bmatrix} {}^{\mathcal{B}}\boldsymbol{R}_{\mathcal{B}/\mathcal{N}} & {}^{\mathcal{B}}\boldsymbol{\theta}_{\mathcal{B}/\mathcal{N}} & {}^{\mathcal{A}_0}\boldsymbol{\delta}_{\mathcal{A}/\mathcal{A}_0} & {}^{\mathcal{A}_0}\boldsymbol{\theta}_{\mathcal{A}/\mathcal{A}_0} \end{bmatrix}^{\mathsf{T}} \tag{A.4}$$

Where the inertial position of the panel is

$$\boldsymbol{R}_{\mathcal{P}/\mathcal{N}} = \boldsymbol{r}_{\mathcal{P}/\mathcal{A}} + \boldsymbol{\delta}_{\mathcal{A}/\mathcal{A}_0} + \boldsymbol{r}_{\mathcal{A}_0/\mathcal{B}} + \boldsymbol{R}_{\mathcal{B}/\mathcal{N}} \tag{A.5}$$

the inertial velocity is determined using the transport theorem,[28] where each position vector is expressed in a convenient frame. The inertial velocity is a function of the position and the rate of the frame it is expressed in with respect to the inertial frame. This presents the need for careful frame selection and expression. To develop the most general solution, each vector will be expressed in the spacecraft body frame. Then the velocity expression is

$$\dot{\boldsymbol{R}}_{\mathcal{P}/\mathcal{N}} = \frac{{}^{\mathcal{B}}\mathrm{d}}{\mathrm{d}t}\left(\boldsymbol{r}_{\mathcal{P}/\mathcal{A}} + \boldsymbol{\delta}_{\mathcal{A}/\mathcal{A}_0} + \boldsymbol{R}_{\mathcal{B}/\mathcal{N}}\right) + \boldsymbol{\omega}_{\mathcal{B}/\mathcal{N}} \times \boldsymbol{R}_{\mathcal{P}/\mathcal{N}} \tag{A.6}$$

To express each relative position vector in the body frame, the transformation of the vector's expressed frame to the body frame is needed. The relative orientation of the hinge attachment frames, the $\mathcal{A}$ and $\mathcal{A}_0$ frames, to their fixed bodies, the $\mathcal{P}$ and $\mathcal{B}$ frames respectively, are defined for any general configuration and recorded as 3-2-1 Euler Angles. This allows flexibility in the system assembly and keeps the analysis applicable to all panel shapes and configurations. The relative orientation between each frame is then converted to corresponding direction cosine matrices. The frames are illustrated in Figure A.1, and because the $\mathcal{A}_0$ frame is fixed in the $\mathcal{B}$ frame, the orientation is time invariant. Similarly, the orientation of the attachment origin on the panel frame relative to the panel, $\mathcal{A}$, is time invariant. Then the relative orientations are

$$[\mathcal{P}\mathcal{A}] = f(\theta_{1,\mathcal{P}/\mathcal{A}}, \theta_{2,\mathcal{P}/\mathcal{A}}, \theta_{3,\mathcal{P}/\mathcal{A}}) \tag{A.7a}$$

$$[\mathcal{B}\mathcal{A}_0] = f(\theta_{1,\mathcal{B}/\mathcal{A}_0}, \theta_{2,\mathcal{B}/\mathcal{A}_0}, \theta_{3,\mathcal{B}/\mathcal{A}_0}) \tag{A.7b}$$

Additionally, the transformations of the generalized orientations are

$$[\mathcal{A}\mathcal{A}_0] = f(\theta_{1,\mathcal{A}/\mathcal{A}_0}(t), \theta_{2,\mathcal{A}/\mathcal{A}_0}(t), \theta_{3,\mathcal{A}\mathcal{A}_0}(t)) \tag{A.8a}$$

$$[\mathcal{B}\mathcal{N}] = f(\theta_{1,\mathcal{B}\mathcal{N}}(t), \theta_{2,\mathcal{B}\mathcal{N}}(t), \theta_{3,\mathcal{B}\mathcal{N}}(t)) \tag{A.8b}$$

The relative orientation between the $\mathcal{P}$ and $\mathcal{N}$ frames are determined then from direction cosine matrices as

$$[\mathcal{P}\mathcal{N}] = [\mathcal{P}\mathcal{A}][\mathcal{A}\mathcal{A}_0][\mathcal{B}\mathcal{A}_0]^{\mathsf{T}}[\mathcal{B}\mathcal{N}] \tag{A.9}$$

This orientation matrix models how the panel rotates relative to the inertial frame and is needed to express the panel inertial rate in the kinetic energy function, where the kinematic differential equation of this orientation is known for 3-2-1 Euler Angles.[28] This attitude is highly nonlinear expression as a function of the time variant general coordinates $\boldsymbol{\theta}_{\mathcal{B}/\mathcal{N}}(t)$ and $\boldsymbol{\theta}_{\mathcal{A}/\mathcal{A}_0}(t)$, as well as the offset orientations $[\mathcal{AP}]$ and $[\mathcal{BA}_0]$.

A.3.2 Elastic Hinge Force and Torque Derivation

Now the interactions between these two bodies are to be defined, where the two bodies interact only through the elastic hinge connection. The contributions from elastic hinges are implemented as restorative forces and torques as a function of the relative displacements and rotations between the two bodies. To do this, a relative equilibrium state is defined such that when the bodies reach this state, there are no internal forces or torques acting between the bodies. In this study, these forcing functions are generic place holder representations, however in future studies, these will be replaced with functions that are determined empirically for a given hinge material. The relative states are tracked through two reference frames, an equilibrium frame, $\mathcal{A}_0$, at which zero force and torque is experienced, and a true position frame, $\mathcal{A}$, as depicted in Figure A.1. The equilibrium frame is fixed in the body frame, however it does not share the same position or orientation as the body center of mass because these forces and torques are not acting directly at the body center of mass. Conversely, the relative position frame is fixed in the panel frame.

Here a derivation of the relative force and torque between two bodies is presented. The classical definition for N generalized forces Q_j is[28,33]

$$Q_j = \sum_{i=1}^{N} \boldsymbol{f}_i \cdot \frac{\partial \boldsymbol{R}_i}{\partial q_j} \tag{A.10}$$

where $\boldsymbol{R}_i$ is the location of the point where the force is being applied. The generalized force expression of a pure inertial torque, $\boldsymbol{L}$ acting on an arbitrary body $\mathcal{E}$, is derived from this as[28]

$$Q_j = \boldsymbol{\tau} \cdot \frac{\partial \boldsymbol{\omega}_{\mathcal{E}/\mathcal{N}}}{\partial \dot{q}_j} \tag{A.11}$$

The internal restorative force and torque of the hinge will act in equal and opposite sense on the bus and panel, however, they will not be acting on the same locations in inertial space due to the displacement of the hinge. Therefore these force and torque vectors are expressed in general coordinates as follows

$$Q_j = \boldsymbol{F}_{\mathcal{A}/\mathcal{A}_0} \cdot \frac{\partial \boldsymbol{R}_{\mathcal{A}_0/\mathcal{N}}}{\partial q_j} - \boldsymbol{F}_{\mathcal{A}/\mathcal{A}_0} \cdot \frac{\partial \boldsymbol{R}_{\mathcal{A}/\mathcal{N}}}{\partial q_j} + \boldsymbol{\tau}_{\mathcal{A}/\mathcal{A}_0} \cdot \frac{\partial \boldsymbol{\omega}_{\mathcal{A}_0/\mathcal{N}}}{\partial \dot{q}_j} - \boldsymbol{\tau}_{\mathcal{A}/\mathcal{A}_0} \cdot \frac{\partial \boldsymbol{\omega}_{\mathcal{A}/\mathcal{N}}}{\partial \dot{q}_j} \tag{A.12}$$

Recognizing that the bus and panel are each rigid bodies and expanding yields

$$\begin{aligned} Q_j = \boldsymbol{F}_{\mathcal{A}/\mathcal{A}_0} \cdot \frac{\partial \boldsymbol{R}_{\mathcal{A}_0/\mathcal{N}}}{\partial q_j} - \boldsymbol{F}_{\mathcal{A}/\mathcal{A}_0} \cdot \frac{\partial (\boldsymbol{\delta}_{\mathcal{A}_0/\mathcal{A}} + \boldsymbol{R}_{\mathcal{A}_0/\mathcal{N}})}{\partial q_j} \\ + \boldsymbol{\tau}_{\mathcal{A}/\mathcal{A}_0} \cdot \frac{\partial \boldsymbol{\omega}_{\mathcal{B}/\mathcal{N}}}{\partial \dot{q}_j} - \boldsymbol{\tau}_{\mathcal{A}/\mathcal{A}_0} \cdot \frac{(\partial \boldsymbol{\omega}_{\mathcal{A}/\mathcal{A}_0} + \partial \boldsymbol{\omega}_{\mathcal{B}/\mathcal{N}})}{\partial \dot{q}_j} \end{aligned} \tag{A.13}$$

Simplifying, the positions and rates relative to inertial cancel out to the following expression

$$Q_j = -\boldsymbol{F}_{\mathcal{A}/\mathcal{A}_0}(\boldsymbol{\delta}_{\mathcal{A}_0/\mathcal{A}}(t)) \cdot \frac{\partial \boldsymbol{\delta}_{\mathcal{A}_0/\mathcal{A}}(t)}{\partial q_j} - \boldsymbol{\tau}_{\mathcal{A}/\mathcal{A}_0}(\boldsymbol{\theta}_{\mathcal{A}/\mathcal{A}_0}(t)) \cdot \frac{\partial \boldsymbol{\omega}_{\mathcal{A}/\mathcal{A}_0}(\boldsymbol{\theta}_{\mathcal{A}/\mathcal{A}_0}(t))}{\partial \dot{q}_j} \tag{A.14}$$

This reduction reveals that the generalized forces can be expressed as a function of the relative displacement and relative orientation only, a desirable simplification. Finally, the force and torque expressions must be defined. For this study, the forces and torques are written as linear spring functions for the sake of simplicity of verification.

$$\boldsymbol{F} = [K_F]\boldsymbol{\delta}_{\mathcal{A}/\mathcal{A}_0}(t) \tag{A.15a}$$

$$\boldsymbol{\tau} = [K_\theta]\begin{bmatrix} \theta_{3,\mathcal{A}/\mathcal{A}_0}(t) & \theta_{2,\mathcal{A}/\mathcal{A}_0}(t) & \theta_{1,\mathcal{A}/\mathcal{A}_0}(t) \end{bmatrix}^\mathsf{T} \tag{A.15b}$$

An advantage to building the hinge model using this approach is the ability to tune these forcing functions to investigate desired behaviors. For example, a major desire for deployment dynamics is damping the motion to achieve rest at full deployment, avoiding kickback and energy dissipation through undesirable material deformations. By including a damping term in this expression, the required damping properties of a material or device can be investigated. Additionally, in cases where a given motion is negligible, constraint forces can be used to arrest the motion in the simulation.

A.4 Spacecraft Bus and Single Panel Model Initialization and Validation

The derivation discussed above is carried out using symbolic tools in Mathematica to auto-generate the equations of motion. The script is written in a general way, such that only the spacecraft and panel mass, inertia, and configuration properties are needed to generate a model. Additionally, the model is verified using numerical tools in Mathematica, where only the state initial conditions are required for the simulation. Generation of the generalized forces is also built in a general way, such that any internal hinge force and torque functions can be given to the system.

Knowledge of the spacecraft bus and rigid panel mass and inertia properties is needed, as well as the reference frame configurations in the zero-force orientation. This information is generated here for a simple model in Table A.1 and Table A.2. Additionally, general initial conditions are generated for this simulation to test the model's performance across all generalized coordinates and are reported in Table A.3. However, in a real deployment test scenario, these initial conditions would be generated to simulate the deployable structure's stowed configuration and would be entirely dependent on the kinematic behavior of the flasher pattern and on constraints of the hinge and panel materials.

Table A.1: Mass and principle inertia parameters of the single panel simulation.

m_B (kg)	m_P (kg)	I_B (kg/m^2)	I_P (kg/m^2)
100	10	$[100, 100, 100]$	$[1, 1, 1]$

Table A.2: Relative positions and orientations of the single panel simulation.

$\boldsymbol{r}_{\mathcal{A}_0/\mathcal{B}}$	$\boldsymbol{\theta}_{\mathcal{A}_0/\mathcal{B}}$	$\boldsymbol{r}_{\mathcal{P}/\mathcal{A}}$	$\boldsymbol{\theta}_{\mathcal{P}/\mathcal{A}}$
$[0.75, 0.433, 0]$ m	$[0, 0, 30]$ deg	$[1, 1, 0]$ m	$[0, 0, 0]$ deg

The results of a verification simulation run are displayed in Figure A.2. The angular momentum is observed to maintain an effective zero momentum, indicating that the forces and torques act internally and only produce relative motion. This is further verified by tracking the barycenter of the bus and panel system and observing that it maintains a constant position through the simulation, indicating all forces and torques act internally.

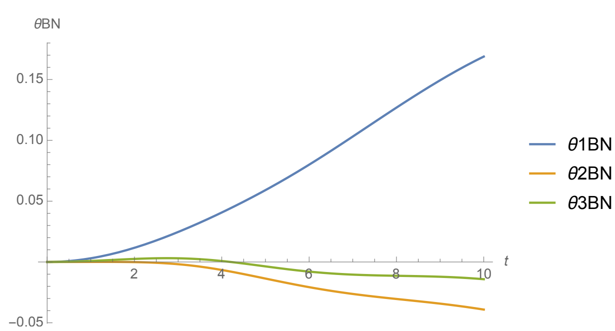

(a) Bus Orientation

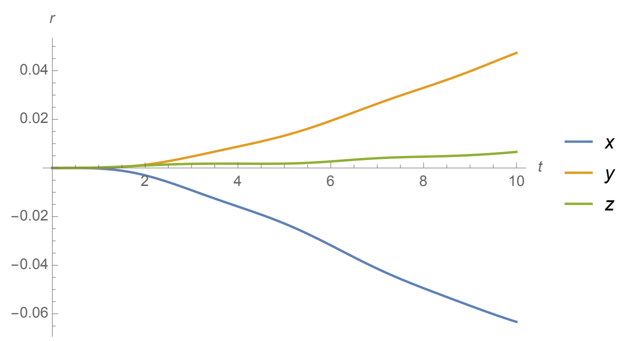

(b) B Frame Bus Position

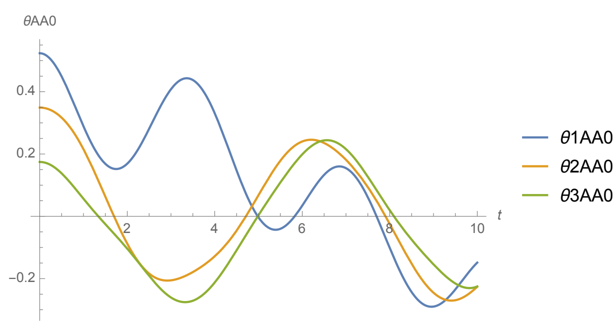

(c) Panel Orientation

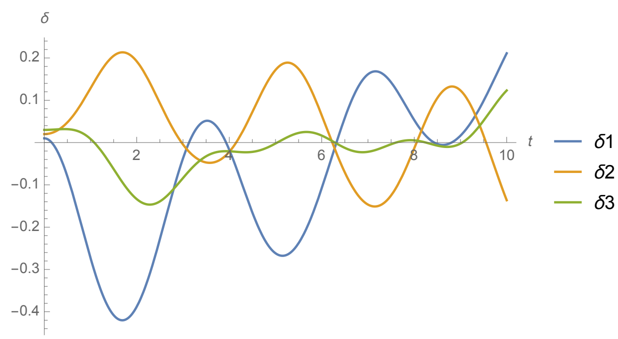

(d) Panel Displacement

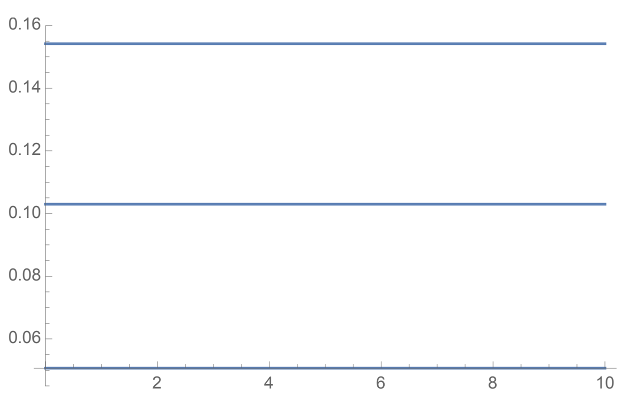

(e) System Barycenter

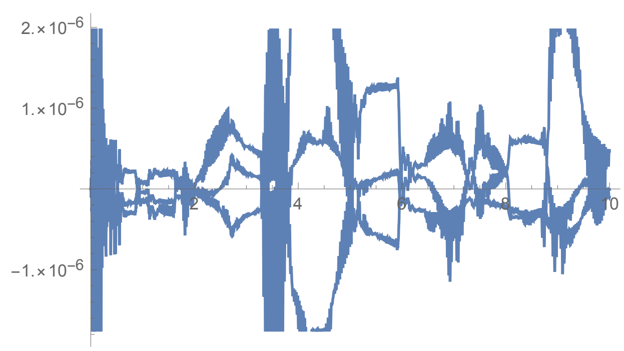

(f) Angular Momentum

Figure A.2: Single panel simulation results and validations.

Table A.3: Initial conditions of the single panel simulation.

$\boldsymbol{R}_{\mathcal{B}/\mathcal{N}}(0)$	$\boldsymbol{\theta}_{\mathcal{B}/\mathcal{N}}(0)$	$\boldsymbol{\delta}(0)$	$\boldsymbol{\theta}_{\mathcal{P}/\mathcal{N}}(0)$
$\mathbf{0}$	$\mathbf{0}$	$[1, 1, 1]$ cm	$[10, 20, 30]$ deg

A.5 Multiple Panel Set Model

A.5.1 Equations of Motion Development

The approach outlined for the single panel case are now expanded to a 4-body, 3-panel case with panel-to-panel interconnections. The derivation for this case is written as generally as possible, where further extrapolation to greater sets of panels would be carried out using the same approach. The model is limited to 3 panels to maintain traceability for the reader. For any N panels, the total kinetic energy of the system is written as

$$T = \frac{1}{2}\boldsymbol{\omega}_{\mathcal{B}/\mathcal{N}}[I_{\mathcal{B}}]\boldsymbol{\omega}_{\mathcal{B}/\mathcal{N}} + \frac{1}{2}m_B\dot{\boldsymbol{R}}_{\mathcal{B}/\mathcal{N}} \cdot \dot{\boldsymbol{R}}_{\mathcal{B}/\mathcal{N}} + \sum_{i=1}^{N}\left[\frac{1}{2}\boldsymbol{\omega}_{\mathcal{P}_i/\mathcal{N}}[I_{\mathcal{P}_i}]\boldsymbol{\omega}_{\mathcal{P}_i/\mathcal{N}} + \frac{1}{2}m_{P_i}\dot{\boldsymbol{R}}_{\mathcal{P}_i/\mathcal{N}} \cdot \dot{\boldsymbol{R}}_{\mathcal{P}_i/\mathcal{N}}\right] \tag{A.16}$$

The relative generalized coordinates will be selected for this model to simplify identifying desired initial conditions and the zero force and torque configurations. Therefore the generalize coordinates are

$$\boldsymbol{q} = \begin{bmatrix} {}^{\mathcal{B}}\boldsymbol{R}_{\mathcal{B}/\mathcal{N}} & {}^{\mathcal{B}}\boldsymbol{\theta}_{\mathcal{B}/\mathcal{N}} & {}^{\mathcal{A}_{0,1}}\boldsymbol{\delta}_{\mathcal{A}_1/\mathcal{A}_{0,1}} & {}^{\mathcal{A}_{0,1}}\boldsymbol{\theta}_{\mathcal{A}_1/\mathcal{A}_{0,1}} & {}^{\mathcal{A}_{0,2}}\boldsymbol{\delta}_{\mathcal{A}_2/\mathcal{A}_{0,2}} \\ {}^{\mathcal{A}_{0,2}}\boldsymbol{\theta}_{\mathcal{A}_2/\mathcal{A}_{0,2}} & {}^{\mathcal{A}_{0,3,1}}\boldsymbol{\delta}_{\mathcal{A}_{0,3,1}/\mathcal{A}_{3,1}} & {}^{\mathcal{A}_{0,3,1}}\boldsymbol{\theta}_{\mathcal{A}_{0,3,1}/\mathcal{A}_{3,1}} \end{bmatrix}^{\mathsf{T}} \tag{A.17}$$

Then the inertial position of each panel will have dependencies on the relative position of itself and any connecting panels. For panels adjacent to the body, or in this example, for i = 1,2

$$\boldsymbol{R}_{\mathcal{P}_i/\mathcal{N}} = \boldsymbol{r}_{\mathcal{P}_i/\mathcal{A}_i} + \boldsymbol{\delta}_{\mathcal{A}_i/\mathcal{A}_{0,i}} + \boldsymbol{r}_{\mathcal{A}_{0,i}/\mathcal{B}} + \boldsymbol{R}_{\mathcal{B}/\mathcal{N}} \tag{A.18}$$

The inertial position vector of the 3rd panel is

$$\boldsymbol{R}_{\mathcal{P}_3/\mathcal{N}} = \boldsymbol{r}_{\mathcal{P}_3/\mathcal{A}_{3,1}} + \boldsymbol{\delta}_{\mathcal{A}_{3,1}/\mathcal{A}_{0,3,1}} + \boldsymbol{r}_{\mathcal{P}_1/\mathcal{A}_1} + \boldsymbol{\delta}_{\mathcal{A}_1/\mathcal{A}_{0,1}} + \boldsymbol{r}_{\mathcal{A}_{0,1}/\mathcal{B}} + \boldsymbol{R}_{\mathcal{B}/\mathcal{N}} \tag{A.19}$$

Again, the inertial velocity of each panel body is determined using the transport theorem,[28] where multiple reference frames are now in use. The frames for expression of these position descriptions

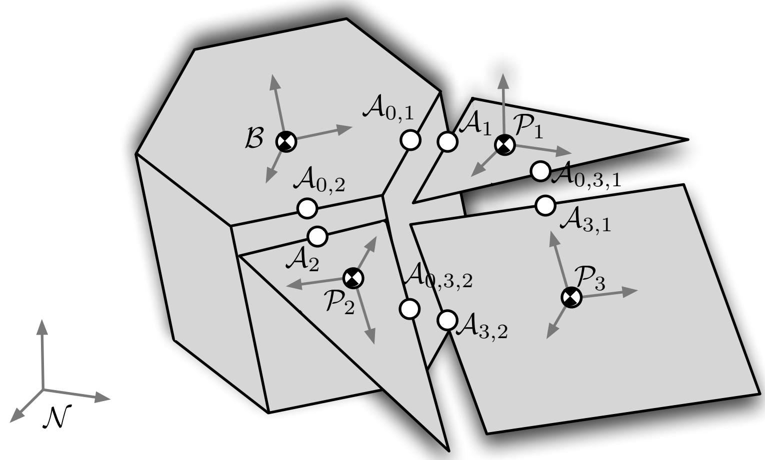

Figure A.3: Reference frame definitions of a 3 panel case.

are chosen to simplify these calculations, however it is not possible to avoid a resulting expression that is heavily non-linear and coupled across the generalized coordinates.

A.5.2 Generalized Forces for Multiple Panel Connections

The interdependence of the third panel is observed in Figure A.3 where displacement and orientation of the panel must be known with respect to the two adjacent panels. However, the generalized coordinates selected only track one of these relative states to avoid a redundant and over-constrained system. Therefore, the other relative state must be backed out through the kinematic chain as follows, coupling the motion to the adjacent panel.

$$\boldsymbol{\delta}_{\mathcal{A}_{0,3,2}/\mathcal{A}_{3,2}} = (\boldsymbol{r}_{\mathcal{A}_{0,3,2}/\mathcal{P}_2} + \boldsymbol{R}_{\mathcal{P}_2/\mathcal{N}}) - (\boldsymbol{R}_{\mathcal{P}_3/\mathcal{N}} - \boldsymbol{r}_{\mathcal{P}_3/\mathcal{A}_{3,2}}) \tag{A.20}$$

Additionally, the rotation rates of the third panel with respect to the second must be calculated from the rates of the adjacent bodies

$$\boldsymbol{\omega}_{\mathcal{A}_{0,3,2}/\mathcal{A}_{3,2}} = \boldsymbol{\omega}_{\mathcal{A}_{0,2}/\mathcal{A}_2} - (\boldsymbol{\omega}_{\mathcal{A}_{0,1}/\mathcal{A}_1} + \boldsymbol{\omega}_{\mathcal{A}_{0,3,1}/\mathcal{A}_{3,1}}) \tag{A.21}$$

With these two additional relationships, the generalized forces and torques can be determined. The simplification found in Equation A.14 be used for the force and torque of each hinge, where the generalized forces acting on the system are the sum of the generalized forces generated by each hinge. The total generalized force expression for the system is the sum of these body forces and torques across the system.

$$\begin{aligned}
Q_j = &-\boldsymbol{F}_{\mathcal{B}/\mathcal{P}_1}(\boldsymbol{\delta}_{\mathcal{A}_{0,1}/\mathcal{A}_1}(t)) \cdot \frac{\partial \boldsymbol{\delta}_{\mathcal{A}_{0,1}/\mathcal{A}_1}(t)}{\partial q_j} - \boldsymbol{\tau}_{\mathcal{B}/\mathcal{P}_1}(\boldsymbol{\theta}_{\mathcal{A}_{0,1}/\mathcal{A}_1}(t)) \cdot \frac{\partial \boldsymbol{\omega}_{\mathcal{A}_{0,1}/\mathcal{A}_1}(\boldsymbol{\theta}_{\mathcal{A}_{0,1}/\mathcal{A}_1}(t))}{\partial \dot{q}_j} \\
&- \boldsymbol{F}_{\mathcal{B}/\mathcal{P}_2}(\boldsymbol{\delta}_{\mathcal{A}_{0,2}/\mathcal{A}_2}(t)) \cdot \frac{\partial \boldsymbol{\delta}_{\mathcal{A}_{0,2}/\mathcal{A}_2}(t)}{\partial q_j} - \boldsymbol{\tau}_{\mathcal{B}/\mathcal{P}_2}(\boldsymbol{\theta}_{\mathcal{A}_{0,2}/\mathcal{A}_2}(t)) \cdot \frac{\partial \boldsymbol{\omega}_{\mathcal{A}_{0,2}/\mathcal{A}_2}(\boldsymbol{\theta}_{\mathcal{A}_{0,2}/\mathcal{A}_2}(t))}{\partial \dot{q}_j} \\
&- \boldsymbol{F}_{\mathcal{P}_3/\mathcal{P}_1}(\boldsymbol{\delta}_{\mathcal{A}_{0,3,1}/\mathcal{A}_{3,1}}(t)) \cdot \frac{\partial \boldsymbol{\delta}_{\mathcal{A}_{0,3,1}/\mathcal{A}_{3,1}}(t)}{\partial q_j} \\
&- \boldsymbol{\tau}_{\mathcal{P}_3/\mathcal{P}_1}(\boldsymbol{\theta}_{\mathcal{A}_{0,3,1}/\mathcal{A}_{3,1}}(t)) \cdot \frac{\partial \boldsymbol{\omega}_{\mathcal{A}_{0,3,1}/\mathcal{A}_{3,1}}(\boldsymbol{\theta}_{\mathcal{A}_{0,3,1}/\mathcal{A}_{3,1}}(t))}{\partial \dot{q}_j} \\
&- \boldsymbol{F}_{\mathcal{P}_3/\mathcal{P}_2}(\boldsymbol{\delta}_{\mathcal{A}_{0,3,2}/\mathcal{A}_{3,2}}(t)) \cdot \frac{\partial \boldsymbol{\delta}_{\mathcal{A}_{0,3,2}/\mathcal{A}_{3,2}}(t)}{\partial q_j} \\
&- \boldsymbol{\tau}_{\mathcal{P}_3/\mathcal{P}_2}(\boldsymbol{\theta}_{\mathcal{A}_{0,3,2}/\mathcal{A}_{3,2}}(t)) \cdot \frac{\partial \boldsymbol{\omega}_{\mathcal{A}_{0,3,2}/\mathcal{A}_{3,2}}(\boldsymbol{\theta}_{\mathcal{A}_{0,3,2}/\mathcal{A}_{3,2}}(t))}{\partial \dot{q}_j}
\end{aligned} \tag{A.22}$$

Where the forces and torques are functions of the displacements at the hinge indicated in the subscripts. As with the one panel simulation, these forces and torques are tested as simple linear spring functions as defined in Equation A.15. The equations of motion of this system can now be generated using Equations A.16 and A.22 in Equation A.1. This results in a system of 24 equations for the 24 generalized coordinates selected.

A.6 Three Panel Model Initialization and Validation

The spacecraft bus and rigid panel mass and inertia properties, position and orientation parameters, and initial conditions are generated here for a multiple panel model in Table A.4, Table A.5, Table A.6, and Table A.7, respectively. These parameters represent a simple toy case that is designed to test performance across the generalized coordinates. The results of the 3 panel case simulation run are shown in Figure A.4.

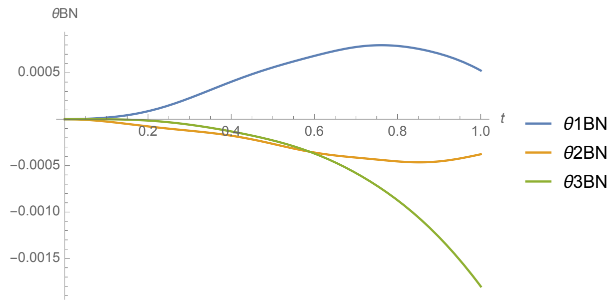

(a) Bus Orientation

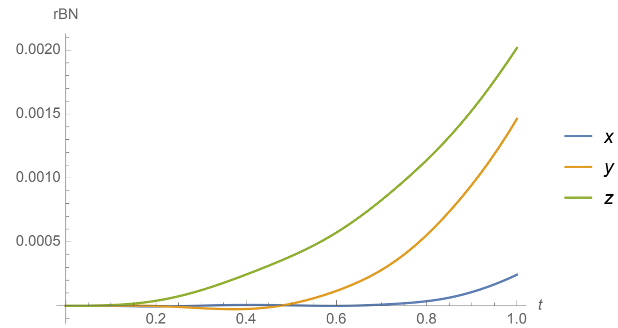

(b) B Frame Bus Position

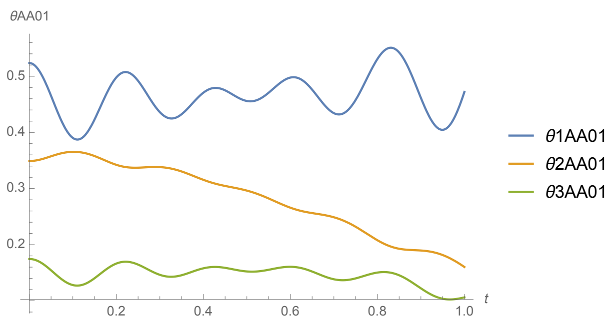

(c) Panel 1 Orientation

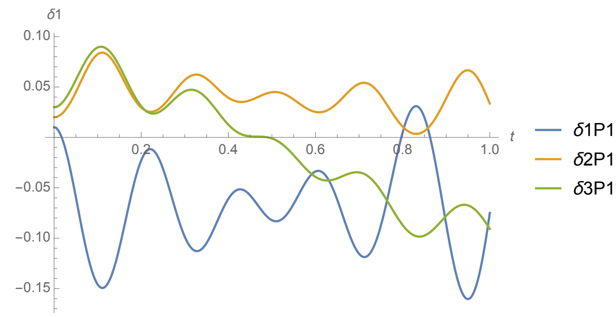

(d) Panel 1 Displacement

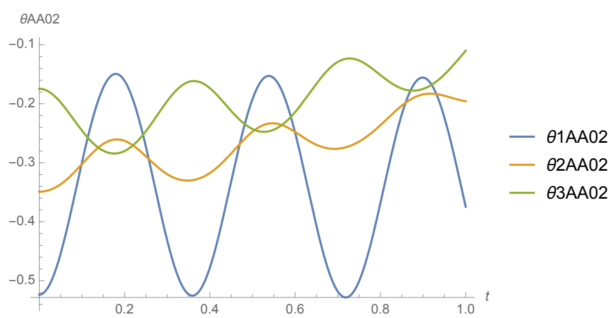

(e) Panel 2 Orientation

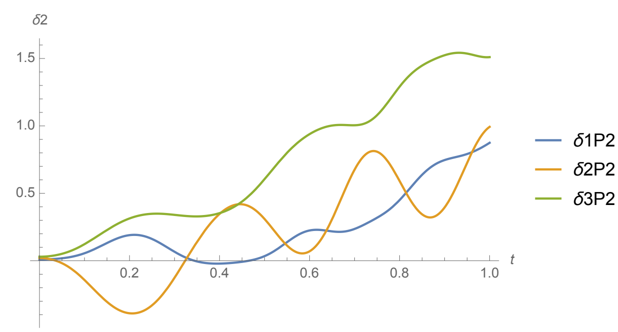

(f) Panel 2 Displacement

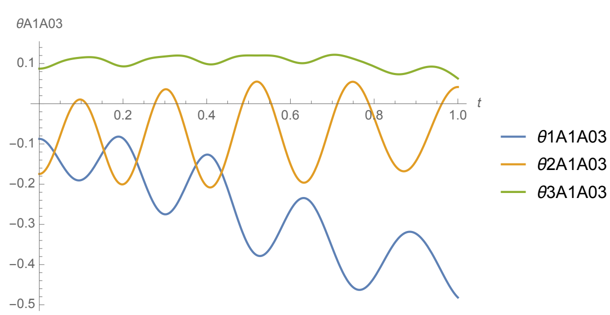

(g) Panel 3 Orientation

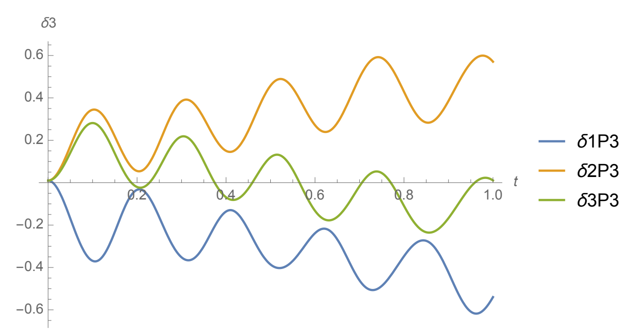

(h) Panel 3 Displacement

Figure A.4: Three panel simulation results.

Table A.4: Model parameters of the single panel simulation check, mass is in kg and inertia is in (kg/m^2) and shows the principle inertias.

m_B	m_{P_1}	m_{P_2}	m_{P_3}	I_B	I_{P_1}	I_{P_2}	I_{P_3}
100	7	7	9	$[100, 100, 100]$	$[1, 1, 0.1]$	$[1, 1, 0.1]$	$[1, 1, 0.1]$

Table A.5: Relative positions (m) of the single panel simulation check.

$\boldsymbol{r}_{\mathcal{A}_{0,1}/\mathcal{B}}$	$\boldsymbol{r}_{\mathcal{A}_{0,2}/\mathcal{B}}$	$\boldsymbol{r}_{\mathcal{P}_1/\mathcal{A}_1}$	$\boldsymbol{r}_{\mathcal{P}_2/\mathcal{A}_2}$	$\boldsymbol{r}_{\mathcal{P}_1/\mathcal{A}_{3,1}}$	$\boldsymbol{r}_{\mathcal{P}_2/\mathcal{A}_{3,2}}$
$[0.75, 0.433, 0]$	$[-0.75, -0.433, 0]$	$[1, 1, 0]$	$[1, 1, 0]$	$[1, 1, 0]$	$[1, 1, 0]$

Table A.6: Relative orientations (deg) of the single panel simulation check.

$\boldsymbol{\theta}_{\mathcal{A}_{0,1}/\mathcal{B}}$	$\boldsymbol{\theta}_{\mathcal{A}_{0,2}/\mathcal{B}}$	$\boldsymbol{\theta}_{\mathcal{P}_1/\mathcal{A}_1}$	$\boldsymbol{\theta}_{\mathcal{P}_2/\mathcal{A}_2}$	$\boldsymbol{\theta}_{\mathcal{P}_1/\mathcal{A}_{3,1}}$	$\boldsymbol{\theta}_{\mathcal{P}_2/\mathcal{A}_{3,2}}$
$[0, 0, 30]$	$[0, 0, -30]$	$[0, 0, 0]$	$[0, 0, 0]$	$[0, 0, 45]$	$[0, 0, 45]$

Table A.7: Initial conditions of the single panel simulation check.

$\boldsymbol{R}_{\mathcal{B}/\mathcal{N}}(0)$	$\boldsymbol{\delta}_{\mathcal{A}_1/\mathcal{A}_{0,1}}(0)$	$\boldsymbol{\delta}_{\mathcal{A}_2/\mathcal{A}_{0,2}}(0)$	$\boldsymbol{\delta}_{\mathcal{A}_{0,3,1}/\mathcal{A}_{3,1}}(0)$
$\mathbf{0}$	$[0.01, 0.02, 0.03]$	$[0.01, 0.02, 0.03]$	$[0.01, 0.01, 0.01]$
$\boldsymbol{\theta}_{\mathcal{B}/\mathcal{N}}(0)$	$\boldsymbol{\theta}_{\mathcal{A}_1/\mathcal{A}_{0,1}}(0)$	$\boldsymbol{\theta}_{\mathcal{A}_2/\mathcal{A}_{0,2}}(0)$	$\boldsymbol{\theta}_{\mathcal{A}_{0,3,1}/\mathcal{A}_{3,1}}(0)$
$\mathbf{0}$	$[30, 20, 10]$	$[-30, -20, -10]$	$[-5, -10, 5]$

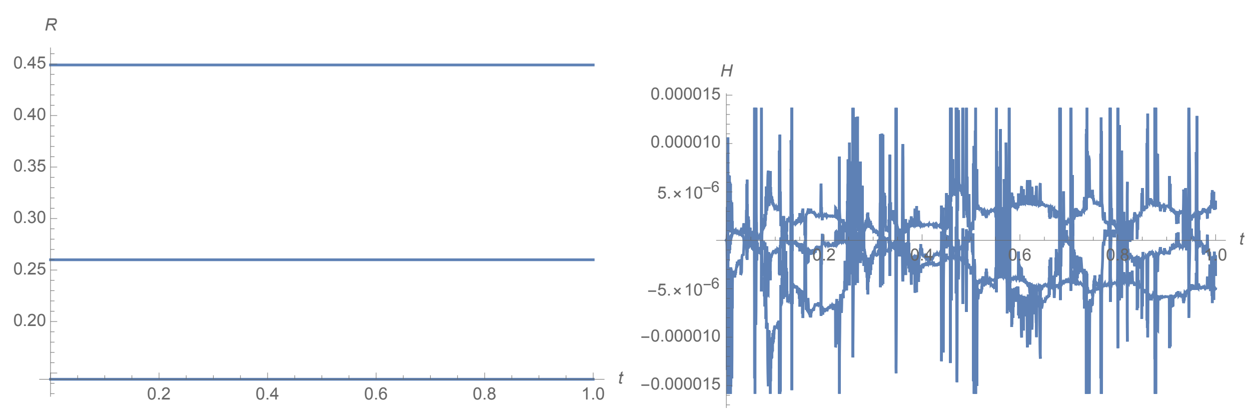

(a) System Barycenter

(b) Angular Momentum

Figure A.5: Three panel simulation validations.